Elastic-Plastic behaviour of AlSiC metal matrix composite rod under combined tension and torsion loading

by

Padmanabhan Raghupathy, M.E.

This thesis is submitted to Dublin City University as the fulfilment of the requirement for the award of the degree of

' Doctor of Philosophy

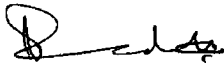Supervisor,   Professor M S J Hashmi, Ph D , D Sc ,
Co-supervisor   Dr B J MacDonald, Ph D

School of Mechanical and Manufacturing Engineering
Dublin City University

September 2003

DECLARATION

I hereby certify that this material, which I now submit for assessment on the programme of study leading to the award of Doctor of Philosophy, is entirely my own work and has not been taken from the work of others save and to the extent that such work has been cited and acknowledged within the text of my work

Signed _____ Date _25| o9 |o3_

Padmanabhan Raghupathy

Student ID 98971255

ACKNOWLEDGMENT

To my mother Hemalatha and father Raghupathy

ABSTRACT

Most machine components and structural members are subjected to complex loading conditions during service. Typical complex loading conditions can be observed in the case of a bolt. When a bolt is tightened to bring machine components together, stresses such as tensile stress (clamp load/area), and torsional or shear stresses (proportional to applied torque) are developed in the shank and bolt threads. To simplify the complex relationship between tightening torque, friction co-efficient and the preload in the fastener, a circular rod is chosen to represent the problem. Investigations were carried out to determine i) how the external tensile load affects the magnitude of the initially applied torque, and ii) how application of torque affects the initially applied axial load or preload in a specimen in elastic-plastic range

A preliminary study on copper specimens was undertaken to gain knowledge about elastic-plastic behaviour under combined tension and torsion loading. Various combinations of combined tension and torsion loading conditions were applied on the specimens to establish the proper functioning of a recommissioned tension-torsion machine and a dedicated LabVIEW program

Experimental investigations on AlSiC MMC rod specimens reveal that the rod can sustain combined axial load and torque well beyond the combined initial yield curve. When the specimen is subjected to an initial axial load or torque followed by torque or axial load respectively, the subsequent load or torque becomes dominant in describing the elastic-plastic behaviour of the specimen. The initial load or torque in the specimen does not affect the subsequent torque or load carrying capacity of the specimen

A specimen subjected to a constant relative extension and angle of twist can sustain the combined axial load and torque well beyond the combined initial yield curve. It is apparent that the specimen carries relatively higher axial load when the load-torque path is closer to the axial load axis. Similarly, the

specimen carries relatively higher torque when the load-torque path is closer to the torque axis

In addition to the experimental investigation, a comprehensive finite element modelling of combined tension and torsion loading of a model was undertaken that includes both geometric as well as large deformation effects for capturing axial and shear stresses

A methodology for the finite element analysis of solid rods under combined tension and torsion loads was developed The numerical models have successfully captured the basic features of the elastic-plastic response of the AlSiC metal matrix composite and demonstrated the effect of particle inclusion in the overall flow properties of the composite, while demonstrating some limitations

LIST OF FIGURES

LIST OF TABLES

NOMENCLATURE

Notation	Description
σ	Axial stress
τ	Shear stress
Y	Yield stress
l	Length
θ	Angle of twist
ϕ	Twist per unit length
h	Height
ε	Axial Strain
γ	Shear Strain
η	Nominal combined axial strain to shear strain ratio
E	Young's Modulus
G	Shear Modulus
r	Radius
a	Radius of the rod
c	Inner radius of the plastic region in a rod
L	Axial load
T	Torque
$\bar{\sigma}$	Effective stress
$\bar{\varepsilon}$	Effective strain
H'	Slope of the effective stress to plastic strain
N	Strain hardening parameter
T_x	Temperature
ℓ	Grain diameter
d	Deformation rate
λ	Lame's constant
s	Cauchy Stress

Notation	Description
D_2	Second invariant of plastic deformation 'd'
J_2	Second invariant of Cauchy Stress 's'
$\overline{U}$	Virtual Displacement
f^B	Externally applied body force
f^{S_i}	Externally applied Surface Traction
R_C	Concentrated load
$H^{(m)}$	Displacement interpolation matrix for element 'm'
$\hat{U}$	Displacement vector
K	Stiffness matrix
$^t R$	Nodal point force vector at time 't'
$^t F$	Nodal point force
Δt	Time increment
T_n	Transformation matrix

CONTENTS

Chapter 4 Experimental Programme

Chapter 5   Experimental Results and Discussion

Chapter 6   Conclusions   216

1 INTRODUCTION

1 1 BASIC PRINCIPLES

Most structural materials undergo an elastic state before a plastic state is reached This applies to both material behaviour of a cross-section and the structure as a whole For a structural member under increasing load, the variation of the load from a fully elastic state to a fully plastic state is shown in Figure 1 1 It can be observed that each point termed plastic hinge, corresponds to a fully plastic state of a certain cross-section in the member The elastic state of the member corresponds to a load level below the first plastic hinge The elastic-plastic state of a member corresponds to a load level between the first and the last plastic hinge Analysis at this load level is called elastoplastic or elastic-plastic analysis The slope of the curve indicates the relative stiffness of the structure, the stiffness decreases as more cross-sections become plastic Elastic-plastic design makes use of the reserve strength beyond the elastic state of the structure, and this *reserve strength* was obtained due to the strain hardening property of the material Strain hardening occurs when a metal is strained beyond the yield point Plastic deformation of the metal creates dislocation Upon extensive deformation, dislocations multiply and increase the strength of the metal An increasing stress is required to produce additional plastic deformation and the metal apparently becomes stronger and more difficult to deform Plastic deformation beyond yield point of the metal requires an increasing load but at a decreasing rate The reserve strength of a structural member, which allows the members to be loaded just over the yield load, is utilized in the elastic-plastic design of the members As a result, a more economical design due to material saving can be achieved when using an elastic-plastic design method

Standardised test procedures such as tension testing, torsion testing, and bend testing are carried out on material to determine its mechanical properties such as Young's

modulus, Yield strength, and Ultimate strength These test procedures can predict with some certainty how the material will behave in actual service Yet, these uniaxial tests were found to be inadequate to describe the material behaviour completely Most machine components and structural members are subjected to complex loading conditions during service Typical complex loading conditions can be observed in the case of a bolt When the bolt is tightened to bring the machine components together, stresses such as i) tensile stress (clamp load/area), ii) torsional or shear stresses (proportional to applied torque) are developed in the shank and bolt threads In addition to these stresses, thread friction and frictional forces between the component surface and nut face are also developed during bolt tightening
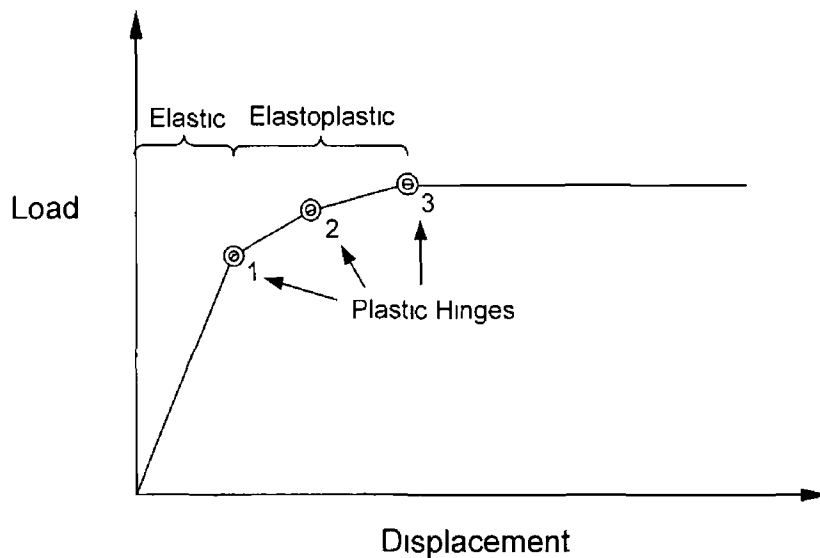
Figure 1 1 Elastic-Plastic state of a structural member

1 2 INTRODUCTION TO THE RESEARCH TOPIC

Structural elements and machine components are usually designed so that material does not yield beyond a plastic strain of the magnitude of the elastic strain under the expected loading conditions The magnitude of the stress, which causes the material to yield under uniaxial or combined loading, can be predicted well using various theoretical 'yield criteria' Structural engineers and machine designers are much concerned with elastic-plastic problems where the plastic strains are of the same

2

order of magnitude as the elastic strain With much attention being paid to the saving of weight in aircraft, missile and space applications, designers can no longer use large factors of safety and designing must be done for maximum load to weight ratio, and this inevitably means designing into the plastic range

Deformation in the elastic-plastic range is more difficult to calculate than elastic deformation because the relationships between the stresses and strains are non-linear and are dependent on the loading history Furthermore the stress distribution in most structural members loaded into the elastic-plastic range is also difficult to determine, because the shape of the elastic-plastic interface is itself related to the stress distribution and is therefore unknown until the complete solution is found However, for a solid circular rod subjected to combined torque and tension, this restriction is removed since the shape of the interface must be annular to preserve axial symmetry [1] One of the many applications wherein a solid circular rod is subjected to combined tension and torsion loading condition is the bolt

1 3 INDUSTRIAL APPLICATION

Greater demand for safety, reliability and maintainability are being placed on products through government regulations and consumer pressure On the other hand, companies are trying to cut raw material cost, improve design and enhance manufacturability Since almost all manufacturing involves some form of component assembly, one logical place to tackle the problem is in the items and methods used to hold these components together

Assembly applications can be classified into three categories as,

- Permanent joints, created by welding two components,
- Semi-permanent joints using rivets or pins and,
- Temporary Joints using bolts and nuts, screws, etc ,

Fastening bolts are still the most frequently used method in joint technology They are by far the most commonly used system for achieving safety, reliability and maintainability

3

Designers are reducing the margin of safety that is built into the machine This change is accountable to the aerospace industry, which works with a very low safety factor as the maximum expected load This forces fastener systems into more acute performance ranges Considerable investigations are still being carried out into bolted joints, especially into quality of the tightening involved and into the bolt itself Bolted joints still pose many problems for engineers, since they involve complex parts working under severe and often limiting conditions

The design and assembly of bolted joints must assure that the joint remains tightly clamped and the fastener is capable of withstanding the static and dynamic loads that are applied Service performance of the joint depends on many factors, such as the properties of the fastener material and the structure being clamped, response of the bolt and the joint under additional load, the tightening process and lubrication It is well known that during the tightening process a fastener is subjected to torsion as well as axial stress conditions Subsequently, when the joint is subjected to external load, the fastener is subjected to additional axial load due to external load It is expected that the plastic yielding of the fastener would occur when the combined axial stress and shear stress value reaches a maximum axial stress governed by von Mises yield criteria, after which the bolt starts deforming producing instability It is important that the components for structural application are designed to experience a maximum load that produces least or no significant deformation

1 4   METAL MATRIX COMPOSITES

Another logical area of improvement is in the material itself Metal matrix composites offer the opportunity to tailor a material with a combination of properties unavailable in any single material Combining the very high tensile strength and modulus of elasticity of silicon carbide particles with the low density of aluminium, a composite material with a higher strength-to-density or modulus-to-density ratio can be obtained The properties thus obtained in a composite material are superior to any known single alloy In addition, because the reinforcing agent in the composite has a relatively high melting point,

4

barring degradation of the fibre by chemical interaction with the matrix, the strength properties of the composite can be retained at relatively high temperatures

In metal-matrix composite an interaction between components does usually occur which leads to interface layers with their own properties The influences of such layers on the behaviour of composites are as follows

- The plastic properties of the matrix near the more rigid fibre can be different from those of the bulk matrix

- An intermetallic compound formed at the interface can give rise to an increase in the strength of a composite to some extent, if this third component is strong enough

- Cracking of a brittle interfaced layer can give rise to an apparent increase in the ultimate stress of a fiber similar to the increase of the limiting stress of a rigid-plastic specimen with a notch

1 5   COMBINED TENSION AND TORSION LOADING

In recent times, more attention has been paid to the experimental investigation and analysis of results using simulation packages to determine the mechanical behaviour of material, under complex loading conditions since uniaxial experiments have been found to be inadequate for revealing the material behaviour completely Experiments carried out by Ali and Hashmi [2] on circular steel rod subjected to combined torque and tension loading reported that the shear stress and axial stress relationship was found to be non-linear Similar experiments carried out by Meguid et al [3-6], to determine the behaviour of thin walled tubular specimen made of Mild steel (En8) under non-proportional straining gave results in good agreement with the von Mises yield condition It is possible to obtain almost the entire positive quadrant of the yield curve from a single test, without unloading and reloading the specimen Further, it was found that at constant angle of twist and increasing the axial load, the experimental shear stress trajectory follows the von Mises yield curve upto a point and subsequently deviates, crossing the von Mises yield curve This can be attributed

5

to the deformation prior to and during the onset of necking of the specimen [7] This research describes the investigation made on the behaviour of copper and AlSiC metal matrix composite material under combined tension and torsion loading The specimens were subjected to different combined loading paths using a purpose built tension-torsion machine to establish the behaviour in the elastic-plastic region until failure Four different types of biaxial nonproportional loading paths were considered In addition, the specimens were subjected to different proportional tension and torsion loading paths The results from the experiments were analysed and found to be consistent with the theoretical analysis of the combined load test based on the Ideal Plasticity Theory, namely that there is no one to one relationship between stress and strain over the yield plateau

In this respect, it was felt that investigation should be carried out to determine how the external tensile load affects the magnitude of the initially applied torque or how the application of torque affects the initially applied axial load or preload in a fastener in the elastic-plastic range To avoid the complex relationship between tightening torque, friction co-efficient and the preload in the fastener, a circular rod was chosen to represent the problem However, during the tightening process other stress components do arise due to the effects of the helix angle and the geometry of the thread, the effect of these stresses were not considered in this study because of the simple design of the test specimen Most of the existing research works concerning the elastic-plastic response of materials have been conducted using thin-walled tubes for the sake of simplicity of analysis since the area under consideration is minimal and subsequently the stress variation is negligible, as the linear elastic torsion theory stipulates that the maximum shear stress occurs at the outer fiber of the material

1 6 FINITE ELEMENT ANALYSIS

The finite element method has become a powerful tool for the numerical solution of a wide range of engineering problems In the finite element method of analysis, the structural member defining a continuum is discretised into simple

6

geometric shapes called finite elements The material properties and the governing relationships are considered over these elements and expressed in terms of unknown values at element corners An assembly process, considering the loading and constraints, results in a set of equations Solution of these equations gives the approximate behaviour of the continuum The finite element software package ANSYS was used to numerically simulate the experimental tests Copper and AlSiC MMC models were simulated on a macro scale for validation of the test results The model was subjected to combined tension and torsion loading conditions The mechanical behaviour of the models were investigated and compared with the experimental results

1 7 SUMMARY

This chapter introduced the elastic-plastic analysis of a structural member, specifically a circular rod subjected to combined tension and torsion loading conditions Industrial applications for such loading conditions were observed to exist in *bolts* Designing a bolt in the elastic-plastic range, when the order of plastic deformation is same as elastic deformation, could reduce the weight of the bolt and consequently the assembly considerably Contribution from high strength and low density AlSiC MMC material enables further reduction in weight of the bolt

2 LITERATURE REVIEW

2 1 INTRODUCTION

To date experimental investigation on combined stresses has been concerned with the validation of test results with analytical and numerical solutions of the elastic-plastic stress-strain relationships proposed by various investigators and verification of different yield criteria A yield criterion is a hypothesis concerning the limit of elasticity under any possible combination of stresses Interpretation of yield criteria is possible either mathematically or by physical justification by conducting experiments The latter approach was mostly followed in this investigation The determination of the axial stress distribution in a rod during plastic yielding in tension is simple, whereas the determination of the shear stress distribution during plastic yielding in torsion becomes complex which restricted the use of a solid rod specimen to reveal the stress-strain relationship under combined tension and torsion loading paths In a rod subjected to torque, yielding starts at the outer periphery of the rod and progresses towards the center Most of the early investigators used thin walled tube specimens to reduce this complexity Moreover, as detailed experimental work under combined axial and torsion loads involves complex loading paths, and hence the need for a versatile test machine, very few attempts have been made to study the behaviour of solid rods This chapter presents a review of the earlier investigations carried out mostly on thin walled specimens and few on solid circular rods

2 2 A REVIEW OF PREVIOUS RESEARCH WORKS IN COMBINED LOADING PATH

2 2 1 Solid circular rods

D S Brooks [1] presented an analysis of a round bar carrying both proportional and non-proportional loading combinations of axial force and torque, to study the effects of compressibility, strain-hardening and monotonic loading paths Ramberg-Osgood curves were used to describe the material behaviour and Prandtl-Reuss incremental

8

stress-strain law and the von Mises yield criterion for analysis (see Appendix-B) Numerical results for both proportional and non-proportional loading conditions were obtained and it was concluded that the transverse stresses arising from elastic compressibility are extremely small in comparison with axial and shearing stresses and may be neglected for all practical purposes In problems involving elastic-plastic deformation, the plastic strain rates may vary with position and time by several orders of magnitude, even for constant total deformation rates For certain metals and alloys, such large variations in plastic strain rate cause significant changes of flow stress

Ali and Hashmi [2] carried out experimental investigations on the elastic-plastic response of a circular rod subjected to non-proportional combined torque and tension loading When the rod is initially subjected to a torque and then, keeping the corresponding angle of twist constant, to a gradually increasing axial load, the rod behaves as if its torque carrying ability has been drastically reduced without in any way affecting its axial load carrying ability Similarly, when the rod is initially subjected to an axial load and then keeping the corresponding axial displacement constant, to a gradually increasing torque, the rod behaves as if its load carrying ability has been considerably reduced without in any way affecting its torque-carrying ability The mechanisms of such reduction in loads were compared with the theoretical predictions based on Gaydon's analytical model [10]

Swift [9] presented the results of a study on the effects of large torsional strains upon the subsequent extensional behaviour of low carbon steels According to Swift, if the torsional prestrain exceeds a given value the specimens failed in a brittle manner when subsequently loaded in tension - the fracture being distinctly different from the normal cup and cone failure which is obtained with smaller torsional pre-strains Swift also found that if there is a reversal to the original condition the large torsional deformation apparently does not affect the ability of the steel to carry tensile loading applied along the longitudinal axis of the specimen

Gaydon [10] developed analytical expressions for the stress distributions and deformations of solid circular bars subjected to combined tension and torsion in the elastic-plastic range The analysis was restricted to a material with a specific Poisson's ratio, (a value of 0 5) and the effect of elastic compressibility was not considered Gaydon considered various combinations of twist and extension and derived expressions for shear stress and axial stress of a cylindrical bar subjected proportional and non-proportional loading in elastic and plastic regions The Reuss equations were used throughout and these were integrated, for different cases, to give the shear stress and tension in the plastic range The stresses rapidly approach their asymptotic values and are within 1 or 2 percent of these values when the plastic strains are still of the same order as the elastic strains

Rockey [11] tested solid rod specimens with large initial torsional strains and subsequent extension in tension He observed that up to a certain value of torsional prestrain the change in ductility is small and the form of fracture being normal cup and cone Whereas for higher torsional prestrains, the specimen failed in helical, low ductility manner with the specimen sheared along the helical plane that experiences the high compressive prestrain For the given testing condition, the transition prestrain was observed to be 47-49 percent The results show that large shear strains reduces the materials subsequent extension ductility, the material failing on those planes subjected to compression in the torsional pre-strain Contrary to Swift's [9] claim that the reversal to the original condition after large torsional deformation will not affect the ductility of the material, Rockey's work claims that large torsional deformation would reduce the ductility of the specimen and the specimen has not returned to exactly the same condition as the unstrained material, on reversal of the torque

Gardiner [12] explained the relationship between torque and tension According to his report, the relationship between torque and tension was governed by both direct and indirect parameters The direct parameters consists of tangible items such as fastener strength level, surface finishes, hardness of the components, lubrication, class of thread fit and resiliency of the clamped assembly The indirect parameters consists of

10

intangible items which affect this relationship and are related to operation performance, assembly methods, tool driver speed, etc , Torque which is the input variable in the relationship represents strain and every rotation on the screw thread produces an elongation in the bolt producing a tension (stress) in the fastening system The response of a fastener system to the assembly operation induces a load on the bolt, which includes axial load and torque, and prevents product failures The combined load should fall within 50-85% of the ultimate strength where optimum vibration resistance occurs

Chapman et al [13] analysed the mechanism of tightening bolted joints and the stress distribution in the bolt They observed that the bolt tightening operation induces both torsional and tensile stresses The bolt behaves elastically when external loads are applied to the joint even when the bolt was tightened to its tension-torsion yield point When the bolt is tightened to the tension-torsion yield point, the joint can withstand higher working loads before opening In addition, fatigue strength of the joint is increased to its maximum value because fatigue failure mainly occurs when the joint opens

2 2 2 Thin Tubes

The conditions under which various materials begin to deform plastically have been the subject of many experimental investigations from the late 18th century Among these investigations are the tests on rock materials, marble and sandstone, zinc and steel and concrete under combined stress Tests on other metals such as iron, copper, nickel, and mild steel were also reported in reference [8] The most detailed experimental investigation under combined stresses in the elastic-plastic range has been carried out by Lode [7]

Meguid and Campbell [3] carried out a number of investigations, both theoretical and experimental, under combined torque and tension for rate dependent material Thin walled circular tubes of both elastic-perfectly plastic and work hardening materials were used in their work Bilinear deformation paths of twist at a constant rate followed by extension at different rates were examined to evaluate the plastic flow of

the material under abruptly changing deformation paths and strain-rates Experimental results were compared with the existing strain-rate dependent theory The experimental results indicate that there exist appreciable differences between the von-Mises equivalent stress versus equivalent plastic strain curves for the different bilinear paths investigated These differences were attributed to strain rate sensitivity of the particular material However, in almost all their experimental works they have considered only one non-proportional biaxial loading path, i e , torsion followed by tension keeping angle of twist constant Numerical solution for various proportional and nonproportional straining paths were obtained The radial and hoop stresses were found to be small compared to the normal and shear stresses on the cross section A closed-form analytical solution has been derived on the assumption that the elastic strains are negligible A series of fully plastic limit loci, each corresponding to a given maximum effective strain rate, for quasi-static straining, an explicit equation for the locus has been obtained

Meguid et al [4] carried out experimental investigation on thin-tubular specimen of annealed mild steel (En8) under combined proportional and nonproportional straining The lower yield region of the proportional tension and torsion loading paths is clearly evident by a segment of neutral loading along yield locus, while the upper yield points are only apparent for cases where the resulting load-torque path in the elastic range is close to torque axis When the combined stress path is closer to the axial stress axis, as soon as the combined axial stress and shear stress reaches von Mises yield curve, the combined stress path follows the yield curve shortly before proceeding in the normal direction to the yield curve When the combined stress path is closer to the shear stress axis, the combined stress path crosses over the yield curve shortly and falls back to the yield curve before proceeding in the normal direction to the yield curve In the non-proportional deformation path the load-torque trajectory during the axial extension at constant angle of twist traced almost the entire positive quadrant of the von Mises yield curve Due to strain hardening little deviation from the von Mises yield curve is observed due to rate-sensitivity of the material

Meguid [5] carried out experiments on strain-gauged thin-walled tubular specimens of annealed medium carbon steel (En8) at room temperature in combined twisting and extension Bilinear deformation paths of twisting at a constant rate followed by extension at three different strain rates were investigated The results indicate that there exist appreciable difference between the von Mises equivalent stress and equivalent plastic strain curves for the three strain-rates investigated These differences are attributed to the rate-sensitivity of the material The plastic strain-rate vector direction initially approaches the direction of the tensile axis much faster than the deviatoric stress vector It was found that neither the Perzyna rate-dependent law (see Appendix-B) nor Prandtl-Reuss rate-independent law could account for the non-coaxiality between the plastic strain-rate and deviatoric stress vectors observed for the adopted bilinear path

Meguid and Klair [6] investigated the plastic behaviour and work-hardening characteristics of medium carbon steel (En8) Perzyna's visco-plastic constitutive law for strain-rate sensitive and work hardening material behaviour, and the strain-rate independent theory of Prandtl and Reuss were compared with the experimental results According to Meguid, both Perzyna's visco-plastic constitutive law and theory of Prandtl and Reuss gave good agreement with the time histories of the lack of coaxiality between the plastic strains and stress trajectory However, neither of these theories could account for the lack of coaxiality between the plastic strain-rate and deviatoric stress vectors observed in the experimental results for the bilinear deformation path

Hohenemer [14] also carried out experimental investigation to verify the validity of the Reuss-stress-strain equations, which allows for the component of the strain in the Levy-Mises equations Hohenemer carried out tests under two different sets of critical conditions one in which the twist is such that the bar is all elastic initially, the other in which the twist is such that the bar is plastic to a given radius initially Pre-strained mild steel thin tube specimens were used to secure a sharp yield point and reduce the rate of hardening to a value small compared with the elastic modulus

13

However, no conclusion was found regarding Hohenemser's experiments from any published paper

Taylor and Quinney [15] used aluminium, copper and mild steel tubes, which were nearly isotropic, to test in combined tension and torsion to verify different yield criteria Thin walled tubes were first subjected to tension into the plastic range and then partially unloaded and twisted until further plastic flow occurred The axial load was held constant while the torque was increased, so that axial and shear stress ratios were not constant The torque-twist or torque-extension diagrams were extrapolated back to zero twist or zero extension to establish, fairly accurate torque at which plastic flow recommenced The degree of anisotropy was kept within allowable limits by observations of the change in internal volume of the tubes during pure tension By first straining each specimen in tension, they were able to pre-strain the material by any desired amount and to detect anisotropy in the material Although Taylor and Quinney ignored the possibility of an elastic increment of strain during plastic flow, they also found the same results regarding the von-Mises yield criteria and concluded that the deviation from the von-Mises criterion was real and could not be explained based on experimental accuracy or isotropy

Morrison and Shepherd [16] subjected thin hollow tubes to tension and torsion to follow a complex path of stress to compare the experimentally found strain paths with those calculated by Prandtl-Reuss and Hencky stress-strain relations Here plastic and elastic strains were comparable The material used was 5 percent nickel steel and 11 percent silicon-aluminium alloy They applied first tension, and then holding the tensile stress constant, applied torsion, followed by further tension and torsion to obtain various strain paths The measured variations of length and twist were in substantial agreement with the predictions of the Reuss equations

Naghdi et al [17] carried out tests with aluminium alloy tubes 0 75 inch internal diameter and 0 075 inch thickness The tubes were initially subjected to tension, followed by torsion with the tension held almost constant, the tube remaining elastic but approaching yield Both tension and torsion were then increased until yield had distinctly occurred Several tests to this kind with various ratios of

14

torsion and tension thus provided data for an initial surface. The loading on each of the tubes was, after complete removal, followed by a re-loading in torsion to a chosen value, and then full unloading. Each tube was subjected to the same sequence of testing as was previously the case and until yielding was again evident. The data from this set of experiments enabled a first subsequent yield surface to be found. A second subsequent yield surface was calculated from further tests on the tubes after a second reloading to a chosen value of torsion, one that was larger than the initial torsion. Most surprising in these results is the lack of cross-effect that torsion produced, prior over strain in torsion apparently had no effect whatsoever on the uniaxial tensile yield stress. The change of shape of the initial von Mises yield curve with increasing pre-tension indicates that isotropic strain-hardening theories are somewhat away from reality

Daneshi and Hawkyard [18] built a tension-torsion machine using hydraulic system for load application. Aluminium and Copper tubular specimens were subjected to extension and twisted while being immersed in liquid nitrogen at 78°K. At 78°K and 292 K, he observed that the elastic parts of the stress-strain curves appear to coincide and the elastic moduli for aluminium and copper increase by about 3-4% with a decrease in temperature from 292°K to 78 K. The limit of proportionality increased for copper at 78°K while the results for aluminium do not clearly support this point. For both aluminium and copper, the work hardening rate was higher at 78°K than 292 K. In reference [19], tubular specimens made of aluminium and copper were tested at room temperature and 78 K, to determine initial yield surface and subsequent yield surfaces after pre-strain in tension and torsion. The results support the von Mises yield criterion as being suitable for defining initial yield at 78 K for a homogeneous and isotropic material. However, there seems to be distortions and translations of subsequent yield surfaces at 78°K and at room temperature. The specimens subjected to loading and reverse loading shows strong Bauschinger effects and little cross effects in the initial and subsequent yield surfaces on perpendicular loading. Initial and subsequent yield surfaces are smooth and convex and strain increment vectors are almost normal to the yield surface

15

Ohashi and Tokuda [20] investigated the plastic behaviour of thin-walled tubular specimens of initially isotropic mild steel under combined loading of torsion and tension The specimens were subjected to stress trajectories consisting of two straight lines at a constant rate of the effective strain The specimens were subjected to tensile or torsional prestrain followed by torsion or tension loading respectively The specimens were also subjected to combined tension and torsion loading after tensile or torsional prestrain It is found that the effect of the third invariant of the strain tensor appeared even for proportional deformation consisting of torsion and axial force Moreover, it is observed that the effective stress drops suddenly with increasing effective strain, and coaxiality between the stress deviator and the plastic strain increment tensor is seriously disturbed just after the corner of the strain trajectory

Phillips and Lu [21] presented results of combined stress experiments with tubular specimens of pure aluminium with stress controlled and strain controlled loading It is observed that creep straining appeared during stress controlled experiment and stress relaxation occurred during strain-controlled experiments Furthermore, they proposed the existence of three regions in stress space a) the region inside the yield surface, b) the region between the yield surface and loading surface, c) the region outside the loading surface A motion of the stress point inside the yield surface produces only elastic strains and it leaves both the yield surface and the loading surface unchanged A motion of the stress point between the yield surface and the loading surface leaves the loading surface unchanged but moves and changes the yield surface, and, in addition, small plastic strains are generated A motion of the stress point towards the outside of the loading surface moves and changes both surfaces and generates plastic strains which are larger than those generated by a comparable motion located between the two surfaces

Khan and Wang [22] carried out experiments on thin-walled tubes made of annealed polycrystalline copper subjected to loading, partial unloading, and then loading in a different direction The experimental data were compared with the

predicted values from the Ziegler and Mroz kinematic hardening models, and the endochronic theory (see Appendix-B) The experimental observations confirmed that the plastic strain increment vector is neither coincident with the deviatoric stress vector, nor is in the direction of the deviatoric stress increment vector, after sudden directional change of loading path Therefore, constitutive models without back stress cannot predict the direction of plastic strain increment correctly for the entire loading path within the prestress loading surface Among the three models, the predictions of the Mroz kinematic hardening model were shown to agree quite closely with the experimentally determined directions of plastic strain increment, especially when the strains reached the larger extreme of the infinitesimal deformation region

Ikegami and Niitsu [23] carried out experimental investigation on the plastic deformation of thin-wall tubular specimen in complex loading conditions The effect of plastic prestrain on the subsequent loading and the stress-strain curve was examined The subsequent loadings were carried out at a different temperature from that of the prestrained temperature The testing temperature ranged from room temperature to 600° C It is observed that

    i)   The plastic hardening is remarkable in the transverse direction to prestraining and the hardening behaviour is represented by the egg-shaped equi-plastic strain surfaces,

    ii)   The effect of temperature history on flow stress is small for monotonic loading, but the effect is observed in the stress-strain relations in reverse loading,

    iii)   The creep strain had the same hardening effect as the plastic strain at room temperature However, the effect of creep strain on plastic hardening is weak at high temperature compared with that of hardening by plastic strain

Wu and Yeh [24] investigated the factors affecting the experimental determination of yield surfaces, such as the elastic moduli and the zero offset strain and the strain domain The initial and subsequent yield surfaces of

17

annealed AISI type 304 stainless steel tubular specimens were determined in the axial-torsional stress space The definition of yield of $5\mu\varepsilon$ equivalent plastic strain was used in the experiments Using a single specimen, the initial yield surface and eight subsequent yield surface were determined The effect of prestrain on subsequent loading was also examined

i) The yield surfaces are both translated and distorted during the course of plastic deformation The translation was found to be in the direction of prestrain or prestress The distortion pattern of the yield surfaces is related to the direction of prestrain or prestress as well

ii) The yield point can be influenced by the number of data points used to approximate the elastic moduli, the corresponding zero offset strain, and the orientation of the probe, but the probing rate has negligible effect

iii) There are uncertainties and difficulties in the determination of the centre of yield surfaces

Jiang [25,26] reported the plastic deformation of thin-walled tubes subjected to combined axial and torsional loads to probe the classic kinematic hardening theory (see Appendix-B) that predicts the material behaviour under non-proportional loading conditions It is observed that the material behaviour is strongly path-dependent, and some extra hardening effect, which varies with the extent of non-proportionality and the kinematic hardening rule has certain capability to describe such path dependency and extra-hardening effect, and that these effects disappears when the steady state is reached It was concluded that the linear kinematic hardening rule gives different material response for different loading paths The material exhibits higher hardening under non-proportional loading as compared to that under proportional loading and this difference cease to be significant at larger stresses

Wu et al [27] conducted experiments on cast and extruded high purity aluminium tubular specimens under monotonic large strain torsion condition Both free-end and fixed end torsions were studied Shear stress-strain curves obtained from free-end and fixed-end torsion tests of long, medium and short specimens were found to be consistent Axial extension increases with shear strain in free-end

18

torsion Hoop strain in free-end torsion is of significant magnitude compared with axial strain at large shear strain level Axial stress is always in compression for the fixed-end torsion and it is significantly influenced by temperature

Khan and Cheng [28], the predictions made in reference [22] were compared with the experimental stress and strain data on copper specimen The multiple directors model for the description of anisotropic plastic behaviour includes two elastic constants G and v along with eight material parameters Most of the material parameters in the model were estimated from experimental data from one-dimensional stress-strain relation and a subsequent yield surface The determination of the remaining material parameters was completed through the numerical implementation of the model According to Khan, a practical anisotropic elastic-plastic constitutive model can describe polycrystalline metals in terms of a large number of randomly distributed director-slip systems

Liang and Khan [29] investigated four constitutive models to predict the mechanical behaviour of the materials in comparison to experimental results The models under consideration were Johnson- Cook (JC) model, Zerilli-Armstrong (ZA) model, Bodner-Parton (BP) model, and Khan-Huang (KH) model (see Section 3 2) According to Liang, JC model has the inherent problem of describing the work-hardening behaviour of metals, such as tantalum, where the work-hardening rate decreases when strain rate increases ZA model does not describe the work-hardening behaviour of materials with strong temperature and strain rate dependencies BP model does not consider the temperature effect Modification of the model leads to increase in material constants The KH model is more capable of predicting the strong work-hardening behaviour in a large strain-rate range than that of the BP model The strain and strain rate must have coupled effect on the description of work-hardening relation of the materials to predict the work-hardening behaviour

Liang and Khan [30], in succession to the previous paper [29], described the elastic-plastic behaviour of three body-centred cubic metals, tantalum, tantalum alloy with 2-5% tungsten, and Aermet 100 steel over a range of strains and strain

19

lates and temperatures A new viscoplastic model was proposed based on the experimental results The material constants of the proposed constitutive model were determined using the uniaxial loading experimental data The proposed constitutive model gives an excellent correlation with the experimental data over a wide strain-rate and temperature range for finite deformation According to them, the agreement between predictions and measured responses was found to be almost perfect

Ishikawa [31] proposed an elasto-plastic constitutive model for large torsional strains using three kinds of equiplastic strain surfaces, a yield surface and two other surfaces from which the power law for stress-strain relation is confined The proposed model is for macroscopic plasticity and the concept in the model is based on the assumed power law During free-end torsion, an axial strain develops as a manifestation of the evolution of deformation – induced anisotropy, and an axial stress is induced during fixed end tests The model predicts these phenomena SUS 304 stainless steel specimens were used for the experiments and were subjected to solution heat treatment before testing Tests were carried out at two different strain rates to study the effect of strain rate on the stress-strain relationship There is a significant difference in the experimental results at the two strain rates, while there is no noticeable difference between the results with fixed end and free end

Khan and Liang [32] carried out experimental investigation to demonstrate the capability of the constitutive model created in the previous paper to predict the behaviour of three BCC metals during nonproportional multiaxial loading The tantalum, tantalum alloy and Aermet steel thin-walled cylindrical specimens were subjected to nonproportional torsion-tension and biaxial compressive experiments to show the material behaviour at finite strain and wide strain-rate range In the torsion-tension loading, the specimen was subjected to free-end torsion first, followed by tension (holding torque constant), and then torsion again (holding force constant) A dramatic strain-rate reduction is observed when changing from torsion to tension since the rotation increased more quickly in

20

order to keep the torque constant during tension The constitutive model prediction was found quite close to the observed response except in the initial change of direction

Francois [33] proposed a modification of the classical elastic-plastic models including distortion of the yield surface to enhance the modelling of metallic materials behaviour in nonproportional loadings Aluminium alloy 2024 T4 tubular thin-walled specimens were used for experimentation under both proportional and nonproportional tension-torsion loading paths The stress deviator S involved in the classical von Mises based expression was replaced by a new distorted stress S_d The proposed new yield criterion allows a simple modelling of the distortion of yield surfaces and has many possible applications such as metal forming, fatigue, forming limit curves, etc ,

Dominique and Cailletaud [34] described the macroscopic behaviour of single-crystal superalloys under tension-torsion loadings on tubular specimens Finite element analysis was used to analyse the complex stress redistributions arising in the specimen The plastic flow was in pure shear for radial tension-torsion for a small amount of tension Then, the torque was decreasing when the plastic flow starts along the axial direction The yield surface was computed from Schmid law Schmid law predicts strain heterogeneity along the circumference of the specimen, while any quadratic criterion, as Hill criterion, predicts a uniform strain distribution

2 2 3 Metal Matrix Composites

Kanetake and Ohira [35] proposed a general theory by connecting the Eshelby's inclusion model and the Ashby's secondary slip model to calculate the flow behaviour, stress-strain curve, of a MMC reinforced by short fibers or particles The theory was established for general combined stress states, in which the effect of shape, size, volume fraction and orientation of dispersing ellipsoidal particle are considered for aluminium MMC dispersed Silicon carbide particles

Adding hard particles can increase the load carrying capacity and the work hardening capacity of a matrix can be achieved by dispersing fine particles

Huda et al [36] similar to Kanatake, carried out analytical study for the stress analysis of MMC The stress was calculated using Eshelby's inclusion model, the Ashby's secondary slip model and Mori-Tanaka's back stress analysis The stress-strain characteristics of the composites mainly depend on the stress-strain characteristics of the matrix material

Shyong and Derby [37] investigated the deformation characteristics of Silicon carbide particulate reinforced aluminium alloy 6061, experimentally and by numerical methods The matrix microstructure was systematically heat treated to natural aged, peak aged, and over aged conditions The tensile strength and stiffness of the composites increased with increasing particle volume fraction for heat treatments if it was over a limiting value The peak-aged specimens had the highest tensile strength, but the natural aged specimen had the highest elongation and ratio of tensile to yield strength The addition of the reinforcing particles causes increase in the stiffness and the ratio of tensile to yield stress, but decreases the strain to failure According to Shyong, the finite element model can predict the overall stress-strain response as well as the local stress and strain fields around the particle However, the model cannot simulate the effect of particle size As the particle size increases, there was a tendency for brittle fracture to occur in preference to debonding of the interface

Sorensen et al [38] reported the analysis of the effect of reinforcement orientation on the tensile response of particle and whisker reinforced metal matrix composites A three dimensional unit cell model was used for numerical simulation The numerically predicted average tensile stress levels are found to be sensitive to small deviations from perfect alignment of the whiskers with the tensile direction The tensile stress-strain response becomes rather insensitive to the precise value of the misalignment angle when the misalignment was sufficiently large The stress levels predicted for a particle reinforced metal show less sensitivity to the reinforcement orientation than found for the short

fibers with aspect ratio 3 For spherical particles whose aspect ratio is unity, there would be no influence of orientation Unit aspect ratio cylinders result in a higher average stress level than the same volume fraction of spherical particles The geometry of the reinforcing phase can have a strong effect on the elastic and plastic response of fiber reinforced and particle reinforced composites

Zhu and Zbib [39] developed a micro mechanically based continuum model to analyse the enhancement of plastic properties of Silicon carbide particulate reinforced aluminium metal matrix composite over matrix materials An energy method was adopted to obtain the overall constitutive relation for the composite based on the local nonuniform deformation fields The energy approach evaluates the macroscopic stress from the rate of plastic dissipation The plastic flow in the composite is strongly dependant upon the particle shape in addition to the volume fraction Particles with large shape index exhibit much more reinforcement than that of spherical particles Prolate particles (whiskers) were more effective than oblate particles (discs) in strengthening the matrix The effect of particle misalignment and clustering were minimal for an aspect ratio of 1, in contrast to large particle aspect ratios where the flow strength drops pronouncedly Composites with ellipsoidal inclusions, either prolate or oblate, have higher strength than those with spherical particles An explicit expression for the composite strength was proposed that accounts for various materials parameters, such as matrix properties, volume fraction parameter, and shape effects

Bhaduri et al [40] described the processing and properties of Silicon carbide particulate reinforced 7010 aluminium alloy matrix composites Addition of Silicon carbide particulate resulted in lower yield and ultimate strengths at room temperature and higher yield and ultimate strengths at temperatures above 200°C compared to base alloy This was due to the premature fracture of the reinforcements in the presence of pre-existing flaws Once the reinforcement fractures the net load carrying capacity of the composite decreases thus resulting in the reduction in the yield stress value The addition of Silicon carbide

23

significantly improves the elastic modulus value The most beneficial effect of Silicon carbide addition was realised at the higher temperatures for the 7010 series alloys

Stefanos [41] investigated the mechanical behaviour of cast Silicon carbide-reinforced aluminium alloy It was reported that Silicon carbide reinforcement substantially increased the work hardening of the material The increase in hardening became more significant with increasing volume fraction of carbide The yield and ultimate tensile strength, and the elastic modulus of the material, increased with heat-treatment and volume fraction of the carbide at the expense of ductility These properties were inferior to those of other reinforced, more complex, aluminium alloys processed by other methods In heat-treated reinforced alloy specimens, the fatigue strength at 10^7 cycles decreases with increasing carbide particle size

Davis [42] reported the flow rule for the plastic deformation of Al-Silicon carbide/Ti particulate MMC Two different types of 3-dimensional models were considered i) a simple cubic lattice of spherical particles and ii) random digital models that are approximately isotropic According to Davis, the second model can reveal the existence of a flow rate The validity of the flow rule in the second model was associated with the absence of shear planes that extend throughout the solid without intercepting any particles Such planes can be drawn in the simple cubic lattice for some shear deformations and particle volume fractions Localised shear bands occurring on these planes results in a shear response essentially identical to that of the unreinforced matrix material

Fang et al [43] described the numerical simulation of particulate reinforced metal matrix composite to predict the effective elastic moduli and elastoplastic stress-strain behaviour Three dimensional finite element simulations on the base of cell models and micro mechanics were used Four particle shapes were considered, spherical, cylindrical, cubic and rectangular parallelepiped In the direction of particle alignment, the weakest composite contains spherical particles, the strongest composite contains rectangular parallelepiped particles,

based on the effective axial moduli The reason was that the aspect ratio of the parallelepiped particle was far larger than that of spherical and cylindrical particles The particle orientation has significant influence on the effective shear modulus The effective shear modulus increases with increase in angle of orientation of the particle with loading axis The work hardening rate increases with increase in particle volume content and the varying particle shape and orientation

Dong et al [44] described the numerical simulation of the mechanical behaviour of short fiber reinforced MMC with a given fiber orientation The flow behaviour of the MMC was investigated by combined cell model in conjunction with the finite element method A combined cell model was developed to represent the geometric description of arbitrarily oriented fibers, taking into account of the fiber aspect ratio and the fiber volume fraction The overall flow behaviour of composites was estimated by averaging and integrating the averaged stress-strain curves of different cells with a weighting fraction of the fiber orientation density

Steglich and Brocks [45] described the Micromechanical modelling of ductile damage by void nucleation due to either particle cracking or particle matrix debonding, void growth and coalescence In this method, the influence of the plastic behaviour and yielding can be separated from the effects of particle size and shape According to Steglich, the principal drawback was that the volume fractions of particles and resulting voids are rather large and hence, violate the basic assumption that the voids are small enough so that they do not interact in the early stages of growth The constitutive equation of Gurson, Tvergaard and Needleman was chosen to describe the behaviour Some discrepancies with respect to the ratio of elongation and reduction of diameter between test results and the cell model was found This discrepancy was due to the following assumptions not being met, i) an initial volume fraction that equals the volume fraction of graphite particles and ii) the voids were spherical and grow in a self-similar shape

Roatta and Bolmaro [46,47] extended the Eshelby model to handle incipient plastic deformation, and to find the elastoplastic field in the general case of ellipsoidal particles under thermal and mechanical loads Under a uniform stress applied at infinity, very far from the particle in the Z-direction, the plastic strain develops in a small region in the z-axis very far from the particle interface According to Roatta, the initial plastic relaxation of the cells transfers stresses to a region located at a zenithal angle of PI/4 and another intense and very localised plastic region develops there The plastic yielding starts spreading all around the particle The finite element simulation illustrated similar plastic yielding as initially localised in the direction of the applied stress and later on spreading around the particle, keeping away from the interface except over the interface at PI/4 The plastic yielding was more intense in prolate inclusions than that in oblate and spherical particles The fiber reinforcement was capable of relaxing stresses by a higher localised plastic deformation The relative importance of the load transfer mechanism of reinforcement was slightly diminished but plastic relaxation provides an additional mechanism for strengthening by stress redistribution

Roatta et al [48] described a generalised Eshelby model allowing interaction among reinforcing particles The influence of interaction among particles over the plastic yielding induced by the presence of inclusions under traction was much more important than the one observed in the case of plastic relaxation due to coefficient of thermal expansions mismatch Spherical inclusions seem to induce higher plastic relaxation volumes for higher volume fractions of inclusions This softening mechanism would predict that stress-strain curves should show a lower slope for higher volume fractions at the onset of plastic strain

Pandorf and Broeckmann [49] reported a microscopic finite element model of a 20% Al_2O_3 particle reinforced 6061 Aluminium alloy MMC under creep loading An idealised unit cell model with a periodic arrangement of particles under plane strain condition was investigated for its creep response The creep behaviour was

found to be strongly influenced by reinforcement particles and the time to fracture was shorter for the reinforced material than for pure matrix material

Rees [50] examined the flow and fracture behaviour of 17% and 25% Silicon carbide particulate reinforced 2124 aluminium subjected to torsion combined with tension or compression The brittle tensile behaviour of an MMC is due to its notch sensitivity Inclusions and poor surface finish increase the stress locally to provide the initiation site for a fracture with limited ductility The stress levels required to yield and fracture the material under tension and compression were similar, but there was a marked difference in their respective ductility's The elements of the classical theory of plasticity such as, i) a von Mises initial yield locus and a plastic potential, ii) isotropic hardening and iii) the normality rule, apply to the particulate MMC

Qin et al [51] reported the effect of particle shape on ductility of Silicon carbide reinforced 6061 aluminium matrix composites Two dimension model composites reinforced with spherical, square, triangle and shuttle-shaped particles were analysed by finite element method The plastic strain concentration in the matrix around the pointed particle corner and residual stress concentration in the pointed particle corner leads to the fracture of the particles at a low level of applied stress, thus decreasing ductility of the composite Eliminating the pointed particle corners decreases plastic strain concentration in the matrix around the pointed particle corner and the possibility of the particle corner fracturing so that ductility of the composite was improved

Poza and Llorca [52-54] investigated the tensile deformation characteristics of 8090 aluminium lithium alloy reinforced with 15% volume percent Silicon carbide particles The influence of the Silicon carbide reinforcements on the deformation and fracture mechanism was significant The unreinforced alloy failed by transgranular shear at approximately 45° where the plastic deformation is localised The failure of the composite, however, was controlled by the progressive fracture of the ceramic reinforcements Particle fracture and damage localisation significantly reduces the composite hardening rate Three

27

Micromechanical models based on the modified shear-lag approach, the Eshelby's equivalent inclusion method, and the finite element analysis of a unit cell, were developed to represent the composite Using the modified shear-lag model, only the tensile strength, and not the complete stress-strain curve can be computed According to Poza, the Eshelby's model was limited to ellipsoidal homogenous inclusions and it was difficult to extend the model to take directly into account the presence of broken reinforcements in the composite These limitations were overcome in the models based on the finite element analysis of a unit cell

Chen et al [55] reported the analysis of three different composite models with 15% volume particles using finite element method for the effect of particle morphology Angular particles with sharp corners, angular particles with blunt corners and circular particles were considered in the analysis Deleting particle sharp corners significantly reduces the local stress concentration in particles Compared with the angular particles, circular particles significantly reduce the local stress concentration in particles If the longer dimension of the angular particle is along the load axis, the angular particles will carry more load than the circular particles distinctly Deleting the particle corners can effectively reduce the possibility of particle fracture, but has less effect on reducing the possibility of matrix ductile failure under the large load

Ismar et al [56] investigated the thermo mechanical behaviour of an aluminium alloy bi-directionally reinforced by antisymmetric continuous fiber lay-up Three different types of reinforcements, isotropic fibres of α-Al_2O_3, Silicon carbide and transversely isotropic carbon were considered The maximum values of inelastic strain were located in front of the isotropic fibers in an area between neighbouring crossed fibers The computation for the carbon fibers exhibits a much more pronounced gradient of the equivalent inelastic strain owing to the small shear modulus The higher the fiber-volume fraction is, the strength and the stiffness of the composite are the larger, with a stress increase nearly linear

to the rise of the fiber-volume fraction All computations were performed under the assumption of a perfectly bonded interface between fiber and matrix

Savaidis et al [57] reported the elastic-plastic finite element analysis for a notched shaft subjected to combined non-proportional synchronous tension and torsion loading The effects of the stress amplitude, the mean-stress and the manual interaction of the cyclic loading components on the mechanical behaviour at the notch-element were investigated The stress amplitude and the mean-stress influence the local elastic-plastic stress-strain response at the notch root The tensile and torsional loadings interact mutually affecting the local elastic-plastic stress-strain response

Kim [58] described the finite element analysis using a generalised axisymmetric element for the plastic deformation behaviour of cylindrical copper samples subjected to torsion The finite element method can simulate the torsional deformation well except for the near-axis region based on the hardness values This was attributed to the limit of the conventional constitutional description, and suggested that non-local effects should be introduced in the constitutive equation

Yang and Qin [59] reported the fiber-fiber and fiber-matrix interaction on the elastic-plastic properties of short fiber composites Numerical results of finite element analysis predict a very high stress domain near the fiber ends due to the material discontinuity When the plastic deformation increases, the high normal stress domain tend to enlarge but constraint from adjoining fibers restrict the deformation of the matrix to continue infinitely The shear stress in the matrix varies sharply near the fiber ends The maximum shear stress appears at the longitudinal interface near the fiber ends The shear stress was transferred from matrix into fiber through the longitudinal interface An increase in fiber content results in a significant increase of the tangent modulus of composites Due to the stress concentration induced by the discontinuity of short fiber, the composite yield at lower level of stress

Lee et al [60] described the study on the stress distribution in particulate Al_2O_3 reinforced Aluminium metal-matrix composites as a function of the interfacial bonding strength The effect of the interfacial strength on the flow response in tension and compression was examined using finite element method The mechanical response in tension was found to be greatly influenced by the interfacial bonding strength between aluminium matrix and ceramic particles With a weak interfacial bonding strength, the elastic region of the stress-strain curve was fairly well predicted by the calculation, whereas the numerical results overestimated the mechanical response in the plastic region showing a higher work hardening rate This difference was attributed to the progressive interfacial decohesion between particles and matrix and the particle cracking during deformation The stress-strain responses and the onset of plastic deformation of the composite with higher interfacial strength were well predicted by the numerical analyses

Cocen and Onel [61] investigated the effect of hot extrusion on the strength and ductility of particulate Silicon carbide reinforced aluminium alloy composites The extruded microstructure has a more uniform distribution of the Silicon carbide particles and the eutectic silicon by comparison with as-cast microstructures The extruded samples have strength and ductility values superior to those of the as-cast samples The addition of increasing amounts of particulate Silicon carbide increases the yield and tensile strength and decreases the ductility The extruded samples of high reinforcement composite exhibited better ductility levels than the forged samples due to the reduction in reinforcement particle size, the absence of particle decohesion, and the improvement of particle-matrix interfacial bond during extrusion process

2 3 SUMMARY

Structural members in many applications are subjected to complex loading conditions Uniaxial tests are incapable of best describing the elastic-plastic behaviour of the material completely Combined loading experiments can

describe the elastic-plastic behaviour of the material closely and satisfactorily Research carried out on solid circular rods and thin-walled tubes subjected to combined tension and torsion loading conditions were presented in this chapter From the literature review presented in sections 2 2 1,2 2 2, & 2 2 3, it is clear that the analytical expressions for axial and shear stress states in a solid rod subjected to combined tension and torsion loading were derived with assumptions such as an elastic-perfectly plastic material model, incompressibility, etc Almost all the research works presented on combined tension and torsion loading were carried out on thin-walled tubular specimens The aim of conducting combined tension and torsion load tests on thin-walled tubular specimens is primarily to determine the material properties, strain-hardening behaviour and initial and subsequent yield surfaces

Previous research works reviewed in section 2 2 2 provides an insight into the effects of different combinations of tension and torsion loading conditions carried on different metallic materials Predominantly tension followed by torsion and torsion followed by tension loading conditions were used In addition, proportional tension and torsion load tests were also carried out to determine the strain hardening and strain rate effects of metallic material behaviour

Previous research works reviewed in section 2 2 3 provides an understanding of the effects of particle inclusion in a matrix material Various numerical investigations were carried out to determine the effects of particle shape, particle size, particle orientation, and particles volume percentage on the behaviour of the composite under different loading conditions Almost all the numerical investigation was based on the unit cell model or an extension of the unit cell model From the review, it is understood that the addition of silicon carbide particles increases the tensile strength of the matrix material at the cost of its ductility The tensile strength increases with the increase in the volume percentage of silicon carbide particles

31

Elements of plasticity theory such as i) a von Mises initial yield locus and a plastic potential, ii) isotropic hardening and iii) the normality rule, apply to the particulate MMC

As a follow up of these previous works, the experimental investigation to be carried out in this study was designed and developed, primarily for silicon carbide particle reinforced aluminium matrix material Based on the review of previous research work, it is evident that the AlSiC MMC material could be considered as a material to produce bolts that are subjected to combined tension and torsion loading conditions during service In addition, the elastic-plastic design of the bolt can substantially reduce the weight of the bolt

3 THEORETICAL INVESTIGATION

3 1 INTRODUCTION

In the study of elastic-plastic behaviour of a material, one of the main tasks is to describe the yield characteristic At the beginning of plastic deformation, yielding was found to occur based on von Mises criterion for most materials [15,62] After some plastic deformation, yield characteristics deviates from von Mises criterion depending on the hardening property of the material The evolution of isotropic and kinematic hardening with plastic deformation has been studied and many models for it have been widely accepted The isotropic hardening rule assumes that the center of the yield surface remains stationary in the stress space, but the size (radius) of the yield surface expands due to strain hardening The kinematic hardening rule assumes that the von Mises yield surface does not change the size or shape, but the center of the yield surface shifts in stress space Some of the models describing elastic-plastic behaviour of a monolithic material were reported in the first part of this chapter The first two models described are based on the numerical analysis of a solid circular rod subjected to combined tension and torsion loads The remaining four models are based on the results obtained from thin walled tube tests The content in the second part of this chapter relates to Finite Element Analysis In this section, the finite element analysis procedure for static, elastic-plastic problem was explained The finite element analysis tool ANSYS approach to solve the elastic-plastic problem was also explained

3 2 THEORETICAL MODELS

Brooks [1] and Gaydon [10] derived analytical expressions for the determination of the combined stress state of a solid rod under combined tension and torsion loading conditions Various empirical equations, such as Prandtl-Reuss, Ramberg-Osgood, describing the stress-strain relationships were used along with

von Mises yield criterion (see Appendix-B) In addition, four constitutive models representing the mechanical behaviour of different monolithic materials were presented The described models were derived from uniaxial experimental investigations and different loading histories

3 2 1 Gaydon Model

Gaydon [10] derived expressions to determine the stress state of circular specimens at different tension and torsion loading conditions In his expressions the Lode parameter μ & v were assumed equal The Reuss equations were used throughout and were integrated to give the shear stress and axial stress in the plastic material von Mises criterion of yielding,

$$\sigma^2 + 3\tau^2 = Y^2$$ (3 1)

was used, where 'Y' is the yield stress in tension

In the combined torsion and tension of a fully plastic cylindrical bar, the elastic component of the strain was assumed negligible, then the only non-vanishing stresses are $\sigma_z = \sigma$ and $\tau_{\theta z} = \tau$ Assuming the transverse sections remain plane and the local rate of strain is a function only of 'r', the expressions for the velocities u, v, w of an element referred to cylindrical coordinates r, θ, z are

$$u = -\frac{l\,r}{2\,l}, \quad v = \frac{\theta\,r\,z}{l}, \quad w = \frac{l\,z}{l},$$

where the origin of coordinates is taken at the center of one end, which is held fixed 'l' is the length of the bar, and θ is the relative twist of the ends, a dot denotes the time derivative

Assuming that there is no work hardening, the Reuss equations [62] for the plastic region are

$$d\epsilon_r = d\,\epsilon_\theta = -\frac{dl}{2l} = -\frac{\sigma\,d\lambda}{3} - \frac{1}{6G}d\sigma,$$ (3 2)

$$d \in_{-} = \frac{dl}{l} = \frac{2\,\sigma\,d\lambda}{3} + \frac{1}{3G}d\sigma, \tag{3 3}$$

$$d\gamma_{\theta_z} = \frac{r\,d\theta}{2\,l} = \tau\,d\lambda + \frac{1}{2G}d\tau \tag{3 4}$$

$$d\gamma_{,} = d\gamma_{r\theta} = 0$$

where $d\lambda$ is a scalar factor of proportionality, and G is the shear modulus

Combined torsion and tension with constant relative extension and twist

Let h denote the initial length of the rod and 'a' the external radius As the load and torque are increased from zero the stresses σ and τ increase until at some moment $\sigma^2 + 3\tau^2 = Y^2$ is satisfied locally While the bar is elastic, σ is independent of 'r' and τ is directly proportional to 'r' Therefore, the maximum shear stress can be observed at the outer most surface of the cylindrical bar and the material at radius 'a' becomes plastic first Subsequently, when the inner radius of the plastic region is 'c', the stresses in the elastic zone are,

$$\left.\begin{array}{l} \sigma = 3G\ln\left(\dfrac{l}{h}\right) \\[2ex] \tau = Gr\left(\dfrac{\theta}{l}\right) \end{array}\right\} \ (0 \le r \le c), \tag{3 5}$$

$$\Rightarrow \frac{\sigma}{\tau} = \frac{3l}{r\theta}\ln\left(\frac{l}{h}\right) \tag{3 6}$$

Eliminating $d\lambda$ from equations (3 3) and (3 4), and using (3 1),

$$\frac{3dl}{rd\theta} = \frac{\sigma}{\tau} - \frac{Y^2\,l\,d\tau}{G\,r\,\sigma\tau\,d\theta} \tag{3 7}$$

for $c \le r \le a$

If the relative rate of extension to rate of twist is constant, then $3\dfrac{dl}{d\theta} = a\alpha$, is a constant and equation (3 7) becomes

$$\frac{a\alpha}{r} = \frac{\sigma}{\tau} - \frac{Y^2\,l}{G\,r\,\sigma\tau}\frac{d\tau}{d\theta} \tag{3 8}$$

35

If the value of τ in an element is constant, σ is constant from equation (3 1), and a solution of equation (3 8) is

$$\frac{a\alpha}{r} = \frac{\sigma}{\tau}$$

(3 9)

Combining equation (3 9) with equation (3 1),

$$\sigma = \frac{\alpha Y}{\left(\alpha^2 + \dfrac{3r^2}{a^2}\right)^{\frac{1}{2}}}, \quad \tau = \frac{\dfrac{Yr}{a}}{\left(\alpha^2 + \dfrac{3r^2}{a^2}\right)^{\frac{1}{2}}}, \quad (c \leq r \leq a)$$

(3 10)

Equations (3 9) and (3 5) are compatible at the plastic-elastic boundary since it follows from equation (3 9) and the definition of α that

$$\frac{\sigma}{\tau} = \frac{a\alpha}{r} = \frac{3}{r}\left(\frac{l-h}{\theta}\right) \approx \left(\frac{3l}{r\theta}\right)\ln\left(\frac{l}{h}\right)$$

to usual approximation in the linear theory of elasticity, $\dfrac{\sigma}{\tau}$ is therefore

continuous at the plastic-elastic boundary This, together with the fact that equation (3 1) is satisfied at both sides of the boundary, proves that σ and τ are separately continuous at the boundary

The load 'L' and torque 'T' needed to maintain the constant relative rate of twist and extension are given by

$$\frac{L}{\pi Y a^2} = \frac{3c^2 G}{a^2 Y}\ln\left(\frac{l}{h}\right) + \frac{2}{3}\alpha\left[\left(\alpha^2 + 3\right)^{\frac{1}{2}} - \left(\alpha^2 + \frac{3c^2}{a^2}\right)^{\frac{1}{2}}\right],$$

(3 11)

$$\frac{T}{\pi Y a^3} = \frac{1}{2}\frac{c^4}{a^4\alpha}\left(\frac{3G}{Y}\right)\ln\left(\frac{l}{h}\right) + \frac{2}{27}\left[9\left(\alpha^2 + 3\right)^{\frac{1}{2}} - \frac{9c^2}{a^2}\left(\alpha^2 + \frac{3c^2}{a^2}\right)^{\frac{1}{2}} - 2\left(\alpha^2 + 3\right)^{\frac{3}{2}} + 2\left(\alpha^2 + \frac{3c^2}{a^2}\right)^{\frac{3}{2}}\right]$$

(3 12)

36

Twist held constant, increasing axial load

When the bar is all elastic initially

Let ϕ be the prescribed constant twist per unit length. Then, while in an elastic state,

$$\sigma = 3G\ln\left(\frac{l}{h}\right), \quad \tau = Gr\phi$$

Suppose that at time t_0, σ has increased to σ_0, l to l_0, and that the outside of the cylinder is just plastic. Then

$$\sigma_0 = 3G\ln\left(\frac{l_0}{h}\right), \tag{3 13}$$

$$\tau_0 = Gr\phi, \tag{3 14}$$

and

$$\sigma_0^2 + 3\tau_0^2 = Y^2 \tag{3 15}$$

Subsequently, when the bar is plastic to a radius 'c',

$$\sigma = 3G\ln\left(\frac{l}{h}\right), \quad \tau = Gr\phi \quad (r \leq c) \tag{3 16}$$

Conditions on the plastic boundary give

$$\sigma^2 + 3G^2c^2\phi^2 = Y^2 \tag{3 17}$$

For $c \leq r \leq a$, we put $d\theta = 0$ in equation (3 4) and eliminate $d\lambda$ from (3 3) and (3 4) Then

$$3G\frac{dl}{l} = -\frac{\sigma}{\tau}d\tau + d\sigma \tag{3 18}$$

But, from equation (3 1),

$$3\tau d\tau + \sigma d\sigma = 0$$

37

Therefore

$$\frac{6G}{Y}\ln l = \ln\left(\frac{1+\sigma Y^{-1}}{1-\sigma Y^{-1}}\right) + const$$

An element at radius r becomes plastic when 'l' is such that

$$3G\ln\left(\frac{l}{h}\right) = \left(Y^2 - 3G^2r^2\phi^2\right)^{\frac{1}{2}} = \sigma_r \qquad (3\ 19)$$

Substituting β for $\left(\frac{l}{h}\right)^{\frac{6G}{Y}}$ we have

$$\frac{\sigma}{Y} = \frac{\beta e^{-\frac{2\sigma_r}{Y}} - 1 + \left(\beta e^{-\frac{2\sigma}{Y}} + 1\right)\left(\frac{\sigma_r}{Y}\right)}{\beta e^{-\frac{2\sigma_r}{Y}} + 1 + \left(\beta e^{-\frac{2\sigma_r}{Y}} - 1\right)\left(\frac{\sigma_r}{Y}\right)}, \qquad (3\ 20)$$

σ_r is given by equation (3 19), and then equation (3 20) gives σ in terms of 'l' and 'r',

and

$$\frac{\tau}{Y} = \frac{2\left(\frac{G}{Y}\right)r\phi\beta^{\frac{1}{2}}e^{-\frac{\sigma_r}{Y}}}{\beta e^{-\frac{2\sigma}{Y}} + 1 + \left(\beta e^{-\frac{2\sigma}{Y}} - 1\right)\left(\frac{\sigma_r}{Y}\right)} \qquad (3\ 21)$$

Suppose, in particular, that ϕ is such that the outside radius 'a' is just about to become plastic when the twisting is completed Then $\phi = \dfrac{Y}{G\sqrt{3}a}$ and therefore

$$\frac{\sigma_r}{Y} = \left(1 - \frac{r^2}{a^2}\right)^{\frac{1}{2}}$$

The bar will have become completely plastic when $\ln\left(\dfrac{l}{h}\right) = \dfrac{Y}{3G}$ Then, at the radius 'a',

38

$$\frac{1+\sigma Y^{-1}}{1-\sigma Y^{-1}} = e^2, \quad \frac{\sigma}{Y} = 0.7616$$

Therefore σ is within 14 percent of Y. If the extension is continued until $\ln\left(\dfrac{l}{h}\right) = \dfrac{Y}{G}$, at $r = a$,

$$\frac{\sigma}{Y} = \tanh 3 = 0.9951$$

and σ is within $\dfrac{1}{2}$ of Y. It is therefore apparent that σ rapidly approaches its asymptotic value Y while the strains are still of an elastic order of magnitude.

Plastic to radius 'b' initially

In this case, suppose that the constant twist is such as to cause the bar to become plastic to radius '*b*'. Prior to the application of the tension load,

$$\tau = Gr\phi \quad (r \le b), \quad \tau = \frac{Y}{\sqrt{3}} \quad (r \ge b) \tag{3.22}$$

From (3.22) it follows that $b = \dfrac{Y}{G\sqrt{3}\phi}$

As the axial stress is applied, τ in the plastic region falls and the plastic radius moves inwards.

An element at radius '*r*' becomes plastic when '*l*' is such that

$$3G \ln\frac{l}{h} = \left(Y^2 - 3G^2 r^2 \phi^2\right)^{\frac{1}{2}} = \sigma_r \tag{3.23}$$

Then

$$\frac{\sigma}{Y} = \frac{\beta e^{-\frac{2\sigma}{Y}} - 1 + \left(\beta e^{-\frac{2\sigma}{Y}} + 1\right)\left(\frac{\sigma_r}{Y}\right)}{\beta e^{-\frac{2\sigma}{Y}} + 1 + \left(\beta e^{-\frac{2\sigma}{Y}} - 1\right)\left(\frac{\sigma_r}{Y}\right)}$$

and

39

$$\frac{\tau}{Y} = \frac{2\left(\dfrac{G}{Y}\right)r\phi\beta^{\frac{1}{2}}e^{-\frac{\sigma_r}{Y}}}{\beta e^{-\frac{2\sigma_r}{Y}}+1+\left(\beta e^{-\frac{2\sigma_r}{Y}}-1\right)\left(\dfrac{\sigma_r}{Y}\right)}$$

Fixed extension and increasing twist

When the bar is all elastic initially

The axial stress is supposed to be σ_0 initially While the bar is completely elastic

$$\sigma = \sigma_0, \quad \tau = Gr\phi \tag{3 24}$$

The bar will become plastic to radius 'c' during the subsequent twisting when $\tau = \tau_0$, where

$$\sqrt{3}\tau_0 = \left(Y^2 - \sigma_0^2\right)^{\frac{1}{2}} \tag{3 25}$$

After few steps of derivation using Reuss equations, the following expressions can be arrived at,

$$\frac{\sigma}{Y} = \frac{\sigma_0}{Y}\left\{\frac{\sec h\left(\dfrac{\sqrt{3}}{Y}\right)(Gr\phi-\tau_0)}{1+\left(\dfrac{\sqrt{3}\tau_0}{Y}\right)\tanh\left(\dfrac{\sqrt{3}}{Y}\right)(Gr\phi-\tau_0)}\right\} \tag{3 26}$$

In order to be specific, let $\sigma_0 = \dfrac{Y}{2}$ and suppose that $r\phi = \dfrac{Y}{G}$, that is the shear strain is $\dfrac{Y}{2G}$

Then

$$\frac{\sqrt{3}\tau}{Y} = \frac{\tanh\left(\dfrac{\sqrt{3}}{2}\right)+\dfrac{\sqrt{3}}{2}}{1+\left(\dfrac{\sqrt{3}}{2}\right)\tanh\left(\dfrac{\sqrt{3}}{2}\right)} = 0\,975 \tag{3 27}$$

40

It is evident that τ rapidly approaches its asymptotic value $\dfrac{Y}{\sqrt{3}}$, being within 3

percent of this value when the shear strain is only $\dfrac{Y}{2G}$

All plastic initially

Initially $\sigma_0 = Y$, $\tau = 0$ everywhere, so that

$$2\sqrt{3}\,\frac{G}{Y}r\phi = \ln\frac{1+\dfrac{\sqrt{3}\tau}{Y}}{1-\dfrac{\sqrt{3}\tau}{Y}} + const$$

In this case when $\tau = \tau_0$, $\phi = 0$, and therefore

$$\frac{\sqrt{3}\tau}{Y} = \tanh\frac{\sqrt{3}}{Y}Gr\phi \qquad\qquad (3\ 28)$$

and

$$\frac{\sigma}{Y} = \sec h\frac{\sqrt{3}}{Y}Gr\phi \qquad\qquad (3\ 29)$$

When $r\phi$ is only $\dfrac{2Y}{G}$, τ is $\dfrac{0\ 998Y}{\sqrt{3}}$ and σ is $0\ 0625Y$ The load 'L' and torque 'T'

are given by

$$\frac{L}{\pi Ya^2} = 2\int_0^1 R\sec h\,R\Phi\,dR,$$

$$\frac{\sqrt{3}T}{\pi Ya^3} = 2\int_0^1 R^2\tanh R\Phi\,dR$$

where $\dfrac{r}{a} = R$ and $\left(\dfrac{\sqrt{3}G}{Y}\right)a\phi = \Phi$

3 2 2 Brooks Model

Brooks [1] presented a method for the analysis of a round bar carrying combinations of axial force and torque Ramberg-Osgood curves were used to

41

describe the material behaviour, and the analysis is based on the Prandtl-Reuss incremental stress-strain laws and the von Mises yield criterion According Ramberg and Osgood, the relation between the uniaxial tensile stress σ_a and the corresponding strain ε_a for monotonically increasing loading may be accurately represented by the empirical law

$$\varepsilon_a = \frac{\sigma_a}{E} + \frac{3\sigma_1}{7E}\left(\frac{\sigma_a}{\sigma_1}\right)^n \tag{3 30}$$

in which σ_1 is the stress at a secant modulus of 0 7E, and n is a strain-hardening parameter depending upon material properties From equation (3 30) the elastic and plastic components of the axial strain are respectively,

$$\varepsilon_a^e = \frac{\sigma_a}{E} \tag{3 31}$$

$$\varepsilon_a^p = \frac{3\sigma_1}{7E}\left(\frac{\sigma_a}{\sigma_1}\right)^n \tag{3 32}$$

In an elasto-plastic round bar, the inner cylindrical core is elastic and the outer annulus is plastic, and the radius of the elastic-plastic interface decreases monotonically from the external radius of the bar

In plastic region, the Prandtl-Reuss incremental stress-strain laws are used, and yielding is assumed to be in accordance with the von Mises criterion Hill [62] has shown that for a material which strain hardens isotropically, these equations may be summarised in tensor notation as

$$\frac{\partial e_{ij}}{\partial p} = \frac{1}{2G}\frac{\partial \sigma'_{ij}}{\partial p} + \frac{3\sigma'_{ij}}{2\bar{\sigma}H'}\frac{\partial \bar{\sigma}}{\partial p}$$
$$e = \frac{1-2\upsilon}{E}\sigma \tag{3 33}$$

In this expressions, H' is equal to the slope of the effective stress $\bar{\sigma}$-generalised plastic strain $\bar{\varepsilon}^p$ curve, where the effective stress $\bar{\sigma}$ is defined as

42

$$\bar{\sigma} = \sqrt{\frac{3}{2}\sigma'_{ij}\sigma'_{ij}} \qquad (3\ 34)$$

The generalised plastic strain $\bar{\varepsilon}^p$ is

$$\bar{\varepsilon}^p = \int d\bar{\varepsilon}^p = \int \frac{\partial \bar{\varepsilon}^p}{\partial \rho} d\rho \qquad (3\ 35)$$

and the generalised plastic strain rate

$$\frac{\partial \bar{\varepsilon}^p}{\partial \rho} = \sqrt{\left(\frac{2}{3}\frac{\partial \bar{\varepsilon}^p_{ij}}{\partial \rho}\frac{\partial \bar{\varepsilon}^p_{ij}}{\partial \rho}\right)} \qquad (3\ 36)$$

Equation (3 33) may also be applied to the elastic portion of the bar, because the plastic components of the strain are zero so that H' becomes infinitely large Owing to the nature of the Ramberg-Osgood curves, it is impossible to obtain a precise distinction between the elastic portion and the plastic portion of the bar However, for most practical materials whose behaviour is represented by equation (3 30), the strain hardening parameter 'n' is usually greater than about 8 and the plastic strains given by the second term in the equation are small in comparison with the elastic strains when the stresses are less than σ_1

For uniaxial tension test, differentiation of equation (3 32) produces

$$\frac{d\varepsilon^p_a}{d\sigma_a} = \frac{3n}{7E}\left(\frac{\sigma_a}{\sigma_1}\right)^{n-1} \qquad (3\ 37)$$

and since $\bar{\sigma} = \sigma_a$ and $\bar{\varepsilon}^p = \varepsilon^p_a$ in this case, it follows that

$$\frac{d\bar{\varepsilon}^p}{d\bar{\sigma}} = \frac{1}{H'} = \frac{3n}{7E}\left(\frac{\bar{\sigma}}{\sigma_1}\right)^{n-1} \qquad (3\ 38)$$

It was assumed that the value of H' given in equation (3 38) holds for all other loading conditions

3 2 3   Johnson and Cook (JC) Model

Johnson and Cook [63] proposed a constitutive model for metals subjected to large-strains, high strain rates and high temperatures The JC constitutive model

is simple and the parameters for various materials of interest are readily available The JC model represents a set of models that consider that the mechanical behaviour of a material is the multiplication effect of strain, strain rate, and temperature

In the JC model, the von Mises flow stress, σ is expressed as

$$\sigma = \left(A + B \, \epsilon^n\right)\left(1 + C \ln \epsilon^*\right)\left(1 - T^{*m}\right) \qquad (3\ 39)$$

where ϵ is the equivalent plastic strain, $\epsilon^* = \dfrac{\epsilon}{\epsilon_0}$ is the dimensionless strain rate

(ϵ_0 is normally taken to be 1 0 s^1), and

$$T^* = \frac{T - T_r}{T_m - T_r}$$

where T_r is a reference temperature and T_m is the melting temperature of the material The five material constants are A, B, n, C, and m

In equation (3 39), the expression in the first set of brackets gives the dependence on strain, the second represents instantaneous strain-rate sensitivity, and the third term represents the temperature dependence of stress This approach does not represent any thermal or strain-rate history effects, but is simple to implement and the parameters are readily obtained from a number of experiments

3 2 4   Zerilli-Armstrong (ZA) Model

Wagenhofer et al [64] proposed dislocation-mechanics-based constitutive relations for material dynamic calculations The effects of strain hardening, strain-rate hardening, and thermal softening based on the thermal activation analysis have been incorporated into a constitutive relation They proposed that each material structure type (FCC, BCC, HCP) has a different constitutive behaviour based on the different rate-controlling mechanism for that particular structure

44

The overall flow stress of a FCC material is controlled by the thermally activated overcoming of dislocation intersections as contained in the constitutive equation analysis of ZA model The ZA model resulted in equation for flow stress, neglecting dynamic recovery,

$$\sigma = c_0 + B_0 \sqrt{\epsilon} e^{-\alpha T} \tag{3 40}$$

where

$$c_0 = \sigma_G + k\ell^{-\frac{1}{2}}$$

and

$$\alpha = \alpha_0 - \alpha_1 \ln \epsilon$$

In which ϵ is the strain, ϵ is the strain rate, ℓ is the grain diameter, T is temperature, $\sigma_G, k, B_0, \alpha_0$ and α_1 are material constants

3 2 5 Bodner-Partom (BP) Model

Bodner and Partom [65] formulated a set of constitutive equations to represent elastic-viscoplastic strain-hardening material behaviour for large deformations and arbitrary loading histories An essential feature of the formulation is that the total deformation rate is considered to be separable into elastic and inelastic components, which are functions of state variables at all stages of loading and unloading The formulation is independent of any yield criteria or loading and unloading conditions

The deformation rate components are determinable from the current state, which permits an incremental formulation of problems Strain hardening is considered in the equations by introducing plastic work as the representative state variable The assumptions of isotropy and isothermal conditions are maintained in this formulation, although strain hardening is known to induce anisotropy

The general formula of the BP model is based on separation of the total deformation rate $d = \{d_{ij}\}$ into elastic and plastic components at all stages of deformation

45

$$d = d^e + d^p \quad or \quad d_{ij} = d_{ij}^e + d_{ij}^p \tag{3 41}$$

The elastic deformation rate $d^e = \{d_{ij}^e\}$ can be related to the Cauchy stress rate by the generalised Hooke's law

$$d_{ij}^e = \frac{t_{ij}}{G} - \frac{\lambda t_{kk} \delta_{ij}}{2G(3\lambda + 2G)} \tag{3 42}$$

where G is the elastic shear modulus and λ is an elastic Lame constant

The plastic deformation rate $d^p = \{d_{ij}^p\}$ is related to the deviator of Cauchy stress, as in the classical Prandtl-Reuss equation

$$d^p = \gamma s \quad or \quad d_{ij}^p = \gamma s_{ij} \tag{3 43}$$

$s = \{s_{ij} = t_{ij} - \frac{1}{3} t_{kk} \delta_{ij}\}$ is the deviator of the Cauchy stress and γ is a proportional factor Squaring equation (3 43) gives

$$\gamma^2 = \frac{D_2^p}{J_2} \tag{3 44}$$

D_2^p is the second invariant of the plastic deformation rate 'J_2' is the second invariant of s

$$D_2^p = \frac{1}{2} d_{ij}^p d_{ij}^p$$

$$J_2 = \frac{1}{2} s_{ij} s_{ij}$$

γ will be determined by specifying D_2^p as a function of J_2

$$D_2^p = f(J_2) \tag{3 45}$$

This formula can be considered to be a multi-dimensional generalisation of the uniaxial result

For one dimensional case, the BP model reduces to the following equations,

$$\epsilon^e = \frac{\sigma}{E}, \tag{3 46}$$

46

$$\epsilon^{p} = \frac{2}{\sqrt{3}}\left(\frac{\sigma}{|\sigma|}\right)D_0 \exp\left(-\frac{n+1}{2n}\left(\frac{Z}{\sigma}\right)^{2n}\right) \qquad (3\ 47)$$

$$Z = Z_1 + (Z_0 - Z_1)\exp\left(-\frac{m\int\sigma\,d\,\epsilon^{p}}{Z_0}\right) \qquad (3\ 48)$$

where the quantity $\frac{\sigma}{|\sigma|}$ imposes the condition that the plastic strain rate has the same sign as that of the applied stress

Foi materials that exhibit strong work-hardening behaviour like OHFC copper, m was made a function of W_p The expression for m was

$$m = m_0 + m_1 e^{-\alpha W_p} \qquad (3\ 49)$$

The expression for Z when integrated after replacing m by the equation (3 49) yields the following relationship between Z and W_p

$$Z = Z_1 + (Z_0 - Z_1)\exp(-m_0 W_p)\exp\left(-\frac{m_0 + m_1 - m}{\alpha}\right) \qquad (3\ 50)$$

There are five material parameters in the BP model In most of the cases, the experimental data for characterising the material parameters are in the form of stress-strain curves at constant strain rates For BP model, two stress-strain curves at different strain rates are sufficient to calculate the material parameters D_o is the maximum strain rate that the material can experience It was recommended by Bodner and Partom that $D_o = 10^4 \mathrm{s}^{-1}$ for quasi-static modelling

3 2 6   Khan-Huang (KH) Model

Similar to BP model Khan and Huang [66] model proposed a new constitutive model that can predict the experimental results in a large strain-rate range including the high work-hardening region The only difference is to determine the proportionality parameter ' γ ' in equation (3 44)

$$\gamma^2 = \frac{D_2^p}{J_2}$$

A constitutive equation is proposed for J_2 as

$$J_2 = f_1\left(\epsilon_2^p\right) f_2\left(D_2^p\right)$$

(3 51)

where ϵ_2^p is the equivalent plastic strain defined by

$$\epsilon_2^p = \frac{1}{2}\epsilon_{ij}^p \epsilon_{ij}^p$$

For one dimensional case, equation (3 51) can be written as

$$\sigma = g_1\left(\epsilon^p\right) g_2\left(\epsilon^p\right)$$

(3 52)

where

$$g_1\left(\epsilon^p\right) = \left[3 f_1\left(\frac{3}{4}\left(\epsilon^p\right)^2\right)\right]^{\frac{1}{2}}$$

$$g_2\left(\epsilon^p\right) = \left[f_2\left(\frac{3}{4}\left(\epsilon^p\right)^2\right)\right]^{\frac{1}{2}}$$

The particular form of $g_1\left(\epsilon^p\right)$ and $g_2\left(\epsilon^p\right)$ were proposed to be,

$$g_1\left(\epsilon^p\right) = \sigma_0 + E_\infty \epsilon^p - ae^{-\alpha\epsilon^p}$$

(3 53)

$$g_2\left(\epsilon^p\right) = \frac{1}{\left[1 - \dfrac{\ln\left(\epsilon^p\right)}{\ln\left(D_0^p\right)}\right]^n}$$

(3 54)

Five material constants are $n, E_\infty, \sigma_0, a,$ and α D_0^p is arbitrarily chosen to be 10^6 s ^{1}

The analytical models described in the previous sections relate to monolithic materials Accurate descriptions of material behaviour makes the constitutive model complicated due to the use of multiple material parameters Similarly, various models may give better descriptions for specific materials In the case of a solid rod, especially a rod of composite material, subjected to combined tension and torsion loading, the description of the material behaviour becomes

48

more complex and cumbersome For this reason, an attempt to predict the combined tensile and torsional stress state in the AlSiC MMC rod was made using finite element analysis code, ANSYS

3 3   INTRODUCTION TO FINITE ELEMENT METHOD

The finite element method is used to solve physical problems in engineering analysis and design The physical problem typically involves an actual structure or structural component subjected to certain loads The idealisation of the physical problem to a mathematical model requires certain assumptions that together lead to differential equation governing the mathematical model Since the finite element solution technique is a numerical procedure, it is necessary to assess the solution accuracy If the accuracy criteria are not met, the numerical solution has to be repeated with refined solution parameters, such as finer meshes, until a sufficient accuracy is reached The choice of an appropriate mathematical model is crucial since the response of the model will be based on the selected mathematical model and the assumptions The response of the physical problem cannot be predicted exactly because it is impossible to reproduce even in the most refined mathematical model all the information that is present in nature and therefore contained in the physical problem

The choice of the mathematical model must depend on the phenomena to be predicted and on the geometry, material properties, loading, and boundary conditions of the physical problem The most effective mathematical model is that one which delivers the answers to the questions in a reliable manner within an acceptable error and with the least amount of effort These errors may be due to the simplifications used in the model and assumption made while modelling

The first step in the finite element analysis is the creation of a geometric representation of the design part The material properties, the applied loading and boundary conditions on the geometry are defined in this step Since the geometry and other data of the actual physical part may be complex, it is usually necessary to simplify the geometry and loading in order to reach a tractable

mathematical model The finite element analysis solves the chosen mathematical model, which may be changed and evolved depending on the purpose of the analysis

An important ingredient of a finite element analysis is the calculation of error estimate, i e estimates of how closely the finite element solution approximates the exact solution of the mathematical model These estimates indicate whether a specific finite element discretisation has indeed yielded an accurate response prediction

The following sections (Section 3 4 to Section 3 11) give an introduction to finite element analysis procedures and methods to solve non-linear problems An attempt has been made to guide the reader through various steps undertaken in the finite element approach to solve non-linear problems The details of the finite element procedures can be obtained from standard textbooks dealing with the finite element methods [see bibliography]

3 4 METHODS OF ANALYSIS

Engineering problems arising in practice usually may be characterised by ordinary or partial differential equations with their associated boundary conditions Solving these problems may be achieved by either difference or integral formulations The first approach replaces the derivatives with finite difference approximations The integral formulation is more versatile because it is also capable of accurate discretisation of irregular solution domains and is based on the use of trial functions with undetermined parameters In this approach, either the weighted residual method or the stationary functional method may be used for the solution

In the weighted residual method, a trial solution expressed in terms of undetermined parameters, is chosen that satisfies all boundary conditions, and when inserted in the differential equation yields a residual The magnitude of the residual is required to be small in any of the four available procedures

(Collocation, Subdomain, Galerkin, and Least squares) and this in turn depends on the choice of the trial solution [67]

The stationary functional method is based on the variational approach and involves the determination of the extremum value of the chosen functional The trial function that gives the minimum value of the functional is approximate solution of the governing differential equation In solid mechanics the functional used is the total potential energy or some variant of this quantity

In finite element method, a continuum is discretized into smaller domains or elements Trial solutions are sought within each element for which, in the variational method, the total potential energy is minimised The idea is that the piecewise discretisation will have a similar result for the entire continuum when summed over all elements

Numerical solution of practical engineering problems consists of two distinct yet related steps

1. Discretize the continuum with the finite element method, defining nodal geometry and element topology, and perform the following steps

   a) Define a piecewise continuous smooth solution trial function for each element and apply either the stationary functional or the weighted residual method to obtain the element equations in terms of unknown nodal parameters

   b) Assemble system equations, the order of which will be the total number of nodal unknowns

   c) Apply the desired displacement boundary conditions to the set of system equations as well as applied mechanical and thermal loads

2. Solve the appropriate system equations by a suitable numerical technique

Subsequently, calculations are made of other required information derived from the basic solution of the physical problem being studied In structural analysis, the element stresses are computed after obtaining element nodal displacements in the previous step

Analysis of a structural system is composed of the following basic carbide steps

51

i   Idealise the continuum as a set of smaller regions known as finite elements

ii   Select nodes at interelement boundaries and element interiors for the purpose of setting up of interpolating functions

iii   Use interpolation functions to express displacement values at element interior points in terms of nodal variables

iv   Develop element force-displacement matrices by applying either the variational principle or the weighted residual method

v   Assemble equilibrium matrices for the entire region in global coordinates for all the element matrices, and solve the resulting set of algebraic equations for the unknown nodal values

vi   Calculate element stresses and strains from the calculated nodal displacements

3 5   FORMULATION OF THE FINITE ELEMENT METHOD

The standard formulation for the finite element solution of solids is the displacement method The displacement-based solution is not effective for certain applications for which a mixed formulation method is employed The mixed formulation method requires a careful selection of appropriate interpolations

3 5 1   Formulation of the Displacement-based Finite Element Method

The displacement-based finite element method can be regarded as an extension of the displacement method of analysis of beam and truss structures The complete structure is idealized as an assemblage of individual structural elements The element stiffness matrices corresponding to the global degrees of freedom of the structural idealization are calculated, and the total stiffness matrix is formed by the addition of the element stiffness matrices The solution of the equilibrium equations of the assemblage of elements yields the element displacements, which are then used to calculate the element stresses Finally, the element

displacements and stresses are interpreted as an estimate of the actual structural behaviour

The basis of the displacement-based finite element solution is the principle of virtual displacements This principle states that the equilibrium of the body requires that for any compatible small virtual displacements imposed on the body in its state of equilibrium, the total internal virtual work is equal to the total external virtual work

$$\int_V \overline{\in}^T \tau \, dV = \int_V \overline{U}^T f^B \, dV + \int_{S_f} \overline{U}^{S_f^T} f^{S_f} \, dS + \sum_i U^{i^T} R_C^i \qquad (3\ 55)$$

where the $\overline{U}$'s are the virtual displacements and the $\overline{\in}$'s are the corresponding virtual strains f^B, f^{S_f}, and R_C^i are externally applied body force, surface traction and concentrated load respectively The virtual displacements are not "real" displacements, which the body actually undergoes because of the loading on the body Instead, the virtual displacements are very much independent from the actual displacement and are used to establish the integral equilibrium equation (3 55)

In equation,

- The stresses σ are assumed to be known quantities and are the unique stresses that exactly balance the applied loads

- The virtual strains $\overline{\in}$ are calculated by the differentiations of the following expressions from the assumed virtual displacements $\overline{U}$

$$\begin{aligned} &\in_{XX} = \frac{\partial U}{\partial X}, \ \in_{YY} = \frac{\partial V}{\partial Y}, \ \in_{ZZ} = \frac{\partial W}{\partial Z} \\ &\gamma_{XY} = \frac{\partial U}{\partial Y} + \frac{\partial V}{\partial X}, \ \gamma_{YZ} \frac{\partial V}{\partial Z} + \frac{\partial W}{\partial Y}, \ \gamma_{ZX} = \frac{\partial W}{\partial X} + \frac{\partial U}{\partial Z} \end{aligned} \qquad (3\ 56)$$

- The virtual displacements $\overline{U}$ must represent a continuous virtual displacement field

- All integrations are performed over the original volume and surface area of the body, unaffected by the imposed virtual displacements

53

The principle of virtual displacements is satisfied for all admissible virtual displacements with the stresses σ obtained from a continuous displacement field $\overline{U}$ that satisfies the displacement boundary conditions when all three fundamental requirements of mechanics are fulfilled

1. *Equilibrium* holds because the principle of virtual displacements is an expression of equilibrium

2. *Compatibility* holds because the displacement field U is continuous and satisfies the displacement boundary conditions

3. *The stress-strain law* holds because the stresses σ have been calculated using the constitutive relationships from the strains $\in$

3 6 FINITE ELEMENT EQUATIONS

In finite element analysis, a body is approximated as an assemblage of discrete finite elements interconnected at nodal points on the element boundaries The displacements measured in a local coordinate system x, y, z within each element are assumed to be a function of the displacements at the 'N' finite element nodal points Therefore, for element 'm' we have

$$u^{(m)}(x,y,z) = H^{(m)}(x,y,z)\hat{U} \qquad (3\ 57)$$

where $H^{(m)}$ is the displacement interpolation matrix, the superscript m denotes element m, and $\hat{U}$ is a vector of the three global displacement components U_i, V_i, and W_i at all nodal points, including those at the supports of the element assemblage The corresponding element strains,

$$\in^{(m)}(x,y,z) = B^{(m)}(x,y,z)\hat{U} \qquad (3\ 58)$$

where $B^{(m)}$ is the strain-displacement matrix, the rows of $B^{(m)}$ are obtained by appropriately differentiating and combining rows of the matrix $H^{(m)}$

The use of equations (3 57) and (3 58) in the principle of virtual displacements will automatically lead to an effective assemblage process of all element matrices into the governing structure matrices This assemblage process is

54

referred to as the direct stiffness method The stresses in a finite element are related to the element strains and the element initial stresses using

$$\tau^{(m)} = C^{(m)} \in^{(m)} + \tau^{I(m)}$$ (3 59)

where $C^{(m)}$ is the elasticity matrix of the element m and $\tau^{I(m)}$ are the given element initial stresses The material law specified in $C^{(m)}$ for each element can be that for an isotropic or an anisotropic material and can vary from element to element

Equilibrium equations that correspond to the nodal point displacements of the assemblage of finite elements can be derived using the assumption on the displacements within each finite element [68] Rewriting equation (3 55) as a sum of integrations over the volume and areas of all finite elements

$$\sum_m \int_{V^{(m)}} \overline{\in}^{(m)I} \tau^{(m)} dV^{(m)} = \sum_m \int_{V^{(m)}} \overline{u}^{(m)I} f^{B(m)} dV^{(m)} + \sum_m \int_{S_1^{(m)} \quad S_q^{(m)}} \overline{u}^{S(m)I} f^{S(m)} dS^{(m)} + \sum_i \overline{u}^{I} R_C^i$$
(3 60)

where $m = 1,2,3 \quad k$, where k = number of elements, and $S_1^{(m)}$, $,S_q^{(m)}$ denotes the element surfaces that are part of the body surface For elements surrounded by other elements, no such surfaces exist, whereas for elements on the surface of the body one or more such element surfaces are included in the surface force integral

The relations in equations (3 57) and (3 58) have been given for unknown element displacements and strains Employing the assumptions in the use of principle of virtual displacements,

$$\overline{u}^{(m)}(x,y,z) = H^{(m)}(x,y,z)\overline{\hat{U}}$$ (3 61)

$$\overline{\in}^{(m)}(x,y,z) = B^{(m)}(x,y,z)\overline{\hat{U}}$$ (3 62)

The element stiffness matrices will be symmetric matrices
Substituting the above expressions in equation (3 60),

$$\bar{U}^I \left[\sum_m \int_{V^{(m)}} B^{(m)I} C^{(m)} B^{(m)} dV^{(m)} \right] \hat{U} = \bar{U}^T \left[\begin{array}{c} \left\{ \sum_m \int_{V^{(m)}} H^{(m)T} f^{B(m)} dV^{(m)} \right\} \\ + \left\{ \sum_m \int_{S_l^{(m)}} H^{S(m)T} f^{S(m)} dS^{(m)} \right\} \\ - \left\{ \sum_m \int_{V^{(m)}} B^{(m)T} \tau^{I(m)} dV^{(m)} \right\} + R_C \end{array} \right] \quad (3\ 63)$$

where the surface displacement interpolation matrices $H^{S(m)}$ are obtained from the displacement interpolation matrices $H^{(m)}$ in equation (3 57) by substituting the appropriate element surface coordinates and R_c is a vector of concentrated loads applied to the nodes of the element assemblage

To obtain from (3 63) the equations for the unknown nodal point displacements, the principle of virtual displacements is applied n times by imposing unit virtual displacements in turn for all components of $\bar{U}$, so that the result is

$$KU = R \quad (3\ 64)$$

where

$$R = R_B + R_S - R_I + R_C \quad (3\ 65)$$

The matrix K is the stiffness matrix of the element assemblage,

$$K = \sum_m \int_{V^{(m)}} B^{(m)T} C^{(m)} B^{(m)} dV^{(m)} \quad (3\ 66)$$

The load vector R includes the effect of the element body forces,

$$R_B = \sum_m \int_{V^{(n)}} H^{(m)T} f^{B(m)} dV^{(m)} \quad (3\ 67)$$

The effect of the element surface forces,

$$R_S = \sum_m \int_{S_1^{(i)}, \; S_I^{(n)}} H^{S(m)T} f^{S(m)} dS^{(m)} \quad (3\ 68)$$

The effect of the element initial stresses,

$$R_I = \sum_m \int_{V^{(n)}} B^{(m)T} \tau^{I(m)} dV^{(m)} \quad (3\ 69)$$

and the nodal concentrated loads R_C

The summation of the element volume integrals in equation (3 66) expresses the direct addition of the element stiffness matrices $K^{(m)}$ to obtain the stiffness matrix of the total element assemblage Similarly, the assemblage body force vector R_B is calculated by directly adding the element body force vectors $R_B^{(m)}$, and R_S and R_I are similarly obtained The process of assembling the element matrices by direct addition is called the direct stiffness method

3 7 FINITE ELEMENT NONLINEAR ANALYSIS

In a materially nonlinear analysis, the nonlinear effect lies in the nonlinear stress-strain relation The displacements and strains are infinitesimally small, therefore the usual engineering stress and strain measures can be employed in the response description

The basic carbide problem in a general nonlinear analysis is to find the state of equilibrium of a body corresponding to the applied loads If the externally applied loads are described as a function of time, the equilibrium conditions of a system of finite elements representing the body under consideration can be expressed as

$$^tR - {}^tF = 0 \qquad (3\ 70)$$

where the vector ^tR lists the externally applied nodal point forces in the configuration at time t and the vector ^tF list the nodal point forces that correspond to the element stresses in this configuration Hence, using the equations (3 67), (3 68), and (3 69) in equation (3 65), we have

$$^tR = {}^tR_B + {}^tR_S + {}^tR_C \qquad (3\ 71)$$

And identifying the current stresses as initial stresses, $R_I = {}^tF$,

$$^tF = \sum_m \int_{^tV^{(m)}} {}^tB^{(m)T}\ {}^t\tau^{(m)}\ {}^tdV^{(m)} \qquad (3\ 72)$$

where in a general large deformation analysis the stresses as well as the volume of the body at time t are unknown

57

The relation in equation (3 70) must express the equilibrium of the system in the current deformed geometry taking due account of all nonlinearities

Considering the solution of the nonlinear response, the equilibrium relation in equation (3 70) must be satisfied throughout the complete history of load application, 1 e , the time variable t may take on any value from zero to the maximum time of interest In a static analysis without time effects other than the definition of the load level, time is only a convenient variable, which denotes different intensities of load applications and correspondingly different configurations

In many solutions, only the stresses and displacements reached at specific load levels can be calculated for the analysis results In some nonlinear static analyses the equilibrium configurations corresponding to these load levels can be calculated without solving for other equilibrium configurations However, when the analysis includes path-dependent nonlinear geometric or material conditions, the equilibrium relations in equation (3 70) need to be solved for the complete time range of interest This response calculation is effectively carried out using a step-by-step incremental solution, which reduces to a one-step analysis if in a static time-independent solution, the total load is applied all together and only the configuration corresponding to that load is calculated However, the analysis of such a case frequently requires an incremental solution, performed automatically, with a number of load steps to finally reach the total applied load

The basic carbide approach in an incremental step-by-step solution is to assume that the solution for the discrete time t is known and that the solution for the discrete time $t + \Delta t$ is required, where Δt is a suitably chosen time increment Hence, considering equation (3 70) at time $t + \Delta t$ we have,

$$^{t+\Delta t}R - ^{t+\Delta t}F = 0 \qquad (3\ 73)$$

where the left superscript denotes at time $t + \Delta t$ Assume that $^{t+\Delta t}R$ is independent of the deformations Since the solution is known at time t, we can write

$$^{t+\Delta t}F = ^{t}F + F \qquad (3\ 74)$$

58

where F is the increment in nodal point forces corresponding to the increment in element displacements and stresses from time t to time $t + \Delta t$. This vector can be approximated using a tangent stiffness matrix $^t K$, which corresponds to the geometric and material conditions at time t,

$$F = {}^t KU \qquad (3\ 75)$$

where U is a vector incremental nodal point displacements and

$$^t K = \frac{\partial {}^t F}{\partial {}^t U} \qquad (3\ 76)$$

Hence, the tangent stiffness matrix corresponds to the derivative of the internal element nodal point forces $^t F$ with respect to the nodal point displacements $^t U$ Substituting equations (3 75) and (3 76) into equation (3 73), we obtain

$$^t KU = {}^{t+\Delta t} R - {}^t F \qquad (3\ 77)$$

And solving for U, we can calculate an approximation to the displacements at time $t + \Delta t$,

$$^{t+\Delta t} U = {}^t U + U \qquad (3\ 78)$$

The exact displacements at time $t + \Delta t$ are those that correspond to the applied loads $^{t+\Delta t} R$ Using equation (3 78) only an approximation to the displacements can be calculated because equation (3 75) was used

Having evaluated an approximation to the displacements corresponding to time $t + \Delta t$ we could now solve for an approximation to the stresses and corresponding nodal point forces at time $t + \Delta t$, and then proceed to the next time increment calculations However, because of the approximation in equation (3 75), such a solution may be subject to very significant errors and, depending on the time or load step sizes used, may indeed be unstable It is therefore necessary to iterate until the solution of equation (3 73) is obtained to sufficient accuracy The widely used iteration methods in finite element analysis are based on the classical Newton-Raphson technique This method is an extension of the simple incremental technique given in equations (3 77) and (3 78) Having calculated an

increment in the nodal point displacements, which defines a new total displacement vector, we can repeat the incremental solution presented above can be repeated using the currently known total displacements instead of the displacements at time 't'

The equations used in the Newton-Raphson iteration are, for $i = 1,2,3$

$$^{t+\Delta t}K^{(i-1)}\Delta U^{(i)} = {}^{t+\Delta t}R - {}^{t+\Delta t}F^{(i-1)}$$
$$^{t+\Delta t}U^{(i)} = {}^{t+\Delta t}U^{(i-1)} + \Delta U^{(i)}$$

(3 79)

with the initial conditions

$$^{t+\Delta t}U^{(0)} = {}^{t}U, {}^{t+\Delta t}K^{(0)} = {}^{t}K, {}^{t+\Delta t}F^{(0)} = {}^{t}F$$

(3 80)

In the first iteration, the relations in equation (3 79) reduce to the equations (3 77) and (3 78) In the subsequent iterations, the latest estimates for the nodal point displacements are used to evaluate the corresponding element stresses and nodal point forces $^{t+\Delta t}F^{(i-1)}$ and tangent stiffness matrix $^{t+\Delta t}K^{(i-1)}$

The out-of-balance load vector $^{t+\Delta t}R - {}^{t+\Delta t}F^{(i-1)}$ corresponds to a load vector that is not yet balanced by element stresses, and hence an increment in the nodal point displacements is required This updating of the nodal point displacements in the iteration is continued until the out-of-balance loads and incremental displacements are small

3 8 COMPUTATIONAL PROCEDURES FOR DETERMINING STRUCTURAL DEFORMATIONS FOR NONLINEAR PROBLEMS SUBJECTED TO STATIC LOADING

3 8 1 Structural nonlinearities

The fundamental characteristic of a nonlinear structure is the changing structural behaviour with changes in load Structural nonlinearities may be caused by a number of factors and are broadly classified into three main categories

   1   Geometric nonlinearity

   2   Material nonlinearities and

   3   Changing status nonlinearities

60

Geometric nonlinearity

If a structure experiences large deformations such as large deflection, large strains and large rotation, its changing geometric configuration can cause nonlinear behaviour

For geometric nonlinearity, a Newton-Raphson iterative procedure is generally used in which the elastic stiffness matrix is supplemented with the geometric stiffness matrix K_G, so that both large displacements and rotations, as well as the effect of in-plane stretching, are taken into consideration, strains are assumed to be small in the formulation given below

For static analysis, the solution algorithm is as follows,

Let 'n' equal the number of load increments and 'i' equal the number of iterations within a loop Then for each load increment ('n' loop), form nK_G, the geometric stiffness matrix based on accumulated element stresses (= 0 for n = 1, and the prime denotes the local coordinate system), nK_E, the elastic stiffness matrix (= $1 K_E^0$ for n = 1, nK_E^i for n>1), and nr_s, residual forces (=0, for n=1, nr_s for n>1)

Then for each iteration ('i' loop) solve,

$$\left[nK_E^{(i-1)} + nK_G \right] \Delta u^{(i)} = \sum_n \Delta p - nr_s^{(i-1)} \tag{3 81}$$

to yield $\Delta n^{(i)}$

Update geometry $u^{(i)} = u^{(i-1)} + \Delta u^{(i)}$ and obtain incremental deformations in LCS

$$\Delta u'^{(i)} = \lambda^{(i)} \Delta u^{(i)} \tag{3 82}$$

where λ is the direction cosine matrix Calculate the element stresses in the LCS and accumulate, based on $\Delta u'^{(i)}$

Obtain residual forces in GCS

$$\Delta s^{(i)} = \left[nK_E^{(i-1)} + nK_G \right] \Delta u^{(i)} \tag{3 83}$$

$$nr_s^{(i)} = nr_s^{(i-1)} + \Delta s^{(i)} \tag{3 84}$$

61

Check convergence, if $|\Delta u|$ > EPS, EPS is a specified accuracy parameter
Compute $K_E^{\prime(i)}$ and $K_E^{(i)}$, element and global stiffness matrices, respectively
Repeat the iteration ('i' loop), if not converged Continue on the incremental
load loop ('n' loop) if convergence is achieved in 'i' loop Stop the computation
on the completion of the load cycle

Material Nonlinearity

A nonlinear stress-strain relationship is a common cause of nonlinear structural
behaviour The relationship between stress and strain is path dependent, so that
the stress depends on the strain history as well as the strain itself

In problems that exhibit material nonlinearity, the Prandtl-Reuss equation for the
plastic strain increments is combined with the von Mises yield criteria for
material characterisation An iterative solution procedure is then employed for
the solution of the associated static problem

Initialise

i   Set loads external (R^E) and internal (R^I) to zero

ii   Set all stresses and deformations (u_o) to zero

iii Set the yield function $F = -\sigma_{yp}$

iv   Set the slope of the strain-hardening curve to its initial value H'_{in}

v   Set the plastic strain ϵ_p to zero

vi   Set Δp, the incremental load

For each incremental load ('j' loop), calculate the total load at j^{th} step,

$$R_j^E = R_{j-1}^E + \Delta p \tag{3 85}$$

Calculate norm

$$\left\| R_j^I \right\| \tag{3 86}$$

and find the residual force ('i' loop)

$$R_i^{res} = R_j^E - R_{i-1}^I \tag{3 87}$$

62

Calculate $\left\|R_i^{rev}\right\|$, if $\left\|R_i^{rev}\right\| < EPSX\left\|R_j^k\right\|$, go to the end of the 'j' loop, calculate K_{ep} (initially K_e) Solve $\Delta u_i = K_{ep}^{-1}R_i^{res}$, the increment of displacement, and calculate $u_i = u_{i-1} + \Delta u_i$ the total elastoplastic displacement

For each element ('n' loop), $\Delta \varepsilon_i = B\Delta u_i$, the total increment in element strain (using e = Bu for small strain) Check the last value of yield function $F_{i,1}$ If $F_{i,1}$ = 0, the element is already on the yield surface, go to the elastoplastic loop If $F_{i,1} < 0$ the element is elastic at the start of the loop Calculate $\Delta \sigma_i = D\Delta\varepsilon_i$ $\sigma_i = \sigma_{i-1} + \Delta\sigma_i$ Then calculate $F_i = \overline{\sigma_i} + \sigma_{yp_{i-1}}$, in which the effective

stress $\overline{\sigma} = \sqrt{\dfrac{3}{2}}\sqrt{\sigma'^T\sigma'}, \sigma' = \left[\sigma'_x \sigma'_y \sigma'_z 2\tau_{xy} 2\tau_{yz} 2\tau_{zx}\right]^T$, in which $\sigma'_x = \left(\sigma_x - \sigma_m\right)$, and so on, and $\sigma_m = \left(\sigma_x + \sigma_y + \sigma_z\right)/3$ If $F_i \leq 0$, then it is elastic and store σ_i F_i, go to the end of the 'n' loop If $F_i > 0$, set $\sigma_A = \sigma_{i-1}, \sigma_B = \sigma_i$ Loop to bring σ_c onto the yield surface

$$\sigma_c = \left(\sigma_A + \sigma_B\right)/2 \qquad (3\ 88)$$

Calculate $F_C = \overline{\sigma} - \sigma_{yp_{i-1}}$ If $F_C < 0$, $\sigma_A = \sigma_C$ If $F_C > 0$, $\sigma_B = \sigma_C$ If $\left|F_C\right| >$ TOL, return to the top of the loop, TOL is the specified accuracy parameter to end the loop Then calculate

$$\begin{aligned} \Delta\varepsilon_{e_i} &= D_{ep}^{-1}\left(\sigma_C - \sigma_{i-1}\right) \\ \Delta\varepsilon_{P_i} &= \Delta\varepsilon_i - \Delta\varepsilon_{e_i} \end{aligned} \qquad (3\ 89)$$

$\sigma_{i-1} = \sigma_C$, and F_i becomes zero

Here is the start of the elastoplastic loop Set $\sigma_i = \sigma_C$, stress on yield surface

$$d\Delta\varepsilon_{ep} = \frac{\Delta\varepsilon_p}{20} \qquad (3\ 90)$$

Loop, $K = 1, n$ (e g , $n = 20$), and calculate D_{ep}, based on σ_C

$$\begin{aligned} \Delta\sigma_k &= D_{ep}d\Delta\varepsilon_{ep} \\ \sigma_{C+k} &= \sigma_C + \Delta\sigma_k \end{aligned} \qquad (3\ 91)$$

63

Use σ_{C+k} to calculate the normal $\dfrac{\partial F}{\partial \sigma} = \dfrac{d\overline{\sigma}}{d\sigma}$ and F_k Calculate

$$d(\Delta\sigma) = \left[\frac{-\dfrac{d\overline{\sigma}}{d\sigma}}{\sqrt{\dfrac{d\overline{\sigma}}{d\sigma}\dfrac{d\overline{\sigma}}{d\sigma}}} \right] \times F_k \qquad (3\ 92)$$

$$\sigma_{C+k} = \sigma_{C+k} + d(\Delta\sigma)$$

Set $\sigma_C = \sigma_{C+k}$, and end 'k' loop Calculate F_i, which should be 0, if not, set to 0 (it may be very small) Store σ_{C+k} and F_i, and calculate the elastic strain increment

$$\Delta\in_e = D_e^{-1}\{\sigma_{C+k} - \sigma_{i-1}\}$$
$$\Delta\in_p = \Delta\in_i -\Delta\in_e \qquad (3\ 93)$$

Store $\in_{p_i} = \in_{p_{i-1}} +\Delta\in_p$ Calculate $H_i' = f(\in_{p_i})$ from input data (which may be assumed to have a constant slope / value) Find the element 'n' loop, end the residual force 'i' loop, and end the load 'j' loop

Changing status nonlinearities

Many common structural members exhibit nonlinear behaviour that is status-dependent Status changes might be directly related to load, or be determined by some external cause such as a roller support either in contact or not in contact

3 9 STRESS COMPUTATION

Stresses in various elements in the structure due to nodal deflections may be calculated to check if the structure can safely withstand the externally applied load Typically, the process first includes computation of element nodal deflections in the LCS from values already computed in the GCS These values are then used along with the element strain transformation and constitutive matrices derived in their LCS to compute element stresses Thus, element stress computation involves the following steps

Step 1

Obtain element node deflections from global values

$$u^e = \lambda q^e \qquad (3\ 94)$$

Step 2

Compute element strains from the strain displacement relationship

$$\in = B u^e \qquad (3\ 95)$$

Step 3

Compute element stresses from strains with the appropriate constitutive law

$$\sigma = D \in$$
$$\sigma = D B u^e \qquad (3\ 96)$$

3 10 SOLID ELEMENTS

For a tetrahedron element, computation of the stresses follow the usual procedure in which nodal deflections are first converted into the LCS and stresses are computed from $\sigma = D B u^e$ using the material constitutive matrix D that pertains to three dimensional stress distribution A hexahedron, on the other hand, is divided into two sets of five suitable tetrahedrons, and stresses are calculated in each element and multiplied by their respective volumes, Their sum is next divided by the volume of the hexahedron to yield the average element stress

3 11 CONVERGENCE OF ANALYSIS RESULTS

Since the finite element method is a numerical procedure for solving complex engineering problems, important considerations pertain to the accuracy of the analysis results and the convergence of the numerical solution

A finite element analysis requires the idealisation of an actual physical problem into a mathematical model and then the finite element solution of that model A proper finite element solution should converge to the analytical solution of the differential equations that govern the response of the mathematical model Furthermore, the convergence behaviour displays all the characteristics of the finite element scheme because the differential equations of motion of the

mathematical model express in a very precise and compact manner all basic conditions that the solution variables such as stress, displacement, strain must satisfy If the differential equations of motion are not known, and /or analytical solutions cannot be obtained, the convergence of the finite element solutions can be measured on the fact that all basic kinematic, static, and constitutive conditions contained in the mathematical model must be satisfied

3 11 1 Convergence Criteria

If an incremental solution strategy based on iterative methods is to be effective, realistic criteria should be used for the termination of the iteration At the end of each iteration, the solution obtained should be checked to see whether it has converged within preset tolerances or whether the iteration is diverging If the convergence tolerances are too loose, inaccurate results are obtained, and if the tolerances are too tight, much computational effort is spent to obtain needless accuracy Similarly, an ineffective divergence check can terminate the iteration when the solution is not actually diverging or force the iteration to search for an unattainable solution

Displacement Convergence Criteria

In this criterion the displacements at the end of each iteration is required to be within a certain tolerance of the true displacement solution Hence, a realistic convergence criteria is

$$\frac{\left\| \Delta U^{(i)} \right\|_2}{\left\| {}^{t+\Delta t}U \right\|_2} \leq \epsilon_D \qquad (3\ 97)$$

where ϵ_D is a displacement convergence tolerance The vector ${}^{t+\Delta t}U$ is not known and must be approximated Frequently it is appropriate to use ${}^{t+\Delta t}U$ in the last calculated value ${}^{t+\Delta t}U^{(i)}$ as an approximation to ${}^{t+\Delta t}U$ and a sufficiently small value ϵ_D

Force Convergence Criteria

A second convergence criterion is obtained by measuring the out-of-balance load vector The norm of the out-of-balance load vector be within a preset tolerance $\in_F$ of the original load increment

$$\left\| {}^{t+\Delta t}R - {}^{t+\Delta t}F^{(i)} \right\|_2 \leq \in_t \left\| {}^{t+\Delta t}R - {}^{t}F \right\|_2 \qquad (3\ 98)$$

A difficulty with this criterion is that the displacement solution does not enter the termination criterion

Energy Convergence Criteria

A third convergence criterion may be used to indicate when both the displacements and the forces are near their equilibrium values In this the increment in internal energy during each iteration is compared to the initial internal energy increment Convergence is assumed to be reached when, with $\in_E$ a preset energy tolerance,

$$\left\| {}^{t+\Delta t}R - {}^{t+\Delta t}F^{(i)} \right\|_2 \leq \in_r \left\| {}^{t+\Delta t}R - {}^{t}F \right\|_2 \qquad (3\ 99)$$

This convergence criterion contains both the displacements and the forces, it is in practice an attractive measure

The use of the full Newton-Raphson method in the incremental solution leads to a higher accuracy in the solution since the solution error diminishes quite rapidly in the last iterations

3 12 IMPLEMENTATION OF FEM

In the present work, numerical simulation of combined tension and torsion loading conditions of an AlSiC MMC rod was carried out using finite element code ANSYS The choice of finite element analysis code plays a vital role in the simulation and analysis of a particular application ANSYS is the only finite element analysis code available in the School of Mechanical and Manufacturing Engineering, Dublin City University, and therefore it was used in this research work Despite some limitations, it was thought to be adequate to the task

In a nonlinear analysis the response to load-displacement relationship cannot be predicted directly with a set of linear equations The solution is obtained by dividing the load into a number of increments, and determining the equilibrium condition for each of the increments The problem with a purely incremental approach is that errors accumulate with each load increment, causing the final result to be out of equilibrium ANSYS overcomes the problem of an incremental solution by using Newton-Raphson equilibrium iterations [69] The Newton-Raphson method iterates to a solution using the equation

$$[K^T]\{\Delta u\} = \{F^a\} - \{F^{nr}\}$$ (3 100)

where $[K^T]$ = Tangent Stiffness matrix

$\{\Delta u\}$ = Displacement increment

$\{F^a\}$ = Applied load vector

$\{F^{nr}\}$ = Internal force vector

The advantage of the Newton-Raphson method is that for a consistent tangent stiffness the Newton-Raphson has a quadratic rate of convergence [70] This means that with each iteration the error in the solution is proportional to the square of the previous error The N-R method requires a measure of convergence to decide when to stop iterating Given the external loads on a body (F^a), and the internal forces (F^{nr}) (generated by the stresses in the elements acting at a node), the external forces must balance the internal forces for a body to be in equilibrium, $F^a - F^{nr} = 0$ In practice, the N-R residual will never be exactly equal to zero When the residual becomes small within a tolerance, the N-R iterations are terminated and an equilibrium solution is obtained

ANSYS by default uses a force/moment and displacement/rotation convergence criteria for determining equilibrium convergence A default tolerance of 0 5% for force/moment residuals and 5% for displacement/ rotation increments is used Force based convergence provides an absolute measure of convergence, as it is a measure of equilibrium between the internal and external forces Displacement based checking should only be used as a supplement to force based convergence

3 12 1 Load steps and substeps

In ANSYS, the applied loading on a structure is described by defining a set of load steps The load in a given load step is applied incrementally Each increment of load is referred to as a substep Every load step and substep is associated with a value of time Substeps can also be referred to as time steps In this research work, analysis of the experimental results was based on rate-independent, static analysis For rate-independent, static analysis time is used as a counter and can be set to any convenient value It is easier to plot the load deflection curve if the time is set equal to the magnitude of the applied load in a static analysis While running an analysis with multiple load steps, newly applied loads are ramped from zero at the start of the load step to their full value at the end of the load step When a load is redefined, its value is ramped from the value it had at the end of the previous load step If all energy put into a system is recovered when the loads are removed, the system is conservative and path independent If the energy is dissipated by the system, such as plastic deformation, the system is non-conservative and path dependent In the later system the actual load history must be followed and require that the load be applied slowly by using many substeps If a structure undergoes large displacements as load is applied incrementally, then the stiffness matrix will not be constant during the loading process

ANSYS activates the large deflection analysis within the static analysis domain using the NLGEOM, ON option This can be summarised as a three-step process for each element, such as

1   Determination of the updated transformation matrix $[T_n]$ for the element

2   Extraction of the deformation displacement $\{u_n^d\}$, from the total displacement $\{u_n\}$, in order to compute the stresses and the restoring force $\{F_e^{n-r}\}$

3   After the rotational increments in $\{\Delta u\}$ are computed, node rotations are updated

The total load was divided into two increments and these were applied one at a time In order to obtain valid solutions at intermediate loads levels, and/or to observe the structure under different loading configurations, six to forty two substeps were introduced in the analysis The Newton-Raphson (N-R) equilibrium iterations drive the solution to equilibrium convergence, within some tolerance, at the end of each load increment That is, before each step solution, the N-R method evaluates the out-of –balance (o-o-b) load vector, ($\{F_{restoring}$ – $F_{applied}\}$) and checks for convergence If the set criteria are not satisfied the o-o-b load vector is re-evaluated, the stiffness matrix is up graded and a new solution is attempted The iterative procedure continues until the problem converges If the convergence cannot be achieved then the program proceeds to the next step and tries to converge again

ANSYS stresses that relying solely on displacement convergence can result in gross errors and recommends force convergence checking Force convergence criterion is the default option The program performs a check for force convergence by comparing the Square root of the Sum of the Squares (SRSS) of the force imbalances against the product of VALUE X TOLERANCE, where the VALUE = SRSS of the applied loads and TOLERANCE = 0 001

Hence, the analysis was organised as follows

1 Load steps

2 Substeps

3 Loads

4 Number of iterations

ANSYS strongly recommends that for large displacements analyses the loads specified in the load steps should be stepped-up as opposed to ramped-on This means that the value of a particular load step will be reached during the first iteration and will be kept constant during the remaining iterations, until the end of the load step This contributes to faster convergence After each increment the deflections caused were calculated by using

$$\left\{F^{\iota}\right\} = \left[k^{\iota}\left(\delta, F\right)\right]\left\{\delta^{\iota}\right\}$$

(3 101)

That is, it was assumed that the stiffness matrix was constant during the application of each load increment The initial tangent modulus was taken from a stress-strain curve obtained from experimental observations The initial stiffness matrix $[K_o]$, was then computed from the tangent modulus and the Poisson's ratio The initial stiffness matrix was used to generate the equations for the next increment and so on, until the process was completed for that particular load step It is important to keep the load increments small, so that the increments in displacement cause negligible changes in the stiffness matrix at each load step The original co-ordinates of the nodes were then shifted by an amount equal to the values of the displacements calculated The new stiffness matrix for the deformed plate was re-calculated and the process was repeated until the total load was reached The matrix notation for the incremental procedure, using the equation (3 100), is

$$\left\{\Delta F_{\iota}\right\} = \left[K_{(\iota-1)}\right]\left\{\Delta \delta_{\iota}\right\},$$

(3 102)

$$\forall \iota \in N^{+} \quad \iota = 1,2,3,4,$$

where ι is the positive integer representing the stage of incremental loading

3 12 2 Elastic-Plastic behaviour

Material non-linearities occur when the stress is a non-linear function of the strain The relationship is also path dependant, that is, the stress depends on the strain history as well as the strain itself The general theory for elasto-plastic analysis provides the user with three main elements the yield criterion, the flow rule and the hardening rule

The yield criterion determines the stress level at which yielding is initiated The flow rule determines the direction of plastic straining (i e which direction the plastic strains flow) relative to x, y, z axes Finally, the hardening rule describes the changes the yield surface undergoes with progressive yielding, so that the various states of stress for subsequent yielding can be established For an

assumed perfectly plastic material the yield surface does not change during plastic deformation and therefore the initial yield condition remains the same However, for a material experiencing strain hardening, plastic deformation is generally accompanied by changes in the yield surface Two hardening rules are available and these are isotropic (work) hardening and kinematic hardening

3 12 3 Multilinear isotropic hardening

For materials with isotropic plastic behaviour, the assumptions of isotropic hardening under loading conditions postulates that, as plastic strains develop, the yield surface simply increases in size while maintaining its original shape For metals, ANSYS recommends the von Mises yield criterion with the associated flow rule and isotropic (work) hardening When the equivalent stress is equal to the current yield stress the material is assumed to undergo yielding The yield criterion is known as the 'work hardening hypothesis' and assumes that the current yield surface depends only upon the amount of plastic work done

The solutions of non-linear elastic-plastic materials are usually obtained by using the linear solution, modified elastic and elasto-plastic materials are usually obtained by using the linear solution, modified with an incremental and iterative approach The material is assumed to behave elastically before reaching yield as defined by Hooke's law If the material is loaded beyond yielding, then additional plastic strains will occur They will accumulate during the iteration process and after the removal of the load will leave a residual deformation In general

$$\varepsilon_n = \varepsilon_{n(elastic)} + \Delta\varepsilon_{n(plastic)} + \varepsilon_{n-1(plastic)} \text{ ,} \qquad (3\ 103)$$

where ε_n is the total strain for the current iteration, $\varepsilon_{n(elastic)}$ is the elastic strain for the current iteration, $\Delta\varepsilon_{n(plastic)}$ is the additional plastic strain obtained from the same iteration, $\varepsilon_{n-1(plastic)}$ is the total and previously obtained plastic strain Convergence is achieved when $\Delta\varepsilon_{n(plastic)} / \varepsilon_{n(elastic)}$ is less than a criterion value, the default for ANSYS is 0 01 This means that very little additional plastic strain is

accumulating and therefore the theoretical curve, which is represented by a series of straight lines (multi-linear approach) is very close to the actual one

For the case of uniaxial tension, it is necessary to define the yield stress and the stress-strain gradients after yielding When σ_- becomes greater than the uniaxial yield stress, then yielding takes place The yield condition is the von Mises yield criterion for one-dimensional state of stress

$$\sigma \geq \sigma_{yield}$$

A set of flow equations (flow rule) can be derived from the yield criterion The associative flow rule for the von Mises yield criterion is set of equations called incremental Prandtl-Reuss flow equations That is, the strain increment is split into elastic and plastic portions Hence, it is necessary to apply the total load on the structure in increments These load steps need only start after the FE-model is loaded beyond the point of yielding The size of the subsequent load steps depends on the problem The load increments will continue until the total load has been reached or until plastic collapse of the structure has occurred As the load increases the plastic region spreads in the structure and the non-linear problem is approached using the full N-R procedure The stiffness used in the N-R iterations is the tangent stiffness and reflects the softening of the material due to plasticity It should be noted that in general, flatter the plastic region of the stress-strain curve, the more iterations needed for convergence

As plasticity is path dependant or a on-conservative phenomenon, it requires that in addition to multiple iteration per load step, the loads be applied slowly, in increments, in order to characterise and model the actual load history Therefore, the load history needs to be discretised into a number of load steps with the presence of convergence tests in each step ANSYS recommends a practical rule for load increment sizes such as the corresponding additional plastic strain does not exceed the order of magnitude of the elastic strain In order to achieve that the following procedure was followed

Load step one was chosen so that to produce maximum stresses approximately equal to yield stress of the material The yield stress was estimated from the experimental stress-strain curves The load to cause yield was validated by performing a linear run with a unit load and by restricting the stresses to the critical stress of the material This was found to be approximately equal to 351 79 MPa for Copper Model and 150 MPa for Aluminium matrix in AlSiC MMC Model Successive load steps were chosen such as to produce additional plastic strain of the same magnitude as the elastic strain or less This was achieved by applying additional load increments no larger than the load in step one, scaled by the ratio E_T / E Such as

$$P_{n+1} = \frac{E_T}{E} P_n \quad \forall n \in N, \tag{3 104}$$

where E is the elastic slope and E_T is the plastic slope, with E_T/E not less than 0 05 One of the applications of nonlinear analysis is the analysis of systems subjected to ultimate loads such as plastic behaviour

3 13 SUMMARY

Elastic-plastic constitutive models proposed by different researchers were presented in this chapter Yielding in a material followed the von Mises criterion at the beginning of plastic deformation, and later deviates outwards from the von Mises yield curve according to the isotropic or kinematic hardening rule The complexity of a constitutive model increases with an increase in the material constants used Six different constitutive models with the least number of material constants were described in this chapter The second part of this chapter presents the finite element approach to elastic-plastic problem The procedure used by the finite element analysis tool ANSYS to solve the elastic-plastic problem was also explained

4 EXPERIMENTAL PROGRAMME

4.1 INTRODUCTION

Considerable development of mathematical theories in the past few decades has increased the accuracy with which the experiments must be performed to examine the validity of the theories. The purpose built tension-torsion machine used to conduct experimental tests in this research work provides adequate accuracy by the use of highly sensitive AC servomotors and servo controllers. A schematic diagram of the experimental setup is shown in Figure 4.1.
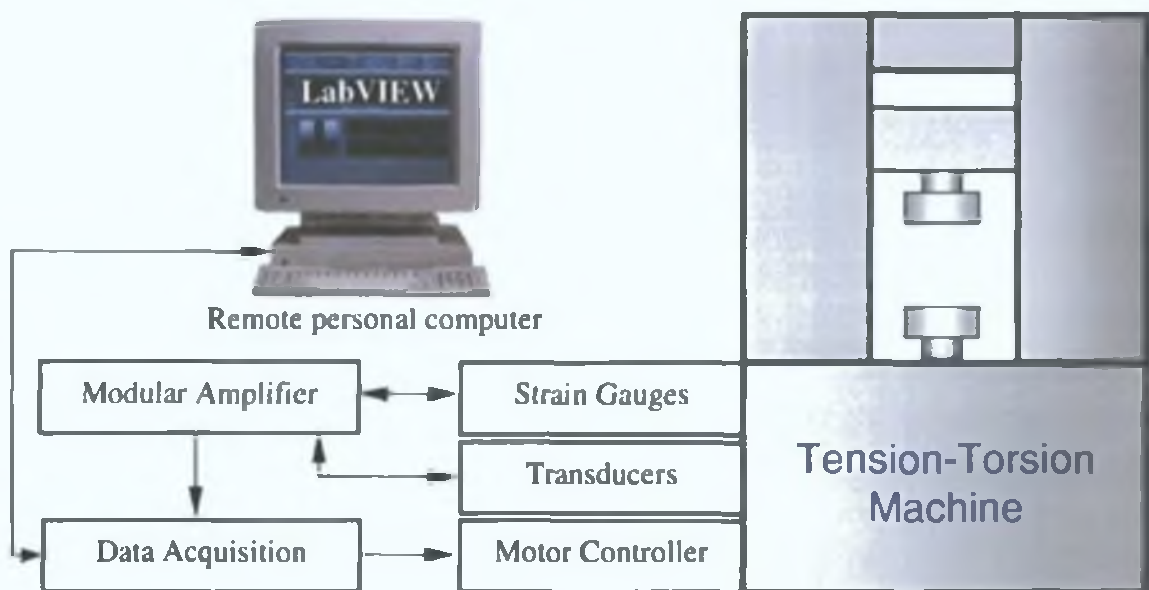

Figure 4.1 Schematic diagram of the experimental setup

At the start of this research work the tension-torsion machine was not functional due to:

   i)   the malfunctioning of the torque motor
   ii)   difficulties encountered in operating the motor controllers
   iii)   improper working of transducer amplifiers

75

The malfunctioning extended function card (EF card) used previously to change the direction of rotation of the motor caused disturbances in operating the servomotors The EF card was removed from the controllers A LabVIEW program was manipulated to change the direction of rotation of the servomotors through the "Bipolar" option At present supplying positive or negative voltage to the servomotor changes the direction of rotation of the servomotor

Individual transducer amplifiers were replaced by the Modular 600 system purchased from RDP Electronics Ltd The modular 600 system houses all the transducer amplifiers including the strain gauge amplifier The signals from the transducers were amplified and supplied to the LabVIEW programme for further processing and recording in an Excel spreadsheet

The machine provides independent control of the axial and torsional strain components The test machine is capable of applying tension and torsion loads simultaneously and individually at different strain rates Two servomotors control the loading of specimen, one for tension and one for torsion The load, the torque, the axial displacement and the angular twist on the specimen can be maintained constant independently This is achieved by controlling the speed and torque of individual motors, through servo controllers

The specimens are prepared to dimensions, as shown in Figure A7 and Figure A8, to properly fit in the grippers of the purpose built tension-torsion machine The machine was controlled from a remote personal computer using LabVIEW software and data acquisition devices Four transducers were used to measure the load, the torque, the axial displacement and the angular twist on the specimen and the measured electrical units were amplified with a modular amplifier and supplied to LabVIEW for further control, display and record The accuracy of the measuring transducer varied with the application In this research work, as a general rule, the transducer output values were calibrated to produce an accuracy of 0 01 units for each of the transducer, i e 0 01mm for LVDT, 0 01Nm for the torque transducer, 0 01kN for axial load cell and 0 01 degrees for angle of twist transducer

A closed loop was created with LabVIEW software, as the program controls the tension-torsion machine according to the signals from the transducer and test conditions The inputs from the transducers are displayed as a function of time in the computer visual display unit (monitor) as well as saved as Microsoft Excel database for further analysis A virtual machine control panel, consisting of variable knobs, Boolean switches and transducer signal indicators, was programmed in the computer and all the controls and indicators in the front panel were properly wired in the block diagram that runs in the background The input signals from the transducer amplifier was analysed and according to the test conditions and front panel inputs, the motors are controlled Four different programs for four loading conditions were built A detailed description of all the devices and the program is presented in the following sections

4 2 TENSION-TORSION MACHINE SETUP

The purpose built machine was designed to conduct tension tests as well as torsion tests on test specimens Tension and torsion loads can be applied individually or simultaneously on the specimens Its overall length, width and height are 84 cm, 100 cm, and 196 cm respectively The weight is little over a ton The components of a tension-torsion machine are mounted on four vertical steel columns The upper fixed specimen gripper is mounted on a horizontal movable crosshead The lower specimen gripper is mounted on a fixed crosshead The lower specimen gripper is capable of rotating about a vertical axis thus applying torsion loads to the specimen The purpose built tension-torsion machine has the following salient features

- Within its maximum limits, the machine is able to apply any desired level of axial load and torque

- It can apply different levels of axial load and torque, both simultaneously and independently

- It can maintain various parameters constant, such as the torque, the angle of twist, the axial load, or the axial displacement

- It is capable of maintaining different strain rates for both types of loading

77

- Continuous data acquisition from load cells and transducers is possible.
- The machine is controlled using a personal computer.
- With slight modification in its setup, the machine could be used as a torque-compression machine.
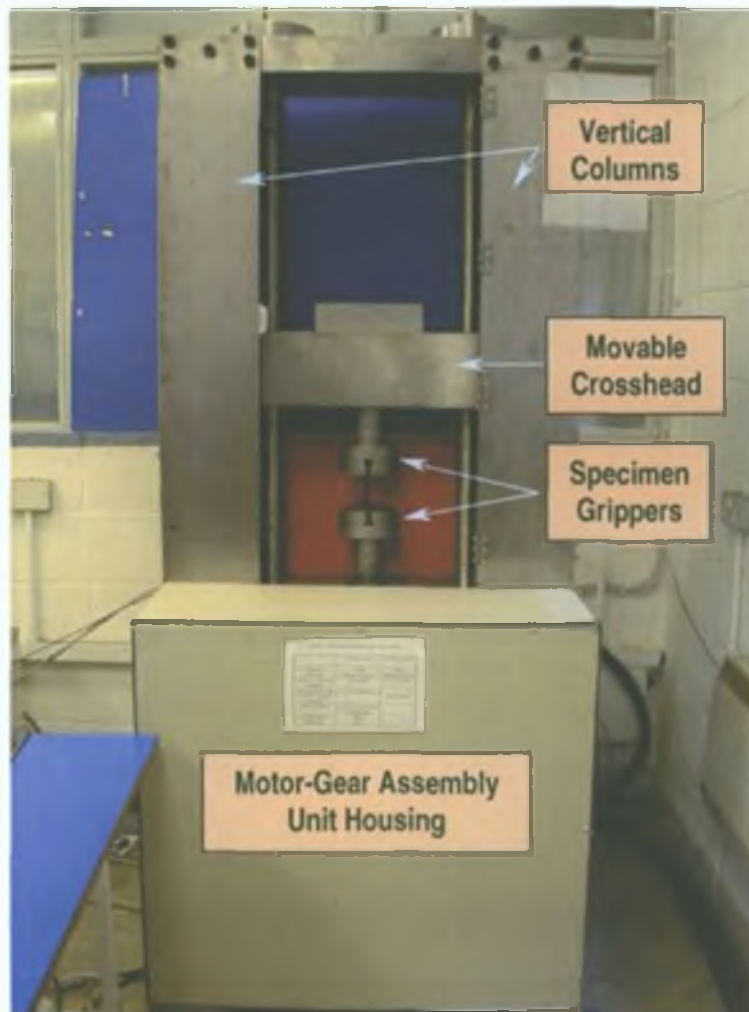

Figure 4.2 Components of the Tension-torsion test machine

Figure 4.2 illustrates the various components of the tension-torsion test machine and Table 4.1 give the specifications of the tension-torsion machine.

	Axis 1 (for Tension)	Axis 2 (for Torsion)
Capacity	100kN	200Nm
Force Rating	100kN upto 48 mm/min	200Nm upto 30deg/sec
Load Range	0-100kN	2-200Nm
Crosshead Speed Range	0 56-48mm/min	
Drive Shaft's Rotational Speed Range		0 15-30deg/Sec
Crosshead Travel	460cm	
Testing Space	420cm	

Table 4 1 The Specifications of the tension-torsion machine

4 2 1   Drive System

The tension-torsion machine is operated by two separate drive systems, one for Axis-1 (for application of tension) and the other for Axis-2 (for application of torsion) Two Moog brushless servomotors of different torque capacities and two 'Carl Bockwoldt' helical gearboxes of different speed ratios are used as drive systems Drive system for Axis-1 provides the necessary tensile force and drive system for Axis-2 provides necessary torsional moment to the specimen The Moog brushless motors were supplied by Devitt technologies Ltd, Ireland

Drive System for Axis-1 (for tension)

The Drive System for Axis-1 was used to apply the necessary axial load on the specimen The drive system consists of

- An AC servomotor
- A Gearbox and
- Timing pulley and belts

AC Servomotor

Drive system for Axis-1 uses a Moog D315-L15 type brushless AC servomotor The motor has a continuous stall torque capacity of 8 1 Nm and nominal speed of 3000 rpm Its continuous stall current is 12 3 Amp The servomotor is an electronically communicated three-phase electric motor with permanent magnet excitation This motor supplies necessary torque that is eventually converted into the required axial force via the gearbox, timing pulleys, timing belt, ball-screws and cross-head

Gearbox

A Carl Bockwoldt three stage CB59-NF80 type helical gearbox was assembled vertically with the servomotor to form the Motor Gear Assembly Unit (MGA Unit-1) The MGA Unit-1 gear ratio is 295 8 and maximum permissible output torque at rated power is 1200 Nm The maximum permissible input speed to the gearbox is 4000 rpm

Timing Pulleys & Belts

Two pairs of similar steel timing pulleys and a pair of polyurethane Bando timing belts were chosen to transmit power from the MGA Unit-1 to the ball screws The pitch and width of these pulleys and belts are 10 mm and 16 mm respectively Hinchlief Precision Components Ltd, UK, supplied the timing pulleys and belts The Power transmission capacity of the timing belts is 30 kW and power transmission efficiency is nearly 98% with no slip or backlash

Drive System for Axis-2 (for torsion)

Drive system for Axis-2 is used to apply necessary torque to the specimen
The drive system consists of

- An AC Servomotor
- A Gearbox and
- Spur gears

AC Servomotor

Drive system for Axis-2 uses a Moog D413-L10 type brushless AC servomotor The motor has a continuous stall torque capacity of 2 7 Nm and nominal speed of 4900 rpm Its continuous stall current capacity is 6 7 Amp The motor applies necessary torque to the specimen through the gearbox and spur gears

Gearbox

A Carl Bockwoldt three stage CB29-NF63 type helical gearbox was assembled with the AC servomotor to form the Motor Gear Assembly Unit-2 (MGA Unit-2) Torque from the motor is amplified by the gearbox and is eventually transmitted to the

specimen via a pair of spur gears The MGA Unit gear ratio is 150 7 and maximum permissible output torque at rated power is 300Nm The maximum permissible input speed to the gearbox is 4000 rpm

Spur Gear

A pair of spur gears of maximum outer diameter 300 and pitch circle diameter 282 mm is used to transmit torque from gearbox 2 to the torsion shaft of the machine The speed ratio is one These casehardened gears are made of steel 'En36' The maximum load carrying capacity of the spur gears is 83 hp at 1000 rpm Both the gears were supplied by 'HPC Ltd'

4 2 2 Control System

Two identical 'Moog T161-003' brushless motor controllers along with a power supply unit, Figure 4 3, are used to control the various input/output parameters and different modes of operation of the tension-torsion machine The controllers provide full velocity servo loop closure with subordinate motor current control Each controller has a continuous current rating of 15 Amp at 50°C ambient temperature and can provide a continuous torque of 13 9 Nm The peak current rating is 30 Amp The T161 controller can close a position control loop around the motor shaft mounted resolver The controllers provide full system protection against overload and output short circuit Each controller was tuned to match its corresponding driving motor using a MCO module The axial load applied to the specimen can be controlled by the torque commands using Controller-1 Similarly, the torque applied to the specimen can be controlled by the torque command using Controller-2

Salient features of the Controller are listed below,

1 The Controller can control the level of torque and velocity of the motors individually and thus help to control axial load/torque and vertical/rotational motion of the machine member

2 The Controller can hold the position of the motor shaft constant, i e can hold the angle of twist or axial displacement of the specimen constant

3 The Controller can change the direction of motion of the motors

Figure 4.3 Controllers and Power supply rack

Besides these controls, many other input/output commands are also available on each Controller such as clockwise, counter clockwise limit switch inputs, motor torque output signal, motor hardware enable/disable input, etc. All these input/output signals are available through a number of connectors/ports, positioned at the back panel of each controller. The circuit connection details are shown in Figure A.1.

Power connector Xμ6, supply power to the motors. Pin 4,5,6,7 are used for power supply to servomotors. The I/O connector Xμ5 facilitates the reading of various input/output parameters of the motors. The input signal (+10V) of the controller is supplied to Pin 19. At the front of the controllers, there are three status LED's to diagnose whether different system and input limits are satisfactory. Port X6 can be used to control various input/output command signals by means of a digital link from a computer. Axis enable input voltage of each controller is 15VDC.

Controller-1

Controller-1 is used to control axial load motor and hence MGA Unit-1. Different levels of output torque from axial load motor are eventually converted to axial load via the gearbox, pulley, belt, ball screw and movable crosshead. Control of torque and rotational speed of the axial load motor, by Controller-1 means control of axial

82

load applied to the specimen and vertical linear movement of the crosshead Clockwise rotation of the axial load motor causes the crosshead to move in upward direction and counter clockwise rotation cause the crosshead to move in downward direction

Controller-2

Controller-2 is used to control torque motor and hence MGA Unit-2 Different levels of output torque from torque motor are eventually transmitted to the specimen as pure torque via the gearbox Thus, control of torque and velocity of torque motor means the control of torque and rotational speed transmitted to the specimen respectively The control of clockwise and counter clockwise rotation of the torque motor means the control of counter clockwise and clockwise twisting of the specimen respectively *Interface connector* At the front panel of each controller, there is a connector X6, which is used to interface the controllers with a personal computer The controllers were manufactured to interface with a computer via an RS232 serial link

4 2 3 Power Supply Unit

A Moog motor-controller power supply unit (160-003type) is used to supply the main power to both controllers as well as to the motors This single-phase power supply unit has a continuous power supply capacity of 1 5 kW Nominal input voltage is 230VAC, 44-66Hz The power supply has sufficient capacity to supply power upto six controllers The power supply unit has an integrated bleed resistor to dissipate excess motor energy during motor regeneration and therefore avoids unacceptable increase in the DC voltage

At the back panel, there are several input/output connectors including AC power connector (X3), External bleed resistor connector (X4), power supply signal and I/O connector (X5), serial interface connector (X6), DC bus connector (X7) and fan connector (X9) In the 'low voltage power & status connector' X5, there are a number of centralized power supplies such as +15VDC-2A line, -15VDC-2A line, +5VDC-7 5A line, etc to supply power to other external devices if necessary The +15VDC-

2A line (Pin 9) was utilized to power the hardware of the motors The +5VDC line (Pm 8) was used for digital input signals

4 2 4 Power Supply

The main 220VAC input was connected to the power supply via the back plane connector X3 Various outputs from the back plane connector X5 were set-up for the following purposes

The +5VDC output from Pin8 and digital ground connection from Pin 12 are used as single digital input signals to select different modes of operation of the motors, such as, run or hold mode, forward or reverse mode, etc From each of these pins, four parallel lines were drawn, two for each controller, and connected to four 'two way' switches to supply either 5 or zero voltage to Pin 3 and 6 of each Xμ7 connector

The +15VDC from Pin 9 was used to make the motor's hardware 'enable' by two 'one way' ON/OFF switches Enabling the motor allow the shaft turn freely with or without load, 1 e , commissioning of the motor An analogue ground connection from Pin 11 was used as the negative terminal of the four external power supply units Both controllers have the same type of connections with the motors and the power supply unit '160-003' Power connector Xμ4 of each controller was connected with the '8 pole power mating connector' of the motor Connections for Xμ4 are made as follows

Pin Number	Input Reference	Wire Colour
4	PE	Green/Yellow
5	W	Brown
6	V	Blue
7	U	Black

Table 4 2 Connection details of Xμ4 connector

4 2 5 Transducers

Axial Load Cell

A donut shaped, 133 5 kN capacity compression type load cell is used to measure the axial load applied to the specimen This *RDP Electronics* force sensor features an unthreaded center through-hole, which is perfect for the application in Tension-torsion machine where the load structure must pass through the center of the load cell The force sensor measures the compression force developed between the base of the load cell and the raised center boss due to the upward movement of the crosshead Bonded foil type strain gauges are used in this load cell Its full-scale non-linearity is +0 5 and maximum excitation voltage is 10VDC Factory calibrated output is 2 8945 mv per voltage excitation, and response of the load cell is 0 216816 mv/kN load applied The load cell was purchased from RDP Electronics LTD, UK, and the Model Number BL - 915

Red	+Excitation	White	+Output
Black	-Excitation	Green	-Output

Table 4 3 Axial load transducer connection details

Axial Load Cell Calibration

Transducers need periodic calibration to ensure the consistency in functioning A linear regression model was constructed for load cell data that relates a known load applied to a load cell to the deflection of the cell The model was then used to calibrate future cell readings associated with loads of unknown magnitude
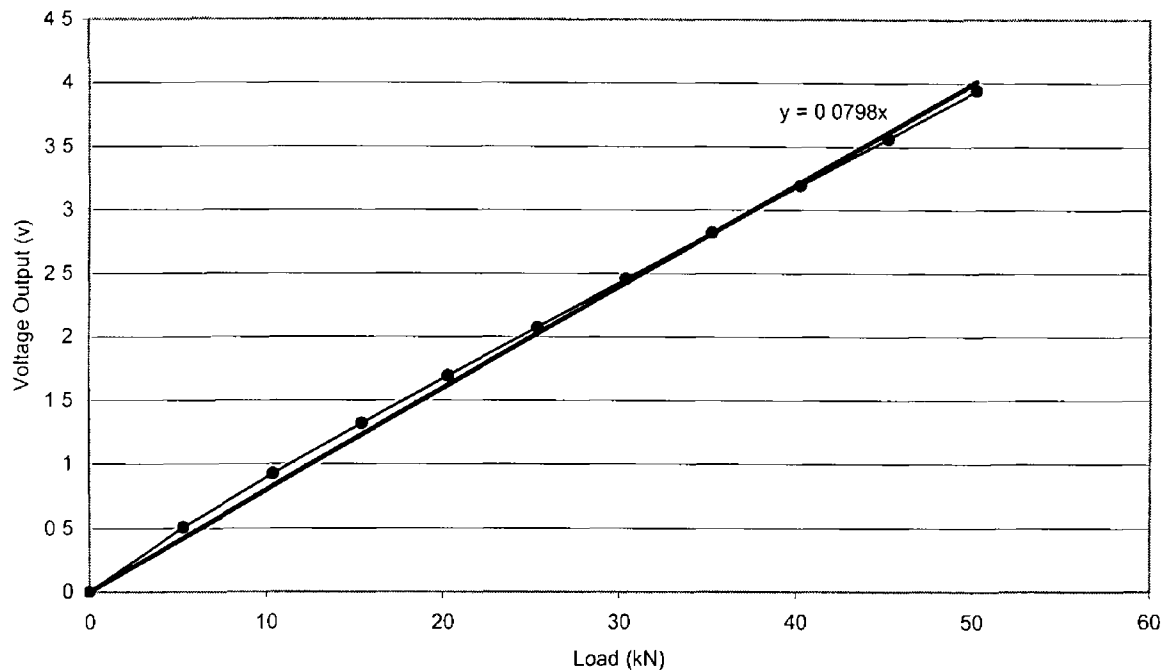
Figure 4 4 Axial load transducer calibration plot

The data collected in the calibration equipment consisted of a known load, applied to the load cell, and the corresponding deflection of the cell from its nominal position Measurements were made over a range of loads from zero to 50 kN in an Instron machine The data was collected in two sets in order of increasing loads and decreasing loads and averaged out The systematic run order makes it difficult to determine whether or not there was any drift in the load cell or measuring equipment over time Another set of data was collected with readings taken after a period between load increments No considerable drift in the load was noticed The calibration experiments provided a good description of the relationship between the load applied to the cell and its response Plotting the data indicates that the hypothesized, simple relationship between load and deflection was reasonable The plot Figure 4 4 shows the data It indicates that a straight-line model best fits the data It does not indicate any presence of outliers, or non-constant standard deviation of the response

Torque Cell

A 'Norbar' rotary type torque transducer of 500 Nm capacity is used to measure the torque applied to the specimen It is a strain gauged torsion bar and can measure both static and dynamic loads The transducer shaft was made from heat-treated stainless steel on to which are bonded strain gauges which are wired to form a wheatstone bridge The strain gauges vary their resistance in direct proportion to the torque applied The change in resistance causes a change in voltage across the bridge that was then amplified by the amplifier module The torque load cell was designed to ignore non-torsional forces The torque cell can operate both in clockwise and anticlockwise directions The full-scale non-linearity of this unit is +0 1 The normal operating speed for this unit is 3000 rpm and has an expected life of 3000 operating hours The maximum bridge excitation voltage of this transducer is 10VDC Factory calibrated output is 0 817 mv per voltage excitation, and response of the torque load cell is 0 04084 mv/Nm torque applied The torque load cell was purchased from Norbar torque tools Ltd, Model Number 50139 / ETS

Pin F	+Excitation	Pin A	+Signal
Pin D	-Excitation	Pin B	-Signal

Table 4 4 Torque transducer connection details

Torque Cell Calibration

Similar to Load cell calibration, torque cell was subjected to different known torques using Digital Torque Wrench The corresponding voltage outputs were collected and a plot was made between the torque and the output voltage The data was collected in two sets in order of increasing loads and decreasing loads and averaged out The systematic run order makes it difficult to determine whether or not there was any drift in the load cell or measuring equipment over time Another set of data was collected with readings taken after a period between load increments No considerable drift in the load was noticed The calibration experiments provided a good description of the relationship between the torque applied to the cell and its
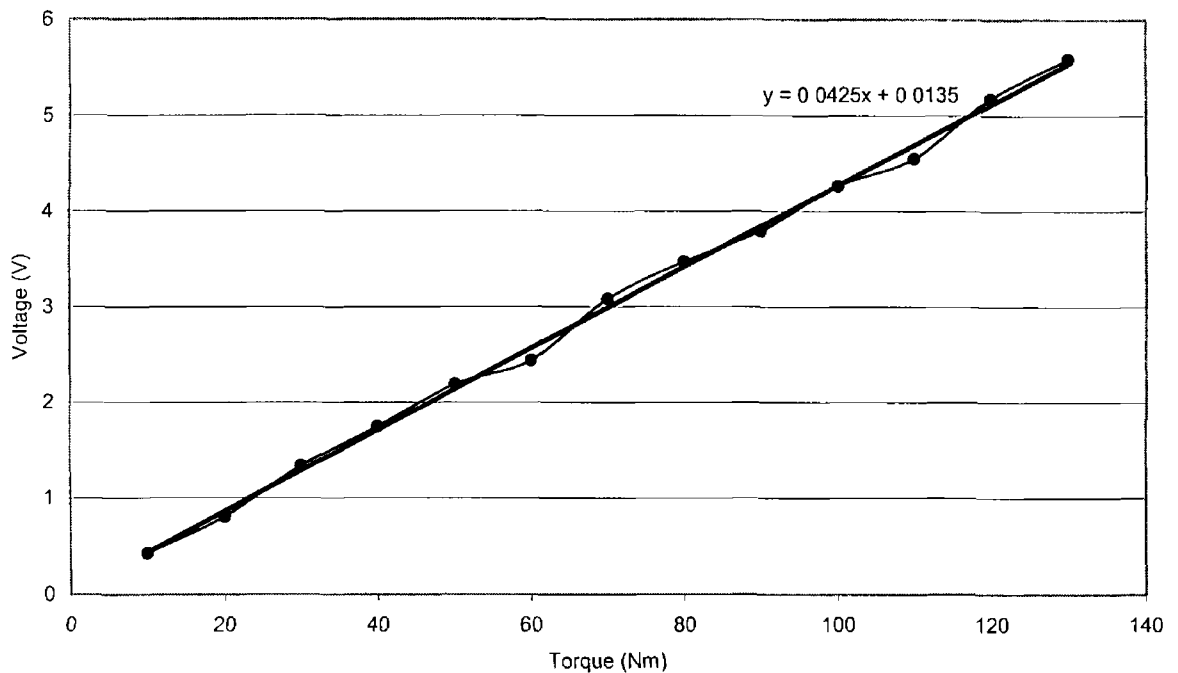
87

response

Figure 4 5 Torque transducer calibration plot

Figure 4 5 shows the linear relationship between the torque and the voltage output

Angular Position Transducer

A DC / DC angular position transducer is used to measure the angle of twist of the specimen The transducer is a transformer in which the output is governed by the angular position of the input shaft in relation to the transducer body The output is electrically isolated from the input The required input is a stabilized 10 VDC from a source impedance of less than 1 ohm The DC output is converted to an AC waveform by an integral oscillator and then fed to the transformer primary winding The output from the secondary winding is converted to DC by an integral demodulator and filter The transducer can rotate 360° mechanical angle continuously Its effective electrical angle is 300 , i e , its output is linear over these 300 Output sensitivity is 33 mv per degree rotation of its shaft with 50mv as residual voltage The linearity-deviation from best straight line is + 0 5 The shaft rotation is clockwise for increasing output

The transducer was purchased from 'Penny+Giles Position Sensors Ltd': Model Number - 3810 / 300.

Red	+Excitation	Brown	+Signal
Black	-Excitation	Blue	-Signal

Table 4.5 Angular position transducer connection details

Angular position transducer calibration

Since the angular position transducer is a transformer, the output voltage depends on the position of the armature. When the torque shaft is rotated at a constant speed, the armature position in the transducer continuously changes causing a steady change in the output voltage. A pointer was setup in the torque shaft to point on a calibrated sheet, as shown in Figure 4.6.

The torque shaft was positioned at different angles and the corresponding voltage output was collected. The procedure was carried out in both clockwise and counter clockwise directions and the data was averaged out. Figure 4.7 shows the plot between the pointer position and the corresponding output voltage in the effective range.

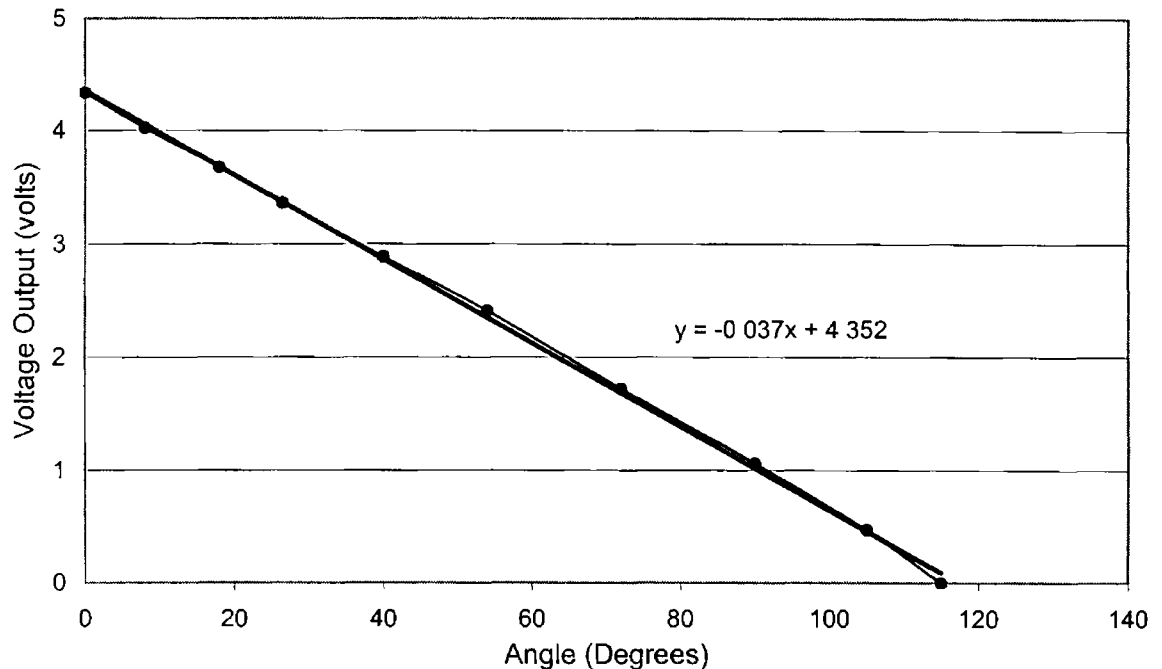Figure 4.6 Angular position transducer calibration setup

Figure 4 7 Angular position transducer calibration plot

Linear Variable Displacement Transducer (LVDT)

To measure the total deformation of the specimen along the axial direction, a *RDP Electronics* Linear Variable Differential Transducer (LVDT) is used This ACT 500A position sensor uses non-contact displacement measurement technique LVDT displacement transducer unit have no contact across the position sensor element ensuring long life The transducer is of guided armature spring return type The captive guided spring return transducer unit has an internal spring, which constantly pushes the armature outwards The armature of the LVDT displacement transducer is guided in low friction bearings The LVDT was mounted on a mounting block with a magnetic base The end of the armature was fitted with a ball-ended probe This type of armature configuration only requires fixing at one end, and so it was selected for this application The effective stroke length of the transducer is +/- 12 5 mm and inward over travel is 1 1 mm and outward over travel is 13 mm The LVDT was mounted on a magnetic base using a fixture and the assembly was fixed on the frame of the tension-torque machine before conducting the test

Linear Variable Displacement Transducer calibration

The LVDT was mounted on a magnetic base placed on a flat metal surface The ball end of the transducer armature was positioned such that it just has physical contact with a rigid surface such as machine frame, as shown in Figure 4 8 The magnetic base was placed in different positions within the range of the LVDT and the corresponding output voltages are collected The procedure was carried out in both inward and outward movement of the transducer armature

Figure 4 8 LVDT Calibration setup

Distance (mm)
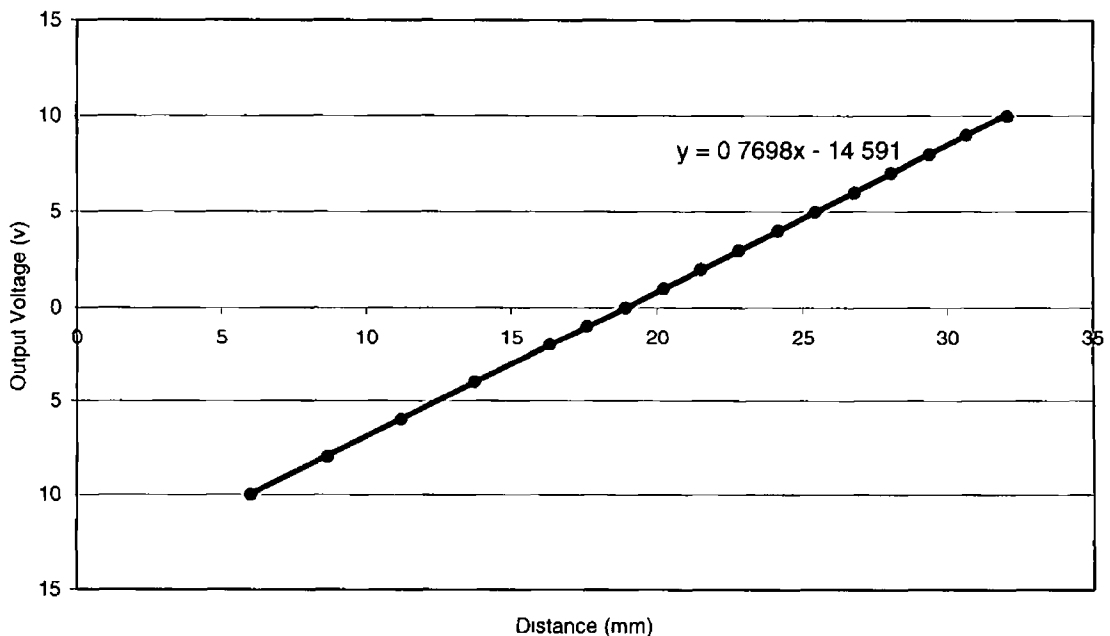
Figure 4 9 LVDT calibration plot

The plot between the transducer armature position and the output voltage shows a linear relationship between the variables, Figure 4 9

4 3 STRAIN GAUGE

Apart from the transducers used in the machine, strain gauges are attached to the specimen to obtain the local strain information of the specimen under different loads Strain is defined as the ratio of the change in length to the initial unstressed reference length A strain gauge is the element that senses this change and converts it into an electrical signal This can be accomplished because a strain gauge changes resistance as it is stretched, or compressed, similar to wire The important factors that must be considered before selecting a strain gauge are the direction, type, and resolution of the strain to be measured The Wheatstone bridge configuration, shown in Figure 4 10 a, is capable of measuring small resistance changes from which minute strains can be obtained The strain gauges are numbered from 1 through 4 The total strain is always the sum of the four strains The total strain is represented by a change in V_{OUT} If each gauge had the same positive strain, the total would be zero and V_{OUT} would remain unchanged
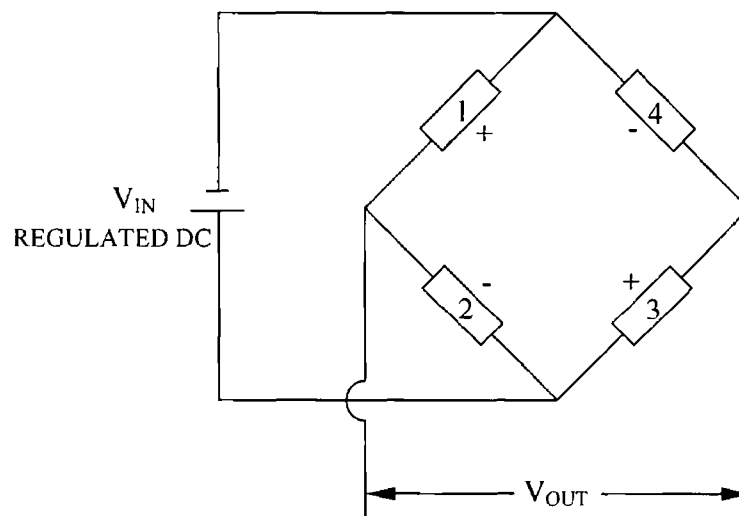
Figure 4 10 a Wheatstone Bridge

Bending, axial, and shear strain are the most common types of strain measured The actual arrangement of the strain gauges will determine the type of strain that can be measured and the output voltage change
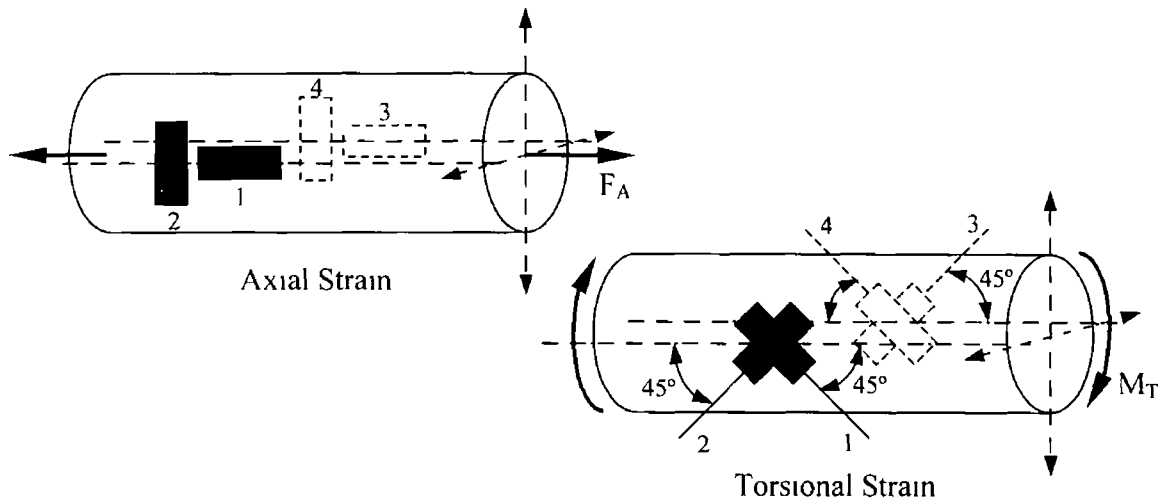

Figure 4 10 b Strain Gauge alignment with the axis of the specimen

Figure 4 10 b shows the arrangement of strain gauges necessary for measuring tensile and torsional strains If a positive (tensile) strain is applied to gauges 1 and 3, and a negative (compressive) strain to gauges 2 and 4, the total strain would be 4 times the strain on one gauge If the total strain is four times the strain on one gauge, this means that the output will be four times larger Therefore, greater sensitivity and resolution are possible when more than one strain gauge was used The strain gauges are properly balanced for zero resistance before the test and the output voltage was supplied to the modular amplifier for further amplification and then to the LabVIEW program Measurement of normal strains was particularly simple to make, and highly reliable techniques have been developed for this purpose By comparing the initial distance between any two corresponding gauge points with the distance in the stressed member, the elongation in the gauge length was obtained Dividing the elongation by the gauge length gives the strain in the direction of load application Since the strains generally encountered were very small, it was possible to employ a highly versatile means for measuring them, using expendable electric strain gauges These are made of very fine wire or foil that was glued to the specimen being

investigated. As the forces are applied to the specimen, elongation or contraction of the wires or foil takes place concurrently with similar changes in the material. These changes in length alter the electrical resistance of the gauge, which can be measured and calibrated to indicate the strain in the specimen. The full potential of accurate strain measurement can be realized only when strain gauges are properly installed. Figure 4.11 shows the strain gauged specimen fixed in the machine grippers.

Figure 4.11 AlSiC MMC rod fixed in machine grippers with instrumentation

The strain gauge installation procedure involves the following steps:

4.3.1 Surface Preparation

Properly prepared surfaces help ensure the strong, stable bonds required for transmission of surface strains to gauge. The bonding surface must be chemically clean and free of paint, weldments, spalling and other defects or contaminants [71]. Five basic operations of surface preparation are:

Degreasing

Degreasing was performed to remove oils, greases, organic contaminants, and soluble chemical residues. Degreasing should always be the first operation. This is to avoid having subsequent abrading operations drive surface contaminants into the surface material. Degreasing can be accomplished using a hot vapour degreaser, an ultrasonically agitated liquid bath, aerosol type spray cans of CSM-1A Degreaser, or wiping with GC-6 Isopropyl Alcohol, Figure 4.12.

Figure 4.12 Degreasing with Solvent

Abrading

In preparation for gage installation, the surface was abraded to remove any loosely bonded adherents (scale, rust, paint, galvanized coatings, oxides, etc.), and to develop a surface texture suitable for bonding, Figure 4.13.

Figure 4.13 Abrading with Silicon Carbide paper

Burnishing of layout lines

The normal method of accurately locating and orienting a strain gage on the test surface was to first mark the surface with a pair of crossed reference lines at the point where the strain measurement was to be made. The lines are made perpendicular to one another, with one line oriented in the direction of strain

measurement. The gage was then installed so that the triangular index marks defining the longitudinal and transverse axes of the grid are aligned with the reference lines on the test surface. The reference, or layout, lines should be made with a tool which burnishes, rather than scores or scribes, the surface, Figure 4.14. A scribed line may raise a burr or create a stress concentration. In either case, such a line can be detrimental to strain gage performance and to the fatigue life of the test part.

Figure 4.14 Burnishing Layout lines

Conditioning

After the layout lines are marked, M-Prep Conditioner should be applied repeatedly, and the surface scrubbed with cotton-tipped applicators until a clean tip was no longer discoloured by the scrubbing, Figure 4.15. During this process, the surface should be kept constantly wet with Conditioner A until the cleaning was completed.

Figure 4.15 Applying Conditioner to Specimen Surface

Neutralising

The final step in surface preparation was to bring the surface condition back to an optimum alkalinity of 7.0pH to 7.5pH, which was suitable for all Micro-Measurements strain gage adhesive systems. This should be done by liberally

96

applying Neutraliser to the cleaned surface, and scrubbing the surface with a clean cotton-tipped applicator. The cleaned surface should be kept completely wet with Neutraliser throughout this operation. When neutralized, the surface should be dried by wiping through the cleaned area with a single slow stroke of a clean gauze sponge. With a fresh sponge, a single stroke should then be made in the opposite direction, beginning with the cleaned area to avoid recontamination from the uncleaned boundary, Figure 4.16.

Figure 4.16 Removing neutraliser with gauze sponge

4.3.2 Gauge Handling

The gauge was removed from the folder and placed on a clean surface with the solder tab facing up. Cellophane tape of 4inch length and wider than the gauge was smoothed onto the gauge and work surface.

Adhesive

The adhesive was applied on the gauge surface and the specimen evenly. Micro-Measurements M-Bond 200 Cyanoacrylate adhesive was used for this purpose. After a minute, wipe the adhesive under the strain gauge by wiping over the cellophane tape and place the thumb over the gauge to apply a steady pressure for 5 minutes. Slowly and steadily, peel off the tape from the specimen. The gauge is now ready for the leadwire attachment.

Leadwire Attachment

The leadwire attachment is the most critical step in strain gauge installation. The tip of the wires to be attached to the strain gauge tab was tinned properly and the solder iron was maintained at proper temperature. A tiny pool of fresh solder was placed on

the tab and the tip of the leadwire was drawn into the pool and allowed to solidify. Drafting tape can be used to position leadwire in case of difficulty in attaching the leadwire with the solder tab in the strain gauge. The leadwire from the strain gauge should now be attached to the instrumentation for calibration and measurement.

Two types of strain gauges purchased from Measurements Group, UK, Ltd were used for uniaxial and biaxial strain measurement. CEA-06-250UN-350 is a general-purpose uniaxial strain gauge used in quarter bridge connection with one active arm. The grid was made of constantan and completely encapsulated in polyamide with large, rugged copper coated tabs for soldering leadwire. For biaxial loading tests, CEA-06-062UV-350 was used in half bridge connection with two active arms. These are two-element 90° rosette for torque and shear-strain measurements. The strain gauges are attached within the gauge length of the specimen.

4.4 MODULAR AMPLIFIER

In the present experimental setup, a number of transducer sensors were positioned in the near vicinity of the specimen. *RDP Electronics* Modular 600 conditions the outputs from these transducers, Figure 4.17.
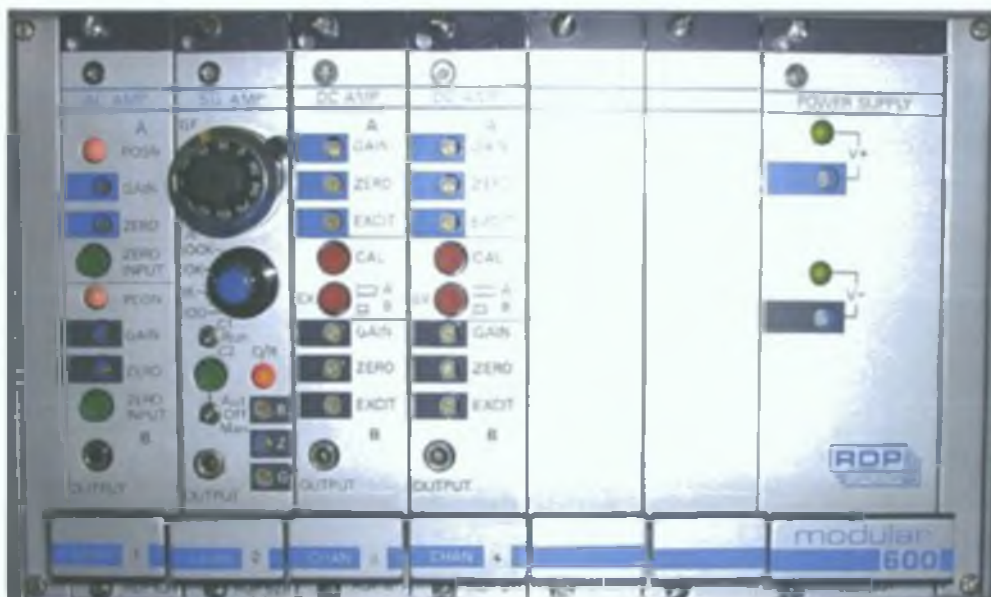

Figure 4.17 Modular 600 System- Transducer signal amplifier

98

RDP Electronics Modular 600 is a Eurocard based system and provides conditioning for a number of different transducer types including LVDT transducer, Strain gauge transducer, Strain gauges, voltage and current inputs and linearisation for RDP Electronics non-contact inductive sensors [72]

The signal amplifiers have 25 mm wide front panels and the full rack arrangement comprise three dual channel amplifiers, one strain gauge amplifier, and a power supply module All modules, apart from the power supply, plug into a back-plane interconnection of transducer inputs and signal outputs The signal amplifier modules also have the output signals available at front panel jack sockets The amplifier modules supply excitation and signal conditioning for various AC and DC transducers The amplifier modules are mounted in a standard housing of "Half width" case frame The back-plane provides an interface between the module 32-way connectors and the transducer and output signal connectors which are accessible from the rear of the case Each module has two 7-pin transducer connectors for channel A and B, and one 5-pin output connector that provides both A & B output signals Transducer connectors are labelled A & B and the output connector as C on the rear panel Since the system has no monitor or interface to address the amplifier modules, the back-plane address lines assume the state equivalent to a channel 0 address To avoid the possibility of more than one output signal being connected simultaneously to the analogue output bus, all the module PCB address switches are set to a different number (0-4) for each channel A warm up time of 30 minutes was allowed for modular amplifier to make sure there was no drift in the transducer and amplified signals

The Modular system includes four transducer-conditioning modules, which are described below,

4 4 1 Module 611-Two Channel DC Amplifier Module

The *RDP Electronics* 611 strain gauge signal conditioning amplifier module is part of the modular 600 system and designed for use with strain gauge and DC

type transducers The 611 module is a plug-in Eurocard module with two channels of transducer energisation and signal conditioning for use with both low and high sensitivity transducers Typical low sensitivity transducers are full strain gauge bridge load cells and torque cells, as the one used in the tension-torsion machine The front panel controls include fine gain, zero and excitation with a push button shunt calibration Both channel output signals are accessible via a 3-pole jack On-board controls allow selection of ±15 V excitation, voltage or current (4-20 mA) output and noise reduction filter Transducer and output corrections are made via circular DIN connectors

The switch settings and the internal controls in the card are set as supplied except the channel number The channel number was set according to the position of the card in the rack The 611 module also provides a shunt calibration facility so that suitable transducers can be calibrated electronically The Torque and Load Cell were excited and the output signal from the transducers were conditioned and amplified in this module before being supplied to LabVIEW

4 4 2 Module 621-Dual Transducer Amplifier Module

The RDP Electronics 621 card is a 2-channel LVDT oscillator/demodulator which may also be used with half bridge and similar inductive-type transducers There is a common excitation supply, but each channel has separate gain and zero controls and outputs, which are selectable for voltage or current Connections are made via circular DIN (audio type) plugs Output signals are also provided on a front-mounted jack which together with fine gain and zero controls, are accessible via holes in the panel A bi-colour LED gives an approximate indication of armature central position Push-button zero input switches allow easy checking of amplifier zero adjustments and a master/slave facility removes beating effects in this multichannel system Since this module has been supplied in an RDP housing, it was configured as a master, i e , first module (Channel 1) The amplifier has outputs of both voltage and 4-2 mA A broad range of adjustments

100

ensures that the voltage and 4-20 mA outputs may be calibrated over all or just parts of the transducer range

4 4 3   Module 628-Strain Gauge Amplifier Module

The *RDP Electronics* 628 strain gauge signal-conditioning amplifier provides precision amplification and calibration of strain gauges outputs The 628 strain gauge amplifier is a Eurocard – based module designed as part of the Module instrumentation system It is a part of the modular 600 system and the module is designed to work with quarter, half and full bridge gauges and features gauge factor selection and switchable micro-strain ranges The module was calibrated for use with gauges of known gauge factor The result is that the output of the strain gauge amplifier can be proportional to micro-strain Direct reading in micro strain units is possible with four switched ranges of 100, 1000, 10000, and 100000 $\mu\varepsilon$ Variable excitation was provided together with coarse and fine amplification controls, automatic or manual bridge balance, gauge factor and number of gauges A four-position, front panel mounted rotary switch alters the gain of the signal amplifier to allow optimum scaling of output to suit input signals equivalent to between 100 and 100000 $\mu\varepsilon$ When used in conjunction with gauge factor potentiometer and number of gauges switch, the output may be calibrated to give 10V for full scale input, e g , with the switch set to 10K, 10000 $\mu\varepsilon$ input = 10V output A front panel mounted, three-position toggle switch allows selection of manual balance or automatic balance With the switch in the OFF position, both balance circuits are disconnected from the bridge When AUTO was selected, pressing the adjacent push button causes the auto-balance circuit to assess any imbalance and inject a voltage into the relevant bridge node sufficient to cancel the imbalance, hence producing zero amplifier output When Manual selected, the 20 turn screw driver-adjusted, front panel mounted balance potentiometer may be used to compensate for any bridge imbalance within the specified range

Voltage and current outputs are available simultaneously Bridge completion for quarter or half bridge systems was provided by resistors mounted on a separate

connector board, which was plugged into the relevant backplane channel A front panel mounted LED indicates when the signal amplifier first stage was saturated, requiring selection of the next highest $\mu\varepsilon$ range

4 4 4 Module 631-Power Supply

The RDP Electronics 631 module provides power to the modular 600 system busses enabling amplifier to pickup their power at the appropriate positions The a c supply to the 631 is via a standard a c lead, which plugs into the back of the 600 system housing

4 5 DATA ACQUISITION DEVICE

4 5 1 Device 1

The National Instrument AT-AO-06 is a high performance, 12-bit analog output board for ISA computers It has six identical output channels, each of which has voltage output and can sink 4 to 20 mA current when connected to an external source The voltage output of each channel is either bipolar or unipolar and was derived from the onboard reference The analog outputs are available at a 50-pin ribbon cable connector The hardware block diagram and I/O connector detail was given in Figure A 2

4 5 2 Device 2

The National Instrument AT-MIO-16E-10 board is a high performance plug and play compatible, multi-function analog, digital, and timing I/O board for the PC AT series computers The board can be easily configured and calibrated using software, as it does not have DIP switches, Jumpers or Potentiometers Due to the DAQ-PnP features, the board is completely software configurable Two types of configuration were performed on the board bus related configuration and data acquisition related configuration Bus-related configuration includes setting the base I/O address, DMA channels, and interrupt request channels Data acquisition related configuration includes such settings as analog input polarity and range, analog output reference source, and other settings The board has two input polarities unipolar with a range

102

of 0 to 10 volts and bipolar with a range of -5 to +5 volts. The analog output channels are configured for bipolar output, as the motors should be run in either direction. The block diagram and I/O connector pin assignment of the board was given in Figure A.3.
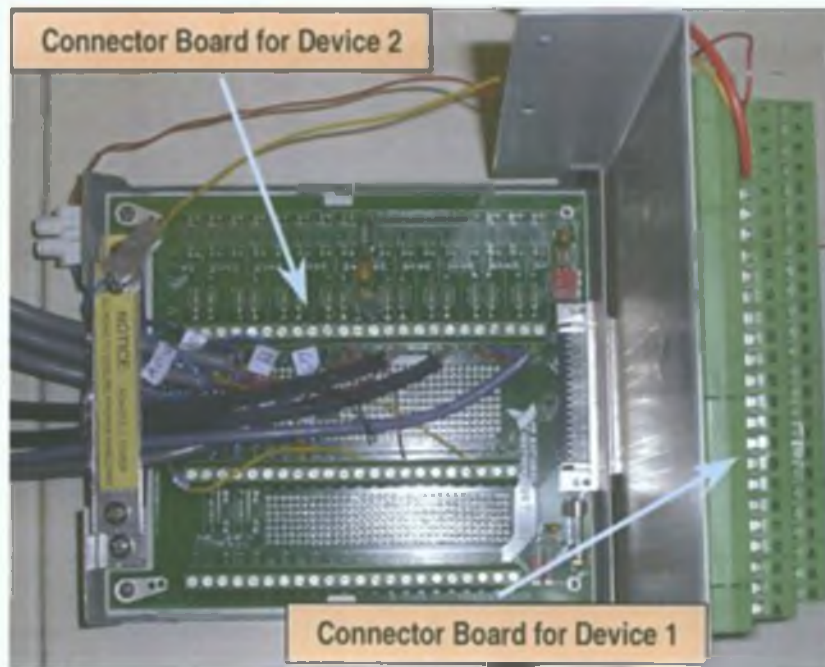

Figure 4.18 Input/Output Connector boards for Device 1 and Device 2

The input/output connector boards for AT-AO-06 and AT-MIO-16E-10 devices were shown in Figure 4.18.

4.6 LABVIEW PROGRAM

LabVIEW (Laboratory Virtual Instrument Engineering Workbench) is a development environment based on the graphical programming language G. The LabVIEW package is specifically designed to permit quick implementation of a computer-controlled data gathering and analysis system, which can be extensively customised to suit a particular application (need). LabVIEW is hierarchical in that any virtual instrument (VI) designed can be quickly converted into a module, which can be a sub-unit of another VI. This is entirely analogous to the concept of a procedure in conventional programming.

LabVIEW was integrated fully for communication with hardware such as GPIB, VXI, PXI, RS-232, RS-485, and plug-in data acquisition boards LabVIEW is a true 32-bit compiler that gives the fast execution speeds of the program, needed for the custom data acquisition, test and measurement solutions [73-78] LabVIEW uses terminology, icons, and ideas familiar to engineers, scientists and relies on graphical symbols rather than textual language to describe programming actions

LabVIEW programs or in other words Virtual Instruments (VI) has a *front panel* and a *block diagram* The front panel is the graphical user interface of the Virtual Instrument This interface collects user input and displays program output The front panel contains controls and indicators A control can take many forms, most of which are "pictures" of real controls used on real instruments-rotary knobs for example All controls have some form of visual feedback to show the user what state they are in A second useful property of the controls is that the reaction to unsuitable input can be specified by the user, thus saving time towards human incompetence Indicators take a large number of forms, some are "pictures" of real indicators such as lights and meters The concept of indicators also includes graphs and charts The block diagram of the VI is almost the backside of the front panel It shows how all the controls and indicators fit together as well as the hidden modules where all the work is done It looks like an electronic schematic diagram and is conceptually wired up in the same way The block diagram contains the graphical source code of the Virtual Instrument In the block diagram the virtual instrument was programmed to control and perform functions on the input and output created on the front panel One of the major issues in LabVIEW programming is to allocate the timing and ordering of operations LabVIEW works in exactly the same way as a conventional programming language The task is handled by the order of the items along with the use of various loop constructs The concept of LabVIEW is "data flow programming"-any item executes when all its inputs are available The standard execution is left-to-right because inputs are generally on the left of an item and outputs on the right Looping and ordering is handled by *Structures*, which look like books

with the number of pages LabVIEW palette sets give the option to create and edit the front panel and block diagram Tools palette contains the tools to edit and debug the front panel and the block diagram objects There are nine tools in the tools palette that are used to build and modify the front panel items The control palette contains the front panel control and indicator objects used to create the user interface The items can be picked from the controls palette There are ten panes on the control palette, each pane having a number of different items These items can be used either as controls or as indicators depending on the need The items are picked from the controls palette and placed in the front panel using the selection tool The functions palette contains the objects used to programme the virtual instrument and to build the source code, such as arithmetic operators, instrument input/output, and file input/output and data acquisition operation

The present program was built to control two motors, as described in sections 4 7 2, with different speeds and directions, and to acquire data from the transducers The motors used are brush less AC servomotors, one for upward and downward movement of the cross head to apply axial load on the specimen and the other for rotary motion, to apply torque on the specimen In addition to this, changing voltage should alter the speed at which these movements are to be carried out There are four transducers installed in the machine to measure the axial load, the torque, the linear displacement and the angle of twist of the specimen mounted in the machine The data from these transducers were recorded and LabVIEW program was executed accordingly forming a closed loop According to the conditions in the front panel of the virtual instrument, the machine was operated and the response from the transducer was recorded and used to control the further execution of the program

The test set is categorized into four types,

1   Constant Torque Test - Increase axial load maintaining the initially applied torque held constant,

2   Constant Angle of Twist Test - Increase axial load maintaining the initially applied angle of twist constant,

3   Constant Load Test - *Increase torque maintaining the initially applied axial load held constant* and,

4   Constant Axial Displacement Test - *Increase torque maintaining the initially applied axial displacement held constant*

To accomplish the four different type of loading conditions, four Virtual Instruments were built as explained in the following sections

4 6 1   Front Panel

The program front panel was split into two sections, one of the sections was attributed to the control of the machine to set up the specimen in the grippers before conducting the test This section of the front panel has a voltage variable digital control for each motor to adjust the speed of the motors, a speed control ON/OFF switch, and a torque control ON/OFF switch for each motor to run the motors The second section was attributed to controlling the machine for the specific test This section of the front panel has controls to drive the motors and to set the limiting parameters for the test such as the axial load, the torque, the angle of twist and the axial displacement

Along with the limit, tolerance values may also to be supplied to approximate the control value Providing a tolerance to the limiting value would reduce the shunting of motors, as there exists another parameter that governs the limiting value In addition to the control switches, five graphical indicators along with digital indicators are created in this section to show the current values of the axial load, torque, angle of twist, axial displacement, and strain gauge parameters Figure 4 19 shows the Front Panel construct of the LabVIEW program for Constant Load Test
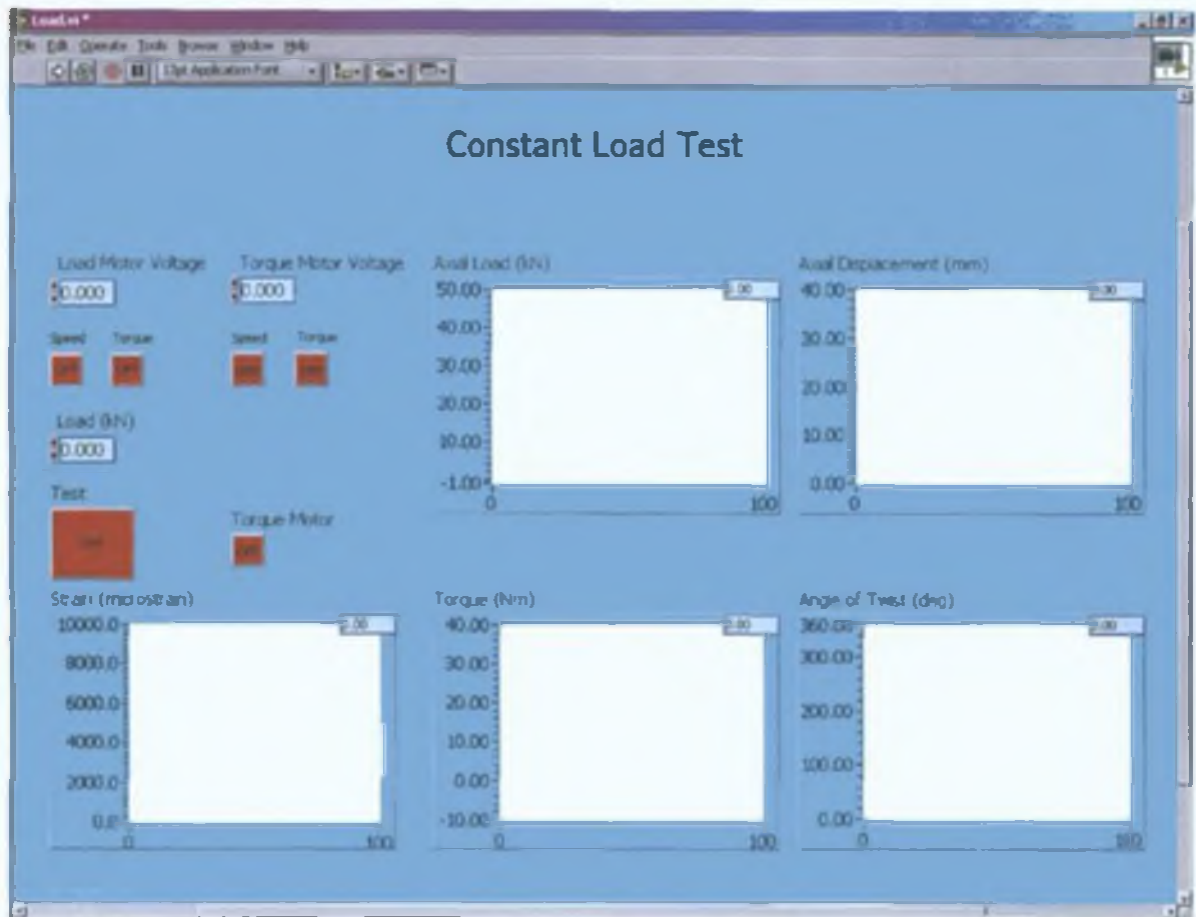
Figure 4.19 LabVIEW Front Panel Construct

4.6.2 Block Diagram

In the block diagram, which is a pictorial solution to a programming task and the source code for the Virtual Instrument, a *While loop* was used to enclose all the objects.

While loop

The *While loop* will execute until a specified condition is no longer *True*. A *Sequence structure* with two subdiagrams or frames was placed inside the *While loop*, as shown in Figure 4.20. The first subdiagram or frame was used to control the machine and the second subdiagram was used to direct the dataflow to a *Microsoft Excel* file. Since the machine was to be controlled in two modes, one for specimen set-up and other for

the test program, a *Case structure* was inserted in the first subdiagram of the *Sequence structure*
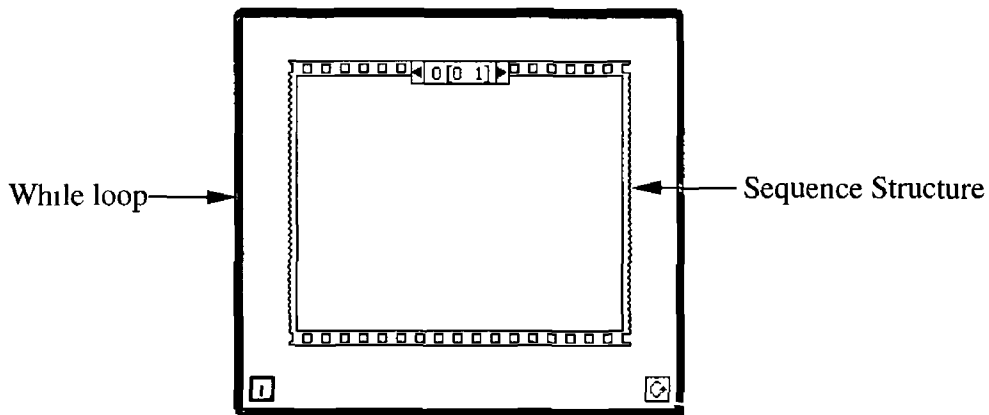
Figure 4 20 While Loop and Sequence Structure

Sequence Structure

LabVIEW works on the concept of dataflow – a function or VI executes when all the inputs are available This is generally smooth when processing a flow of data but there are applications when this was not the case One of the principal areas where the trouble arises is in timing If the programming was not done carefully, events could occur at different times and in different sequences To impose a sequential execution of events LabVIEW uses *Sequence structure,* Figure 4 20 The *Sequence structure* has a number of panels lying on top of one another These panels execute one after the other in sequence While doing so, information was transferred between panes using *Sequence Local Sequence Local* was created anywhere on the perimeter of the sequence panel and can be supplied from an output on one panel to inputs on other panels

Case Structure

A *Case structure* has two or more subdiagrams or *Cases,* only one of which is executed when the structure is executed, Figure 4 21 This depends on the value of an integer, Boolean, string, or a numeric scalar wired to the external side of the selection

terminal or selector In this case, the Boolean switch was used for switching between machine set-up, and test program, which are separately built in the two cases
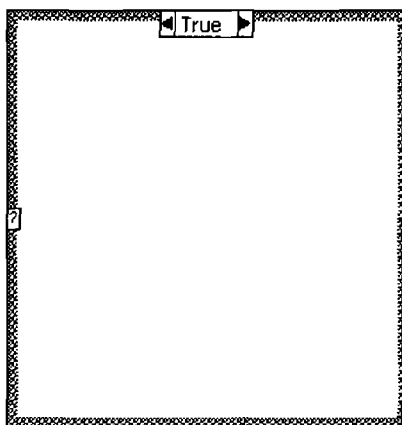
Figure 4 21 Case Structure

If the test switch is ON in the front panel, the control flows to the test program otherwise to the machine set-up In the machine set-up frame, Figure A 4, the objects necessary for operating the machine such as instrument input/output VI, data acquisition operations, and arithmetic operations are placed

4 6 3   File Output and Input

There are a number of operations to be done with the data collected during a test and the software should be able to let that be done LabVIEW can read and write four types of files

Spreadsheet These files consist of ASCII text with tabs in suitable places for importing into a spreadsheet The VI's that control this form write one array to the file at a time, Figure A 5

Character These are similar to spreadsheet files in that they consist of ASCII text, but the format is free

Binary Consist of the data in computer format instead of ASCII They are more compact than character files and do not suffer from round-off errors However, they need to be translated into ASCII by other programs

109

Data log These are similar to binary files except that the data can be more of complex types (e g clusters) They must be read in the same format as they are written which constrains them to be read by a similar LabVIEW program to the one, which wrote them

4 6 4 Data Acquisition

The communication between the tension-torsion machine and the test program VI was achieved by using Data acquisition VI's in the program LabVIEW has a collection of VI's that work with the data acquisition hardware devices The data acquisition (DAQ) VI's help to develop complete instrumentation, acquisition, and control applications Three data acquisition VI's namely *Analog Input VI*, *Write to Digital Line VI*, and *Analog Output VI* was used in the test programs

Analog Input VI The *Analog Input VI* measures the signal attached to the specified channel and returns the value The VI performs a single, untimed measurement of a channel Five such VI's are used as sub VI's in the test program to measure the axial displacement, the axial load, the angular twist, the torque, and the strain gauge, Figure A 4 Each parameter was measured as voltage using this VI Each transducer was calibrated to determine its performance characteristics under various loads before conducting the actual test The product of the reciprocal of the slope of the characteristic curve (listed in Table 4 6) and the input signal gives the respective parameter The parameter was then shown in the front panel graphical indicator and logged into the spreadsheet at regular intervals

Write to Digital Line VI *Write to Digital Line VI* sets the output logic state of a digital line to high or low on a specified digital channel Two *Write to Digital Line VI*'s are used as sub VI's in the test program, one for each servomotor In the second and fourth loading paths, the motor controlling the input parameter should be set to zero speed as soon as the predefined strain value was reached When the transducer input parameter exceeds the predefined parameter value the

Write to Digital Line VI sets the corresponding motor to zero speed thereby preventing any further straining in that axis

Analog Output VI The *Analog Output VI* performs simple analog output operations Two *Analog Output VI*'s are used in the test program, to control the servomotor The *Analog Output VI* applies the specified voltage to the servomotor through the corresponding servo controller

The motor was supplied with a voltage as required, through an Analog output data acquisition VI Two supply voltages operate the motor, one to enable the motor axis and the other to supply the voltage to run the motor at a specific speed or torque Two Case structures are used for each motor control First Case structure returns 0 or 1 depending on the position of the Speed switch The numerical value was then multiplied with the value from the knob control and the product was returned to the other case structure, which returns either the product or zero to the Analog Output data acquisition VI The analog output data acquisition VI sends the appropriate voltage to the respective motor through the DAQ device A Write to Digital Line VI sets the output logic state of the digital line to high or low on a digital channel, which is 0 in this case to enable or disable the motor axis

The same set of objects was duplicated for the other motor and the line and devices configured Device 1,AT-AO-6 was used for load motor and Device 2, AT-MIO-16E-10, for torque motor Apart from the Analog Output VI's to control the motors, Analog Input VI's are placed in the frame to read the input signal from the transducers Each transducer was assigned a separate channel but uses the same DAQ device, which is Device 2 This signal input was scaled by a factor, which is the gradient of the characteristic curve obtained for each transducer during calibration, Table 4 6 The product was returned to an indicator in the front panel as well as to the next frame in the sequence structure to be written to a spreadsheet

In the test program frame, shown in Figure A 6, Analog Input VI's for all the transducer, as in the machine setup frame, was placed The voltage signal from the respective transducer depending on the test was compared with the set value in the front panel and according to the resulting output the signal was returned to one of the

111

two Case structures If the signal was high, the first Case structure was activated and if it was low, the second Case structure was activated

In individual case, both the torque motor and load motor was operated as the case necessitates The flow diagram is same for the four tests, with difference in the parameter compared and operation of the torque and load motors The assigned channels and gradients for the individual transducer inputs are tabulated below

Transducer Parameter	Device Channel	Calibration Gradient
Load	0	12 5313
Angle of Twist	1	30
Linear Displacement	2	1 3
Torque	3	23 42
Strain Measurement	4	Depending on the Scaling Factor in Amplifier

Table 4 6 LabVIEW Channel Assignment & Scaling factor

4 7   EXPERIMENTAL PROGRAMME

The main problem in elastic-plastic analysis of a structural member is to determine the internal stresses and strains in the member, when given external loads and strains are applied to its outer surfaces The common engineering tests such as tension test, torsion test, bend test, etc, are incapable of completely revealing the mechanical behaviour of a material for any conditions of loading To this end an attempt was made to extract simple generalisation of the stress-strain relationship under complex loading conditions

4 7 1   Determination of Yield Point

The interpretation of the strength of a material in simple tension is essential to compare the strengths of the material when subjected to combined tension torsion loading The accuracy of the stress evaluation in the elastic-plastic region depends on the definition of yield point

112

Lode Backward Extrapolation Method Taylor & Quinney [15] used Lode backward extrapolation method to determine the yield point According to this method, yield stress is determined by backward extrapolation of stress-strain curve to intersect the elastic line, or to the line of zero plastic strain This method requires an excessive amount of overstrain to define a yield point and one specimen can be used for the determination of only one point According to Taylor & Quinney, this method of determining the yield point applies well to copper and annealed iron and to mild steel However, in case of aluminium there is in many cases an appreciable creep or gradually increasing strain with constant stress Under these conditions, the stress-strain curve is not unique, but it is still possible to discuss the relationship between the distortions produced by various distributions of stress On reloading a specimen after removing the initially applied load, the load at which a rapid increase in strain occurs in definite even though a slow creeping begins at a lower load

Proportional limit method The proportional limit method of determining yield point is another method Wu et al [24] applied this method for the determination of yield surfaces of annealed AISI type 304 stainless steel The proportional limit is defined as the greatest stress that a material will sustain without a deviation from the law of proportionality of stress to strain The linear relationship between stress & strain continues up to a point after which plastic deformation of the material takes place According to Wu et al [24] a proof strain of 5 $\mu\varepsilon$ or 10 $\mu\varepsilon$ may also be classified as a proportional limit This method allows barely enough plastic strain to define clearly the inception of the yield point Even with the use of closed loop servo-controlled hydraulic testing machines with sophisticated computer-controlled circuits, a proof strain of 5 $\mu\varepsilon$ or 10 $\mu\varepsilon$ can slightly harden the specimen In addition, existence of variation in practical details such as accurate control of straining of specimen, and technical difficulty to have two identical specimens makes this method not reliable Moreover use of a single specimen to determine the whole initial yield surface

113

and the subsequent yield surfaces do not consider the accumulation of the hardening effect during loading history

Proof Stress method Beyond proportional limit, upon further increase of the load, the strain no longer increases linearly with stress, but the material still remains elastic This condition will prevail until some point, called elastic limit or yield point, is reached The stress at this point is usually called the *offset yield strength* or the *proof strength* The proof strength is defined as the stress at which the strain exceeds an extension of the initial proportional part of the stress-strain curve by a specified amount, the offset Typically, a value of 0 2% offset strain is accepted in engineering applications Proof stress method was applied in the determination of yield points in this research work, since the method produced consistent and reliable results

4 7 2 Loading Cases

Designing structural members such as bolts in the elastic-plastic range, when the plastic strain is about the same magnitude as the elastic strain, could reduce the weight of the member considerably Bolted joints are predominantly used in assembly of machine components The amount of criticality involved in the design of bolts perhaps reflects on how well it holds the assemblies or machine components With the emphasis being made on the reduction of material and weight in the machine components, bolts should take up as little weight as possible When the bolt is designed in the elastic range, usually it becomes oversized Designing a bolt in the elastic-plastic range considering the strain-hardening property of the material should not affect the stability of the assemblies or machine components Copper and AlSiC metal matrix composite as a material with higher strain-hardening property was considered in this research work The circular rod and tube specimens were subjected to various combinations of tension and torsion loading under proportional and non-proportional loading paths The specimen was subjected to a number of combinations of tension and torsion loads to determine the elastic-plastic

114

behaviour and strain-hardening property Three different loading cases were considered in accordance to the bolt tightening

Proportional loading

The clamping force or preload developed by the bolt during tightening process is proportional to the wrenching torque applied to the bolt head The slope of the relationship between the clamping force and the wrenching torque is dependant on the friction between the bolt and the mating parts [13,82,83] To illustrate the above situation, the specimen was subjected to combined tension and torsion applied in such a way as to produce strain trajectories consisting of straight lines at different angles as shown in Figure 5 25 Tests are carried out by simultaneous elongation and twisting of the specimen with constant ratios of nominal engineering shear strain rate γ to axial strain rate ε at a nominally constant equivalent total strain rate $\eta = \left(\varepsilon^2 + \gamma^2 / 3\right)^{\frac{1}{2}} = 2 \times 10^{-3} s^{-1}$ [4] The combinations of the axial strain rate and the shear strain rate for the proportional loading tests are given in Table 4 7

$R = \dfrac{\gamma}{\varepsilon}$	ε	γ	η
R = 0 4663	5 36x10-3	2 5x10-3	5 552x10-3
R = 0 84	5x10-3	4 2x10-3	5 557x10-3
R = 3 732	3 926x10-3	6 8x10-3	5 552x10-3

Table 4 7 Nominal strain rates for proportional loading paths

Non-proportional Loading

Due to strain hardening, the yield strength of the material is increased This leads to the inflation or distortion of the subsequent yield points for a material under combined loading It is possible to obtain almost the entire positive quadiant of the von Mises yield curve in a single non-proportional loading

115

experiment, without unloading and reloading [4] The four types of non-proportional combined tension-torsion loading paths are,

- Type I-Application of axial load to certain level, followed by the application of torque to the specimen maintaining the initially applied load, until failure of the specimen

- Type II-Application of torque to certain level, followed by the application of axial load to the specimen maintaining the initially applied torque, until failure of the specimen

- Type III-Application of axial load to certain level, followed by the application of torque to the specimen maintaining the initial axial extension of the specimen, until failure

- Type IV-Application of torque to certain level, followed by the application of axial load to the specimen maintaining the initial angle of twist constant, until failure of the specimen

Type I Constant Axial Load Test

The specimen was subjected to an initial axial load in the elastic region, say 25 percent of uniaxial proof yield axial load $\left(L = \dfrac{L}{YL} \right)$ and subsequent application of torque, maintaining the initially applied axial load constant throughout the test, until the failure of the specimen The load motor was run until the preset axial load was reached, and then the torque motor was enabled and continues to rotate until the specimen fails Anticipating the reduction in axial load when the applied torque reaches a critical value, the LabVIEW program was written in such a way that the load motor was enabled when the existing load in the specimen reduces from the preset value, consequently extending the specimen so as to keep the axial load constant When the combined stress reaches a critical value both the torque motor and the load motor rotates steadily, straining the specimen to compensate for the reduction in axial load and torque, until failure This procedure was repeated for other initial load values of 50 percent, 75

116

percent, 100 percent yield load to determine the effect of initially applied axial load on the torque carrying capability of the specimen

Type II Constant Torque Test

The specimen was subjected to a predetermined torque, say 25 percent of the yield torque, and subsequent application of axial load at a steady strain rate Unlike in Type I loading path, the torque remains constant even while the axial load increases This is due to the reason that the specimen in torsion still remains elastic, partly plastic across the cross section This continues almost till the very end of the test when the specimen fails Just before failure, the initially applied torque tends to reduce rapidly and to maintain the torque in the specimen, the torque motor rotates further until failure The same procedure was adopted for 50 percent, 75 percent, and 100 percent of the yield torque as initially applied torque

Type III Constant Axial Displacement Test

The specimen was subjected to an initial extension and subsequent application of torsion, maintaining the initial extension constant throughout the experiment To achieve this, the load motor was enabled to apply a predetermined extension to the specimen, about 25 percent yield axial load and switched to HOLD mode to maintain the extension The torque motor was then enabled to apply torque at a steady strain rate until the specimen fails, irrespective of the change in the axial load values The same procedure was repeated for axial displacements corresponding to 50 percent, 75 percent and 100 percent yield axial load values

Type IV Constant Angle of Twist Test

The specimen was subjected to a twist of an initial angle of twist corresponding to 25 percent of the yield torque and subsequent application of axial load, maintaining the initial angle of twist constant until the failure of the specimen The torque motor was enabled to apply torque to the specimen up to a predetermined angle of twist corresponding to 25 percent yield torque On achieving the required angle of twist, the motor was switched to HOLD mode to

117

maintain the angle throughout the test, and then the axial load motor was enabled The load motor was switched to RUN mode until the failure of the specimen The same procedure was repeated for angular twists corresponding to 50 percent, 75 percent and 100 percent of yield torque values

Non-proportional loading with prestrain

After tightening the bolt, application of external load will further increase the stresses thus causing the combined stresses to approach the yield stress Prestraining beyond the yield point followed by combined tension and torsion loading produces a distorted pattern of the yield surfaces and was related to the direction of prestrain or prestress [20,22,23] The effect of prestrain in tension or torsion followed by nonproportional loading on the stress-strain curve was examined in this loading case The specimen was subjected to prestrain in tension or torsion, unloaded and then loaded in torsion or tension The effect of different axial and torsional prestrains was reported in section 5 3 2

4 7 3   Specimens used in Experiments

Two different materials, copper and AlSiC MMC, were used in this research work Copper as a material with high ductility and strain-hardening properties was chosen to provide an initial insight into the mechanical behaviour of specimens subjected to combined tension and torsion loading, before testing specimens made of AlSiC MMC material The results obtained from different combinations of tension and torsion loads were used to verify the elastic-plastic behaviour of copper specimens, von Mises yield criterion and to establish proper functioning of the recommissioned tension-torsion machine In addition, the conduction of the combined tension and torsion loading tests on AlSiC MMC rod specimens were fine-tuned based on the experience acquired from the combined load tests carried out on copper specimens

118

Copper Rod and Tube Specimen

For ductile metals such as copper, large plastic deformation often leads to failure by localised deformation and shear band Previous research has shown that the activation volume is much larger for BCC metals and decreases with plastic strain for FCC metals It is important to note that heat is generated by the plastic deformation In the present investigation, experiments were conducted in quasi-static loading conditions Since the deformation occurs slowly, most of the generated heat is conducted and/or convected away from the slowly deforming regions and the specimen remains in an isothermal condition

Two different types of specimens were used in the investigations Thin walled tubular specimens were used to determine the material properties, such as shear modulus and Poisson ratio, in addition to the combined tension-torsion load tests When a specimen was subjected to torsion the shear stress was maximum at the outer most fibre As the torque in the specimen increased, plastic yielding occurred at the outer most fiber and moves towards the axis of the tubular specimen When the thin-walled tubular specimens were subjected to torsion, they started buckling To avoid buckling, and to limit its effect, aluminium inserts were inserted into the tubes and glued at the ends with Loctite 648-epoxy glue Loctite 648-epoxy glue exhibits higher Young's Modulus in service than Copper, which will enhance the structural stability at the pinned ends of the specimen The specimens were held using modified specimen holders The specimen holder was modified to accommodate the tubular specimens in the tension-torsion machine gripper, which was specially designed to conduct combined tension-torsion or compression-torsion tests

Solid circular rod specimens were machined to general test specimen dimensions with suitable heads at the ends, Figure A 7 The heads were designed to apply torque and tension to the specimen gauge length

AlSiC MMC Rod and Tube Specimen

Metal matrix composite materials are designed and engineered to exhibit properties that are most desirable for a given application The properties of the composite will depend upon the particular constituents and volume function used, but most MMC's show improvement in stiffness, wear and fracture resistance over the matrix material The yield, ultimate tensile strength, and the elastic modulus of the material increases with heat treatment and volume fraction of particles at the expense of ductility The specimens were made of AlSiC metal matrix composite with 17 8% volume fraction of 3 μm SiC particles in a 2124 aluminium matrix Aerospace Metal Composites Limited, Farnborough, UK, supplied the material AMC217xe is a high quality aerospace grade aluminium alloy (AA2124) reinforced with 17 8% by volume of ultra fine silicon carbide particles of 3-60 μm size The raw material was manufactured by a special powder metallurgy process The process uses a high-energy mixing process, which ensures excellent particle distribution and enhances mechanical properties Principal alloying elements are given in Table 4 8

Cn	Mg	Mn	Silicon carbide(p)
Matrix wt%	Matrix wt %	Matrix wt %	Composite wt %
3 8-4 0	1 5-1 7	0 5-0 7	19-21

Table 4 8 Principal alloying elements in AlSiC metal matrix composite

The specimen was outsourced to be produced by extrusion and heat treated (T4), before machining to desired dimensions The solid rod specimen, shown in Figure A 8, was held in the gripper using special holder that is capable of applying axial and torsional loads, Figure A 9

4 7 4 Determination of axial and shear stresses in a rod

A solid circular rod subjected to pure tension becomes plastic across the entire cross section beyond yield point Due to this change, the axial load carrying

capacity of the rod reduces Depending upon the nature of the material, the rod may sustain little over the yield stress due to strain hardening Until the ultimate tensile strength, there is no significant change in the cross sectional area (diameter) of the rod Beyond the ultimate tensile stress point necking of the rod starts During necking most of the plastic yielding and straining is restricted to a narrow zone of necking This leads to abrupt increase in the true stress-true strain, and follows von Mises normality rule

In case of torsion, the deformation is inhomogeneous inside the sample, which makes the derivation of stress-strain curves from the measured torque-angle relations difficult One of the commonly accepted methods for the determination of the stress-strain relation for rod-shaped cylindrical samples from torsion tests is the Nadai evaluation [8], which is based on two assumptions

The shear strain, γ is proportional to the distance from the axis of the sample, 'i', $\gamma = \dfrac{\theta r}{l}$ where θ is the angle of torsion over the gauge length 'l'

The shear stress (τ) is determined by the shear strain, $\tau = \tau(\gamma)$

From these assumptions for the surface of the sample, the

$$\tau = \left(\gamma = \frac{R\theta}{l} \right) = \tau_N(\gamma) = \frac{1}{2\pi R^3} \left(\theta \frac{dM}{d\theta} + 3M \right) \qquad (4\ 1)$$

relation can be derived where

$$M = 2\pi \int_0^R \tau(r) r^2 dr \qquad (4\ 2)$$

is the applied torque

At a given angle of torsion the stress-strain relation $\tau_N(\gamma)$ determined by the Nadai evaluation from the measure $M(\theta)$ curve can be converted to $\tau_N(r) = \tau_N(\gamma = \theta_r)$ which describes the variation of stress as a function of r

A rod subjected to pure torsion becomes plastic at the outer most fiber initially Continued application of shear stress increases the size of the plastic annulus and

121

moves towards the axis of the rod Theoretically, at any time of the torsion testing, there exists an elastic core until failure of the specimen Using the elastic shear stress formula when the rod was twisted beyond yield point results in higher stress values than that exists in the specimen, due to the presence of elastic and plastic sections

In the present research, the shear stress values beyond yield point was computed by graphical interpolation method depending on the strain hardening behaviour of the specimen

According to Brooks [1], the shape of the elastic-plastic interface in a component is related to the stress distribution For a round bar carrying combinations of axial load and torque, the shape of the interface must be annular to preserve axial symmetry For the current work, the shear stress for the basic shear stress-shear strain curve in such a component was calculated using the torque and the initial cross sectional area of the rod specimen, according to the elastic formula $\tau = \dfrac{TR}{J}$

This obviously over indicate the shear stress, once yielding has started The shear strain was calculated using the angle of twist and the gauge length of the rod specimen A typical plot of the resulting shear stress and shear strain relationship of a rod subjected to pure torque is illustrated in Figure B 1, in Appendix-B Because of error in this plot in the elastic-plastic region, it is necessary to manipulate the data to more accurately reflect shear stress-shear strain profile This was done following Brooks approach [1] that resulted in a real shear stress-shear strain curve illustrated in Figure B 3 The detailed explanation on the graphical method is given in Appendix-B

4 7 5   Finite Element Modelling in ANSYS

This section describes the creation of solid Copper and AlSiC particulate composite models Application of the axial and the torsional loads and boundary conditions were also explained

Copper Model

The copper sample was modelled using the ANSYS preprocessor. Both a 3-D solid element (*Solid95*) and a 3-D surface element (*Surf154*) were used to build the finite element model. Only the gauge length of the copper specimen was modelled since the complete model could not be map meshed. The gauge length was extended by 4 mm, Figure 4.22 and this section was used for load application. During results analysis, the values from this section are ignored.
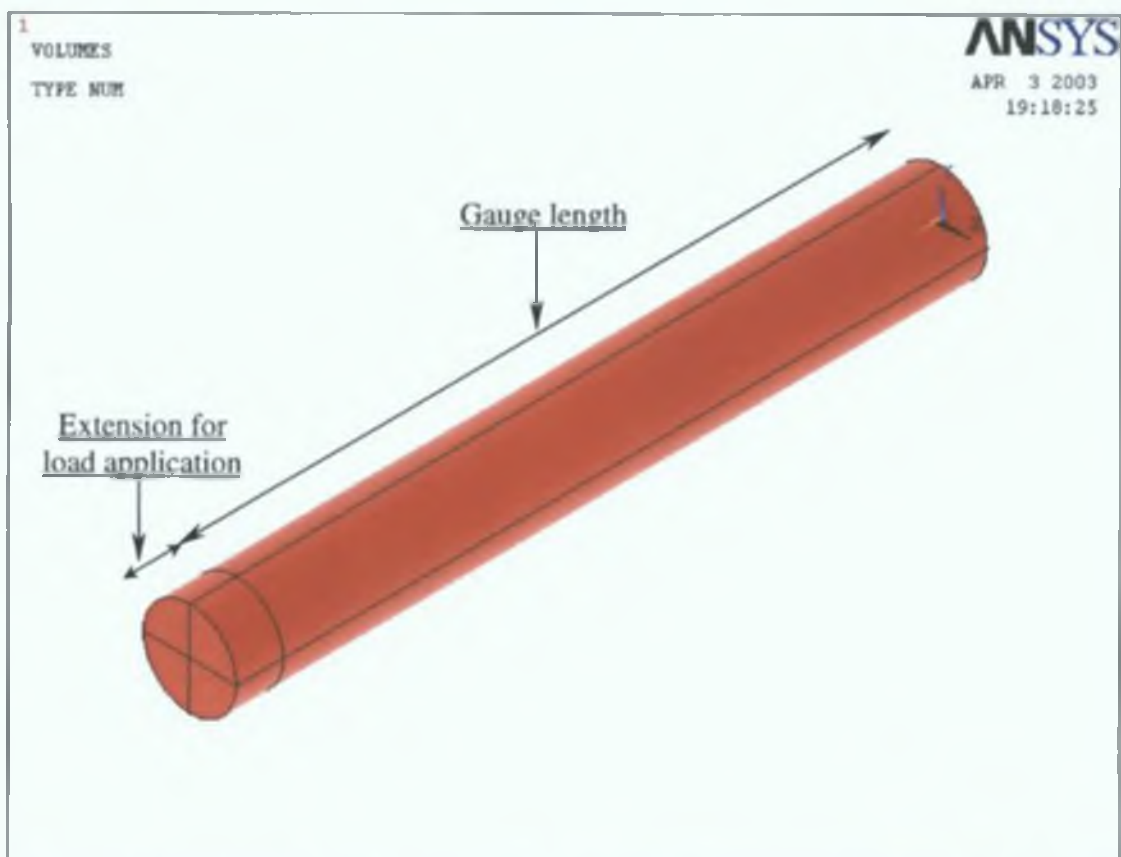
Figure 4.22 Copper Model representing the gauge length and the extended volume

Numerical simulation involves analysis of combined tension and torsion loading that needs a cylindrical model with all four quadrants. The model represents the sample gauge length with all the four quadrants across the length of the sample. A Multilinear material model was used to describe the elastic-plastic behaviour

of the model, as shown in Figure 4.23. Hooke's law was used in the elastic range and rate independent isotropic hardening material obeying von Mises yield criteria was used for the plastic region. The stress-strain data obtained from experimental results were used in creating the material model.
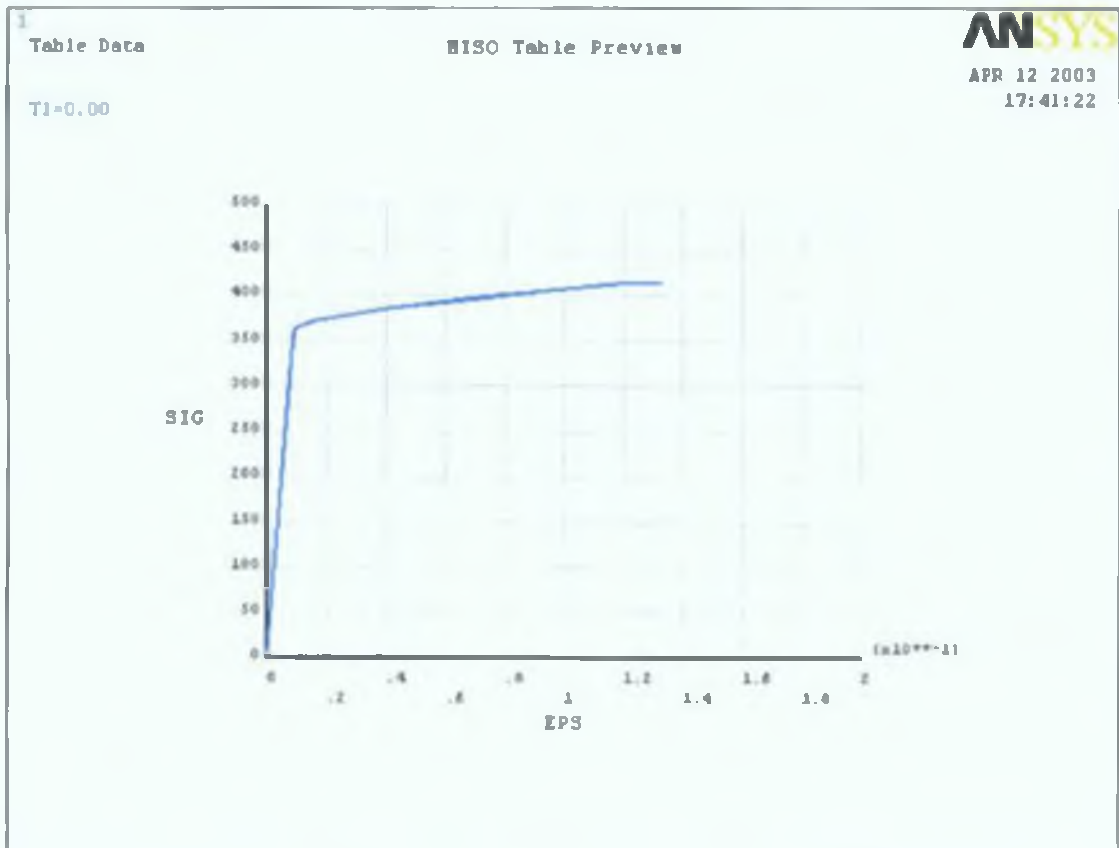
Figure 4.23 Multi Linear Material Model used for Copper Rod Model

The model was meshed with *Solid95* elements which are generally used for modelling of 3-D solid structures. The element is defined by 20 nodes having three degrees of freedom at each node. *Solid95* can tolerate irregular shapes without as much loss of accuracy and these elements are well suited to model curved boundaries. *Surf154* elements are overlaid onto the area adjoining the gauge length and are used to apply the torsional load on the model.

Mapped meshing of the model volume produced 512 numbers of elements with 2341 nodes Uniform mesh density all through the volumes enables proper loading and accurate determination of elastic-plastic deformation of the model during the simulation The axial load was applied on 41 nodes selected as a component along the Z-axis Torsional loads were applied as surface pressure on the *Surf154* surface elements Torque value was converted to pressure from the following expression,

$$F = \frac{T}{R} \quad \& \quad F = P \times 2 \times \pi \times R \times L \qquad (4\ 3)$$

$$\Rightarrow P = \frac{T}{R \times 2 \times \pi \times R \times L} \qquad (4\ 4)$$

where 'R' is the outer radius of the model, and 'L' is the extended length of the model on which the pressure was applied

AlSiC Metal Matrix Composite Model

The Composite material used in this work was aluminium alloy reinforced with silicon carbide particles The particles were in the size range from 3 μm to 60 μm as shown in Figure 4 24 In general, an arbitrary distribution of particles, which may include local clustering, may better represent the actual state of the composite

This however, will complicate the problem and make it difficult to proceed with numerical approach In the present work, an idealised situation was used in which the particles were assumed to be uniformly distributed in the matrix in the form of periodic arrays
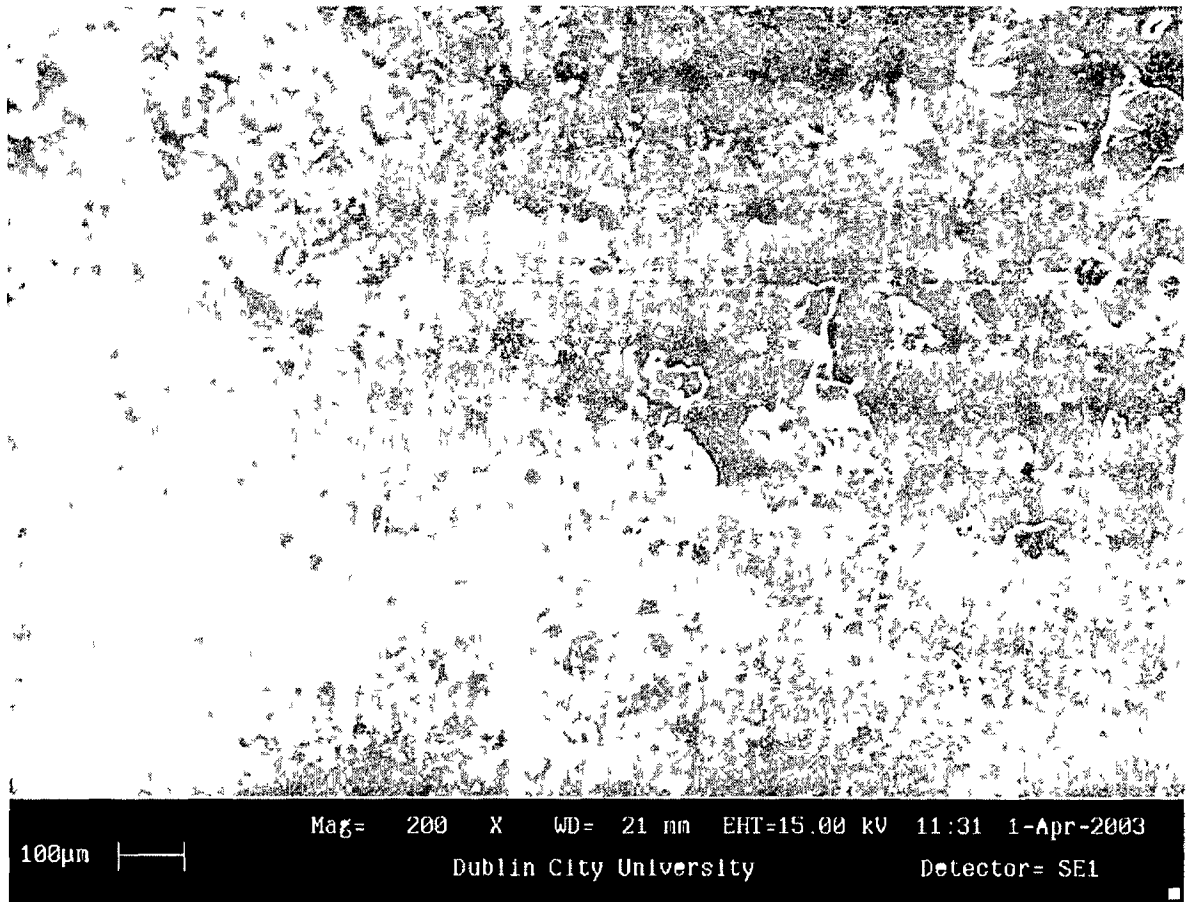
Figure 4 24 Distribution of Silicon Carbide particles in Aluminium matrix

In order to investigate the influence of the silicon carbide particle reinforcement on the elastic-plastic deformation behaviour of the composite, a periodic array of four spherical hard phases in each quadrant in the matrix material was modelled for the prediction of axial and shear stresses during combined tension and torsion loading Figure 4 25 shows the array of spherical particles in each quadrant of the model

Because of restrictions in element numbers and maximum degrees of freedom, the AlSiC metal matrix composite sample was reduced by 3600 times to represent the finite element model The reduced finite element model consists of 17001 *Solid95* and *Surf154* elements and 23915 nodes in total Limitation in the number of elements that can be used to mesh a model restricted further

126

refinement of the elements. Consequently the model was meshed with coarse elements. The simulated model appeared to be coarse. Both the silicon carbide hard phases and Aluminium alloy matrix was meshed using a tetrahedron element shape. The silicon carbide hard phases were meshed with 4 point size elements in a 10 point scale, and the Aluminium alloy matrix material was meshed with 1 point size elements in a 10 point scale. The extended volume was map meshed with *Solid95* elements. In addition to *Solid95* elements, the surface effect elements, *Surf154*, were laid on the circumference of the extended volume in order to apply torsional load. Ideal bonding was assumed to exist between the silicon carbide particles and the aluminium alloy matrix material.
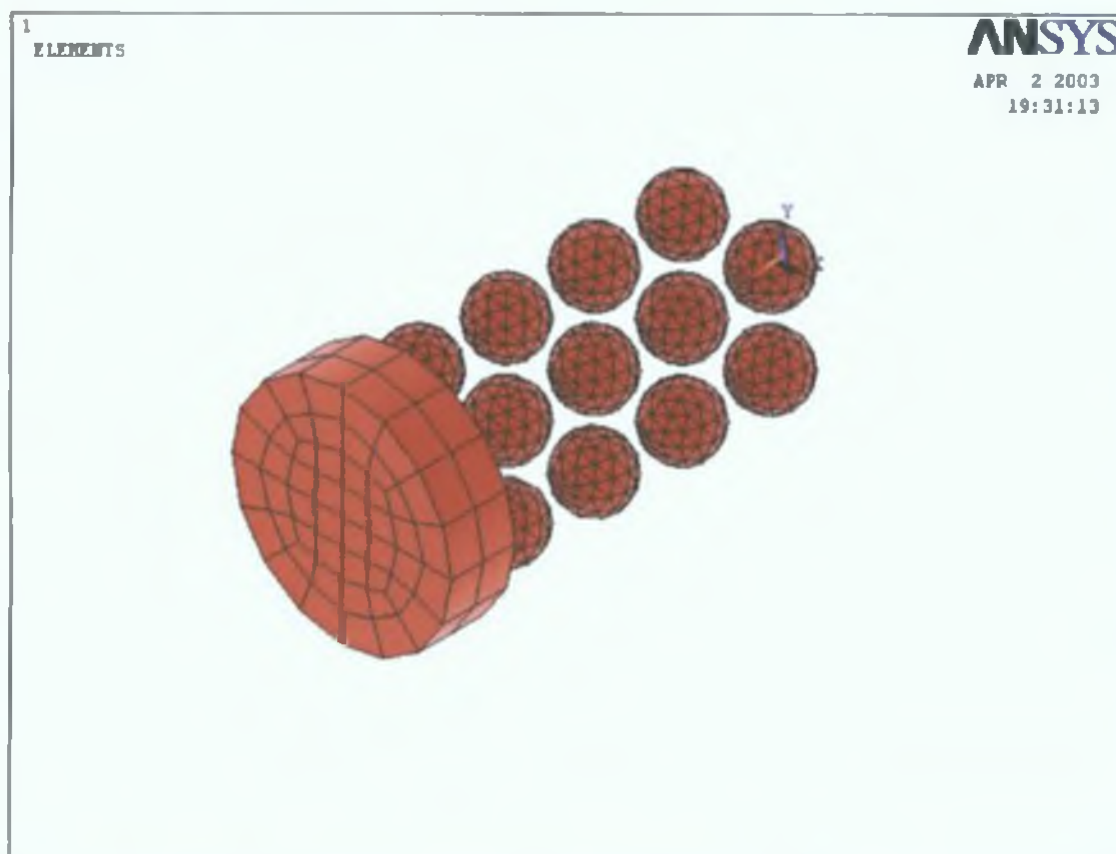
Figure 4.25 Model representing Silicon carbide particles and the extended volume

An elastic-plastic von Mises yield criterion combined with a bilinear true stress-true strain curve was used to represent the material non-linear effects of Aluminium alloy matrix. Figure 4.26 shows the plot of the constitutive model used in the finite element analyses. The silicon carbide particle reinforcements were assumed to behave as a linear elastic, isotropic solid.

Figure 4.26 Bilinear Material Model for Aluminium matrix

4.8 SUMMARY

The purpose built tension-torsion machine was recommissioned using data acquisition devices and LabVIEW programme. The machine was able to conduct different combinations of combined tension and torsion loading tests. To validate the experimental results finite element models were simulated. Both copper and AlSiC metal matrix composite models were simulated using finite element analysis code ANSYS.

5 EXPERIMENTAL RESULTS AND DISCUSSION

5 1 INTRODUCTION

Structural members subjected to external load achieve extra strength by an initial permanent deformation Plastic deformation of the metal creates dislocation Upon extensive deformation, dislocations multiply and increase the strength of the metal An increasing stress is required to produce additional plastic deformation and the metal apparently becomes stronger and more difficult to deform [79-80] In practice, the stresses imposed by service loadings such as in bolts are likely to be complex When safety factors are reduced to save weight, the stresses in the material will approach the yield condition In most conventional engineering alloys, plasticity will offer the safety margin required The present study examines whether AlSiC MMC can be employed in a similar manner when operating close to yield point under combined axial and shear stress states A preliminary investigation was also carried out on copper to determine the elastic-plastic behaviour under combined tension and torsion loading conditions

The experimental programme consisted of pure tension, pure torsion, and combined tension and torsion tests on Copper and AlSiC metal matrix composite material Solid circular rod and thin-walled circular tube specimens were used in the experimental investigation Uniaxial tension and torsion tests were carried out on the specimens to determine the material properties such as Young's Modulus, Yield Strength, Shear Modulus and Poisson ratio using the purpose built tension-torsion machine The tension-torsion machine was calibrated before conducting the experiments for accurate measurements of the axial load, the torque, the axial displacement and angle of twist in the specimen

During uniaxial and combined loading experiments, the axial load and the torque values were accurately obtained from the respective transducer in the machine

The LVDT was located close to the specimen and supplies the axial displacement in the specimen gauge length The angle measuring transducer supplied the angle of twist in the specimen

The specimens were subjected to various combinations of axial load and torque as followed,

- Proportional tension-torsion loading in which the specimen was subjected to combined tension and torsion with different constant relative axial extension and angle of twist

- Initial axial load followed by the application of torque, maintaining the initial axial displacement constant

- Initial torque followed by the application of axial load, maintaining the initial angle of twist constant

- Initial axial load followed by the application of torque, maintaining initially applied axial load

- Initial torque followed by the application of axial load, maintaining the initially applied torque

Proportional loading tests were carried out by simultaneous elongation and twisting of the specimen with constant ratios of nominal engineering shear strain rate γ to axial strain rate ε at a constant equivalent total strain rate η All other tests were carried out at quasi-static strain rates from 2×10^{3} s^{1} to 3×10^{3} s^{1} in both the axes This chapter was intended to examine and discuss the experimental results obtained from the above-mentioned tests

5 2   DETERMINATION OF MECHANICAL PROPERTIES

5 2 1   Tension Test

Uniaxial tension tests were carried out on solid circular rod specimen to determine the mechanical properties such as Young's Modulus (E) and Axial Yield Stress (σ_Y) The virgin specimen was subjected to pure tension in the tension-torsion machine at 3×10^{3} s^{1} strain rate The pair of axial load and axial extension data was continuously measured using the transducers and LabVIEW

130

and recorded every second Three such virgin specimens were subjected to pure tension under same loading conditions and the stresses and strains were averaged The Young's Modulus 'E' was calculated from the slope of the initial linear portion of the axial stress-axial strain curve From a few such preliminary tests it was possible to identify, that loading, unloading and reloading the specimen in tension at constant strain rate within elastic limit does not change the Young's Modulus Therefore, the later uniaxial tests do not involve unloading and reloading of the specimens The proof yield stress was determined at 0 02% offset strain from the initial elastic slope
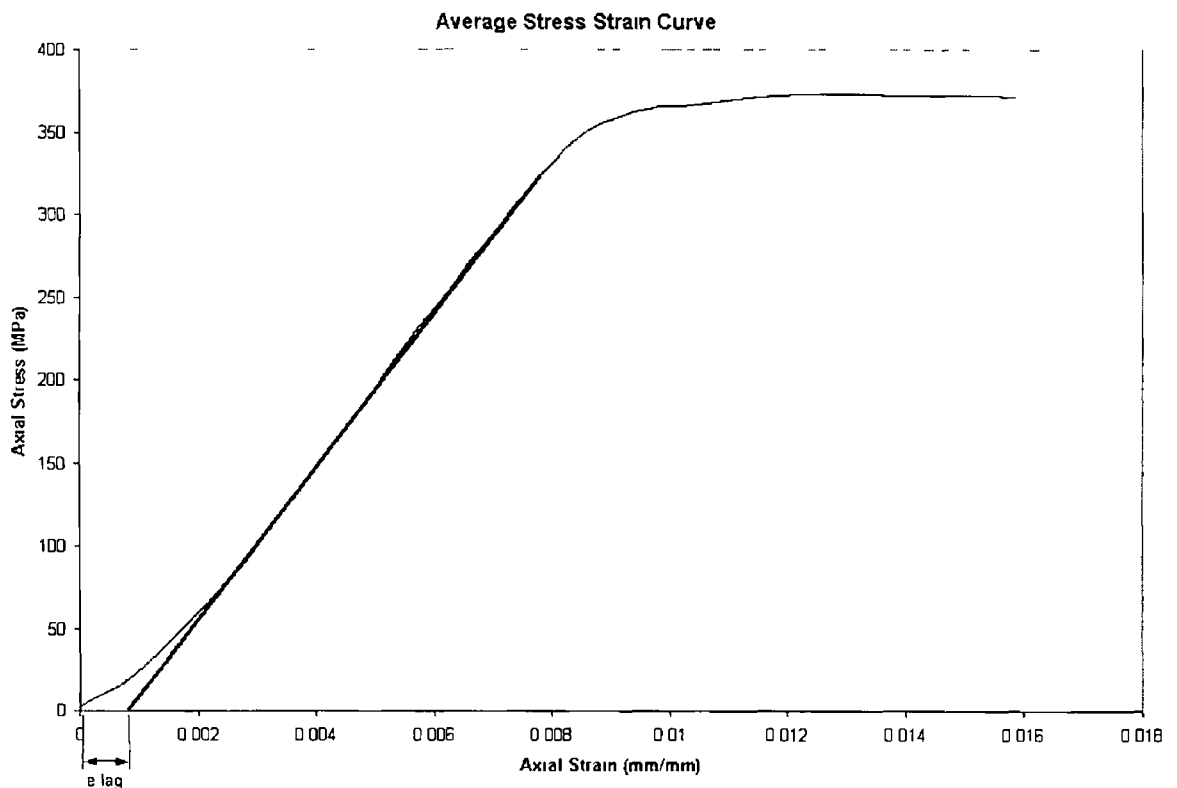
Figure 5 1 Offset Strain in determination of Mechanical Properties

For an accurate determination of yield point and Young's Modulus, the zero offset strain as shown in Figure 5 1 and denoted by 'e-lag' should be accounted for The quantity e-lag was measured by intersecting the straight line with the strain-axis and was therefore related to the value of yield point and Young's

131

Modulus Ideally, *e-lag* should be zero However, due to the nature of the servo-controlled machine and the components, the data scattered to some extent as shown in the Figure 5 1 Therefore some amount of *e-lag* is likely to be present Two strain gauges of type CEA-06-250UN-350 manufactured by Measurements Group UK Ltd were properly bonded to the center of each specimen gauge length used in the determination of elastic constants One of the strain gauge was aligned along the longitudinal axis of the specimen and the other gauge made 90° to the longitudinal axis A proof strain of 0 02% offset strain was used to define yielding of the specimen Yield was considered to occur if there is few consecutive points with proof strain exceeding 0 02% offset strain Three specimens made of virgin material were used to determine the yield point and average value was considered as yield point

For each specimen, Young's Modulus '*E*' was obtained by testing the virgin material within elastic range The specimen was given a small amount of loading, around 50-70% yield load The pair of stress and strain data was continuously acquired while the specimen was being elastically loaded NIDAQ data acquisition devices were used to acquire the data at one second interval The Young's Modulus '*E*' was then calculated using this set of data After each loading, the specimen was unloaded back to zero stress To ensure accuracy, the loading was repeated Each time, a Young's Modulus '*E*' was obtained, the average value was taken as the Young's Modulus '*E*' of the material

Figure 5 2 shows the average axial stress-axial strain plot for Copper rod The yield axial stress and the Young's Modulus 'E' was found to be 367 MPa and 45 5 GPa, respectively

Figures 5 3 shows the axial stress-axial strain plot for Copper tubes The yield axial load was determined using this plot to apply initial axial load on the specimen in combined tension-torsion tests

Figure 5 4 shows the axial stress-strain curve for AlSiC MMC rod The strain lag (*e-lag*) was found to be larger in AlSiC rod than in the case of Copper rod This may be due to the initial setting of additional specimen gripping components

132

used with the AlSiC MMC specimen A sharp yield point and steep hardening curve can be observed from the Figure 5 4 The yield axial stress was found to be 387 MPa

Figure 5 5 shows the axial stress-axial strain curve for AlSiC MMC tube specimen under axial loading It is evident from the graph that the specimen can withstand axial load well beyond the yield point The rate of increase in the axial stress is marginally affected with high strain hardening of the specimen The yield axial stress was found to be 384 5 MPa

5 2 2 Torsion Test

Torsion tests were conducted on Copper and AlSiC metal matrix composite specimens to determine the mechanical properties such as the Shear Modulus, Poisson ratio Tests were conducted on both rod and tube forms of the material to establish the similarity in the material properties

Figure 5 6 shows the average shear stress-shear strain plot for the copper rod The Shear Modulus 'G' was found to be 17 336 GPa, and the Poisson ratio is 0 31

Figure 5 7 shows the shear stress-shear strain plot for Copper tubes The yield torque was determined using this plot to apply initial torque on the specimen in combined tension-torsion tests

Figure 5 8 shows the shear stress-shear strain curve for AlSiC MMC rod Shear yield stress was found to be 296 MPa The specimen yielded initially at the outer periphery and move towards the axis of the rod developing a shear stress gradient along the radius The natural stress was calculated using the graphical method explained in section 4 7 4 Figure 5 9 shows the shear stress-shear strain plot obtained using elastic formula and the graphical method for AlSiC metal matrix composite rod

Figure 5 10 shows the shear stress-shear strain curve for AlSiC MMC tube under pure torsion The specimen failed immediately after reaching the yield point due to poor strength of the specimen in shear The thin walled tubular specimen can

133

withstand loads well beyond the yield point in axial loading, whereas the specimen failed prematurely after yield point in torsional loading The yield shear stress was found to be 222 MPa

Especially when the rod is subjected to torsion, yielding of the specimen first occurred at the outermost fibre and moved towards the center At the inception of yield in the rod, the outer annulus becomes elastic-plastic while the central core remains elastic, thereby a gradient in the shear stress exists along the radius of the rod Assuming this variation in shear stress along the radius to be negligible in tubular specimen due to thin wall, a close approximate of the shear stress and shear strain curve can be obtained using tubular specimens

Each graph, that depicts an experimental result, shows the averaged results from three experiments for copper specimens and two experiments for AlSiC MMC specimens In all the experiments, the scatter of points remained within 2% of the averaged value The mechanical properties of different materials used in the experimental programme are listed in Table 5 1

	Yield Load (kN)	Yield Stress (MPa)	Yield Torque (Nm)	Young's Modulus E (GPa)
Copper Tube	5 164	392 857	8	-
Copper Rod	18 447	367	22 381	45 426
AlSiC$_p$MMC Tube	15 5	384 483	87	-
AlSiC$_p$ MMC Rod	10 94	387	9 75	42 151

Table 5 1 Mechanical properties of materials used in the experimental investigation

5 3 COMBINED TENSION AND TORSION LOAD TESTS

Combined loading path experiments reveal more critical material response than monotonic deformation experiments such as tension test [81] In this study, experiments under proportional and nonproportional combined tension and torsion loadings were conducted for different loading paths During the experiments, the specimens were subjected to different combined tension and torsion loading conditions Preliminary experiments were conducted on Copper to determine the elastic-plastic behaviour of a homogenous material under

various combinations of tension and torsion loading The effect of axial prestrain and torsional prestrain was also investigated and the results presented in section-5 3 1

Section 5 3 2 describes the elastic-plastic behaviour of aluminium reinforced with silicon carbide particulate composite material under various combinations of tension and torsion loading This is followed by the numerical analysis of various loading paths using the FEA code ANSYS Results from the experiments were compared with the ANSYS simulation results

5 3 1 Experimental Results of Copper Rod and Tube Specimen

The Copper rod specimens were subjected to four different combined tension and torsion loads with constant relative extension and twist Four different ratios of axial strain rate to shear strain rate were used to carry out the proportional loading tests The axial and shear strain trajectories are shown in the Figure 5 11 A constant nominal combined strain rate of $2 \times 10^3 s^{-1}$ was applied to the specimen for all the four tests The combination of axial strain rate and shear strain rate are given in Table 5 2

$R = \gamma/\varepsilon$	ε	γ	$\eta_{nominal}$
R = 0 5774	$1 9 \times 10^3 s^{-1}$	$1 0084 \times 10^3 s^{-1}$	$1 987 \times 10^3 s^{-1}$
R = 1 0	$1 72 \times 10^3 s^{-1}$	$1 72 \times 10^3 s^{-1}$	$1 986 \times 10^3 s^{-1}$
R = 1 732	$1 4056 \times 10^3 s^{-1}$	$2 4345 \times 10^3 s^{-1}$	$1 974 \times 10^3 s^{-1}$
R = 3 732	$0 833 \times 10^3 s^{-1}$	$3 0988 \times 10^3 s^{-1}$	$1 988 \times 10^3 s^{-1}$

Table 5 2   Nominal strain rates for proportional loading paths

The maximum torque and axial load that can be sustained by the specimen under each of the four stress trajectories is illustrated in Figure 5 12 In the first load case, when the shear strain rate to axial strain rate ratio was 0 58, the specimen became plastic all through the cross section sooner due to higher axial straining compared to shear straining, reducing the possibility of torque reaching more than 8 4 Nm The axial load reaches 18 1, which is 97% of ultimate axial load that the specimen can sustain in uniaxial loading condition This clearly shows that under lower torsional values the specimen's axial load carrying capability is

not affected significantly The specimens were subjected to three other shear strain rate to axial strain rate ratios of 1, 1 73, and 3 73 As the shear strain rate increased with respect to the axial strain rate, higher torque is attained in the specimen as shown in the Figure 5 13, before the plastic instability and subsequent necking of the specimen When the specimen was subjected to higher shear strain rate than axial strain rate, and when the combined axial stress and shear stress reached a critical value, the specimen yields in torsion than in tension Thus, at the inception of yielding, a plastic annulus formed at the periphery of the specimen, which grew towards the center of the rod as the combined tension and torsion load is increased This yield behaviour of the specimen is characterised by the reduction in the axial load carrying capacity of the specimen, which is clearly evident from the maximum values of the axial load reached in the subsequent three strain trajectories, Figure 5 14 Higher strain hardening of the specimen and consequently higher load carrying capacity is observed at higher shear strain rate to axial strain rate ratios Presence of elastic core and strain-hardened plastic annulus enabled the specimen to sustain higher axial and torsional loads than the specimens subjected to lower shear strain rate to axial strain rate ratios In torsion the specimen yields at the outer fibre and traversed monotonically towards the center Thus theoretically there exists a core, which is still elastic until failure The existence of elastic core even after attaining the critical yield value enables the specimen to sustain higher axial load Thus the axial load carried by the specimen subjected to highest shear strain to axial strain ratio of 3 73 was around 12kN, which is 66% of the yield axial load in pure tension test Whereas the maximum torque attained in the specimen subjected to the lowest shear strain rate to axial strain rate ratio of 0 58 was 8 4 Nm, which is 37 6% of the yield torque obtained from pure torsion test This is due to the absence of an elastic region to sustain higher torques Higher strain hardening of the specimen was observed at higher shear strain rate to axial strain rate ratios A typical behaviour of the specimen

observed in all four loading paths is that the torque never approaches a value of zero before failure This is clearly evident from Figure 5 12

5 3 2 Nonproportional Loading

Constant Axial Displacement

The Copper rod specimen was inserted between the grippers and a small amount of torque and axial load were applied to eliminate the gap and slackness between the specimen and gripper The specimen was then subjected to an initial extension The initial extension corresponds to the extension at 15, 34, 71 & 98% of yield axial load The initial extension of the specimen was followed by the application of torque The initial axial load and subsequent torque was applied at a constant strain rate of $2x10^3 s^{-1}$

It can be observed from Figure 5 15, that as the torque is increased gradually, the initially applied axial load remained constant until the combined axial and shear stresses reached the von Mises yield curve It then decreases very marginally until the combined axial stress and shear stress produced maximum stress of 225 MPa At this point, the axial stress reduced drastically at the same shear stress When the initial axial load was 34, 71 & 98% of yield axial load, increase in torque decreased the axial stress marginally until the combined axial stress and shear stress produced von Mises yield condition This suggests that the increase in torque affected higher initial axial load in the specimen The axial load in the specimen then decreased rapidly as the shear stress exceeded 1 5 times the combined yield stress When the specimen was subjected to an initial axial load corresponding to 71% & 98% yield axial load and then torque was applied, the axial load started to decrease at a greater rate at the initial stage of loading and tend to drop rapidly after about 1 5 times the yield shear stress From the von Mises yield criteria for combined loading, the material starts yielding at lower torque when the initially applied axial load is increased This follows the yield criteria $\sigma^2 + 3\tau^2 = Y^2$, where 'σ' is the axial stress, 'τ' is the shear stress and 'Y' is axial yield stress After reaching the yield plateau the combined stresses in the

specimen deviated away from the yield curve marginally and follows the yield plateau as shown in Figure 5 15 The maximum shear stress achieved in all four loading paths exceeded unity due to the strain hardening property of the material The copper tube specimens were subjected to 68, 80, 87, and 95% yield axial load followed by the application of torque maintaining the initial axial displacement constant In all the loading cases a gradual drop in the initially applied axial load was observed on the application of torque, within the elastic region as shown in Figure 5 16 When the combined stresses reached von Mises yield curve, the drop in the initial axial load was found to be drastic and follows close to the von Mises yield curve on the elastic-plastic region The result suggests that the axial load that can be sustained by the specimen largely depend on the amount of elastic cross-section in the specimen Figure 5 17 shows the effect of shear strain on the initial axial load The rate of drop in the axial load is more in the initial stages of shear strain The drop in axial load reduces after 0 01 shear strain before saturating at 0 05 shear strain

Constant Angle of Twist

The Copper rod specimen was subjected to 32, 61,88, & 102% yield torque and the angle of twist was held constant The axial load was then applied to the specimen already under torque The torque remained constant at the initial stages of axial loading until the applied axial load reached a value which when combined with the torque causes the material to yield Thereafter for any increase in the axial load the torque reduces rapidly until the axial load reached a maximum of about 1 2 times the yield axial load as shown in Figure 5 18 At this stage any attempt to increase the axial load causes the onset of plastic instability and necking The axial load decreases rapidly at a constant torque until the specimen fails through fracture A peculiar behaviour observed in all the four loading paths is that the shear stress never approached zero before failure of the specimen Beyond plastic instability the axial stress dropped rapidly upto 275 MPa and failed in brittle manner as shown in Figure 5 18 Presence of plastic

138

cross section at the neck of the specimen supported the torque that was present at the time of failure The true stress state shows a trend of rise in the combined shear and axial stresses normal to the von Mises yield curve These results shown in Figure 5 18 indicate that the specimen subjected to higher initial torque followed by increasing axial load, yields plastically at an early stage than the specimen subjected to a lower initial torque This is due to the fact that the combined stress level meet the von Mises yield plateau at an early stage and deviate away into the elastic-plastic region and follow the yield plateau until necking starts The combined stress in the specimen with the lower initial torque meet the von Mises yield plateau drawn using maximum stresses just prior to the onset of necking The combined stress levels in both the cases do not follow the yield plateau drawn with the values of initial yield stresses in tension and torsion

The copper tube specimen was subjected to 42, 71, and 88% initial yield torque followed by the application of axial load An increase in the axial load in the specimen causes the torque to drop at a constant rate as shown in Figure 5 19 The combined stress curve crossed the von Mises Yield curve and as soon as it reached the yield axial stress, dropped rapidly upto 35 MPa Beyond this point, the plastic instability starts and the specimen lost both axial load and torque carrying capacity before failure The absence of an elastic region restricted the axial load carrying capacity of the specimen Figure 5 20 shows the safe extent to which the rod specimen can sustain combined axial stress and shear stress The combined axial and shear stress points were obtained for individual load path, when the combined axial and shear strain in the specimen is equivalent to twice the yield strain in pure tension

Torsional Prestrain

A range of sequential tension-torsion-tension tests was carried out on copper rod specimens to determine the effect of torsional prestrain on load carrying capacity of the specimen The specimens were subjected to three different torsional

prestrains such as 0 42, 0 84, and 1 26 From Figure 5 21, it is evident that the specimen subjected to 0 42 shear strain can sustain axial stress of 14 74% more than the yield axial stress in pure tension Similarly, the specimens subjected to shear strains of 0 84 and 1 26 can sustain axial stress of 25% and 27% more than the yield axial stress in pure tension, respectively In addition, the ductility of the specimen is significantly reduced by 56%, 59% and 62% for the specimens subjected to 0 42, 0 84, and 1 26 shear strains respectively Large shear strains can reduce the materials subsequent extensional ductility, the material failing on those planes subjected to compression in the torsional prestrain [11]

When the torsional prestrain exceeds a given value, the specimens fails in a brittle manner when subsequently loaded in tension, the fracture being distinctly different from the normal cup and cone failures which were obtained with smaller torsional prestrains Figure 5 22 illustrates the effect of torsional prestrain on the elastic properties of the material A marginal change in the Young's Modulus of the torsional prestrained specimen is observed when compared to the virgin specimen The effects of torsional prestrain on the elastic constants depend on the amount of plastic deformation

Figure 5 23 illustrates the axial extension in the specimen due to torsional prestrain The free-end extension in the specimen due to large torsional deformation was found to increase linearly This suggests that the fixed end large deformation torsion test might induce compressive stresses upon the specimen

The results from these tests indicate quite clearly the influence of the torsional prestrain The material close to the extreme fibre had lost much of their ductility and that the rate of torsional ductility varied with the distance from the centroid of the specimen

Axial Prestrain

In this set of experiments, the specimen was subjected to an initial plastic strain in the axial direction and unloaded followed by the application of torque From the results shown in Figure 5 24, it is evident that the specimens subjected to

lower axial prestrains can take more torque compared to the specimens subjected to higher prestrains The torque achieved in prestrained specimens was comparatively less than that was achieved in a virgin specimen The variation in the torque carrying ability after plastic axial prestrain was found to be insignificant This is due to the absence of elastic region in the specimen The shear modulus of the specimen remained the same for all the prestrain values

5 3 3 AlSiC Metal Matrix Composite Tube and Rod Specimens

The mechanical properties of particulate-reinforced metal matrix composites are controlled by a complex interaction between the matrices and reinforcements Researchers have proposed different strengthening mechanisms such as, i) load transfer between the matrix and reinforcement, ii) enhanced dislocation density in the matrix, iii) matrix and interfacial precipitation The addition of a reinforcing phase of different elastic properties induces strain concentration In order to maintain the displacement compatibility across the interface when the load is applied, dislocations are generated at the composite interface The interaction of matrix with the reinforcing phase determines the mechanical behaviour of the composite [50-54]

Proportional Loading Tests

The AlSiC MMC rod specimens were subjected to three different combined tension and torsion loads with constant relative extension and twist Three different ratios of axial strain rate to shear strain rate were used to carry out the proportional loading tests The axial and shear strain trajectories are shown in the Figure 5 25 A constant nominal combined strain rate of $5\ 55 \times 10^{-3} s^{-1}$ was applied to the specimen for all the three tests The combination of axial strain rate and shear strain rate are given in Table 5 3

$R = \dfrac{\gamma}{\varepsilon}$	ε	γ	η
R = 0 4663	5 36x10-3	2 5x10-3	5 552x10-3
R = 0 84	5x10-3	4 2x10-3	5 557x10-3
R = 3 732	3 926x10-3	6 8x10-3	5 552x10-3

Table 5 3   Nominal strain rates for proportional loading paths for AlSiC MMC Rod

141

The maximum torque and axial load that can be sustained by the specimen under each of the three stress trajectories is illustrated in Figure 5 26 In the first load case, when the shear strain rate to axial strain rate was 0 47, the specimen achieved a maximum torque of 16 7 Nm and thereafter the torque was maintained constant until failure of the specimen at 14 5 kN axial load which is 132 6% yield axial load The specimen subjected to a shear strain rate to axial strain rate of 0 84 can sustain torque upto 19 1 Nm and remained constant until the failure of the specimen at 12 9 kN axial load From the above two load cases, it is evident that the torque carrying ability of AlSiC MMC material is significantly affected at higher axial strain rate compared to shear strain rate The addition of the reinforcing particles increased the stiffness but decreased the strain to failure

In the third load case where the shear strain rate to axial strain rate ratio was maintained at 1 73, the maximum axial load and torque achieved were 9 5 kN & 22 9 Nm respectively Figure 5 26 illustrates the axial load carrying ability of AlSiC MMC rod The increase in axial load is not restricted significantly by the increase in torque, though the rate of increase in axial load is reduced This suggests that AlSiC MMC rod can sustain stresses in the longitudinal direction along the axis of the specimen rather than the transverse section The specimens in the three different load cases failed in a brittle manner

Figure 5 27 shows the effect of axial load on torque As the shear strain increased, the torque in the specimen subjected to shear strain rate to axial strain rate ratios of 0 47 & 0 84 achieved maximum torque and saturated with no further increase The specimen subjected to shear strain rate to axial strain rate ratio of 1 73 can sustain higher torque after yield point though the rate of increase in torque is reduced Figure 5 28 shows the effect of torque on the axial stress The axial stress in all three loading paths is not significantly affected by the increase in torque

Constant Axial Displacement Tests

The AlSiC MMC rod specimen was subjected to an initial axial displacement corresponding to 35%, 62%, and 90% yield axial load, followed by the application of torque, maintaining the initially applied axial displacement

The specimen subjected to 35% yield load followed by the torque sustains the initially applied axial load until the shear stress reaches a value of 340 MPa Beyond 340 MPa of shear stress, the axial stress in the specimen reduces substantially 30% reduction in axial stress was observed before failure as shown in Figure 5 29 The failure of the specimen was brittle in nature

In the specimen subjected to an initial axial displacement corresponding to 90% yield load, followed by the application of torque, the initially applied axial stress reduced significantly, upto 50% of the initial axial load before failure Irrespective of the initial axial load applied on the specimen, the shear stress achieved in the specimen before failure remained constant at 420 MPa Evidence of strength in the specimen after von Mises yield curve suggests that the load carrying capacity of the AlSiC MMC material is substantially increased by the strengthening effect of the silicon carbide particle reinforcements

Figure 5 30 shows the trend in reduction of initially applied axial stress upon subsequent twist in the specimen As the shear strain in the specimen increased, the existing axial stress reduces steadily until failure of the specimen

The AlSiC MMC tube specimen was subjected to an initial axial load of 34% yield axial load followed by the application of torque The initially applied axial stress remains constant until the shear stress reached von Mises yield curve In the second case the specimen was subjected to an initial axial load of 63% yield axial load followed by torque As the torque in the specimen increases, the initially applied axial load marginally decreases until the von Mises yield stress Beyond the von Mises yield curve substantial reduction in the initially applied axial load is observed Similarly in the third load case, the specimen was subjected to an initial axial load of 88% yield axial load followed by torque As the torque in the specimen increases, substantial reduction in the initially applied

axial load is observed within the elastic region, followed by drastic reduction beyond von Mises yield curve The reason for this reduction in the axial load is that the combined axial and shear stress reached von Mises yield stress sooner In all the three load cases, the specimen failed in brittle manner

It is evident from the Figure 5 31 that the initial axial load significantly affects the torque carrying capacity of AlSiC MMC tube specimen, the specimen failing along the plane of compression The maximum shear stress achieved in combined stress state is 210 MPa whereas the yield shear stress is 222 MPa

Constant Angle of Twist Tests

The AlSiC MMC rod specimens were subjected to an initial angle of twist corresponding to 51%, 79%, and 97% yield torque and subsequent application of axial loading

In the first load case, when the specimen was subjected to an initial torque of 51% yield torque, subsequent application of axial load does not affect the shear stress in the specimen until the axial load reached yield axial load Beyond the von Mises yield curve, very marginal drop in the combined stresses is observed until the combined stresses reached a value 10% more than the yield axial stress Upon further increase in the axial load, the shear stress reduces drastically as shown in the Figure 5 32 The torque carrying capacity of the specimen is significantly reduced upon reaching the axial yield stress In the third load case, the specimen was subjected to an initial torque of 97% yield torque, followed by the application of axial load On the application of axial load, the torque in the specimen started reducing marginally after the von Mises yield curve until it reaches an axial stress of 200 MPa Beyond this axial stress, the torque reduces drastically as in the other two load cases The specimen failed in brittle manner when the axial stress reached 530 MPa in all the three loading paths Figure 5 33 shows the safe extent to which the rod specimen can sustain combined axial stress and shear stress The combined axial and shear stress points were obtained

144

for individual load path, when the combined axial and shear strain in the specimen is equivalent to twice the yield strain in pure tension

The AlSiC MMC tube specimens were subjected to an initial angle of twist corresponding to 38%, 58% and 95% yield torque followed by the application of axial load In all the three experiments, the shear stress reduces rapidly in the initial stages of axial load application due to stress relaxation Beyond 75 MPa, the shear stress remains constant until the von Mises yield curve Marginal drop in the shear stress was observed before the failure of the specimen

Figure 5 34 illustrates that the specimen subjected to an initial angle of twist corresponding to 95% yield torque failed when the axial stress was not more than 170 MPa, whereas the specimen subjected to an initial angle of twist corresponding to 38% yield torque failed when the axial stress reached 420 MPa This shows that the specimen subjected to lower initial torque values can withstand higher axial stress The load carrying capacity of the specimen is drastically reduced as the initial torque in the specimen is increased

At the beginning of the plastic deformation, the yield behaviour of the specimen was found to be close to the von Mises criterion in stress space When the plastic deformation is small, the change in shape of the yield surface is also small

Constant Axial Load Tests

In constant axial load experiments, the AlSiC MMC rod specimen was subjected to an initial axial load followed by torque, maintaining the initially applied axial load According to von Mises yield criteria, the initially applied axial load should decrease upon the application of torque beyond von Mises yield stress The experimental results suggests that the initially applied axial load could be maintained constant as shown in Figure 5 35, by increasing the axial strain in the specimen The axial strain remained constant until the combined axial stress and shear stress reaches von Mises yield stress Beyond this point, the axial load was maintained constant by increasing the axial strain, as shown in Figure 5 36

The specimens were subjected to 37%, 64% & 92% of yield axial load followed by torque Figure 5 36 illustrates that the rate of axial strain increased with increase in the initially applied axial load It is evident from the graph that the axial load can be maintained constant by increasing the axial strain The initial axial load in the specimen, as shown in Figure 5 37, marginally affects the torque carrying capacity of the specimen When the initial axial load was 37% yield load, the torque attained in the specimen was 25Nm, whereas yielding of the specimen occurred premature in higher initial axial loads and the torque attained in the specimen was 22 Nm The strain increase in the specimen beyond yield point was observed to be 0 1, when the specimen failed in brittle manner

Constant Torque Tests

In constant torque experiments, the specimen was subjected to an initial torque followed by the application of axial load, maintaining the initially applied torque The initially applied torque can be maintained constant as shown in Figure 5 38 by increasing the shear strain in the specimen Three different initial torques of 61%, 91%, & 104% of yield torque was applied followed by the application of the axial load Unlike constant load test, the shear strain started increasing invariably at the same axial strain of 0 055 as shown in Figure 5 39 The rate of increase in the shear strain rate to maintain the initially applied torque is higher for higher initial torque The specimen failed prematurely while tending to maintain the initially applied torque The strain increase beyond yield point was observed to be around 0 025 when the specimen failed in brittle manner

5 4   MODELS REPRESENTING THE ELASTIC PLASTIC BEHAVIOUR OF ALSIC AND COPPER ROD SPECIMENS

Limited quantity and depth of tests, and the approximate nature of the theoretical considerations based on simplifying assumptions have forced machine components designers to apply large safety factors The elastic-plastic reserve

strength of the structural members is in general higher than the computed values, which can be utilized while designing the components [84-92]

Based on the experimental results of copper and AlSiC metal matrix composite rod specimens, the author believes that the following empirical equation best describes the elastic plastic behaviour of the rod specimens under combined tension and torsion loading condition

From the combined tension and torsion test results, it is evident that the axial stress-shear stress curve can be best fitted on a polynomial equation of degree four For a copper rod, the safe axial stress to shear stress relationship beyond the elastic region and within the elastic plastic limit was found to be

$$\sigma_{EP}^2 + 3\tau_{EP}^2 = C_{Copper} Y^2$$

where $\begin{cases} C_{Copper} \leq 1 \ 02 times \ axial \ stress \\ C_{Copper} \leq 1 \ 1 times \ shear \ stress \end{cases}$, shown in Figure 5 20

Similarly, for an AlSiC MMC rod, the safe axial stress to shear stress relationship beyond elastic region and within the elastic plastic limit was found to be

$$\sigma_{EP}^2 + 3\tau_{LP}^2 = C_{AlSiC} Y^2$$

where $\begin{cases} C_{AlSiC} \leq 1 \ 2 times \ axial \ stress \\ C_{AlSiC} \leq 1 \ 6 times \ shear \ stress \end{cases}$, shown in Figure 5 33

5 5   ANSYS RESULTS

The commercial need for the simulation of materials in process has led in recent years to the development of many process models The models are usually finite element based and are aimed at allowing the detailed analysis of the processes This investigation proposes models to investigate the elastic-plastic behaviour of Copper & AlSiC metal matrix composite material A detailed analysis using the model enables optimisation prior to manufacturing of the material and the related expense [93,94] The model has been created and implemented using ANSYS finite element software and validated against the results obtained from experiments

147

In this section, finite element modelling of the experimental specimen, Copper and AlSiC MMC, is described The main objective of the Finite Element Analysis is not only to estimate the failure loads of the specimens, but also to trace the entire load versus deflection path The Finite Element Analysis was performed using 3D solid elements that were capable of representing large deformation geometric and material nonlinearities In the current study, two Models, listed in Table 5 4, have been analysed

Model	Elements		Total Elements	Total Nodes
	Surf154	Solid95		
Copper	32	480	512	2341
AlSiC MMC	32	16969	17001	23915

Table 5 4 Constituents of Copper and AlSiC MMC simulation models

An elastic-plastic von Mises yield criterion combined with a multilinear constitutive model was used to describe the elastic plastic behaviour of the copper model The yield stress used was 351 79 MPa and the Young's Modulus and Poisson ratio are 40 552 GPa and 0 3 respectively The material properties were obtained from the experimental results

The deformation behaviour of aluminium alloy reinforced with relatively rigid silicon carbide particles, that do not deform plastically, was numerically simulated on a microscopic scale using the finite element program ANSYS A multiphase model consisting of aluminium matrix and silicon carbide particles is used for the simulation of the microstructure The bonding strength of the interface between matrix and particles is assumed to be infinite for strong bonding and there was no decohesion during deformation The size of the silicon carbide particles in the matrix is 30 μm The matrix was assumed to be bilinear isotropically elasto-plastic hardening solid The elastic constant, 'E_{matrix}', and Poisson ratio, 'υ_{matrix}', was considered to be 73 GPa and 0 33, respectively The nonlinear part of the curve was approximated to a linear path with a tangent

modulus (ET) of 608 MPa, using the ultimate tensile strength (485 MPa) and the corresponding elongation. The silicon carbide particle reinforcements were assumed to behave as linear elastic and isotropic solids, and their elastic properties are Young's Modulus $E_{particle}$ = 420 GPa and Poisson ratio $\upsilon_{particle}$ = 0.14 [95]

This research aims at developing versatile finite element methodology for predicting the effect of combined tension and torsion loading conditions on the failure load of the experimental specimens

Finite element studies are useful when used in conjunction with an experimental testing program. Examining the combined effects of axial and shear stresses on the sample using FEA method allows for a more extensive parametric investigation of the underlying behaviour than is possible in a laboratory setting. This study conducted a comprehensive finite element modelling of combined tension and torsion loading of the model that include both geometric as well as material large deformation effects for capturing axial and shear stresses. Finite element modelling of experimental specimens allow for a better understanding of stress flow in the member and to better investigate the influence of shear stress on axial stress and vice versa

An incremental iterative strategy based on Newton-Raphson method was used to capture the non-linear load versus deflection behaviour of the specimen. Before each solution, the Newton-Raphson method evaluates the out-of-balance load vector, which is the difference between the restoring forces (the loads corresponding to the element stresses) and the applied loads. The program then performs a linear solution, using the out-of-balance loads, and checks for convergence. If convergence criteria are not satisfied, the out-of-balance load vector is re-evaluated, the stiffness matrix is updated, and a new solution is obtained. This iterative procedure continues until the problem converges

5.5.1   Finite Element Analysis on Copper Model

Constant Axial Displacement Test Simulation

The copper model representing the experimental specimen gauge length was subjected to constant axial displacement followed by the application of torque. The entire simulation was carried out in 2 load steps and 18 substeps.

In the first load step, an axial displacement was applied to all the nodes at the end of the model gauge length, selected as a component. Figure 5.40 shows the components used to apply axial and torsional loads.
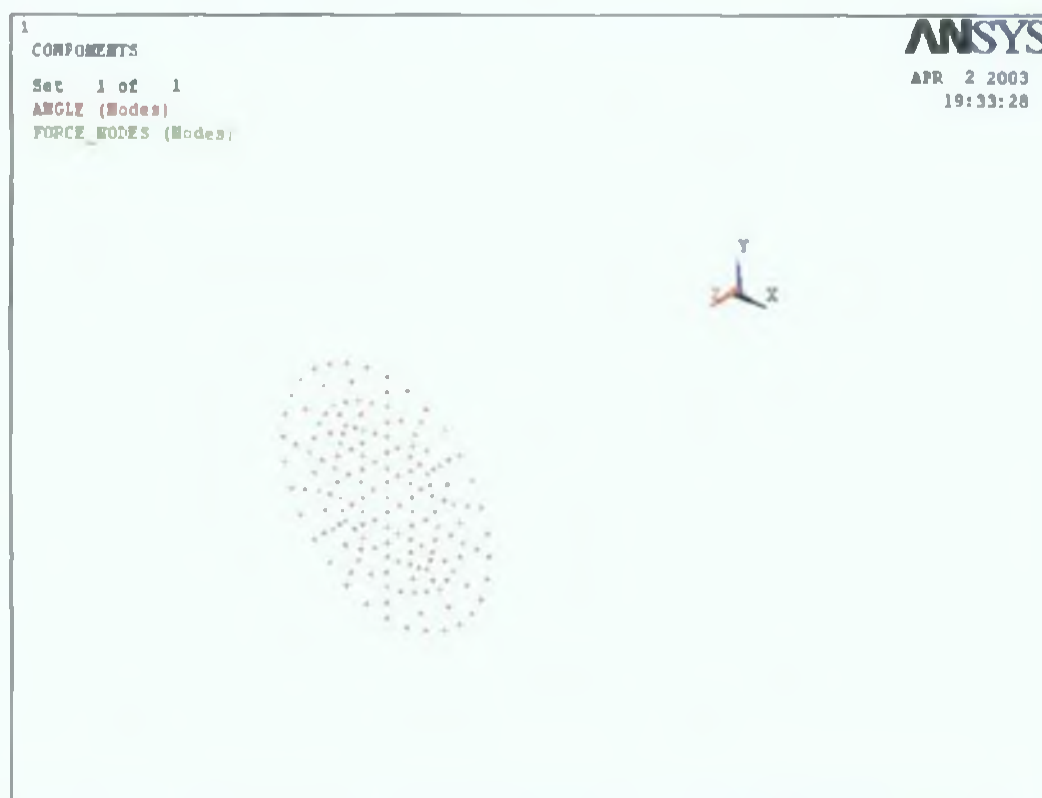
Figure 5.40 Components used to apply axial and torsional loads

The initial axial displacement of the component corresponds to the displacement in pure tension simulation for 15% yield axial load. *SPARSE* solver with nonlinear geometric deformation was used to solve this load step in 6 substeps. In the second load step, pressure calculated from the equation in section 4.7.5

was applied to all the surface elements overlaid on the circumference of the extended volume This load step was solved in 12 substeps Similarly, the copper model was subjected to three other initial axial displacements corresponding to 34%, 70% and 98 5% yield axial loads followed by torque All the simulations were carried out in 2 load steps and 18 substeps as described above Figure 5 41 illustrates the axial stress-shear stress relationship in a specific node (Node number 125) over the entire loading path It is evident from the graph that the simulation can very closely predict the axial stress- shear stress relationship in combined tension and torsion loading condition The initially applied axial stress remained constant until von Mises yield curve, and then followed the von Mises yield curve The von Mises yield curve shown in the graph was calculated from the experimental results, i e 0 02% offset strain, whereas the yield stress used in the material model corresponds to zero offset strain The difference can be observed from the yield points in the curve prior to von Mises yield curve The trend of elastic-plastic deformation of the model can be observed from the numerical simulation result

Figure 5 42 and 5 43 illustrates the axial displacement and angle of twist in the specimen at the end of the second load step The axial displacement was found to increase linearly over the entire length of the model during the first load step No further increase in the axial displacement was noticed in the second load step The angle of twist at the end of the simulation was found to be 12 degree at the end of the model gauge length The shear strain was found to be maximum at the periphery and decreased linearly along the radius towards the axis, where it is zero

Figure 5 44 and 5 45 illustrates the axial stress distribution at the end of the simulation on the surface and across the cross section of the model respectively Axial stress gradient across the cross section suggests that plastic yielding has occurs at the outer periphery, which reduces the load carrying capacity of the model The maximum axial stress was found to be at the axis of the model

Figure 5 46 shows the shear stress distribution across the cross section of the model at the end of the simulation Nonlinear reduction in the shear stress was found to exist along the radius of the model towards the axis The nonlinearities in the shear stress reduction depend on the amount of plastic deformation in the model

Figure 5 47 describes the von misses equivalent stress distribution in the model Large variation was found to exist across the cross section with 35 347 MPa at the axis of the model and 360 315 MPa at the periphery

Constant Angle of Twist Test Simulation

The simulation model representing copper rod specimen was subjected to constant angle of twist followed by the application of axial load The simulation was carried out in 2 load steps and 42 substeps Constant angle of twist test simulations were carried out for 60%, 88%, 97% initial yield torque followed by axial loading

In the first load step, all the nodes at the end of the model gauge length selected as a component, were rotated and constrained at 2 5 degrees in the cylindrical UY about Z-axis The initial constraint developed shear stress in the model that corresponds to 31% of yield torque This load step was solved in 6 substeps

In the second load step, the axial force corresponding to the maximum axial load achieved during the experiment was applied on the component (Force Nodes) The total axial force was divided and distributed among the nodes This load step was solved in 36 substeps to enable smooth loading and iteration procedure within the ANSYS

Figure 5 48 shows the axial stress-shear stress relationship in a specific node on the circumference of the model over the entire loading path The maximum axial stress achieved in the simulation by the selected node is 300 MPa, which is 82% of the yield axial load It is evident from the figure that the numerical simulation results do not match the experimental results This is due to the use of existing material model in ANSYS that does not describe elastic-plastic behaviour of the

material under consideration, properly Figure 5 49 and 5 50 the axial strain and shear strain distribution in the model at the end of the simulation in cylindrical coordinate system Figure 5 51 and 5 52 shows the axial stress distribution on the model and in the cross sectional area respectively for 97% yield torque It can be observed that the average axial stress along the gauge length is around 271 MPa at the end of the simulation Figure 5 53 shows the shear stress state across the cross section of the model Though the initial shear stress at the start of second load step was 217 MPa, it was found to be 150 MPa at the end of second load step due to the von Mises yield criteria Figure 5 54 shows the von Mises equivalent stress distribution across the cross section of the model

5 5 2   Finite Element Analysis on AlSiC metal matrix composite Model

The primary advantage in using finite element method is that the effects of geometry of the microstructure on the effective properties of composites can be considered, and detailed microscopic stress fields can be predicted However, the previous studies carried out on this research topic were not concerned with the effects of particle-particle and particle-matrix interactions on the elastic-plastic behaviour of composites, since they used only single fiber unit cell models In this investigation, a micromechanical model containing multiple particles in aluminium matrix and finite-element method were used to account for the interactions and to calculate the microscopic deformation and effective properties of fiber reinforced composites with matrix material

In order to investigate the influence of the reinforcement particles on the deformation behaviour of the composite, a periodic array of four spherical hard phases in each quadrant in the matrix was modelled for the prediction of combined axial and shear stresses The elastic region of the axial stress-shear stress curve as well as the onset of plastic deformation was well predicted by the numerical analyses

153

Constant Axial Displacement Test Simulation

Figure 5 55 shows the axial stress distribution over the surface of the AlSiC MMC model Maximum axial strain was found to occur in elements away from the silicon carbide particles The strength of the silicon carbide particle restricts the deformation of the model Figure 5 56 shows the shear stress distribution over the surface of the AlSiC MMC model The maximum shear stress is observed in elements far away from the silicon carbide particles This suggests that the aluminium matrix is subjected to large deformation than silicon carbide particles

Figure 5 57 describes von Mises equivalent stress distribution on the model Almost all the elements on the surface of the model are subjected to same von Mises equivalent stress except the elements close to the particles, where the stress were found to be comparatively less The von Mises equivalent stress was found to decrease towards the axis of the model

Figure 5 58 and 5 59 illustrates the distribution of axial stress and shear stress in the aluminium matrix and silicon carbide particles respectively Predominantly the stresses are carried by the silicon carbide particles as demonstrated in the figures Both tensile and compressive stresses are present in the elements representing silicon carbide particles The stress gradient between silicon carbide particle and aluminium matrix is very coarse due to coarse elements size

As the load transfer mechanism of particulate composites is very complex and is influenced by the interaction between matrix material and silicon carbide particles, the finite element method was used in this analysis Numerical results of finite element analysis for the AlSiC MMC system were presented to illustrate particle-particle and particle-matrix interactions and effect of fiber discontinuity on the local stress fields Figure 5 58 shows normal stress distributions in the matrix and the particle It is noted that there is a very high stress domain near the fiber boundary due to the material discontinuity This high normal stress may easily cause debonding of the interface between fiber and matrix When plastic deformation increases, the high normal stress domain will enlarge Although

154

theie is high normal stress domain in the matrix near the fiber ends, constraint from adjoining fibers will not allow deformation of the matrix to continue infinitely

The sheai stress fields in the matrix and the particle are shown in Figure 5 59 The shear stress in the matrix varies sharply near the fiber boundary The maximum shear stress appeared at the longitudinal interface near the fiber boundary The shear stress is transferred from matrix to fiber through longitudinal interface In the present analysis, the difference between the elastic moduli of particle and matrix is very large, so the discontinuity of fibers will affect local stress fields near the particle boundary only The reason is that a relatively ductile matrix can develop a plastic deformation to relax part of the stiess concentration near the fiber boundary

Figure 5 60, 5 61 and 5 62 describes the axial stress, shear stress and von Mises equivalent stress distributions on the silicon carbide particles respectively Large variation in the stresses is present in the elements representing two of the 16 silicon carbide particles

Figure 5 63 shows the von Mises equivalent stress along an arbitrary line chosen to pass through all the four silicon carbide particles in one quadrant Maximum stress was found to exist in the silicon carbide particle elements Within the silicon carbide particle elements huge variation in the stress can be, observed from the figure This is due to strain variation at the particle matrix interface that led to higher stresses at the interface and least strain variation within the particle The center elements in the silicon carbide particles are subjected to von Mises equivalent stresses of around 990 MPa whereas at the circumference the stiesses vary between 1120 MPa to 1473 MPa This clearly describes the strengthening effect due to the addition of silicon carbide particles in Aluminium matrix The equivalent stress is inhomogeneously distributed due to the large difference in the elastic properties of the hard phases and the matrix material This led to areas within the model where the equivalent stress is much higher

than the applied load The stress concentration in the vicinity of the particles is due to the strain constraint in the presence of silicon carbide particles

Constant Angle of Twist Test Simulation

Figure 5 64 illustrates the axial stress distribution on the surface of the AlSiC MMC model at the end of constant angle of twist simulation run The maximum axial stress was found to be present in the elements close to the particles on the circumference of the model Figure 5 65 shows the shear stress distribution, which in contrast to axial stress was found in elements far away from the particles

Figure 5 66 demonstrates that the elements in the particles and the adjoining aluminium matrix elements were subjected to the maximum von Mises equivalent stress Large von Mises equivalent stress variation was found to exist on the surface of the model, which suggests that the applied load is predominantly carried by the silicon carbide particles Figure 5 67 and 5 68 shows the axial stress and shear stress distribution across the cross section of the model The maximum axial and shear stress was found to exist in the silicon carbide particles at the end of the simulation The shear stress present in the aluminium matrix elements is almost negligible Due to the coarse nature of the elements in the silicon carbide particle and aluminium matrix huge variation in the axial stress can be observed

Figure 5 69 and 5 70 show the axial stress and shear stress distribution on the particles respectively Comparatively the stress distribution patterns are found to be similar to constant axial displacement test The maximum stresses are found to exist in elements close to abscissa

Figure 5 71 illustrates von Mises equivalent stress distribution in the particles Variation of the von Mises equivalent stress was found to persist in the order of 10 times Figure 5 72 shows the variation in the von Mises equivalent stress along a line passing through all the silicon carbide particles in one of the quadrants

The cumulative results obtained from constant axial displacement tests simulation is shown in Figure 5 73 The axial and shear stress values were calculated using the formula given in section 4 7 4 Difficulty in picking the proper element to represent the stress state was encountered during analysis The results from the figure suggests that a close estimation of the axial and shear stress state at any particular loading condition can very well be predicted using this model The large difference between the elastic-plastic properties of aluminium matrix and silicon carbide particle is observed in the simulation Figure 5 74 shows the axial stress-shear stress relationship in the aluminium matrix during the simulation along with that of the composite material The difference in the elastic-plastic properties could be attributed to the strengthening effect of the particle inclusion in the matrix Figure 5 75 shows the simulation results from Constant Angle of twist test run The model shows the trend of elastic plastic deformation of AlSiC rod similar to that observed experimentally The combined stresses followed the von Mises yield curve closely showing almost no hardening effect This is due to the use of existing material model in ANSYS that does not describe the elastic-plastic behaviour of the specimen used in the experimental investigation properly
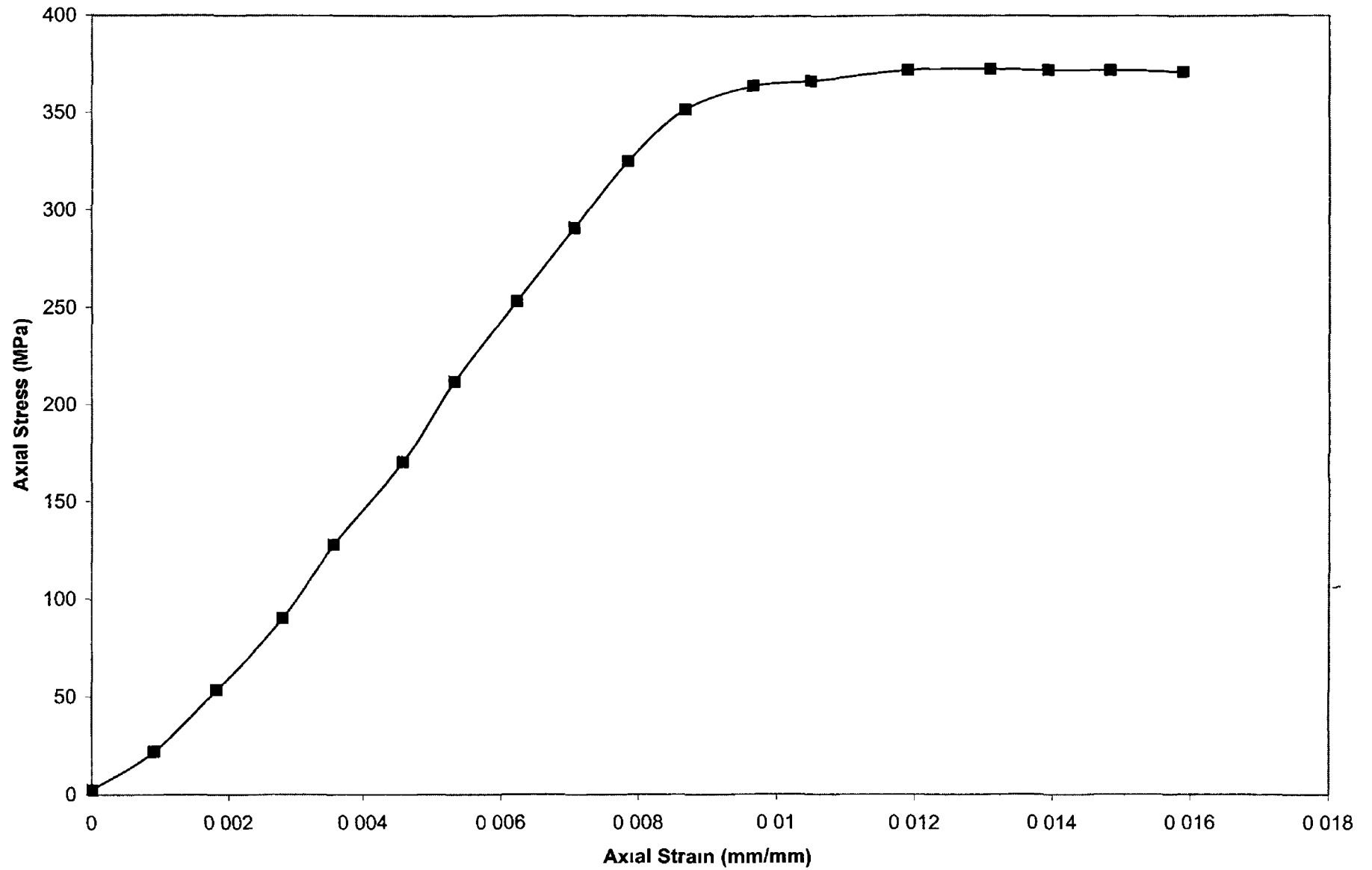
Figure 5 2 Axial Stress-Strain Curve for Copper Rod
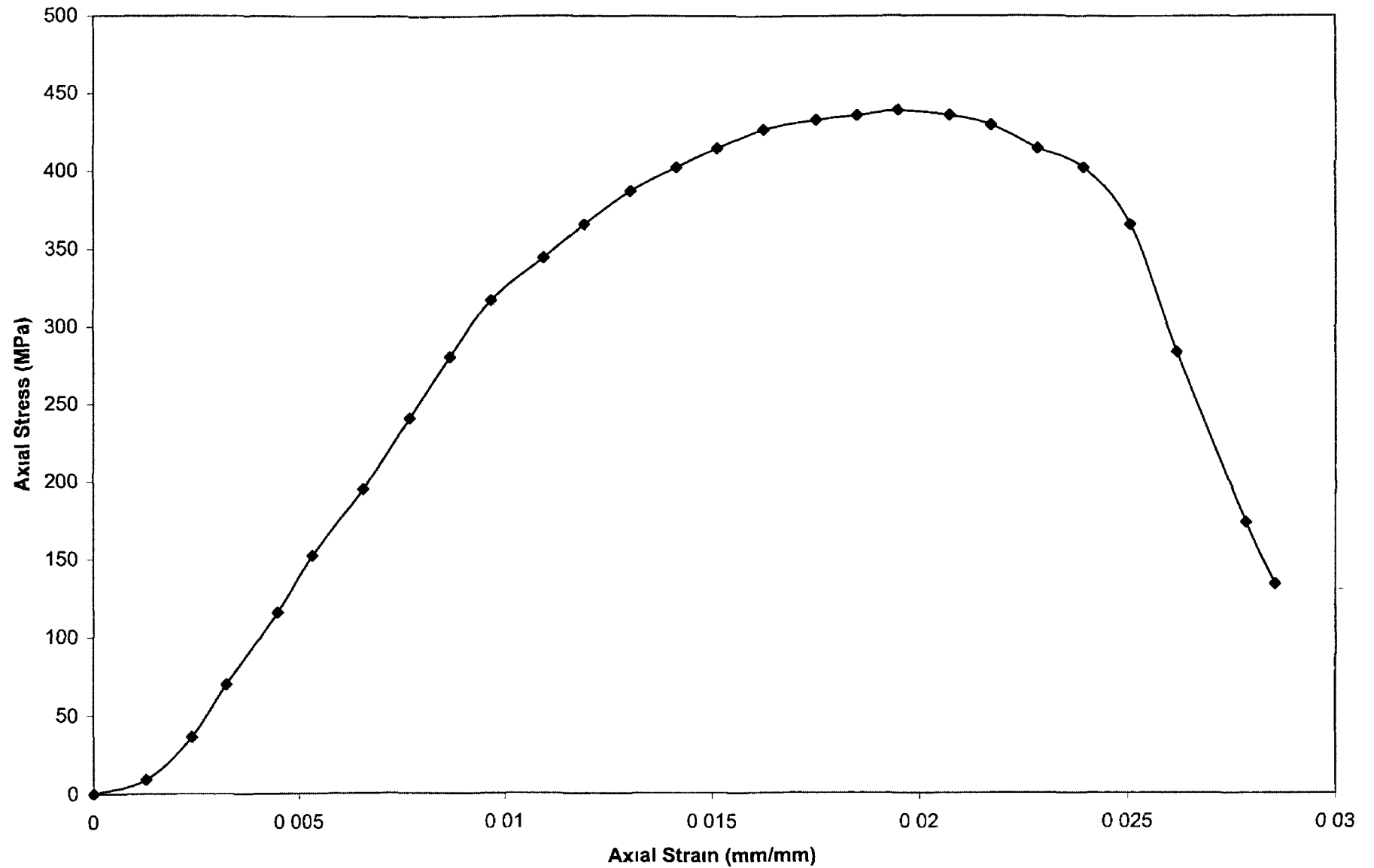
Figure 5 3 Axial Stress - Axial Strain Curve for Copper Tube
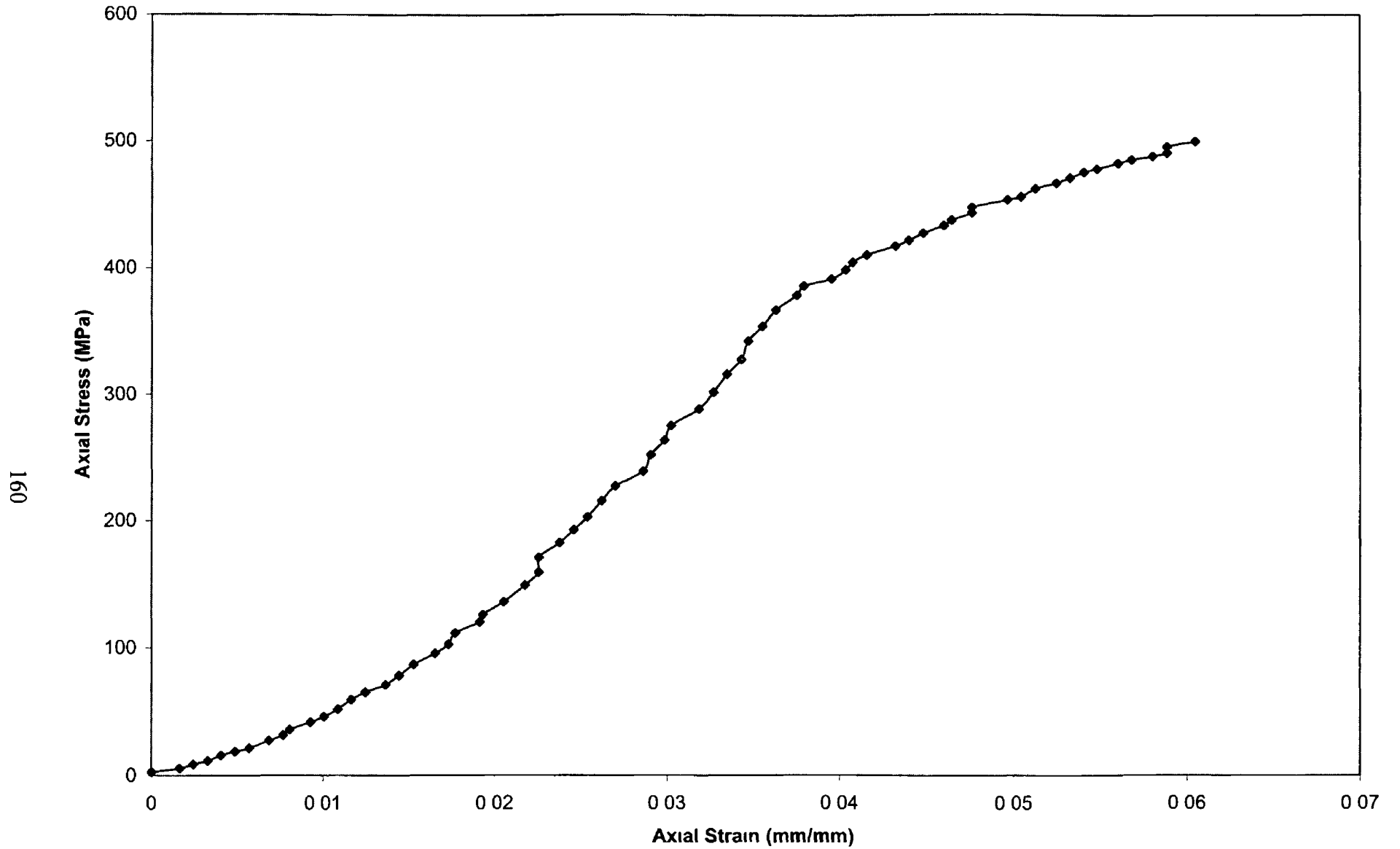
Figure 5 4 Axial Stress - Axial Strain Curve for AlSiC MMC Rod
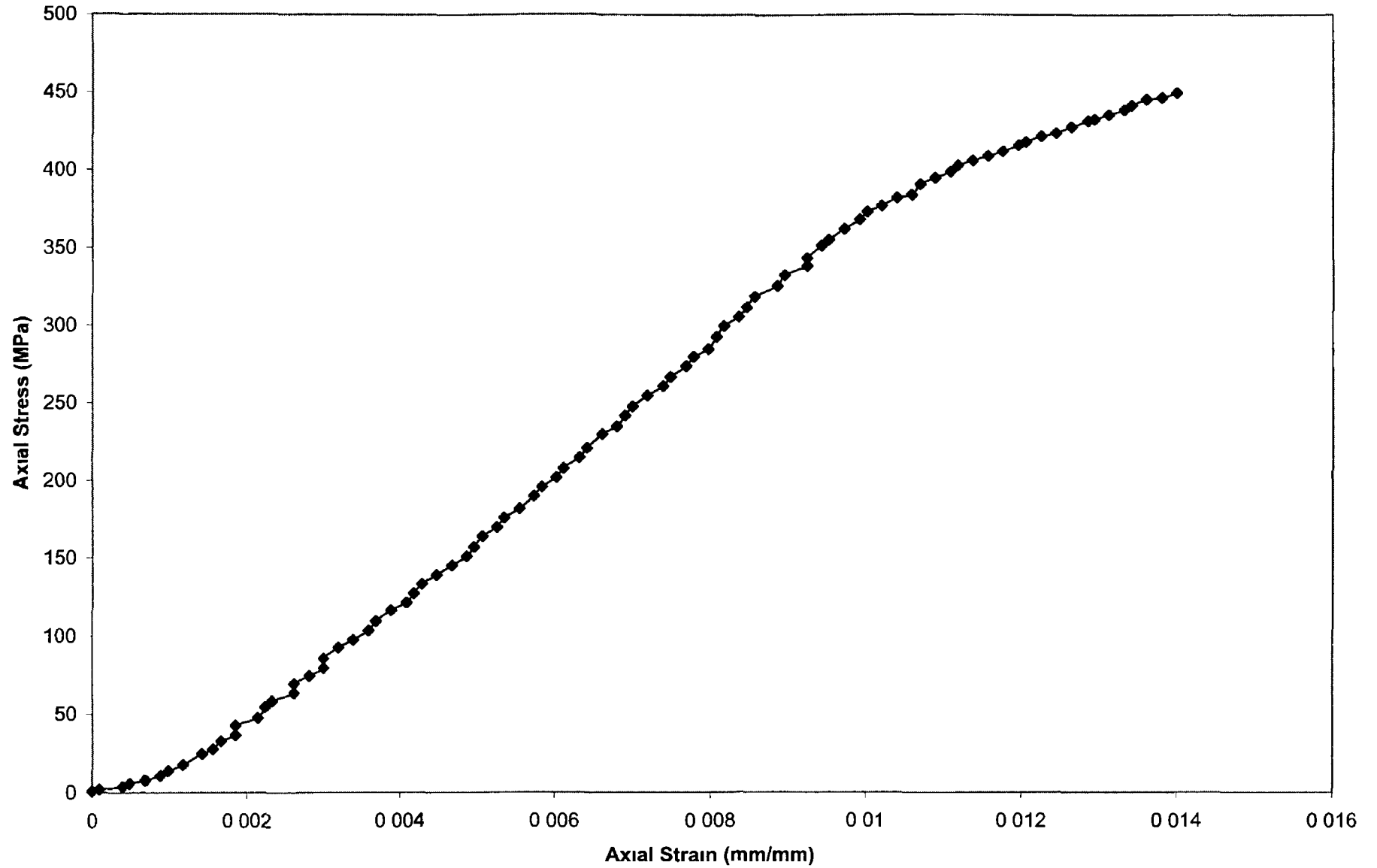
Figure 5 5 Axial Stress - Axial Strain Curve for AlSiC MMC Tube
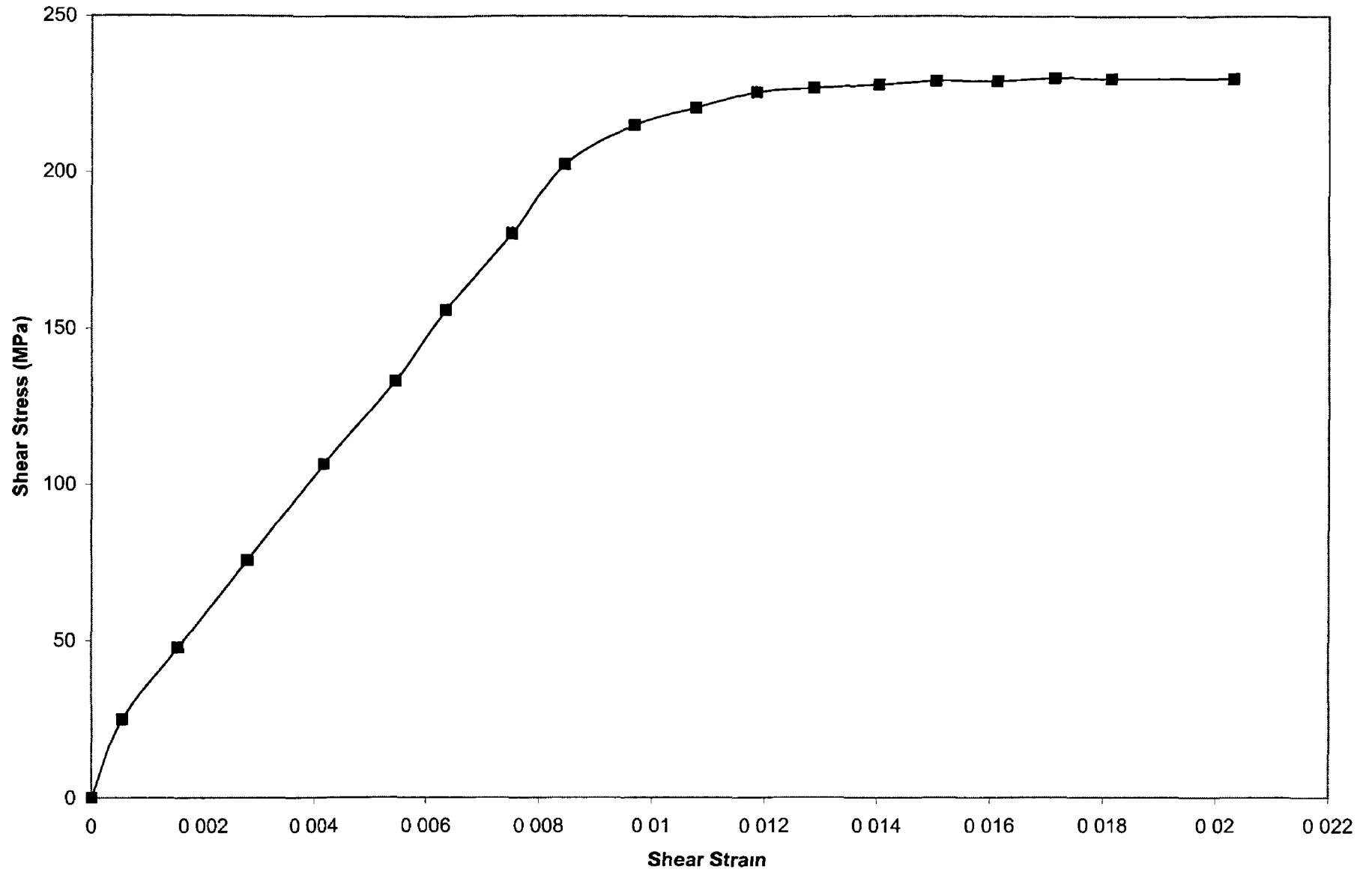
Figure 5 6 Shear Stress - Shear Strain Curve for Copper Rod
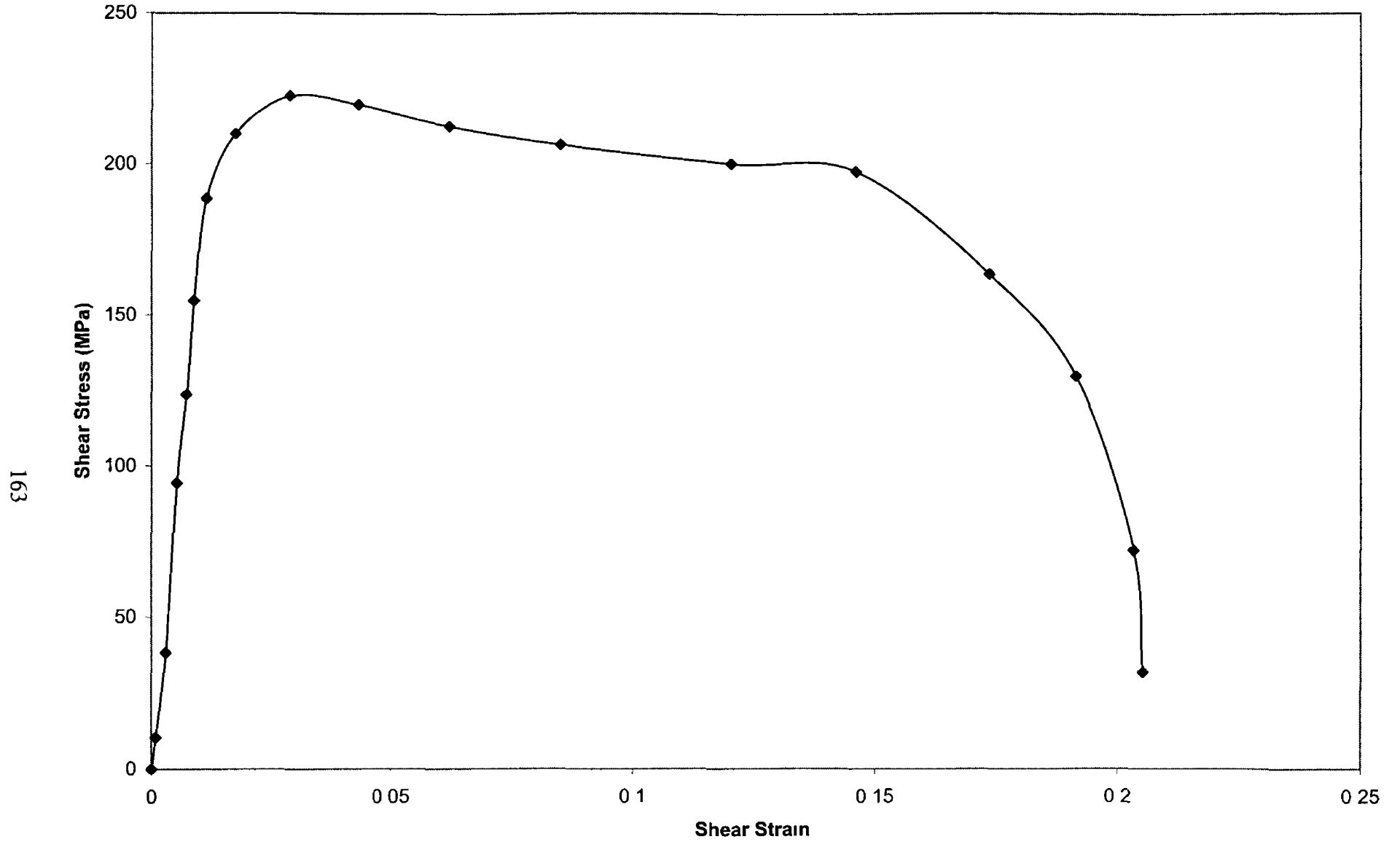
Figure 5 7 Shear Stress - Shear Strain Curve for Copper Tube
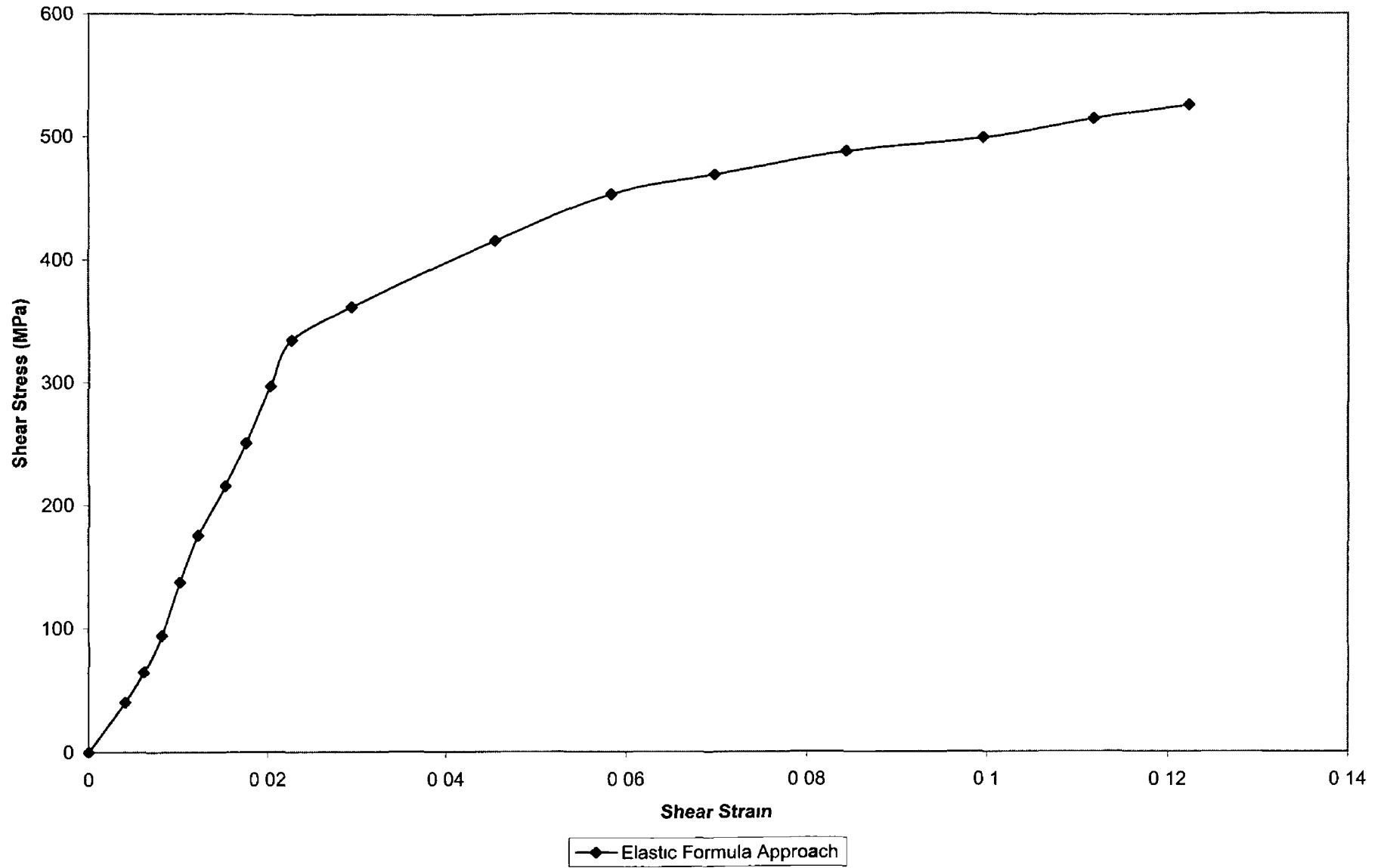
Figure 5 8 Shear Stress - Shear Strain Curve for AlSiC MMC Rod
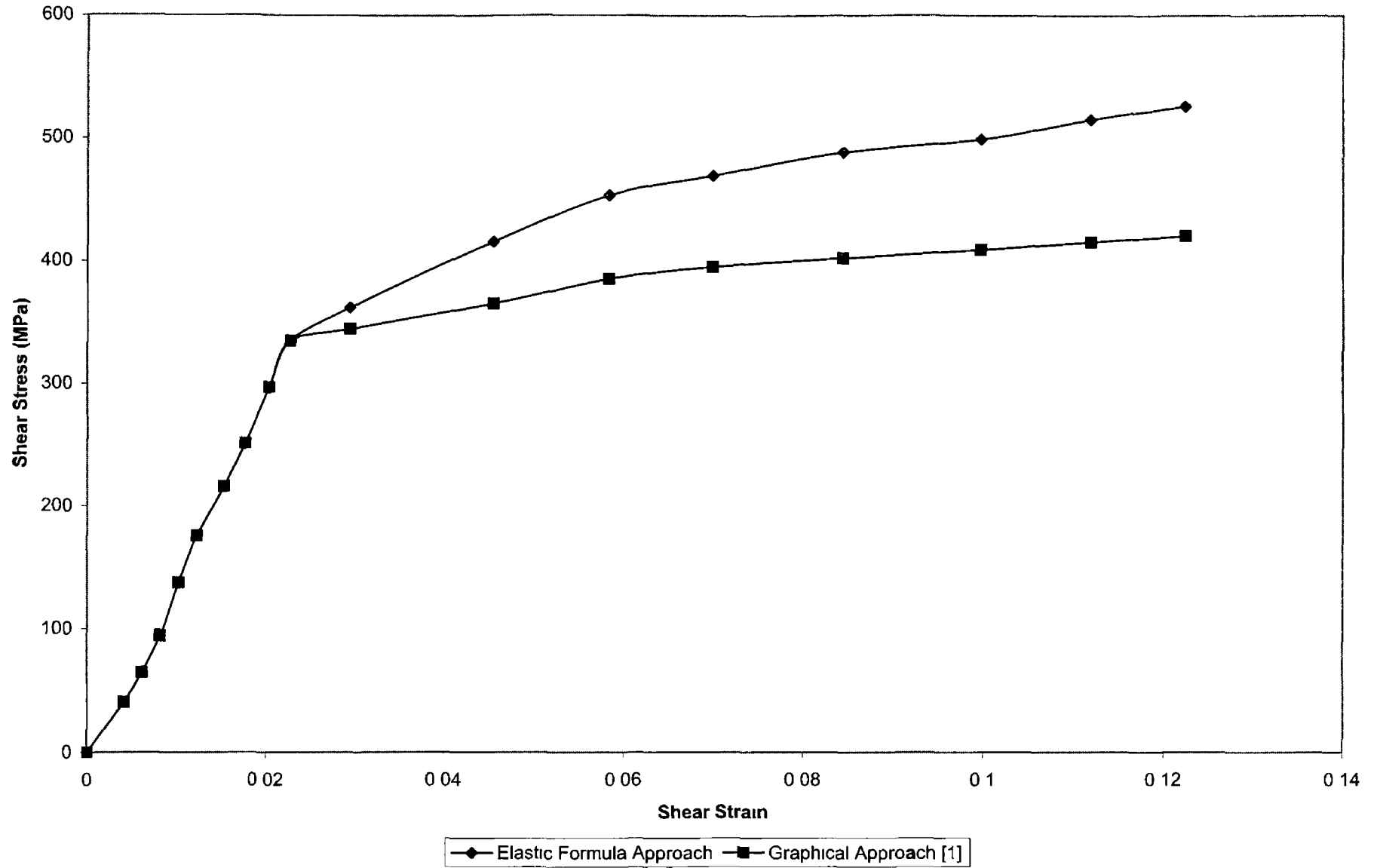
Figure 5 9 Shear Stress - Shear Strain Curve for AlSiC MMC Rod
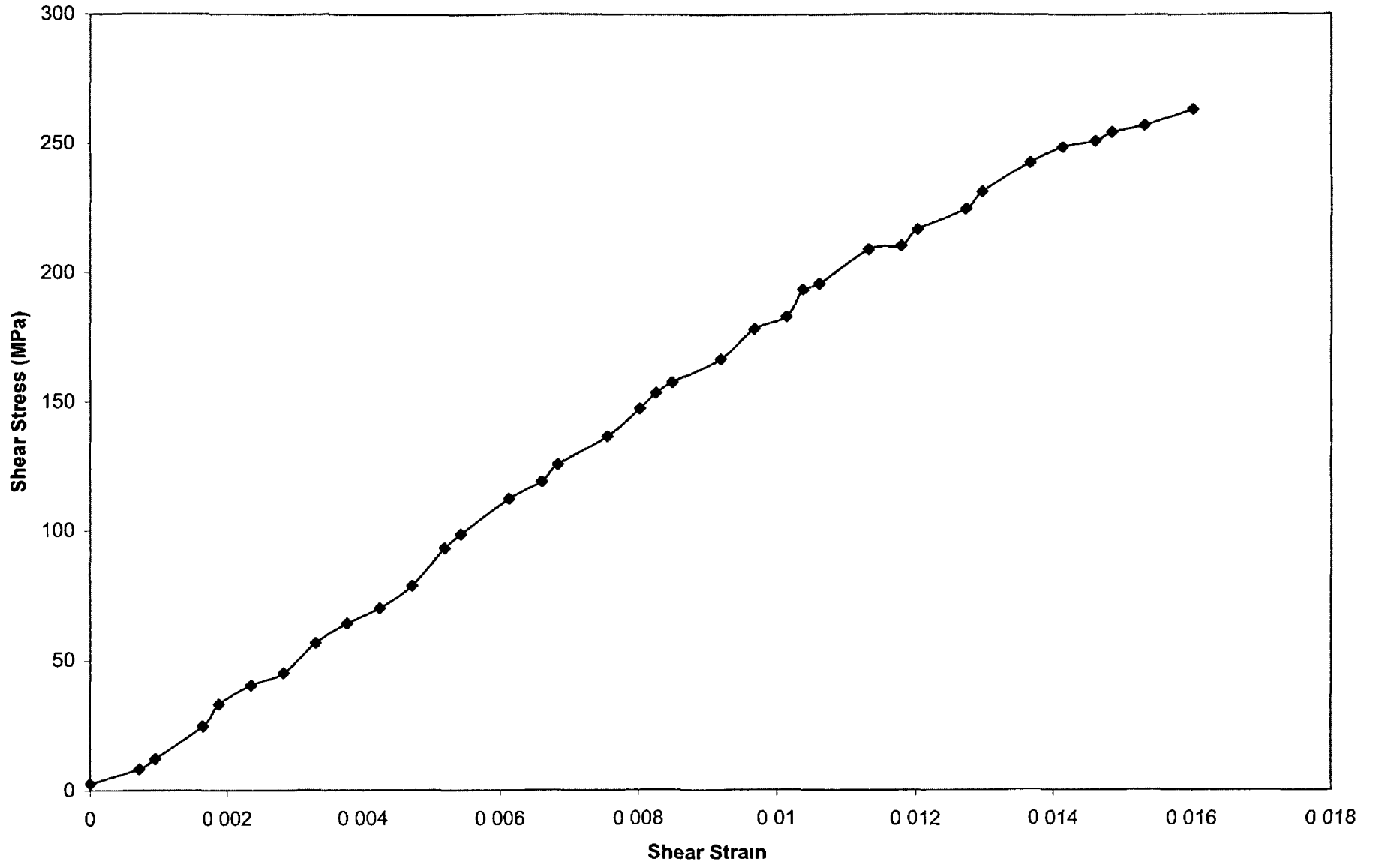
Figure 5 10 Shear Stress - Shear Strain Curve for AlSiC MMC Tube
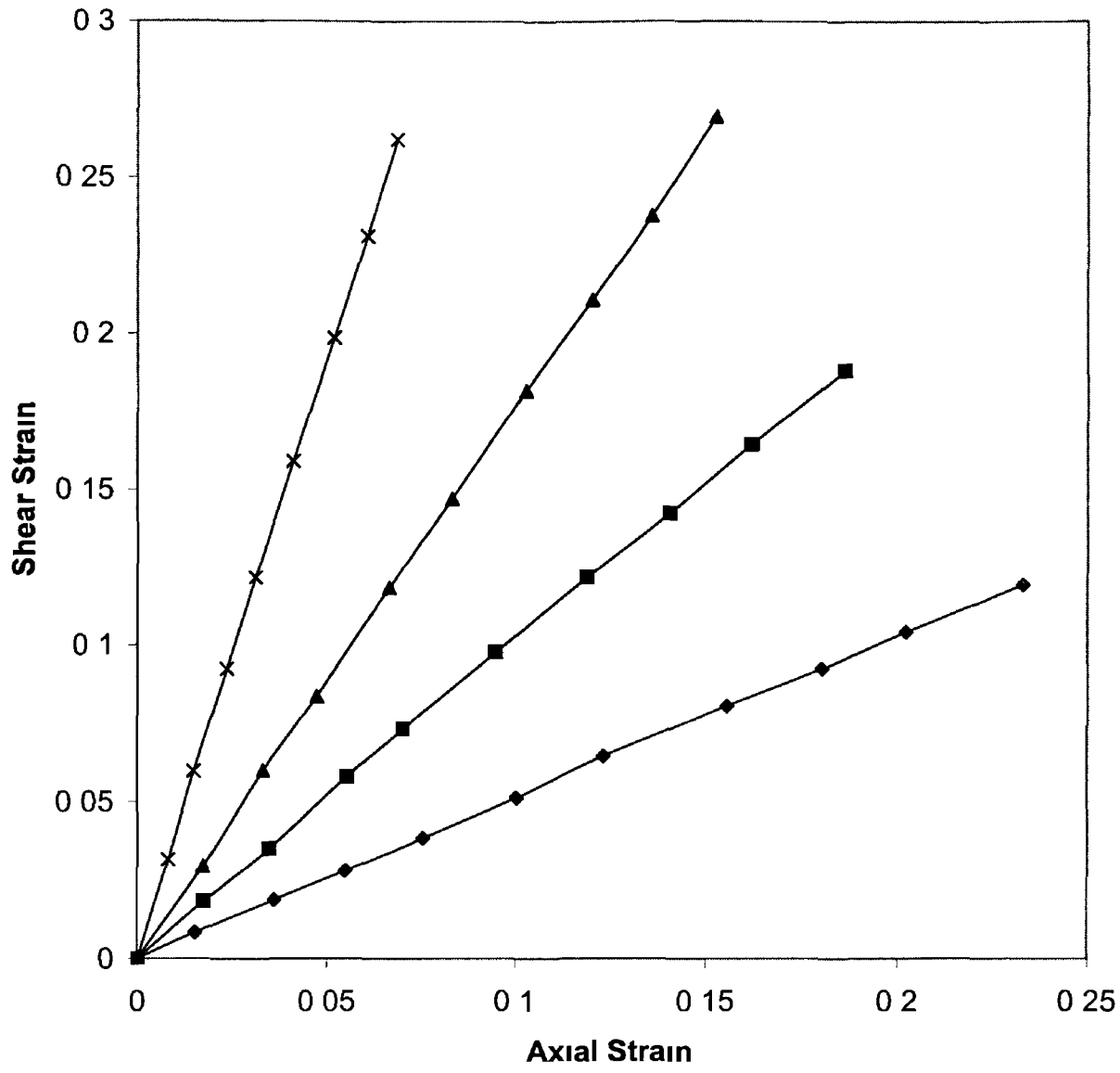
Figure 5 11 Proportional Axial Strain to Shear Strain Ratios
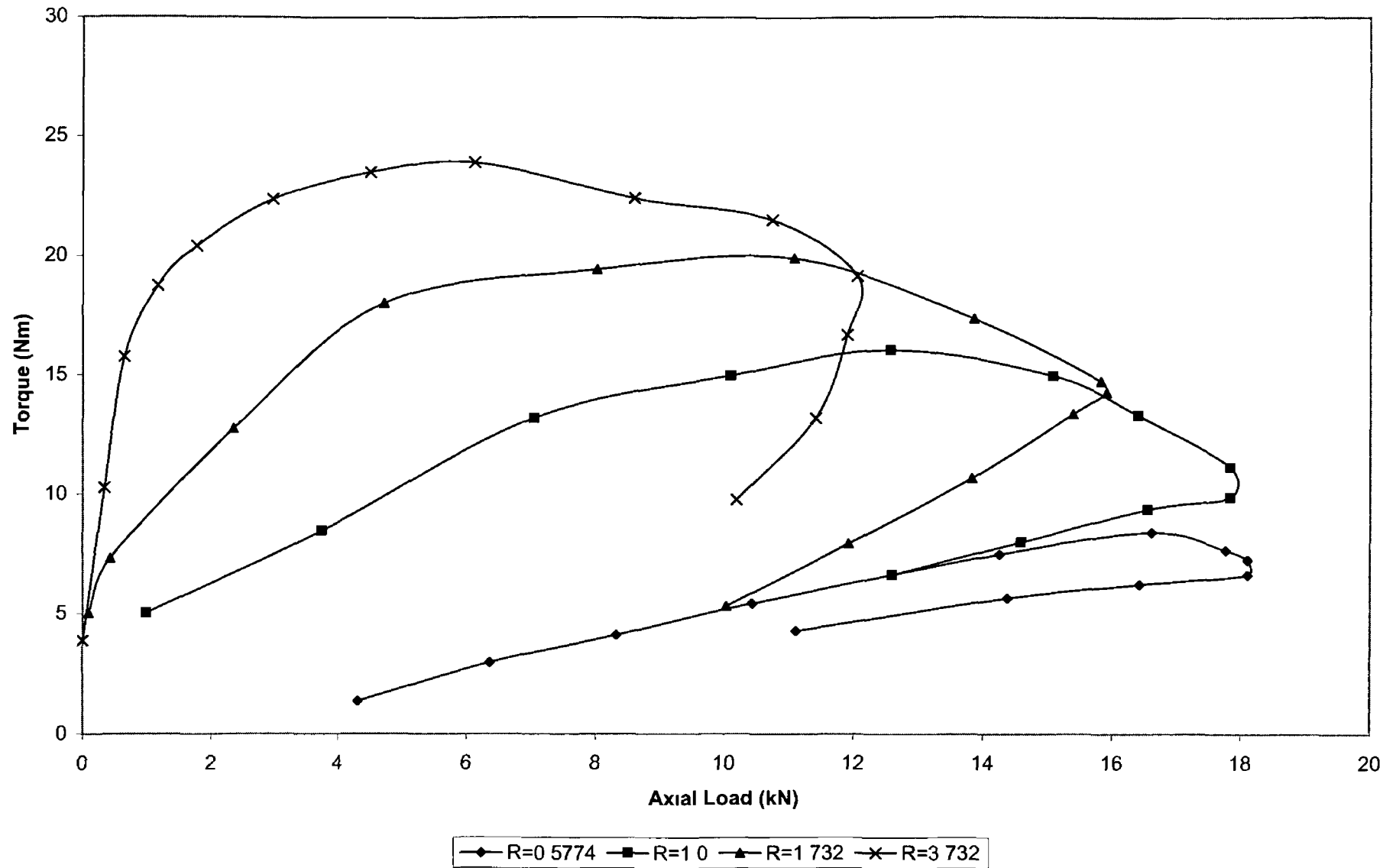
Figure 5 12 Proportional Axial Load-Torque Curve for Copper Rod
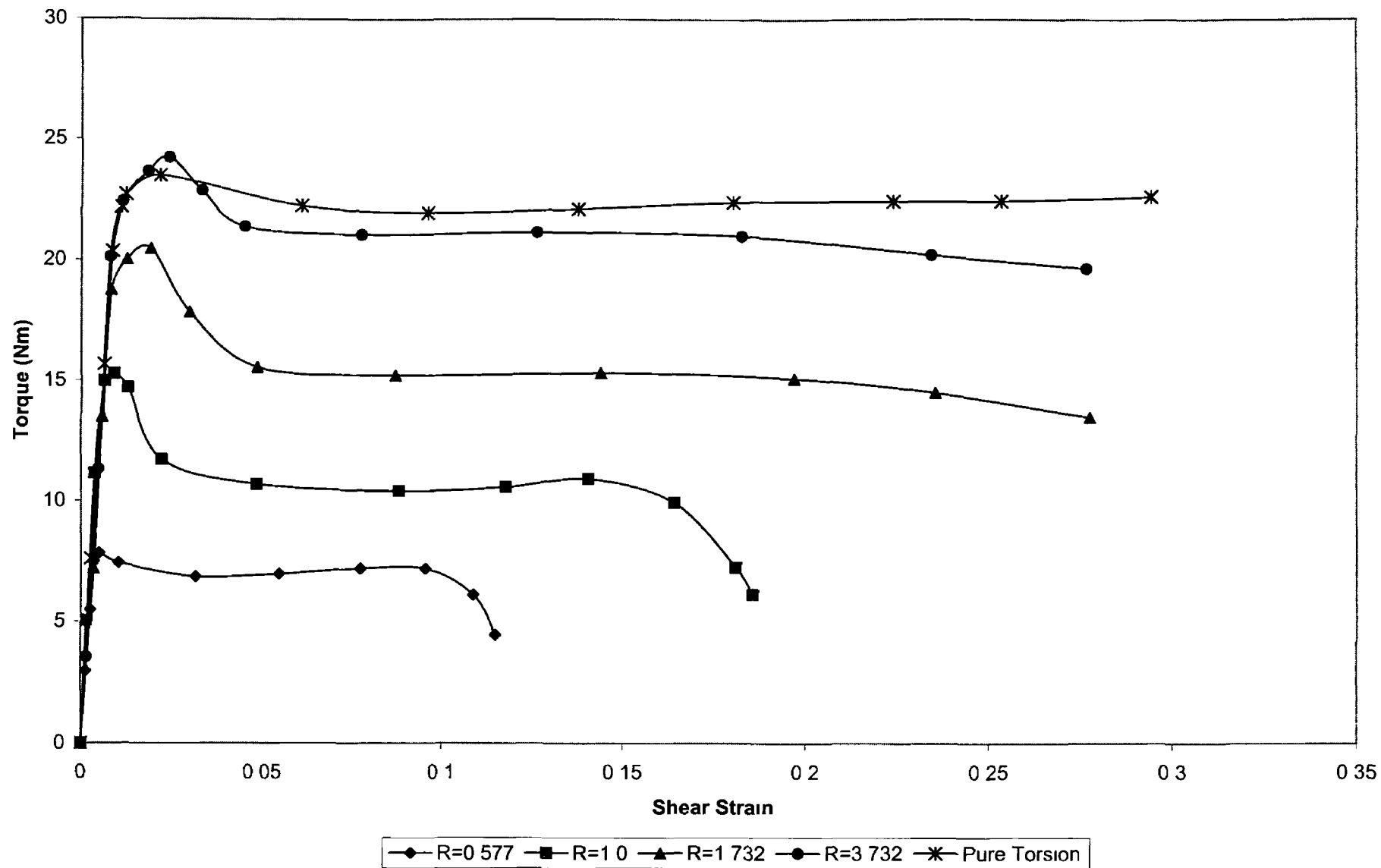
Figure 5 13 Effect of Axial Load on Torque in Proportional Loading for Copper Rod
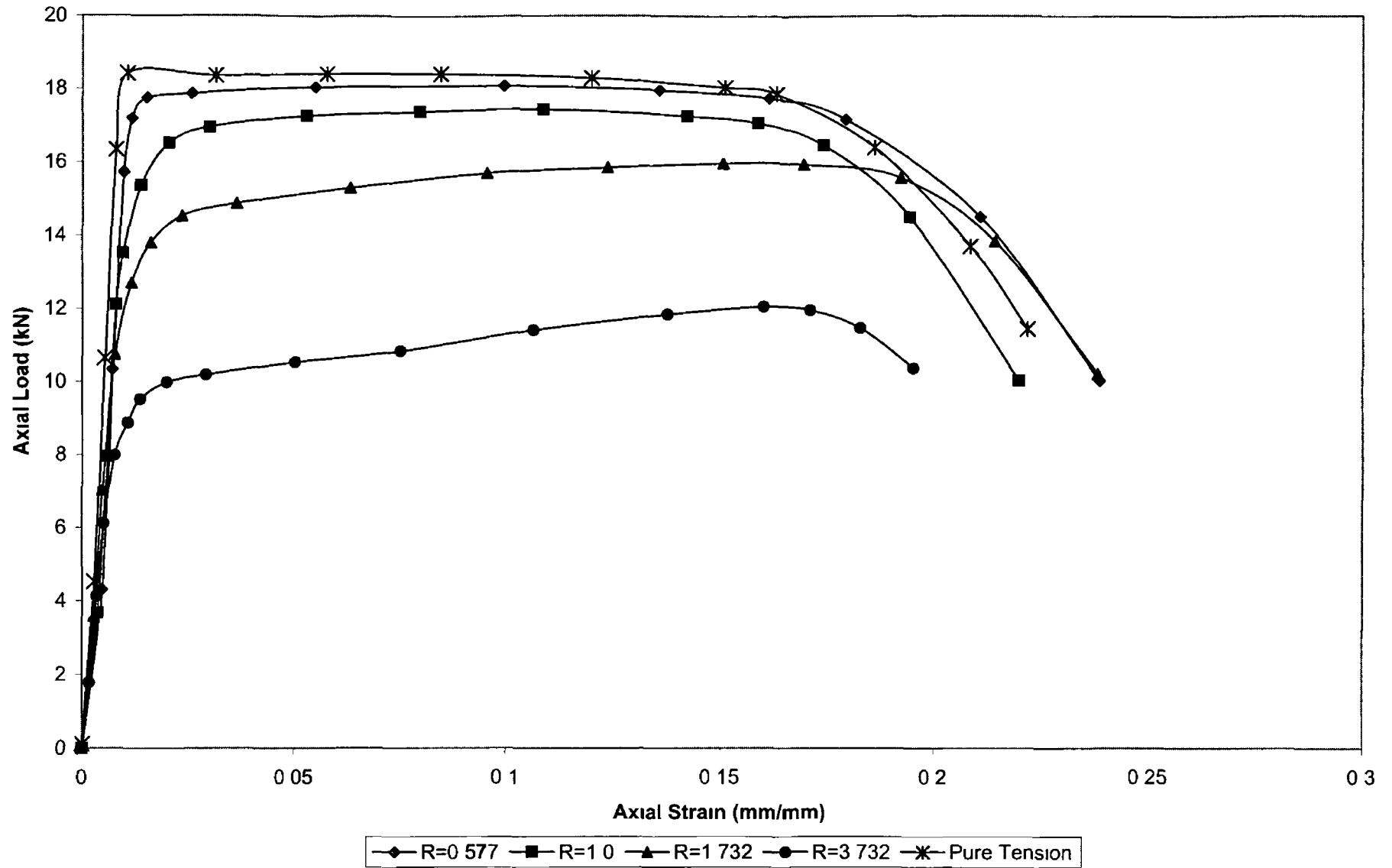
Figure 5 14 Effect of Torque on Axial Load in Proportional Loading for Copper Rod
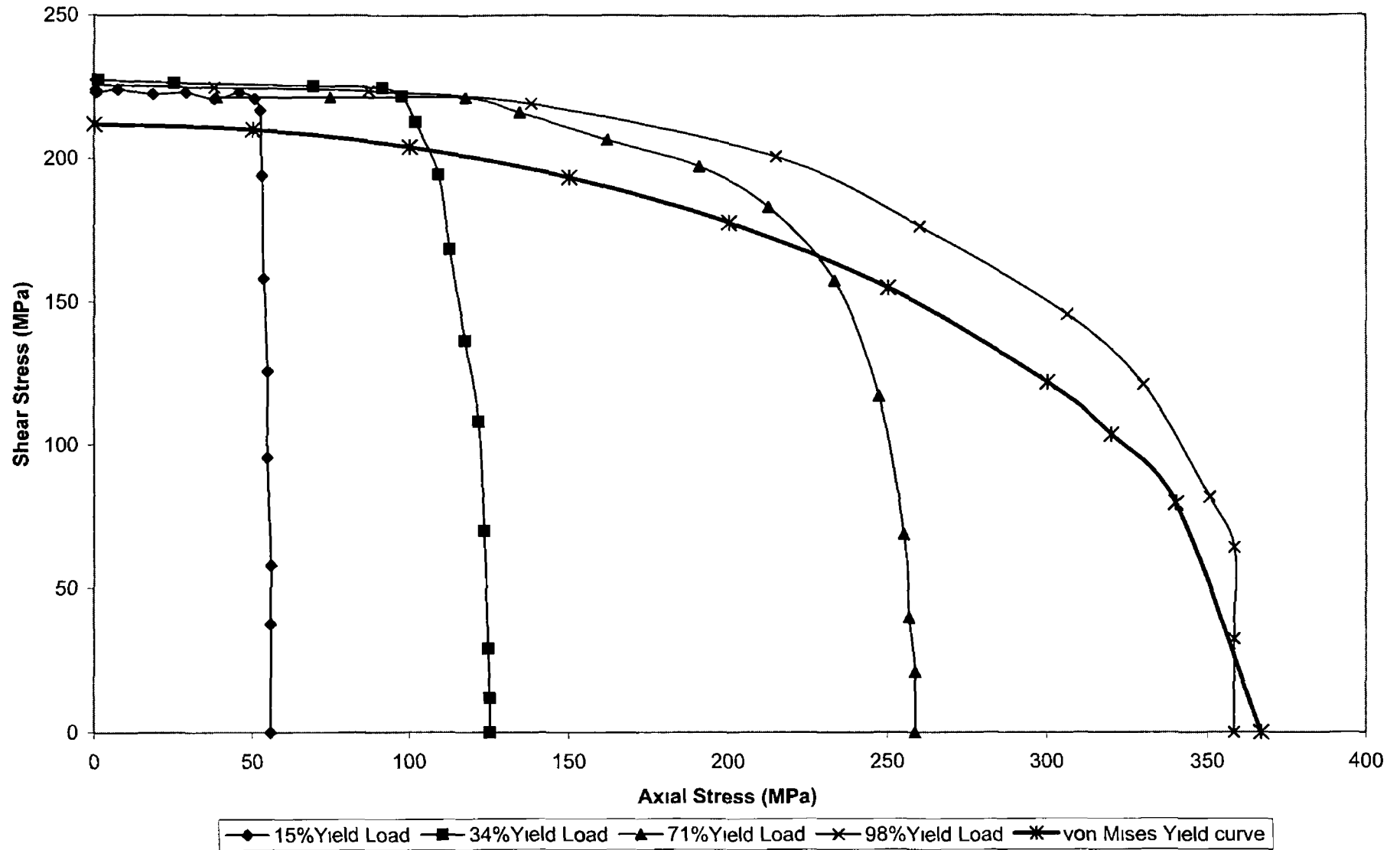
Figure 5 15 Axial Stress - Shear Stress Relationship for Copper Rod
(Constant Axial Displacement)
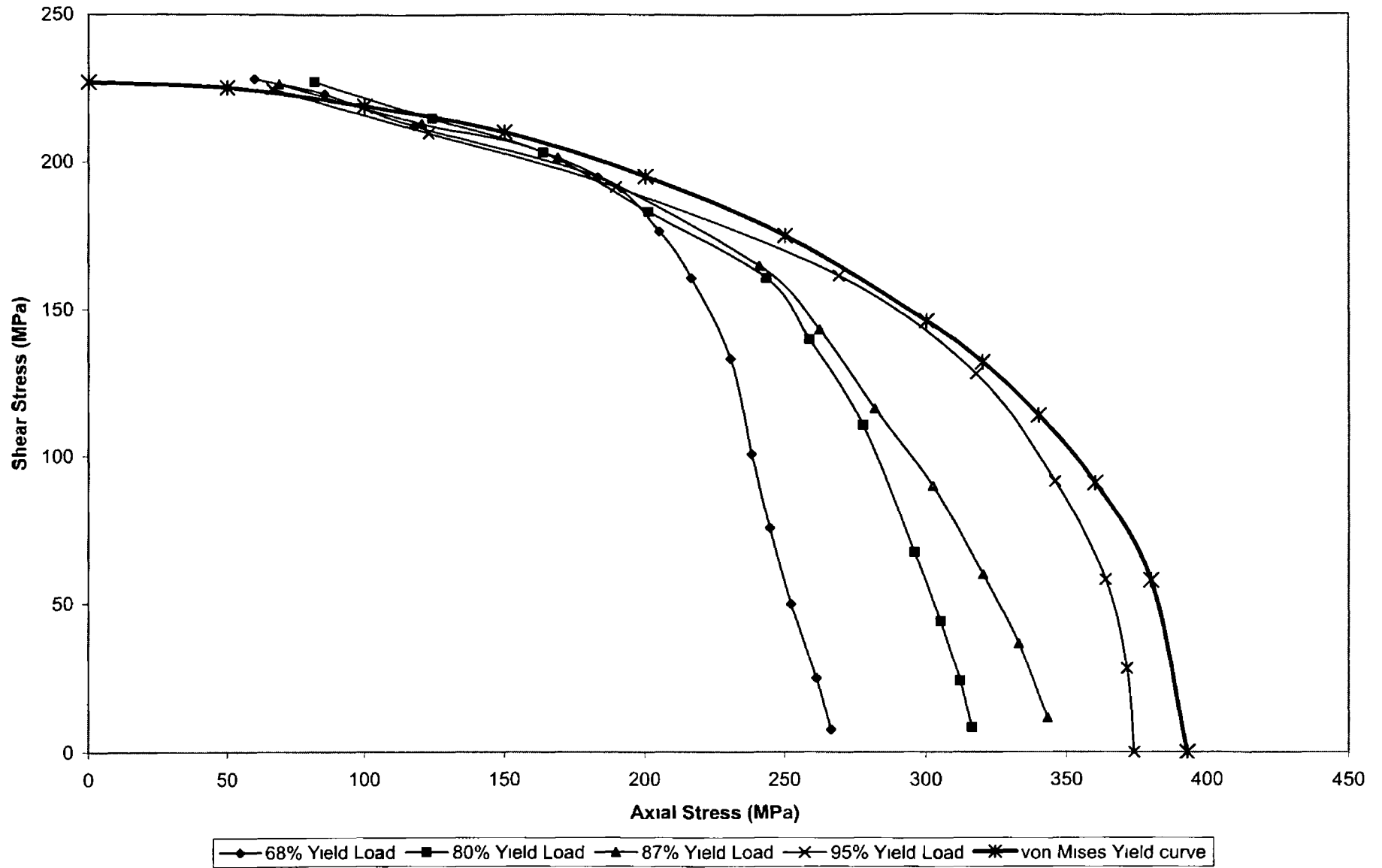
Figure 5 16 Effect of Shear Stress on Axial Stress for Copper Tube (Constant Axial Displacement)
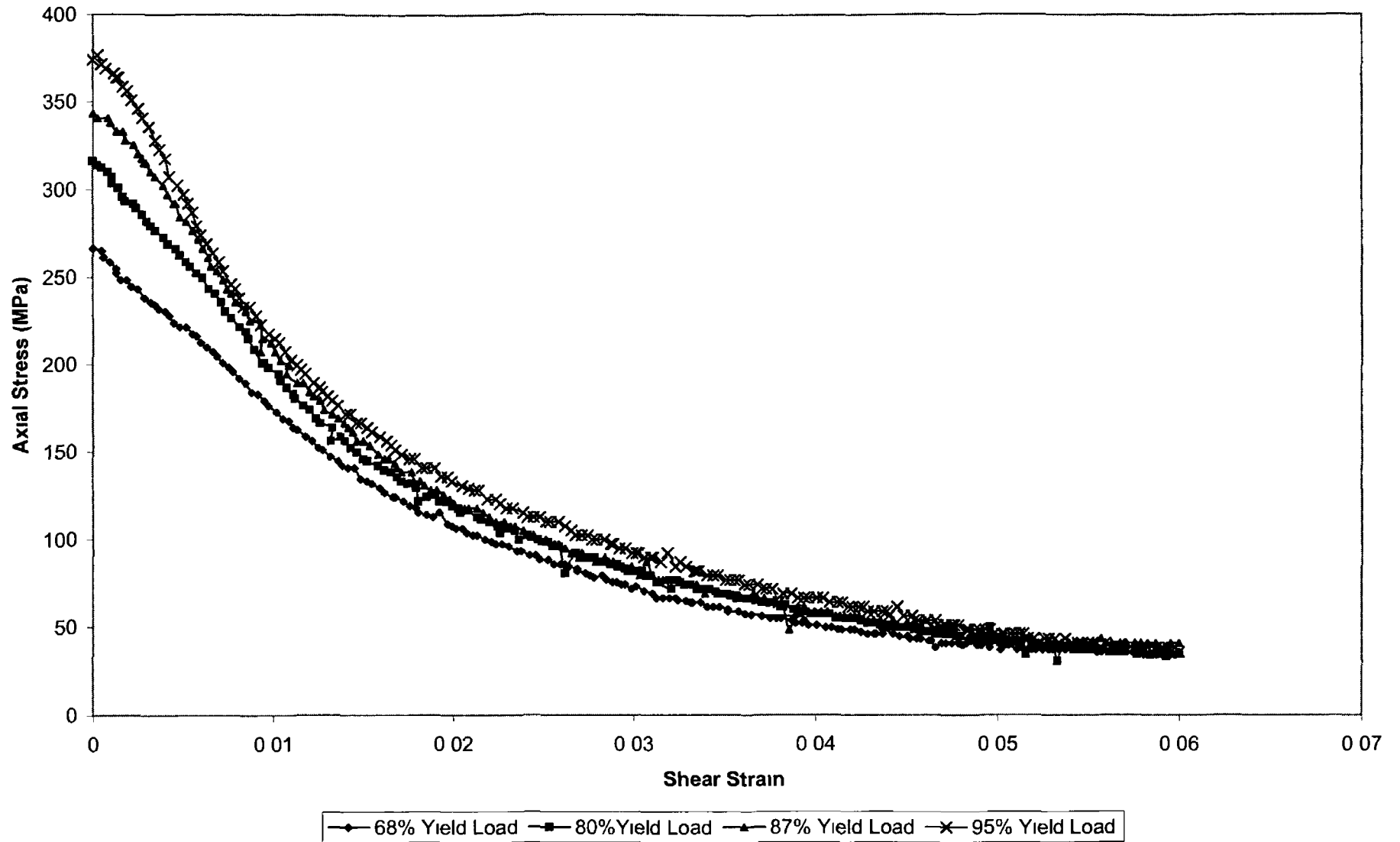
Figure 5 17 Effect of Shear Strain on Axial Stress for Copper Tube
(Constant Axial Displacement)

173
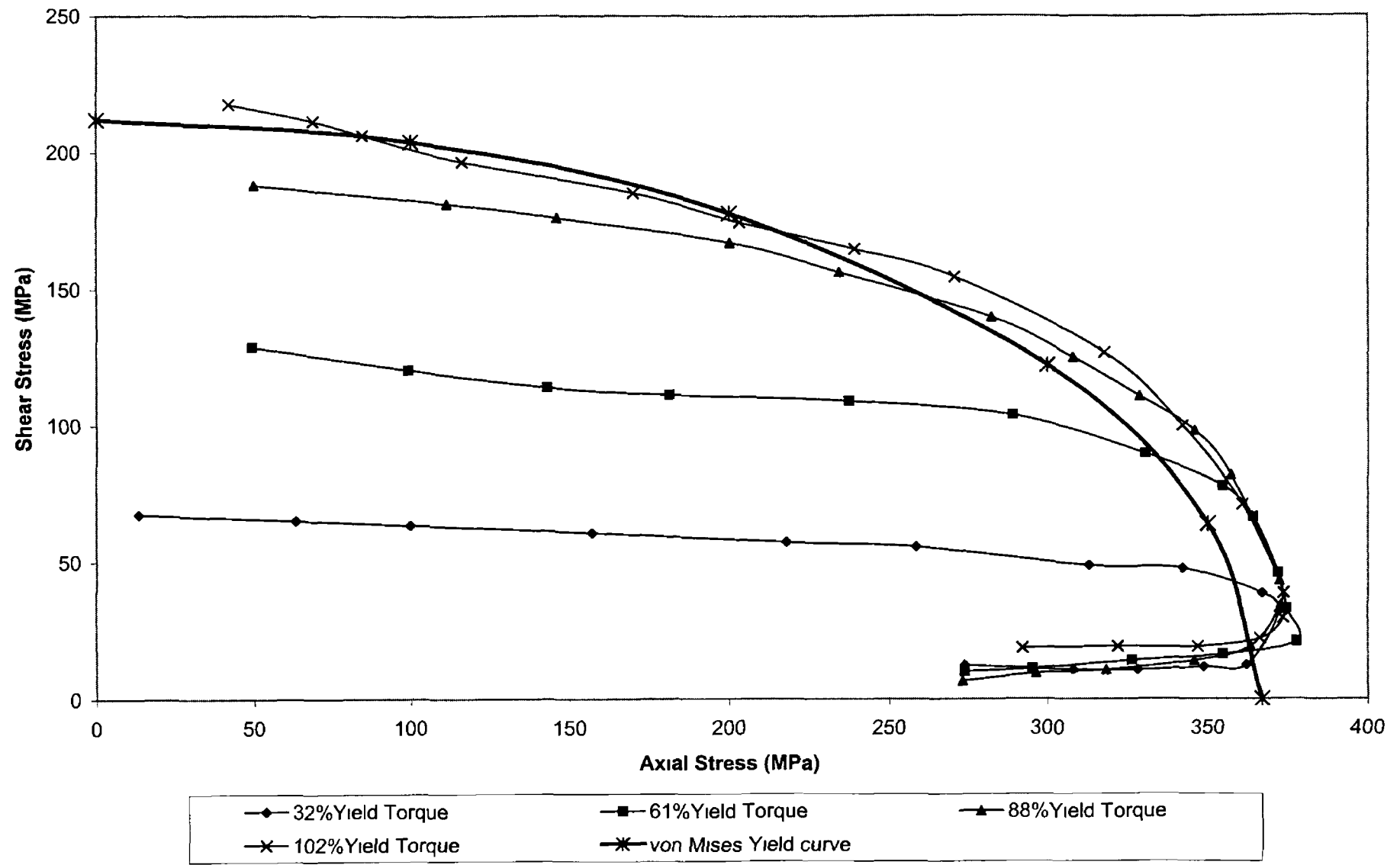
Figure 5 18 Axial Stress - Shear Stress Relationship for Copper Rod (Constant Angle of Twist)
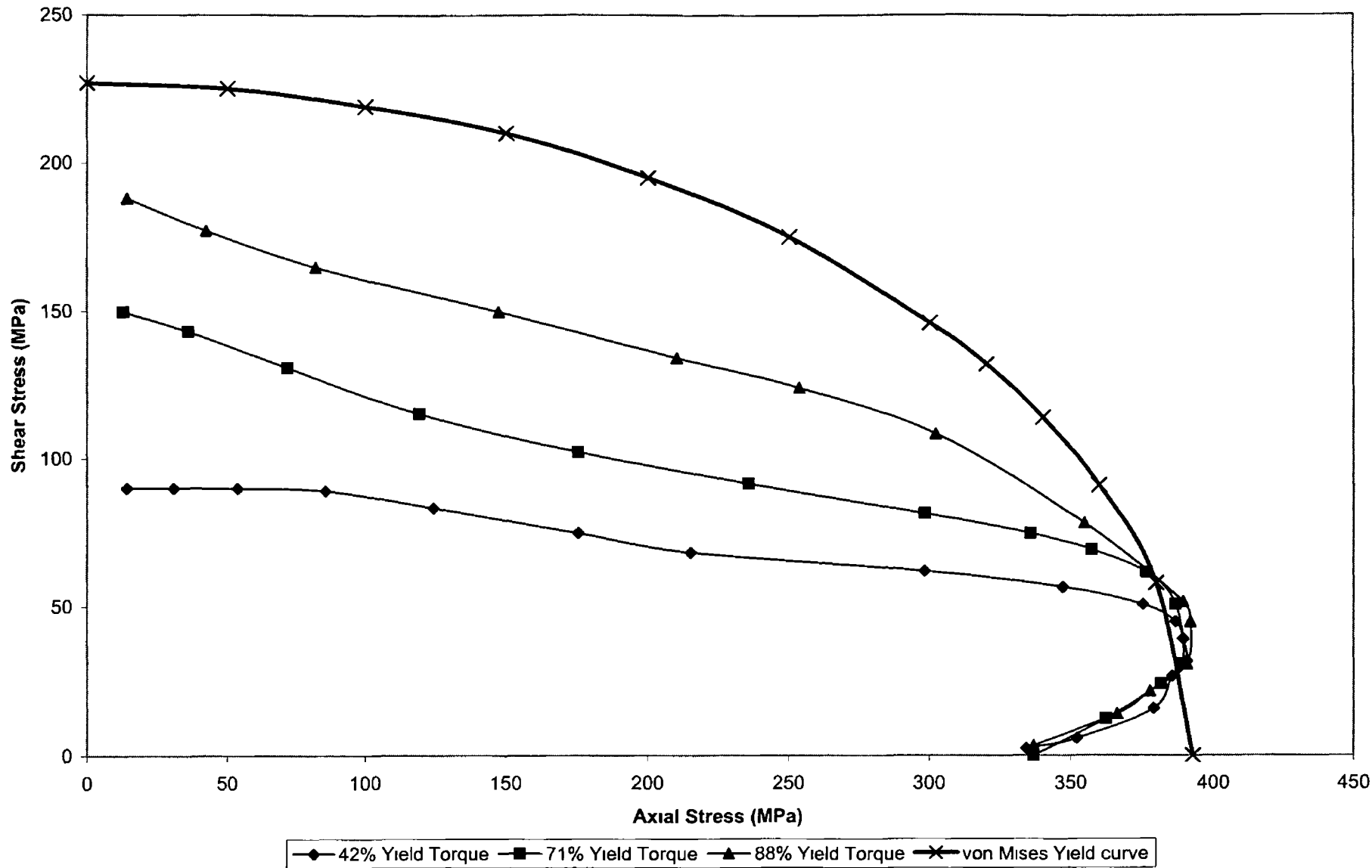
Figure 5 19 Effect of Axial Stress on Shear Stress for Copper Tube (Constant Angle of Twist)
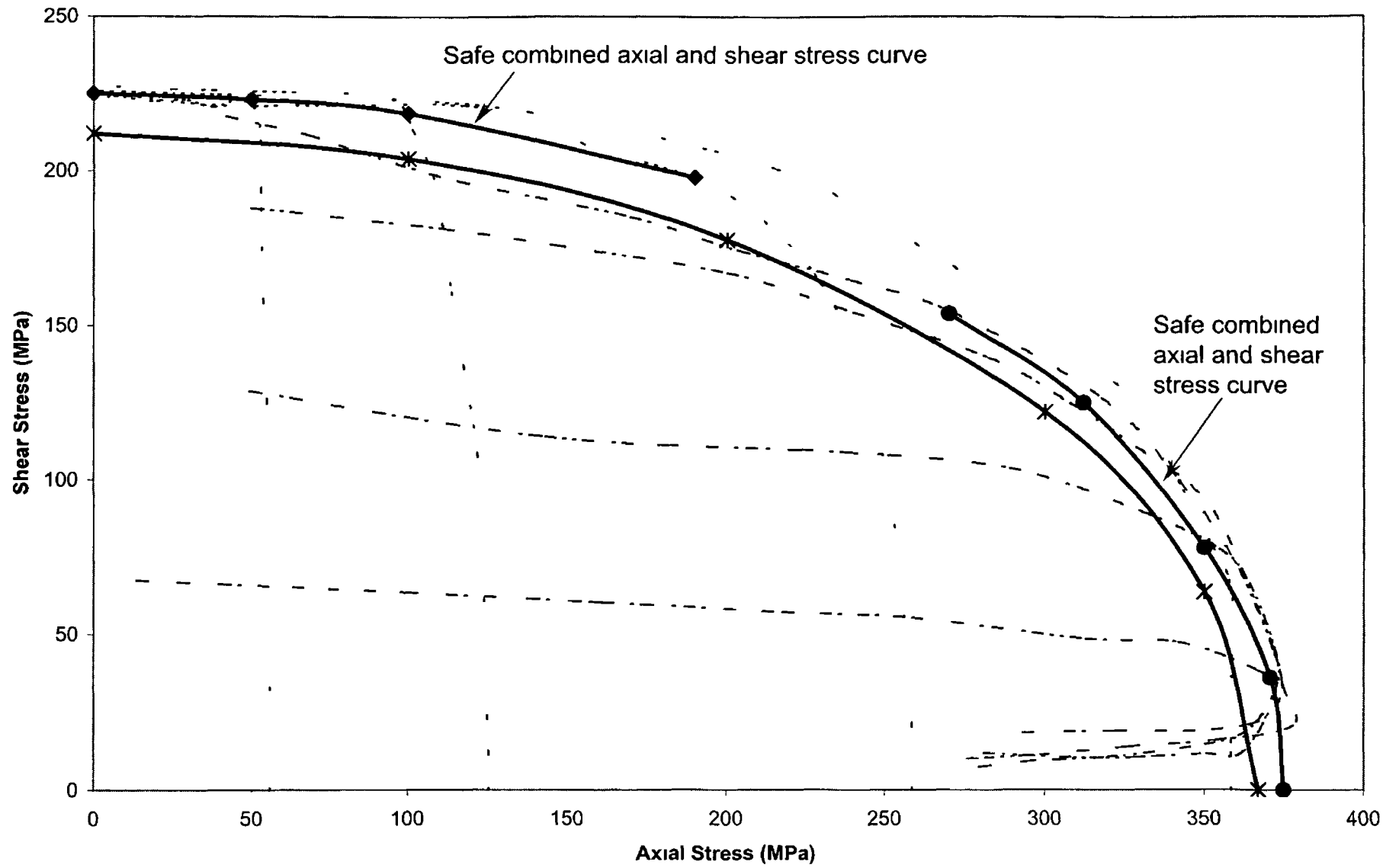
Figure 5 20 Safe Axial Stress & Shear Stress for Copper Rod
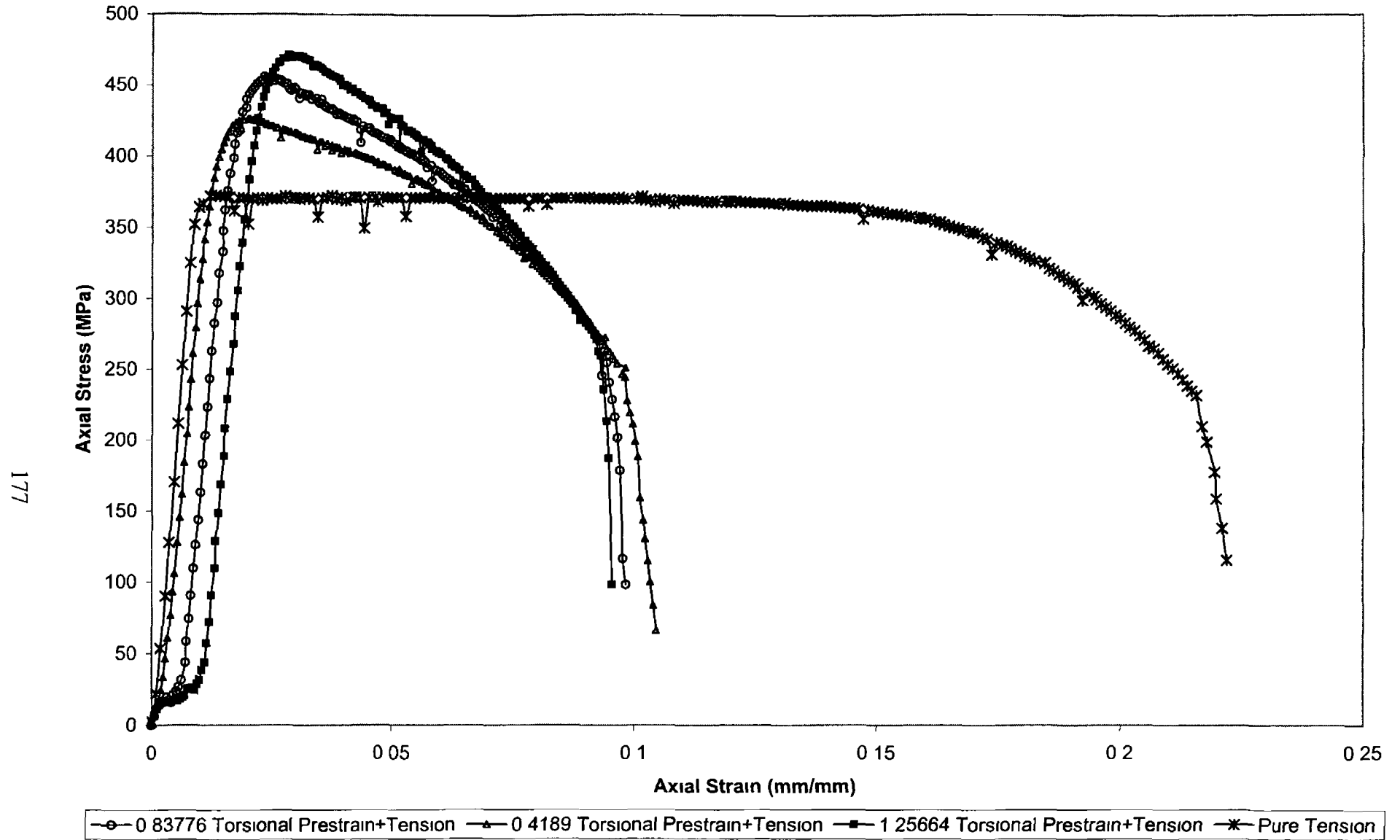
Figure 5 21 Effect of Torsional Prestrain on Strength for Copper Rod
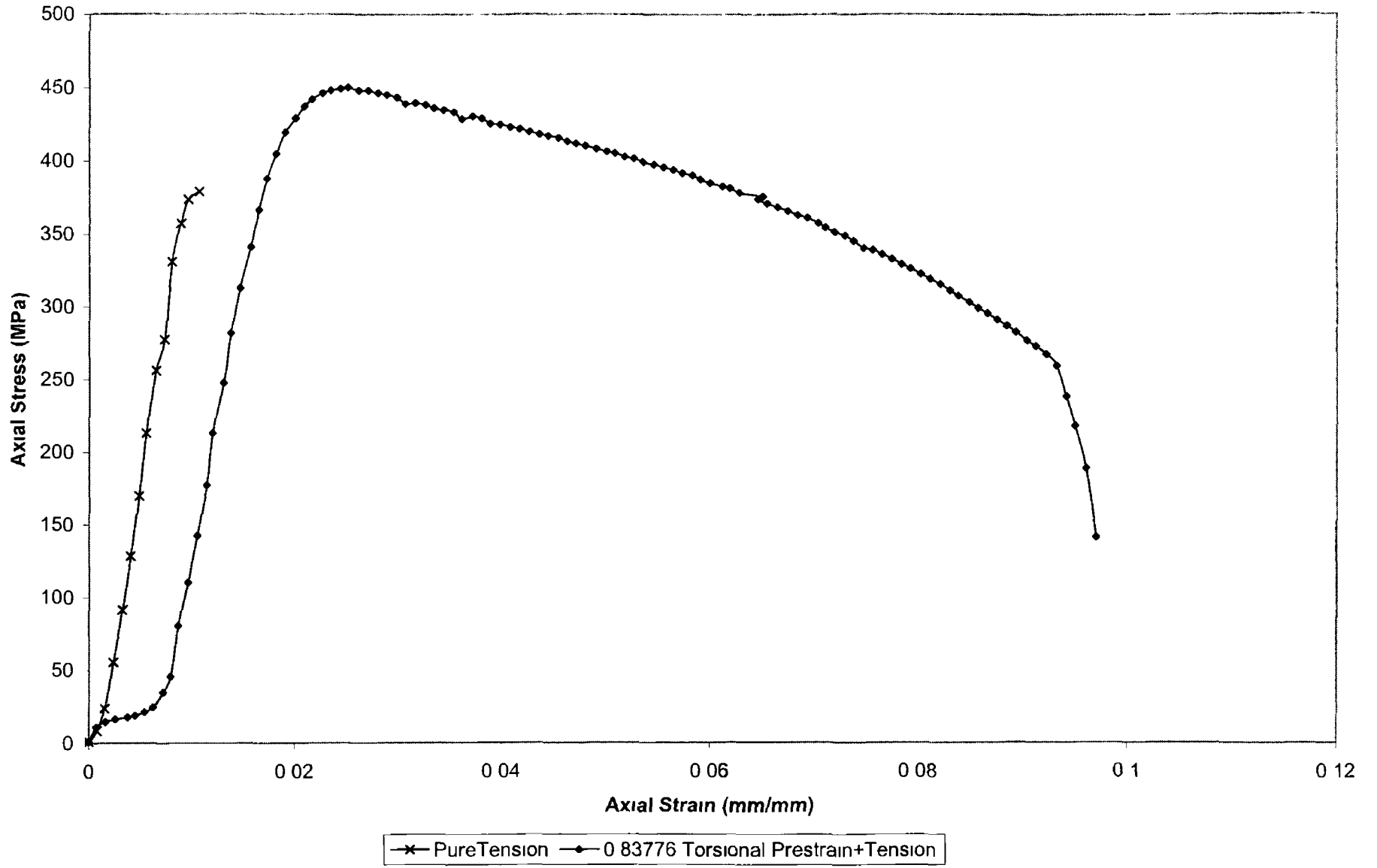
Figure 5 22 Effect of Torsional Prestrain on Elastic Modulus for Copper Rod
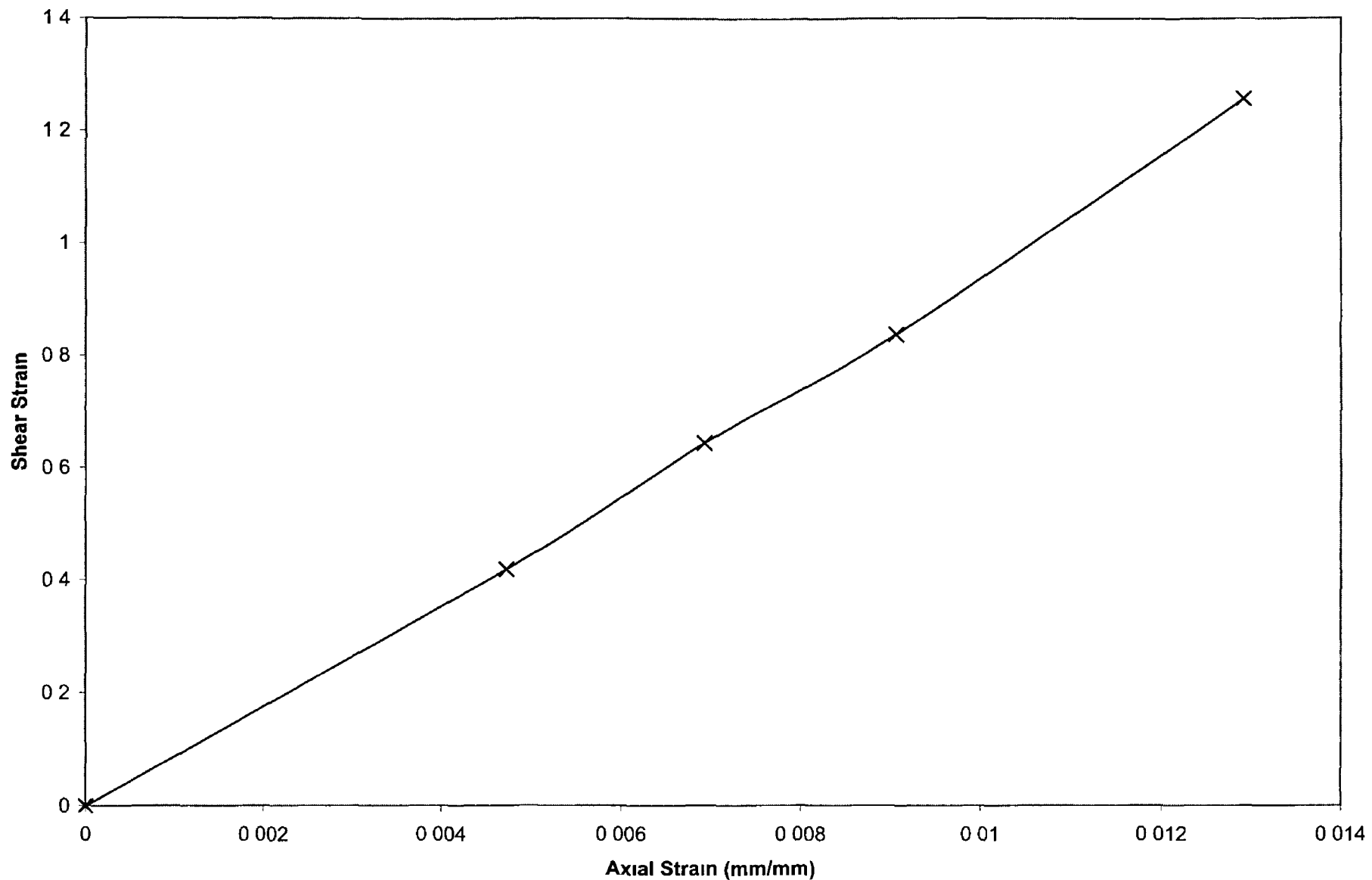
Figure 5 23 Free-end Axial Extension due to Torsion
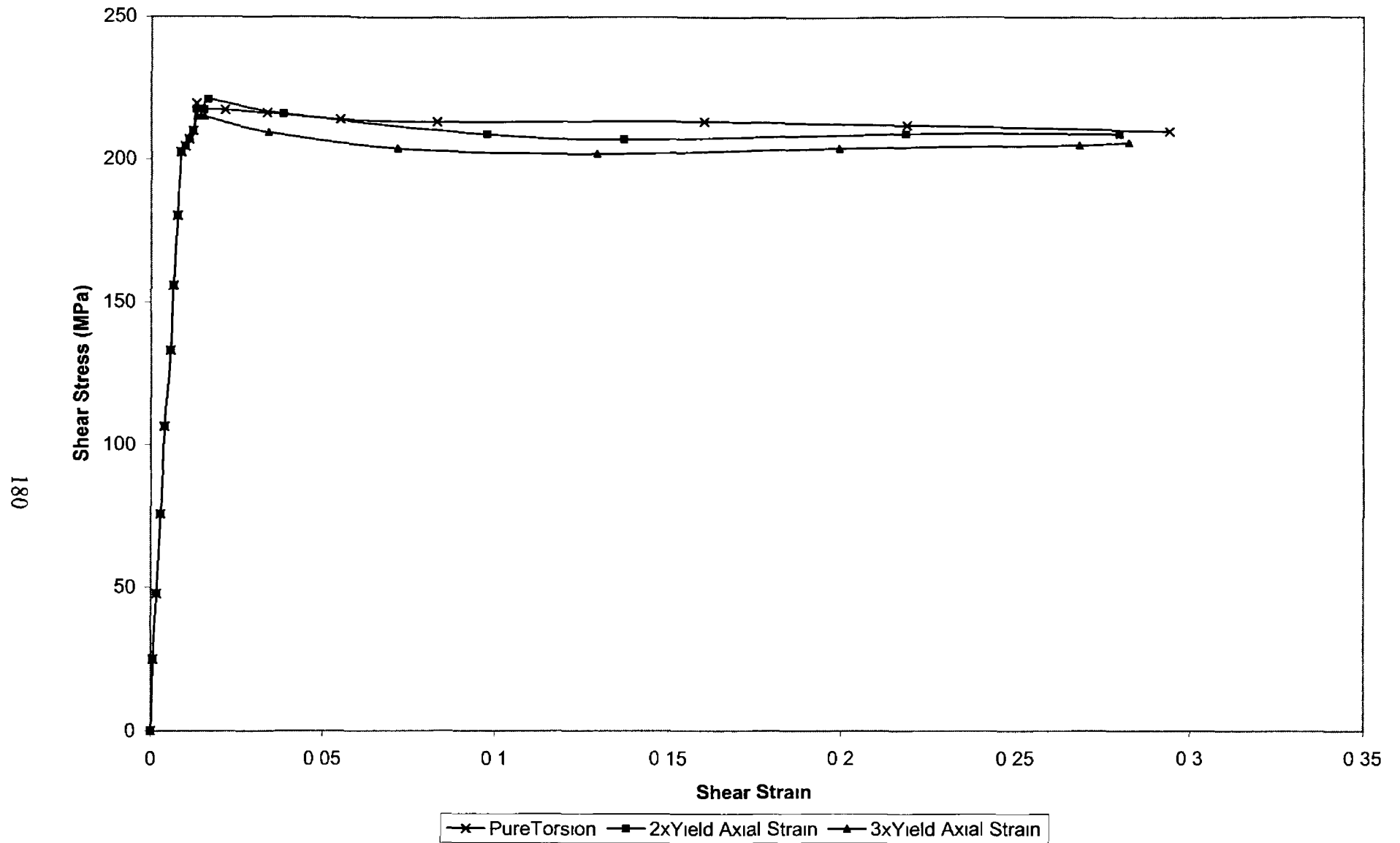
Figure 5 24 Effect of Axial Prestrain on Shear Strength for Copper Rod
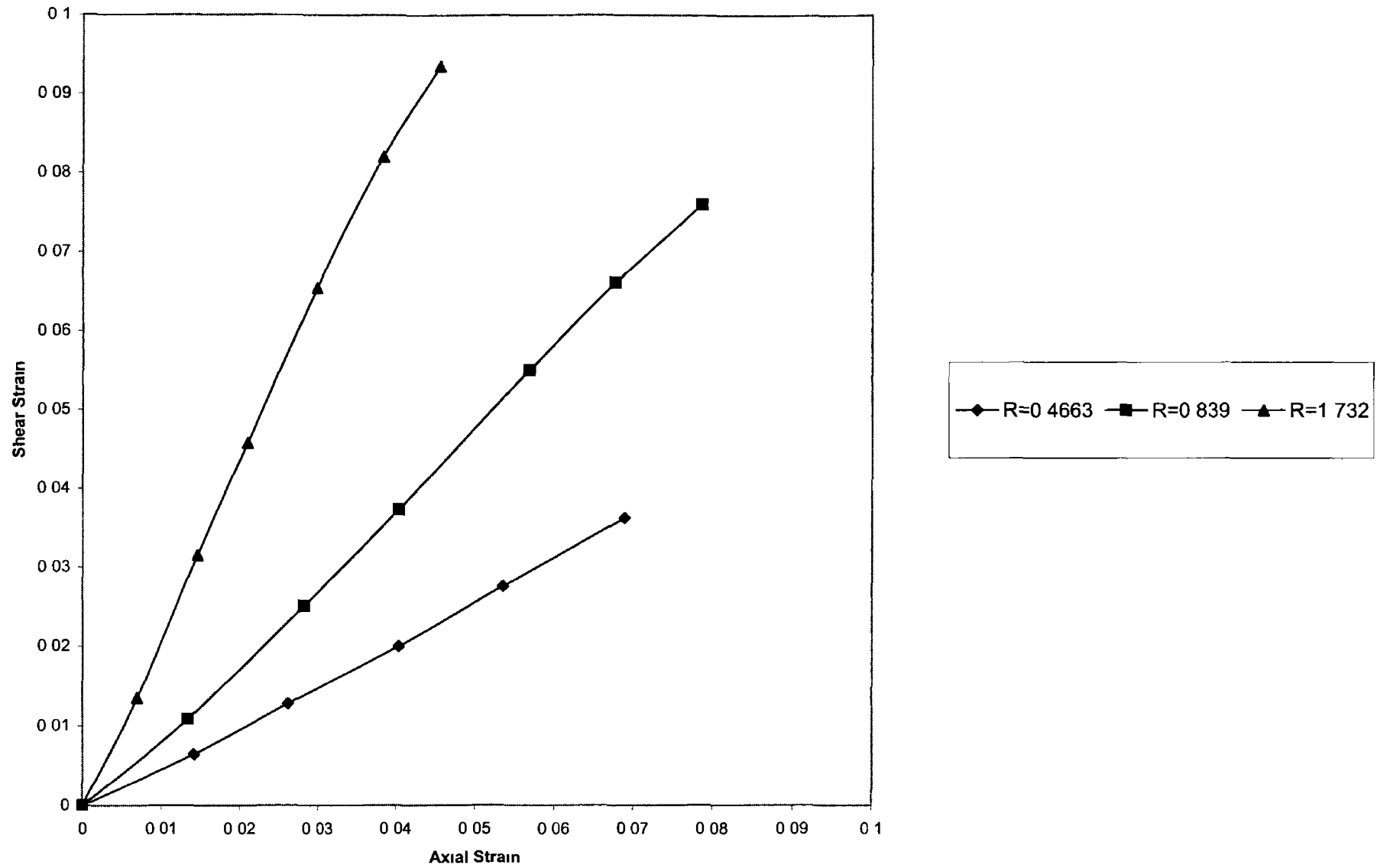
Figure 5 25 Proportional Axial Strain to Shear Strain Relationship (R) for AlSiC MMC Rod
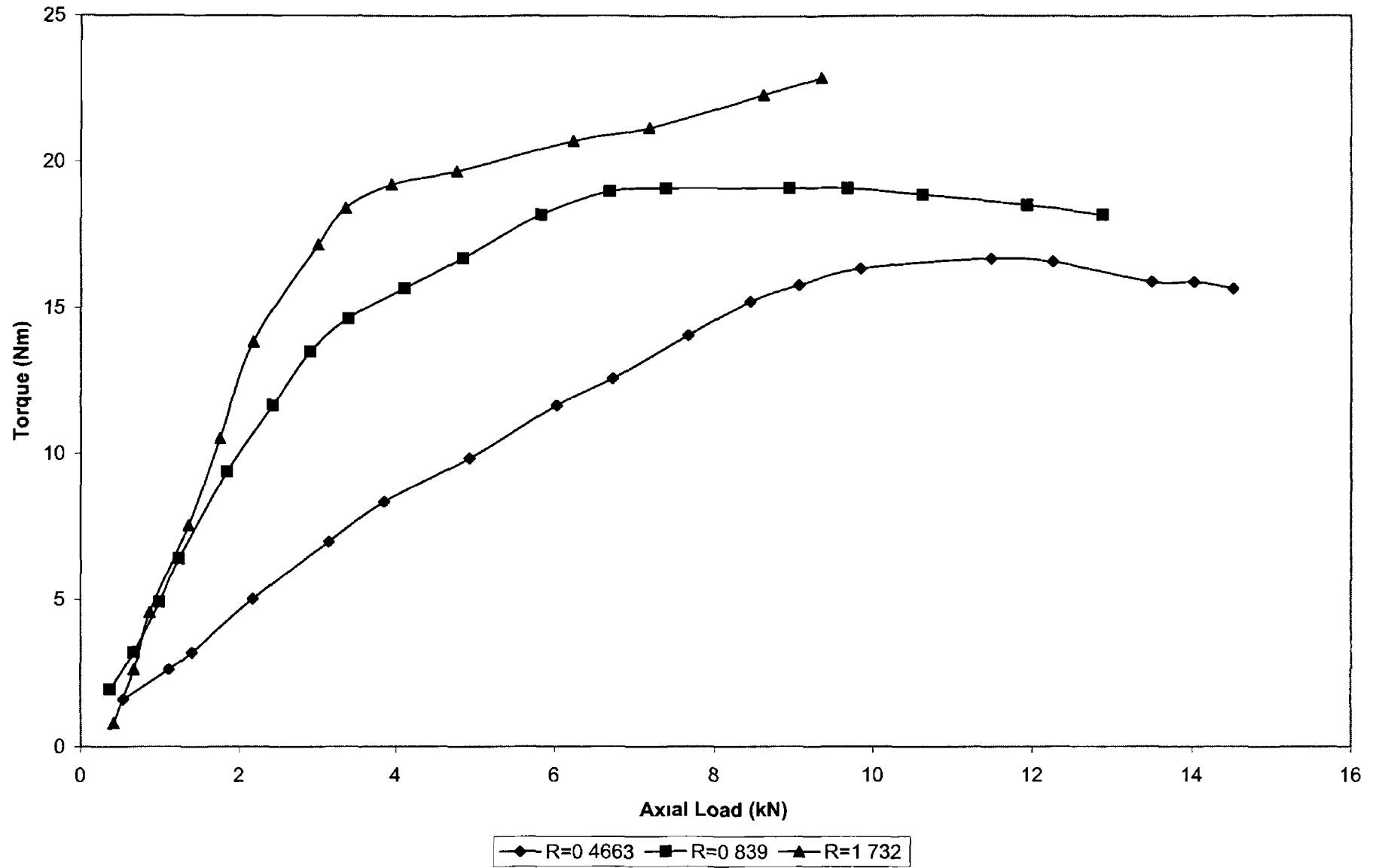
Figure 5 26 Proportional Axial Load-Torque Curve for AlSiC MMC Rod
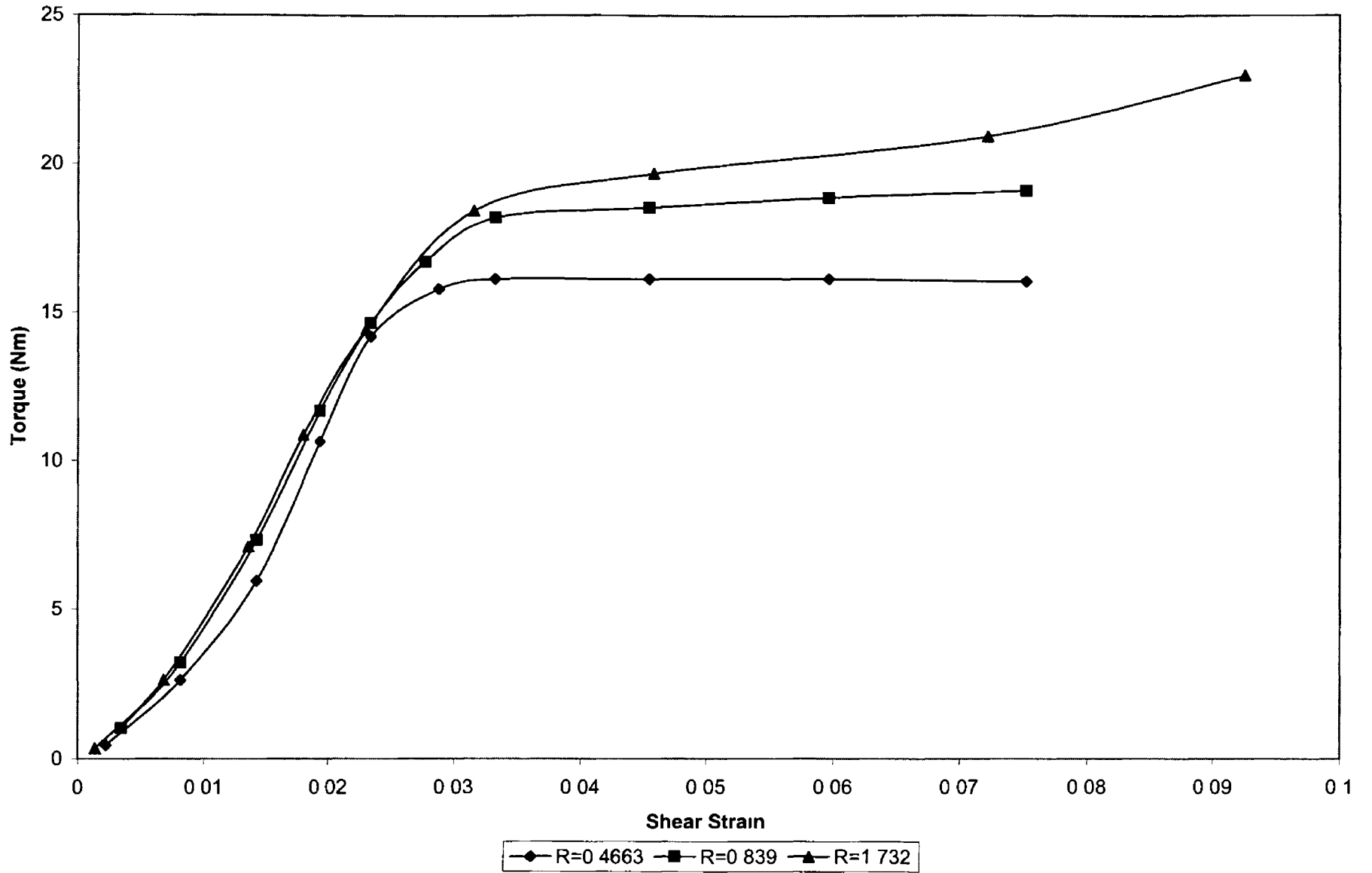
Figure 5 27 Effect of Axial Load on Torque in Proportional Loading for AlSiC MMC Rod

183
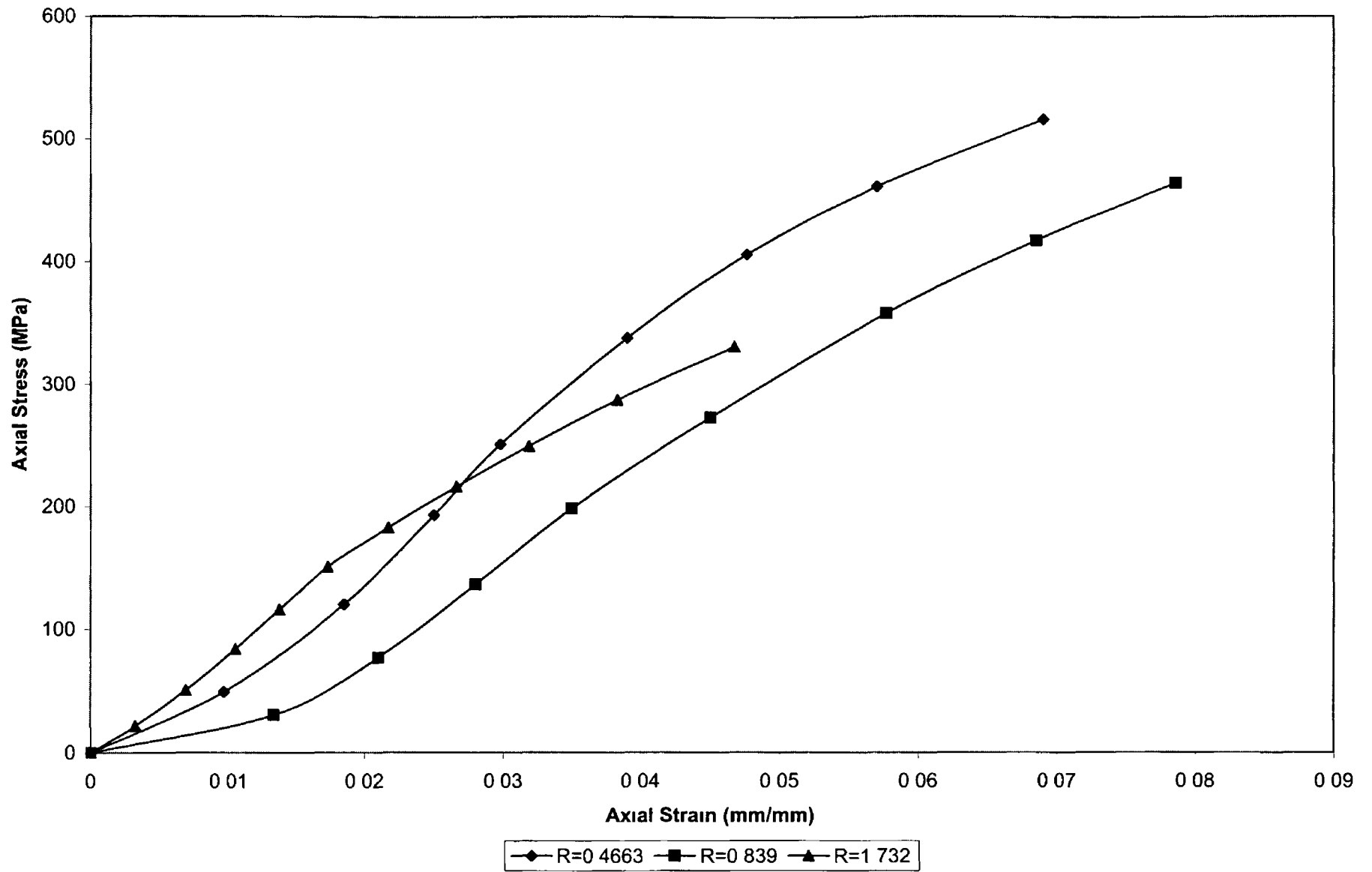
Figure 5 28 Effect of Torque on Axial Stress in Proportional Loading for AlSiC MMC Rod
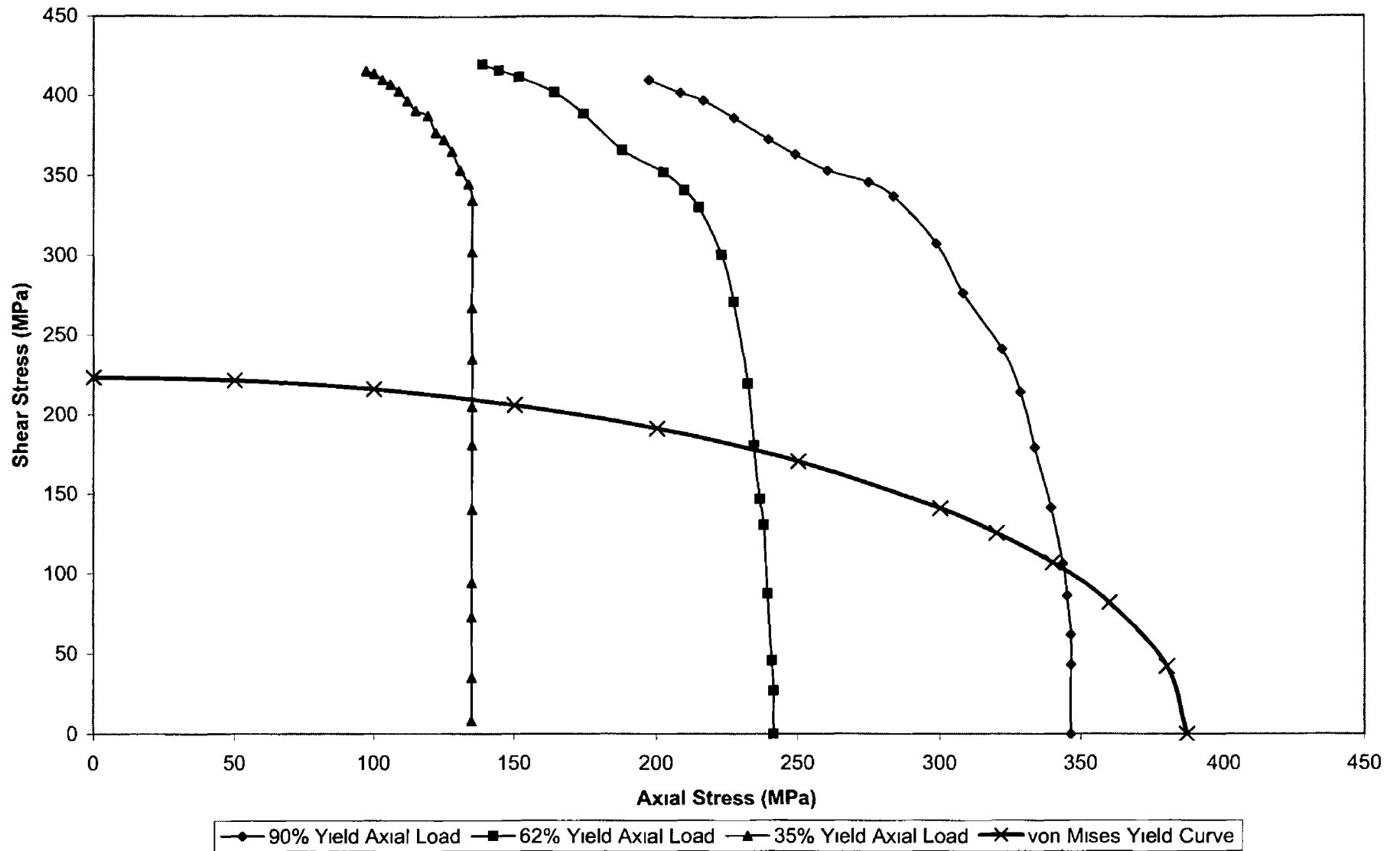
Figure 5 29 Effect of Shear Stress on Axial Stress for AlSiC MMC Rod
(Constant Axial Displacement)
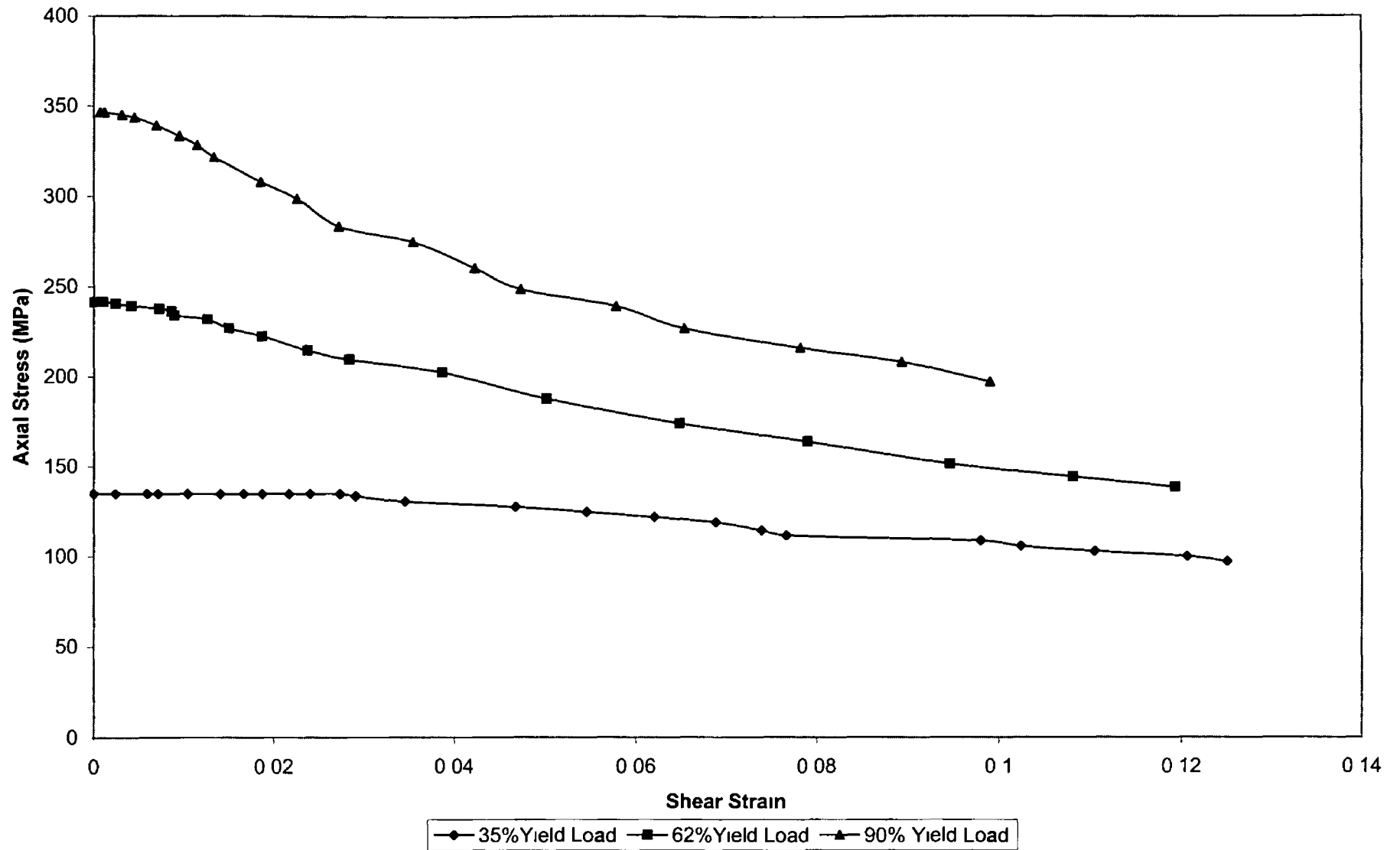
Figure 5 30 Effect of Shear Strain on Axial Stress for AlSiC MMC Rod
(Constant Axial Displacement)
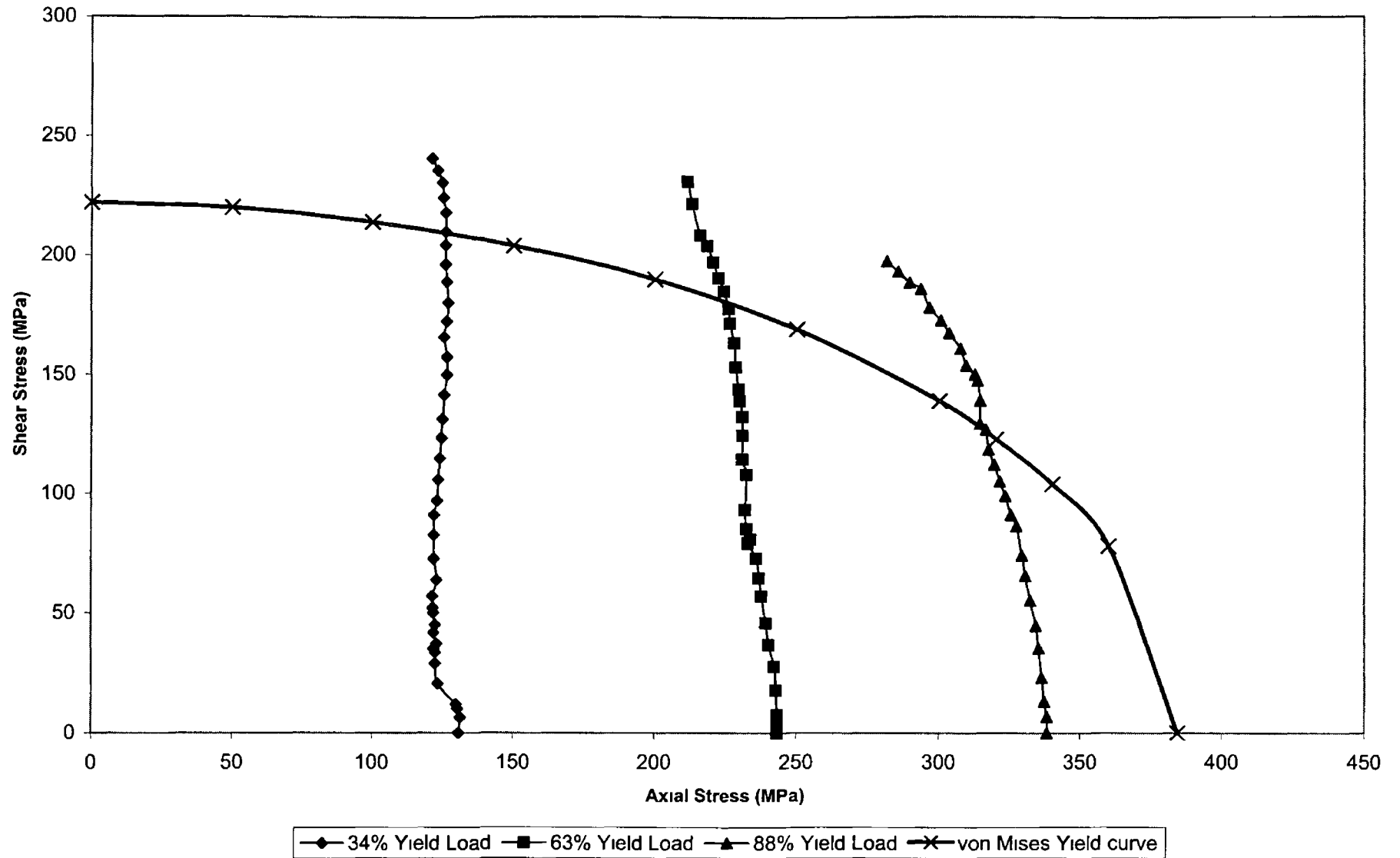
**Figure 5 31 Effect of Shear Stress on Axial Stress for AlSiC MMC Tube
(Constant Axial Displacement)**
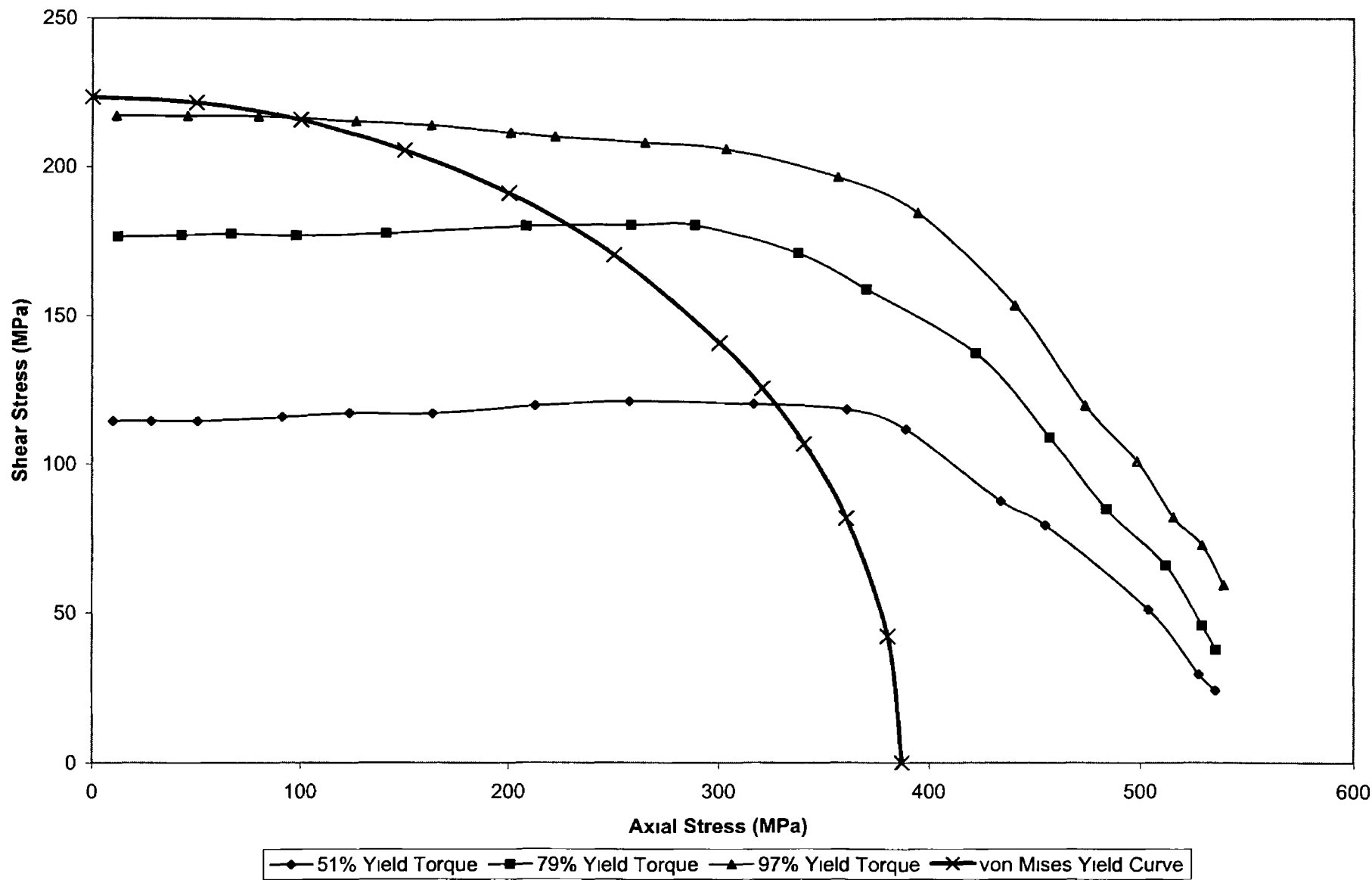
Figure 5 32 Effect of Axial Stress on Shear Stress for MMC Rod (Constant Angle of Twist)
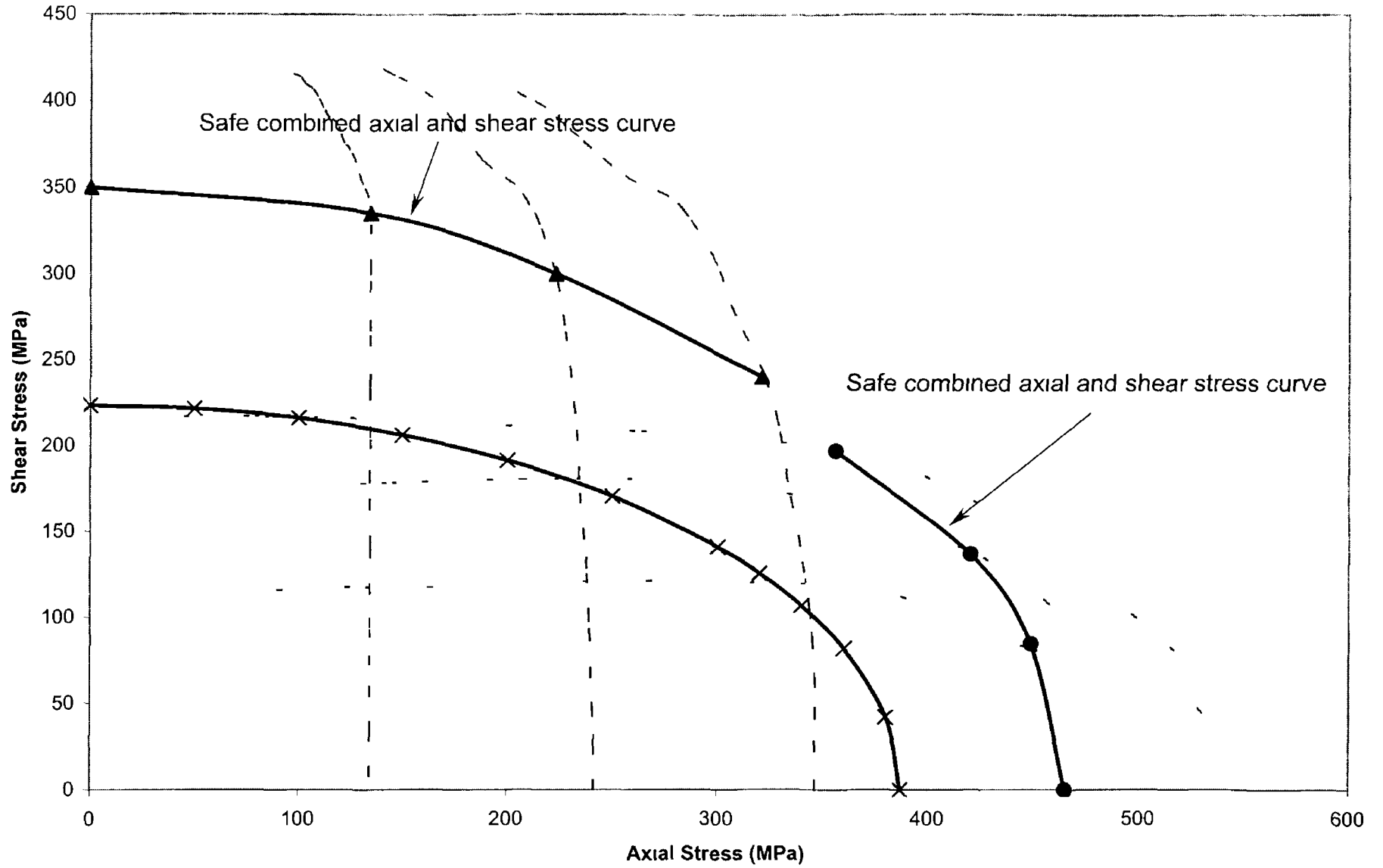
Figure 5 33 Safe Axial stress & Shear stress for AlSiC MMC Rod
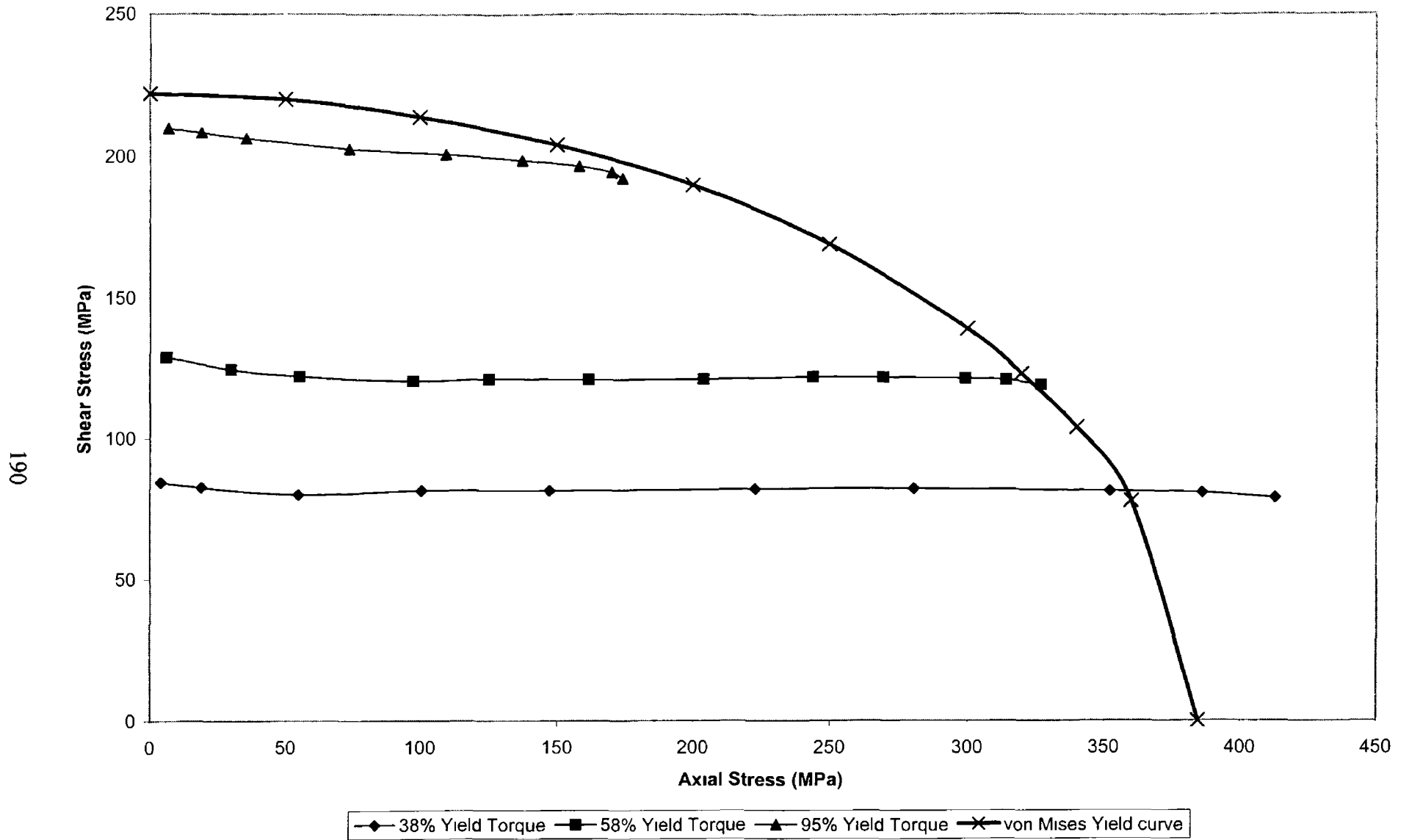
Figure 5 34 Effect of Axial Stress on Shear Stress for AlSiC MMC Tube (Constant Angle of Twist)

191
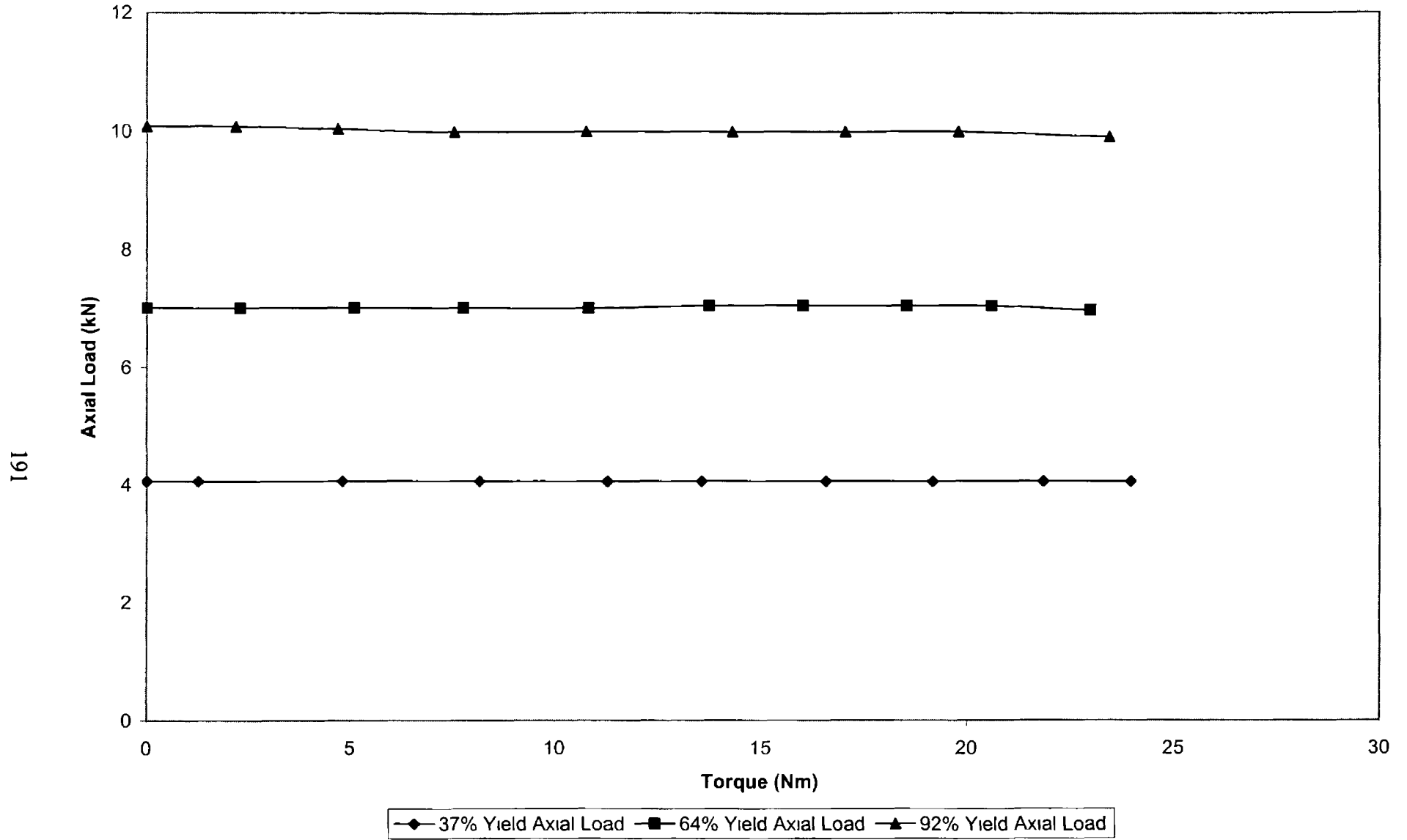
Figure 5 35 Axial load-Torque Curve for AlSiC MMC Rod (Constant Axial Load)
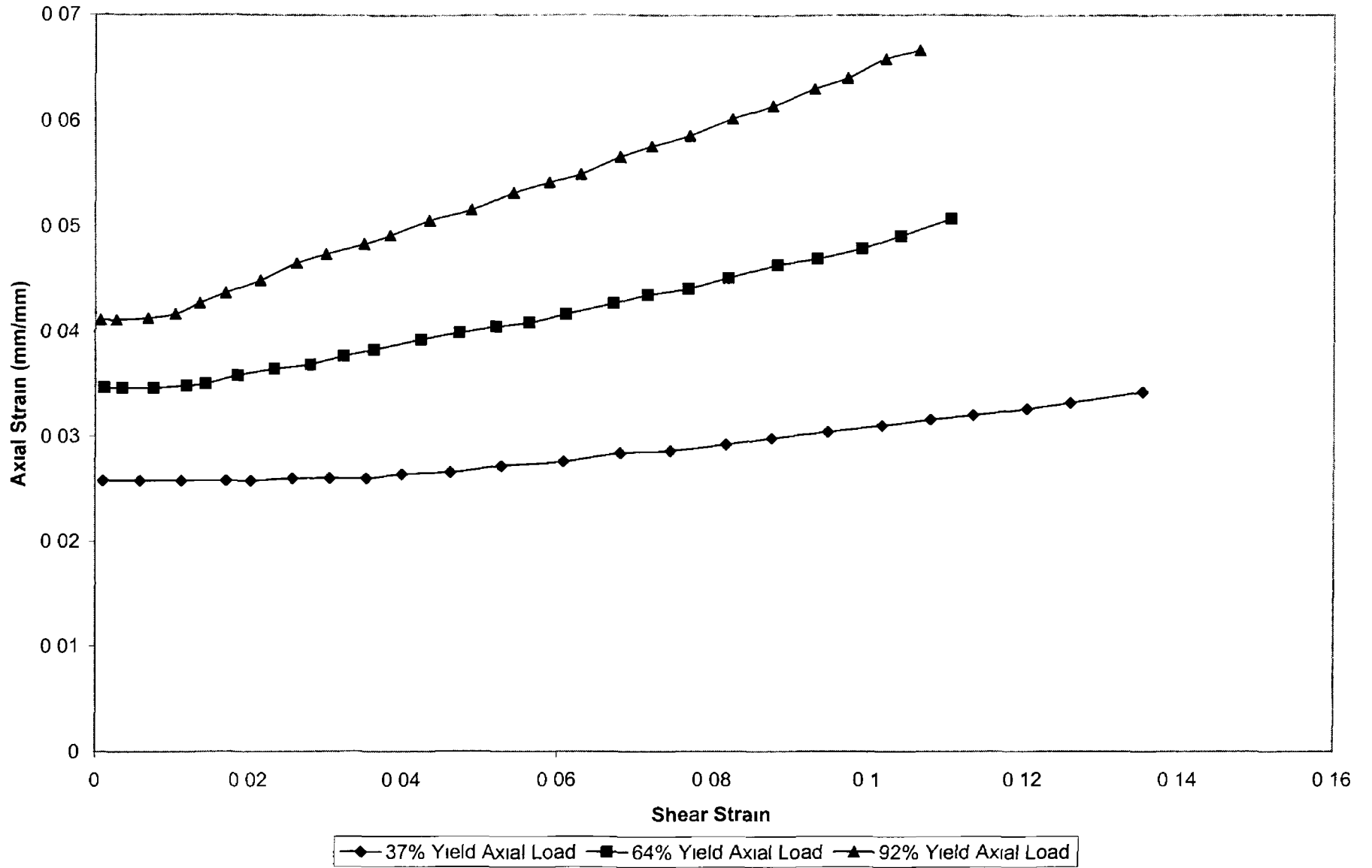
Figure 5 36 Axial-Shear Strain Relationship for AlSiC MMC Rod (Constant Axial Load)
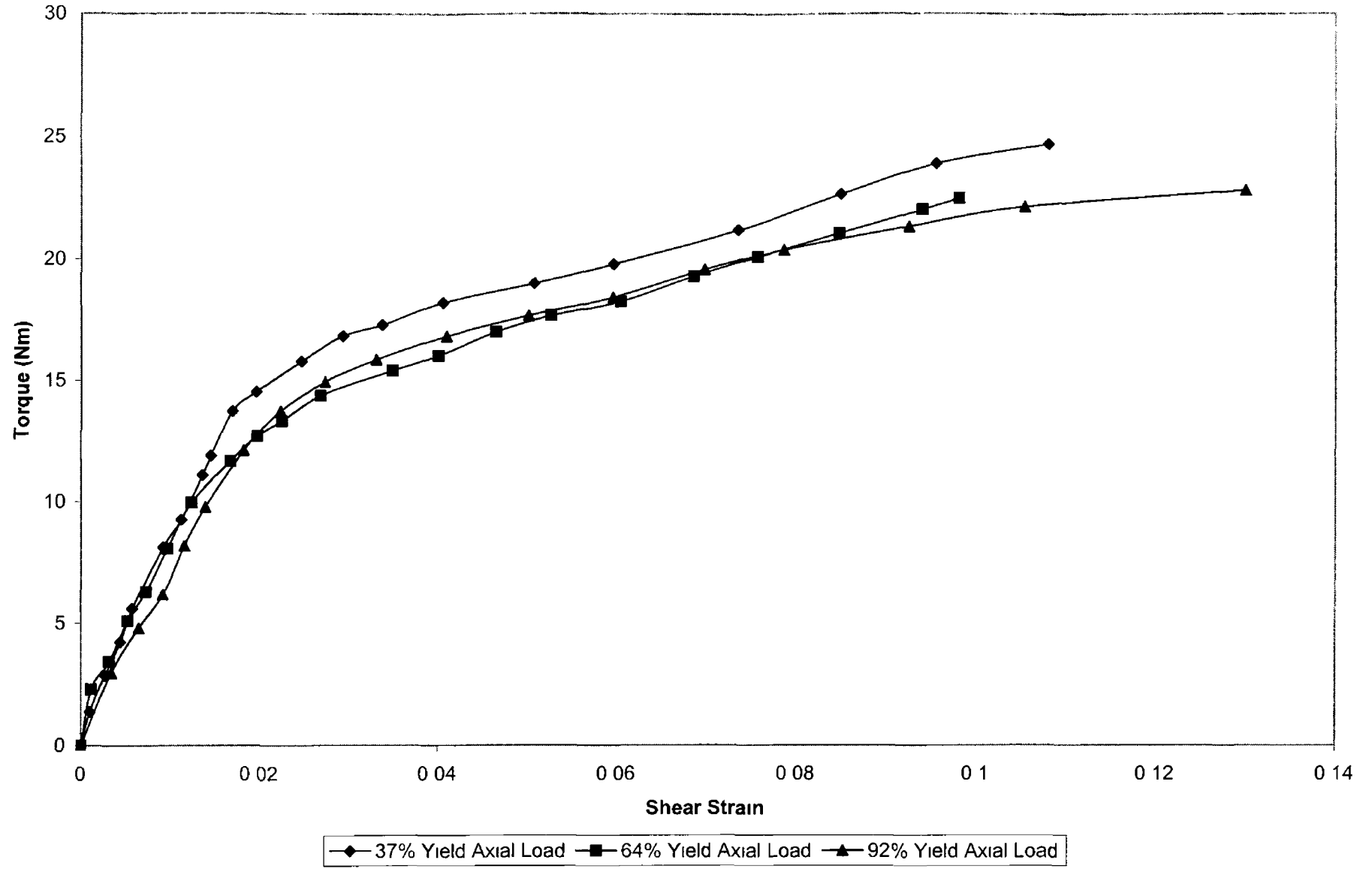
Figure 5 37 Torque-Shear Strain Relationship for AlSiC MMC Rod (Constant Axial Load)
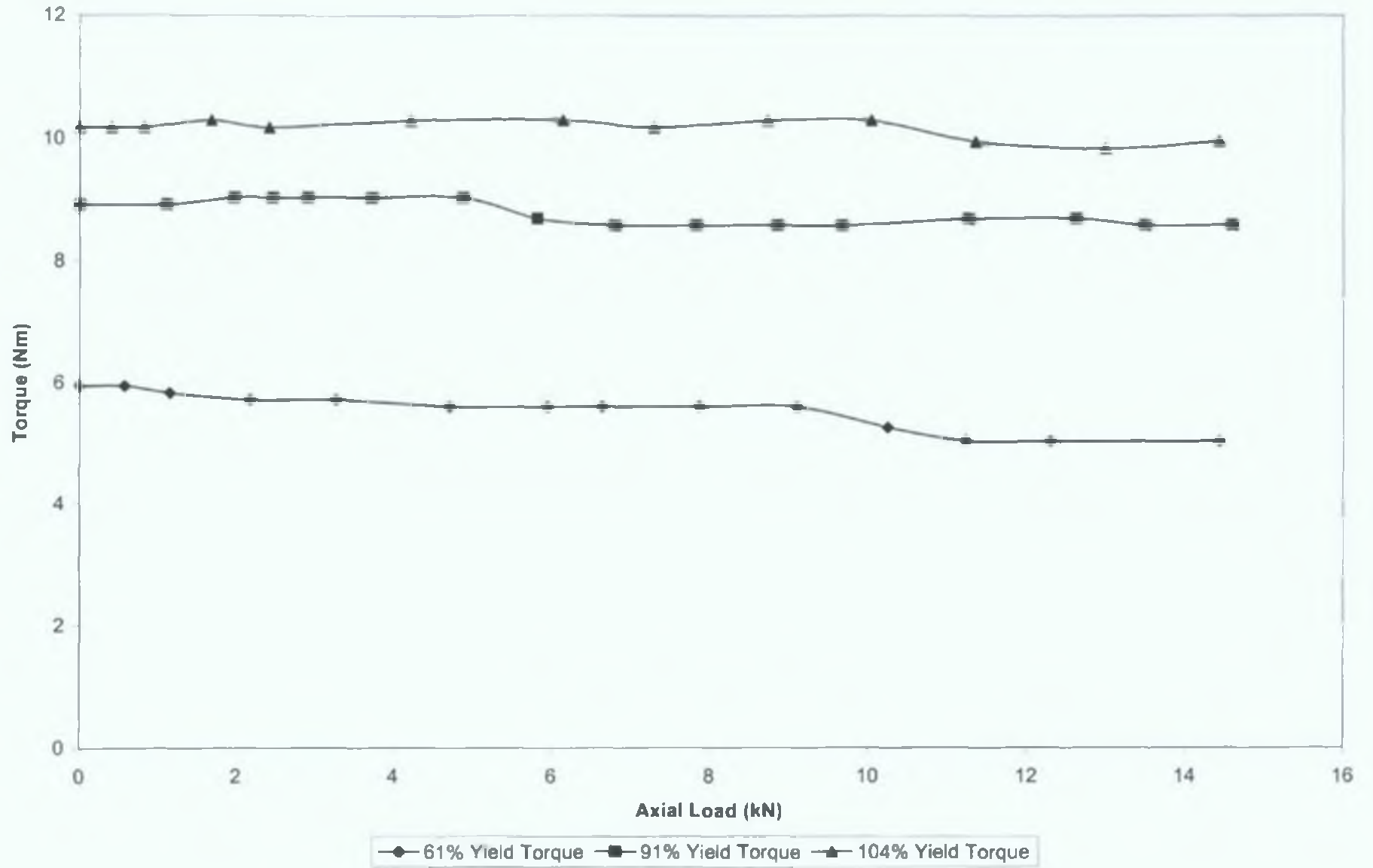
Figure 5.38. Axial Load-Torque Curve for AlSiC MMC Rod (Constant Torque)
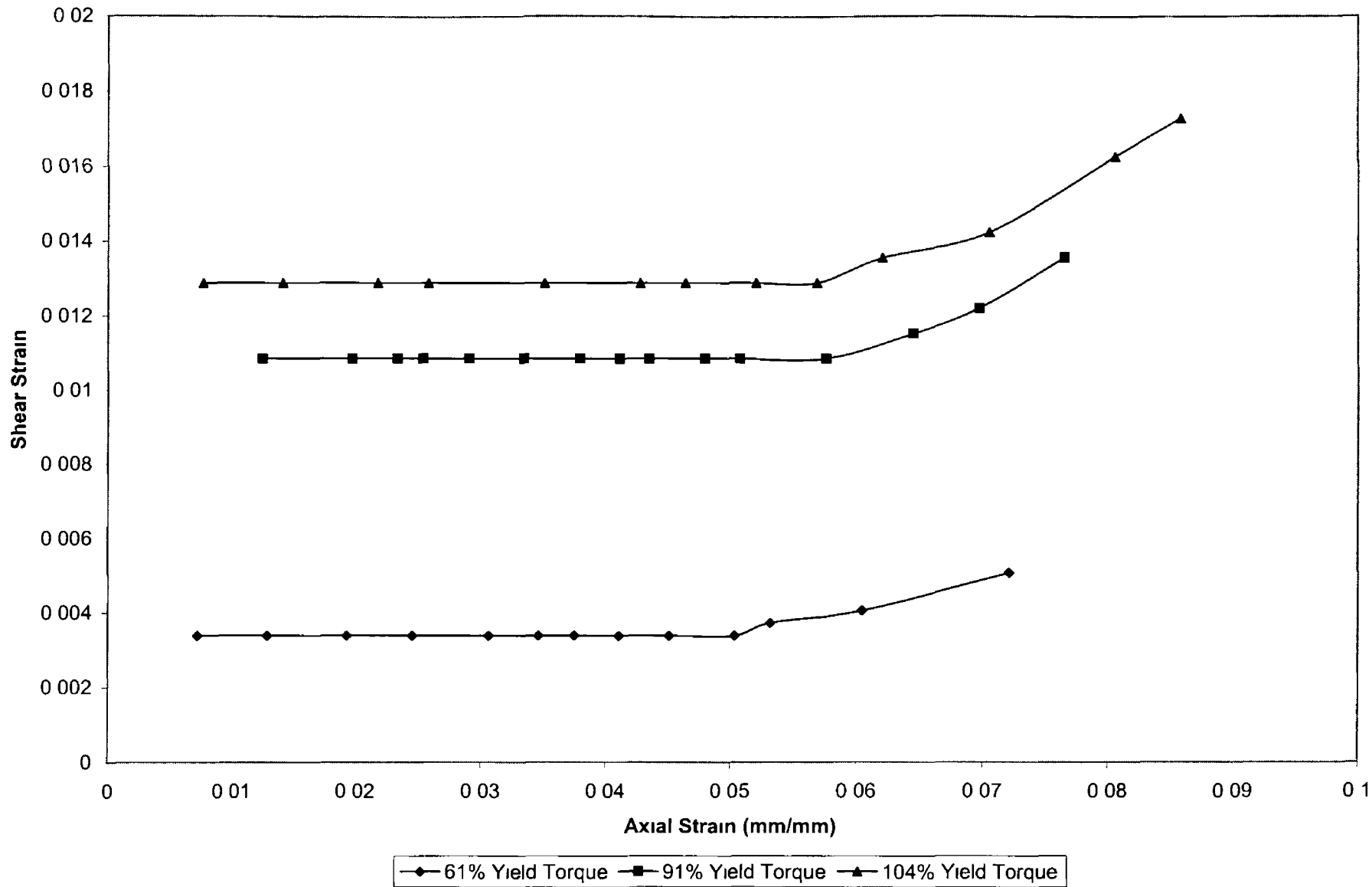
Figure 5 39 Axial Strain-Shear Strain Relationship for AlSiC MMC Rod (Constant Torque)
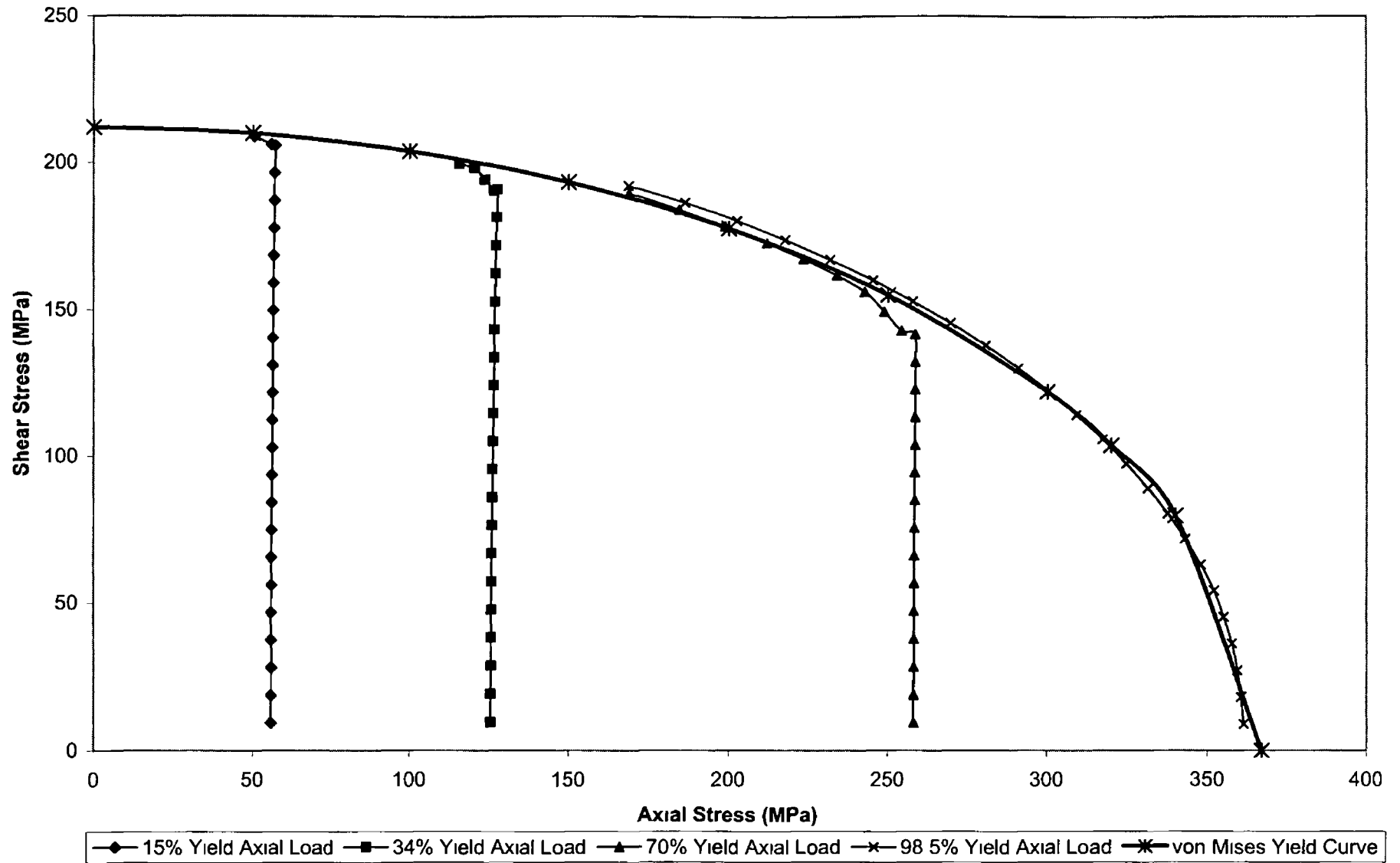
Figure 5 41 Axial Stress-Shear Stress Relationship from FEA Analysis for Copper Rod
(Constant Axial Displacement)
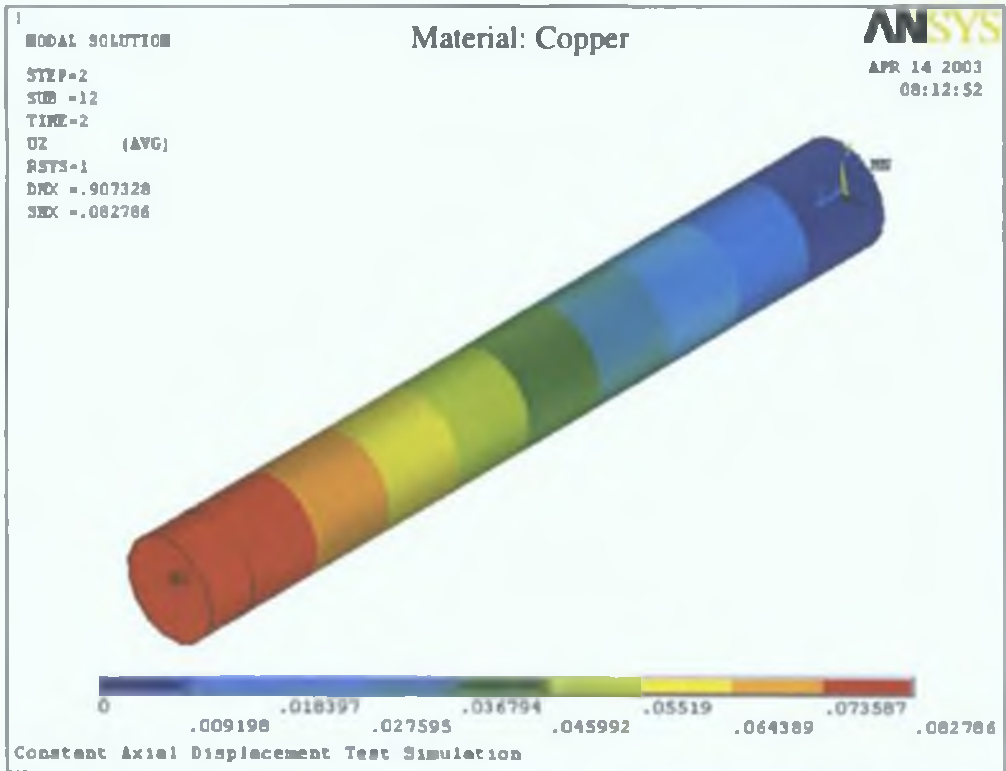
Figure 5.42 Axial Displacement at the end of Simulation (Constant Axial Displacement Test)
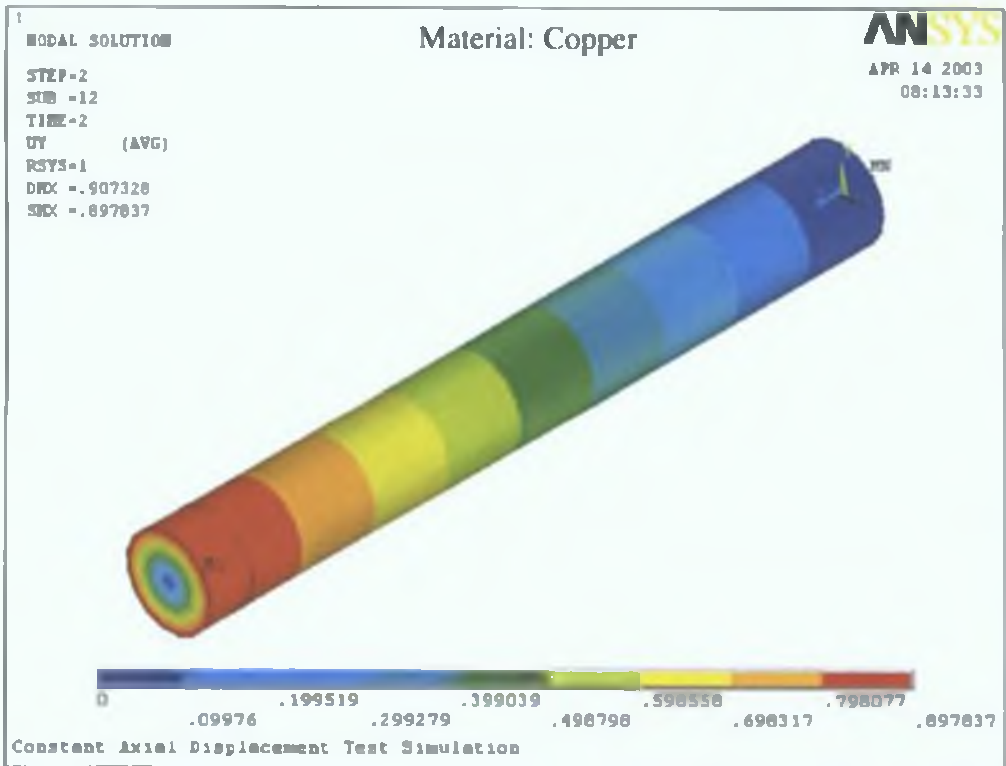
Figure 5.43 Angle of Twist at the end of Simulation (Constant Axial Displacement Test)
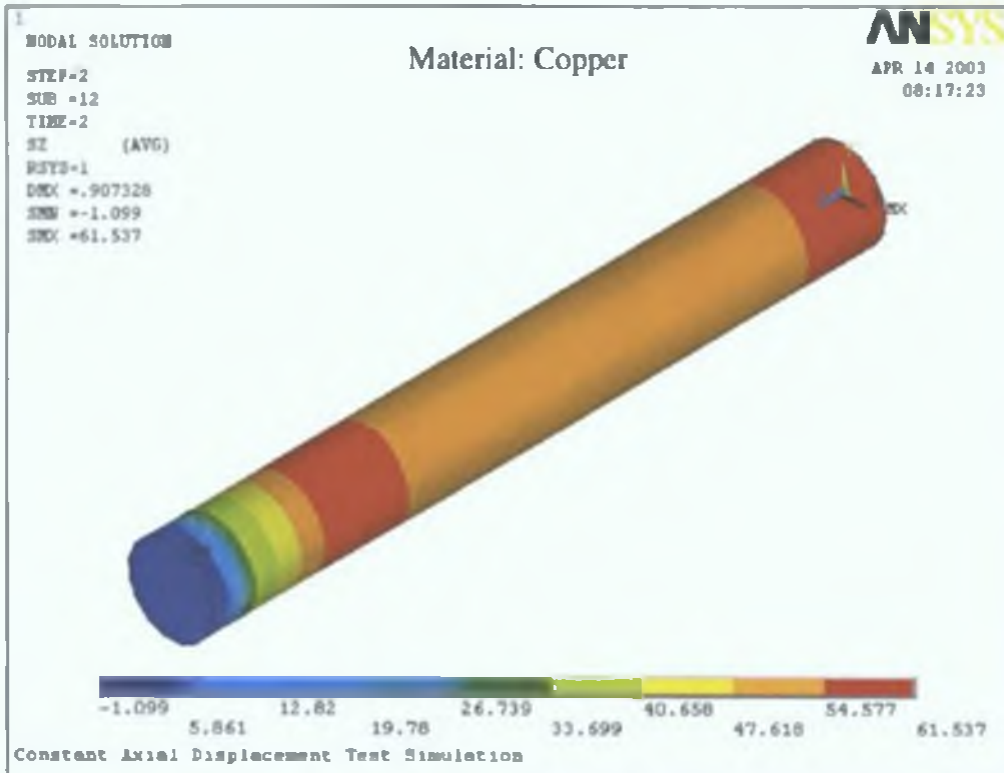
Figure 5.44 Axial Stress at the end of Simulation (Constant Axial Displacement Test)
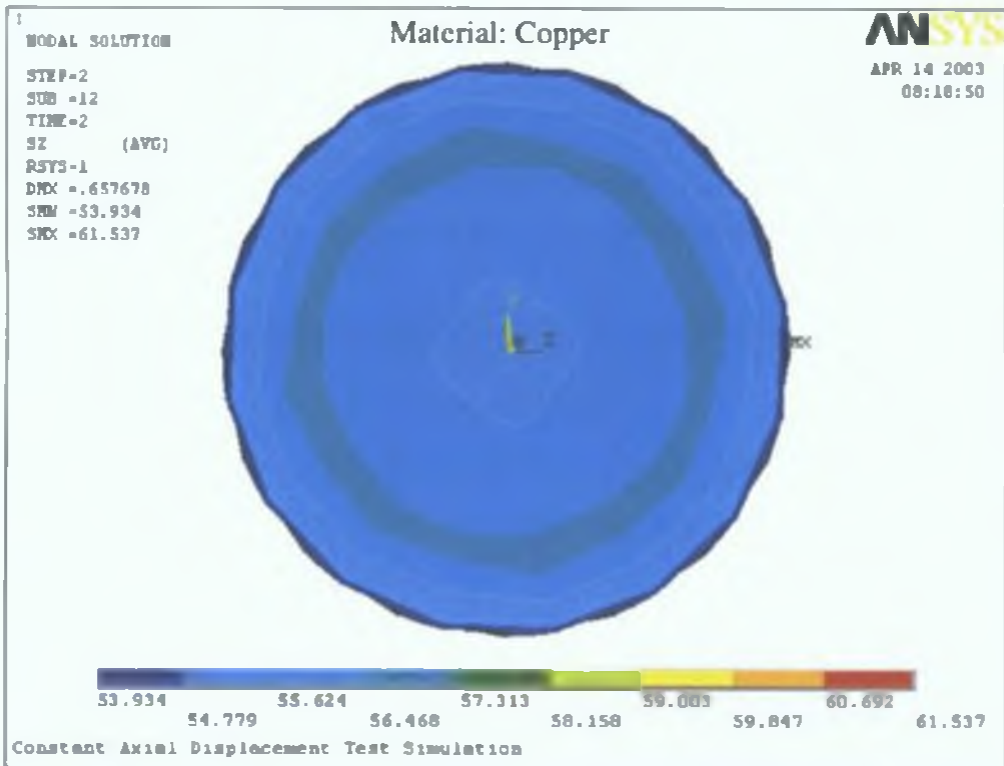
Figure 5.45 Axial Stress distribution across the Model (Constant Axial Displacement Test)
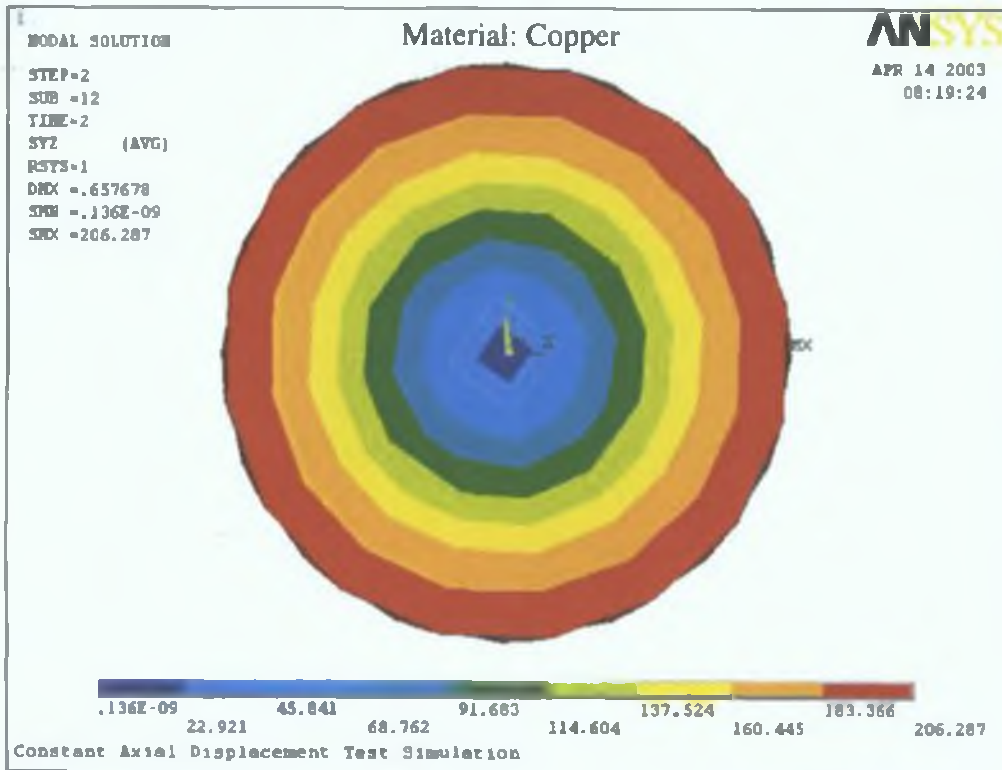
Figure 5.46 Shear Stress distribution across the Model (Constant Axial Displacement Test)
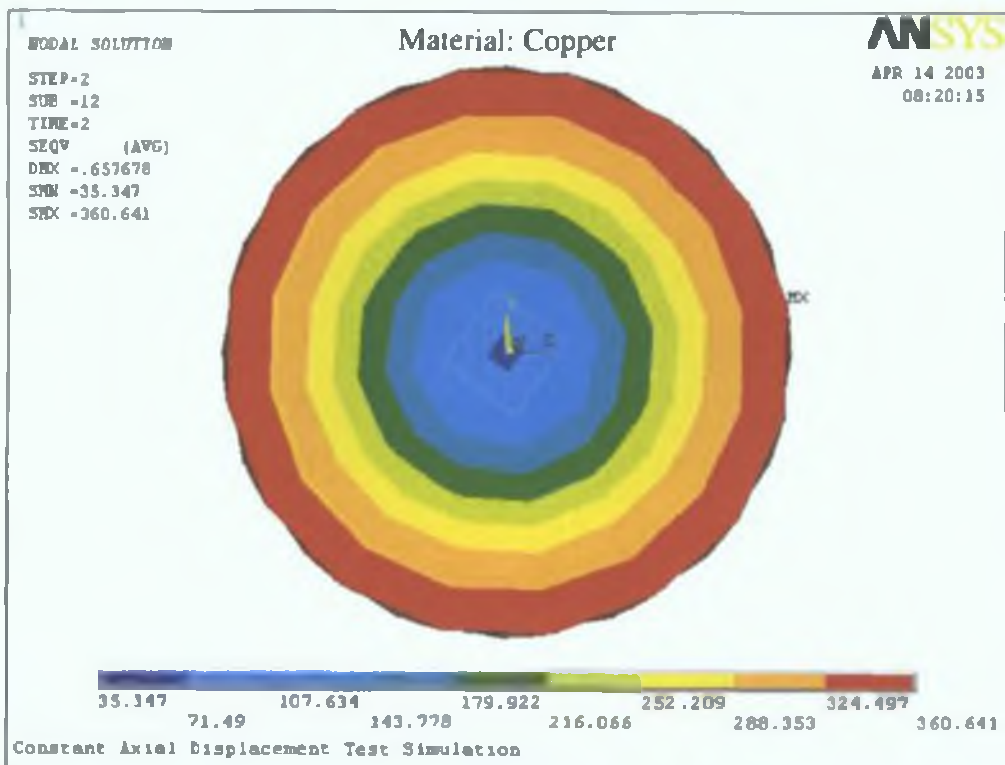
Figure 5.47 von Mises Equivalent Stress distribution across the Model

(Constant Axial Displacement Test)
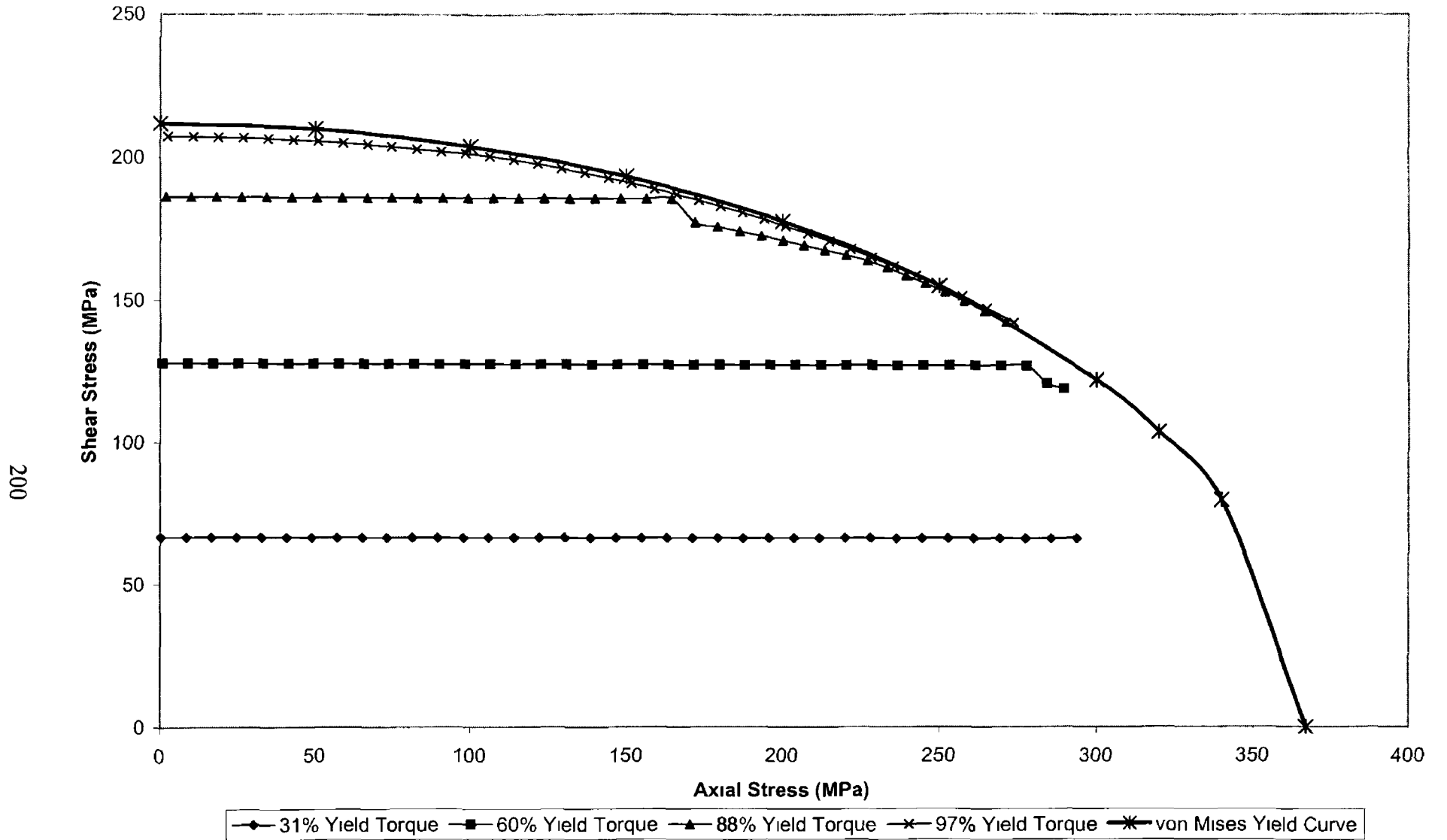
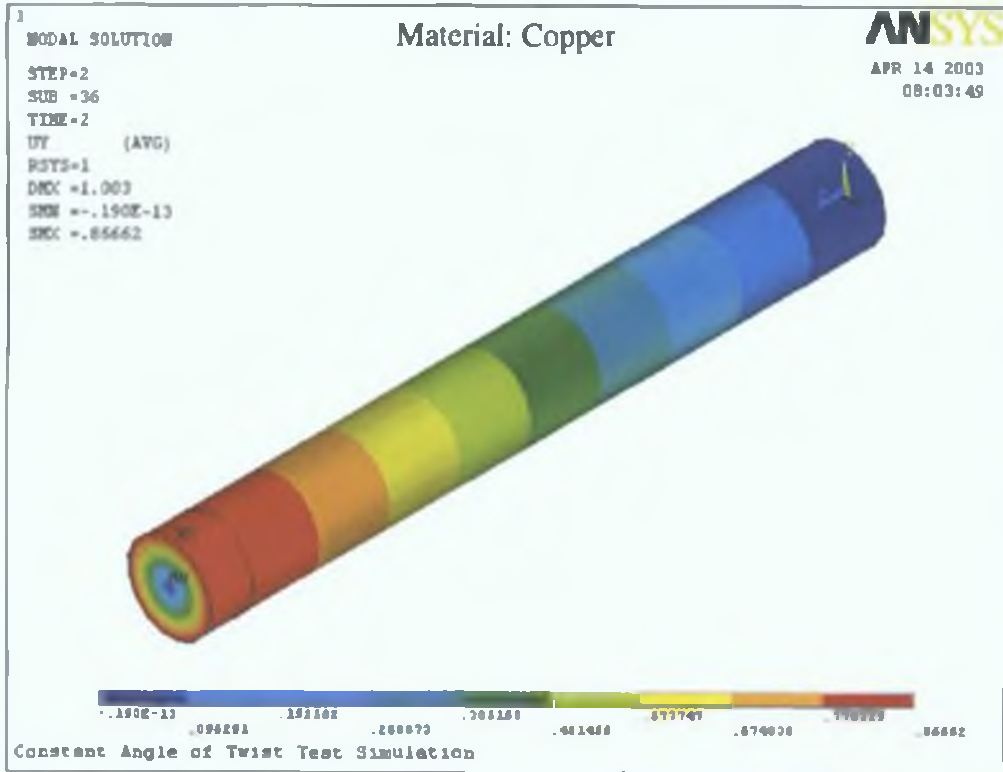Figure 5 48 Axial Stress-Shear Stress Relationship from FEA Analysis for Copper Rod
(Constant Angle of Twist)

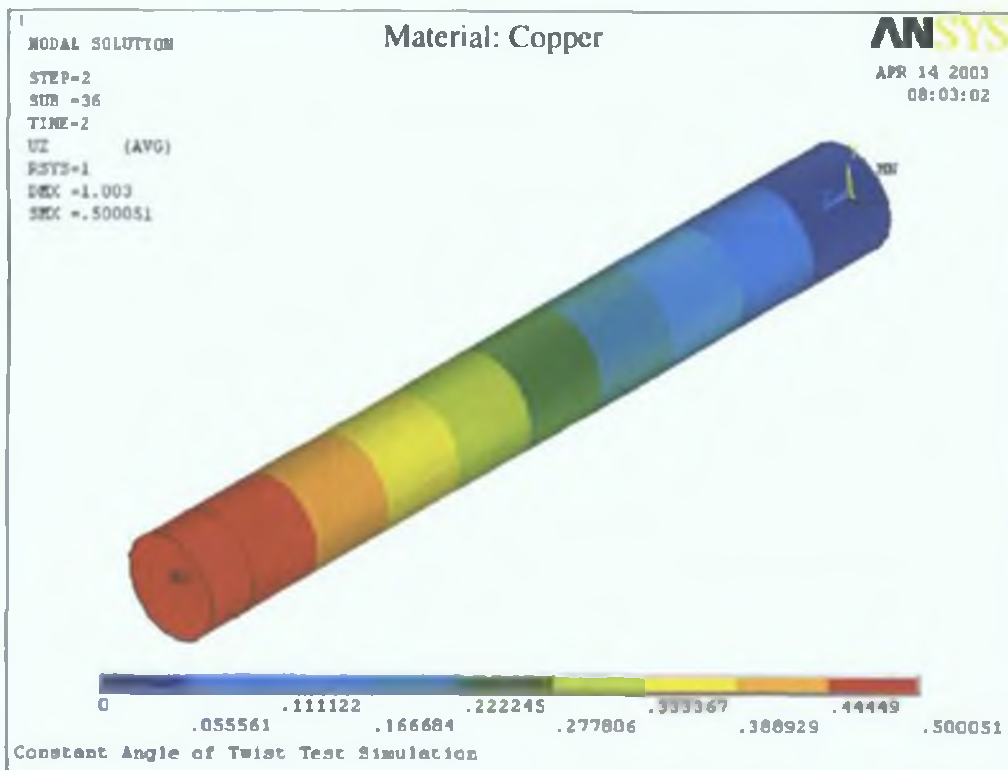Figure 5.49 Angle of Twist at the end of Simulation (Constant Angle of Twist Test)

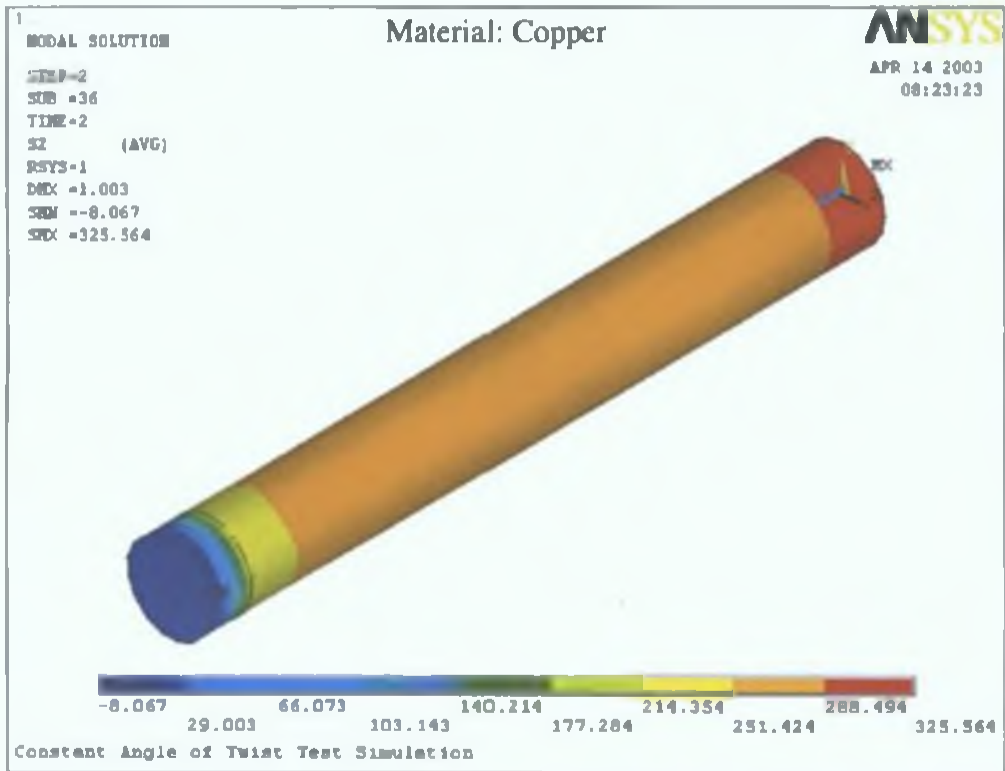Figure 5.50 Axial Displacement at the end of Simulation (Constant Angle of Twist Test)

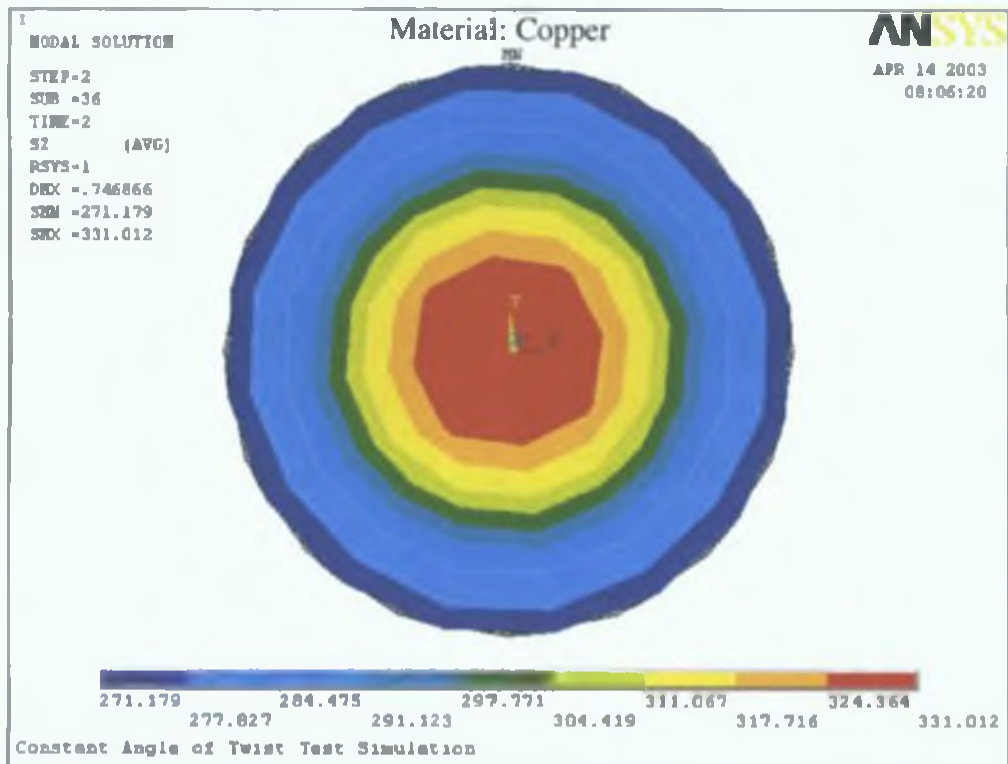Figure 5.51 Axial Stress at the end of Simulation (Constant Angle of Twist Test)

Figure 5.52 Axial Stress distribution Across the Model (Constant Angle of Twist Test)
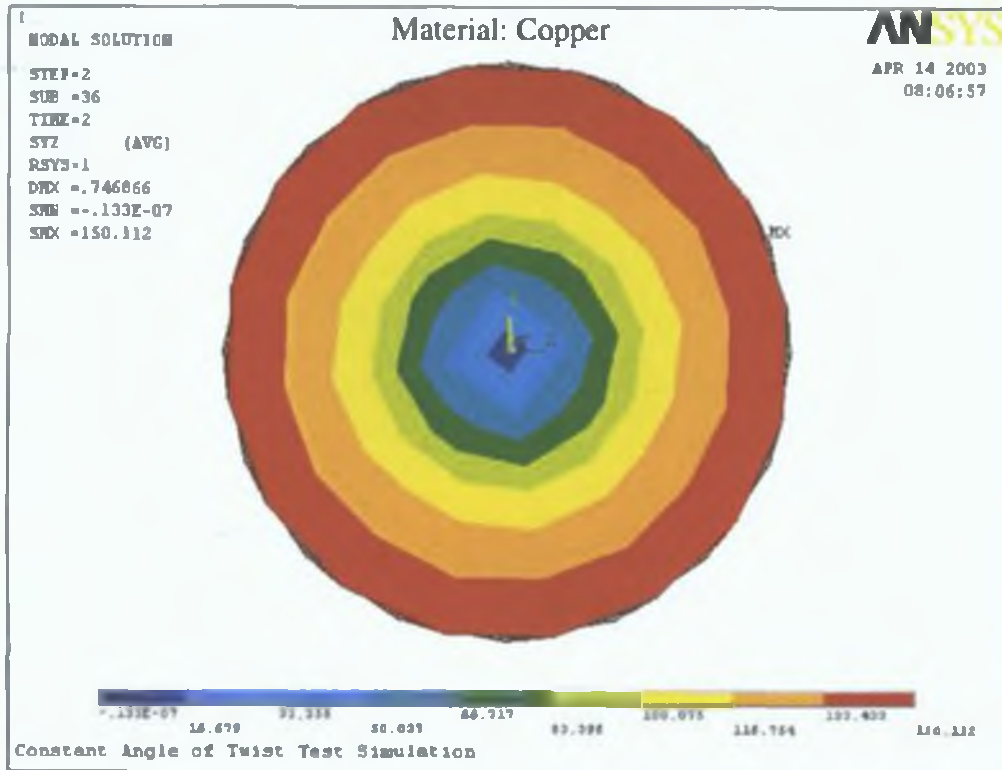
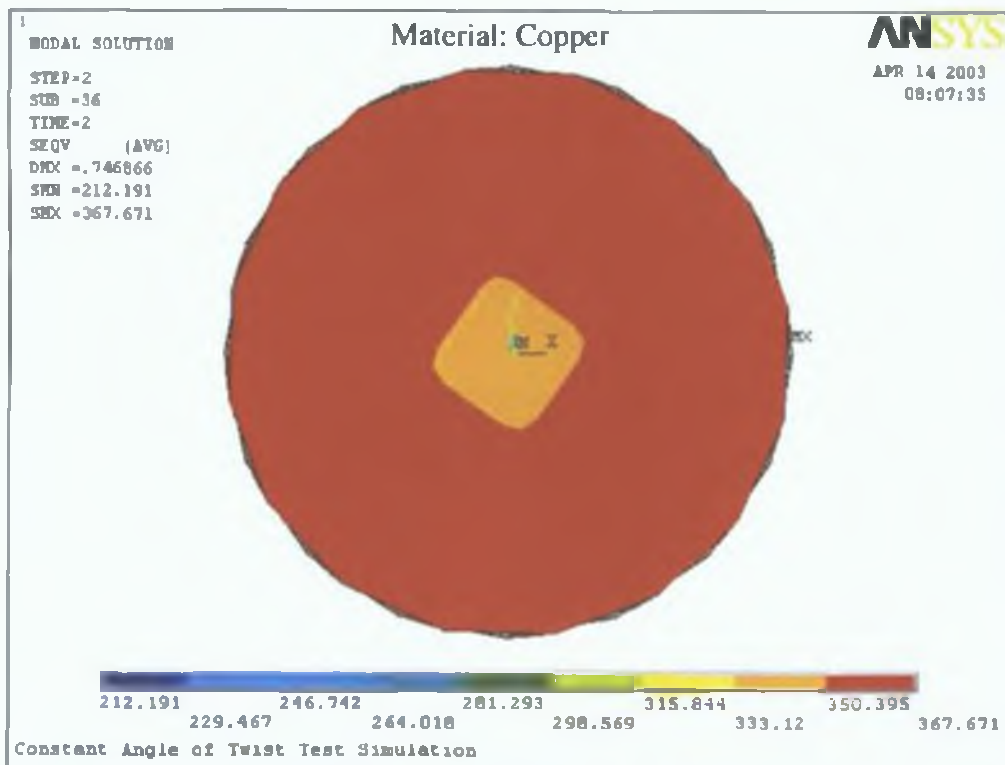Figure 5.53 Shear Stress distribution across the Model (Constant Angle of Twist Test)

Figure 5.54 von Mises Equivalent stress distribution across the Model
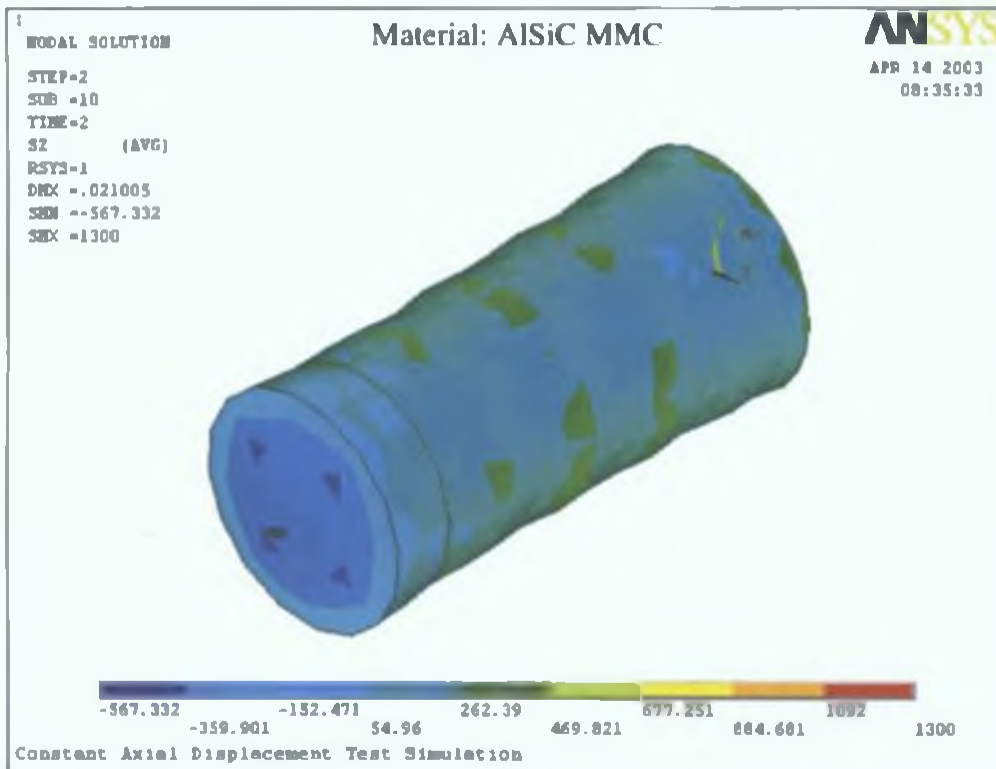
(Constant Angle of Twist Test)

203

Figure 5.55 Axial Stress at the end of Simulation (Constant Axial Displacement Test)
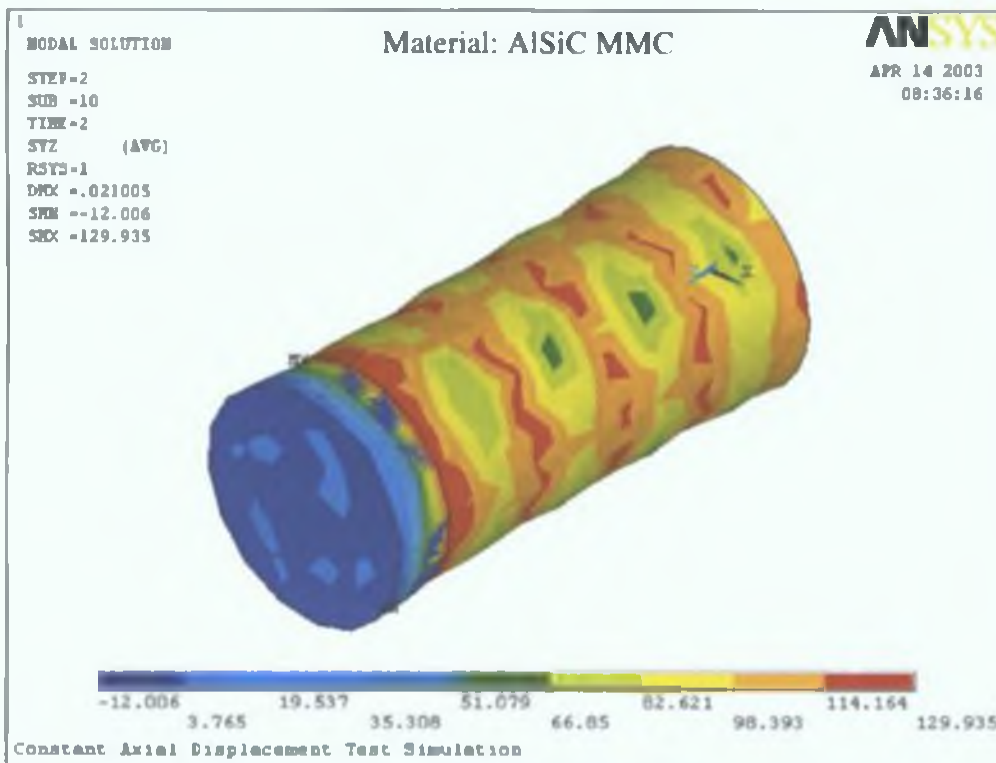
Figure 5.56 Shear Stress at the end of Simulation (Constant Axial Displacement Test)
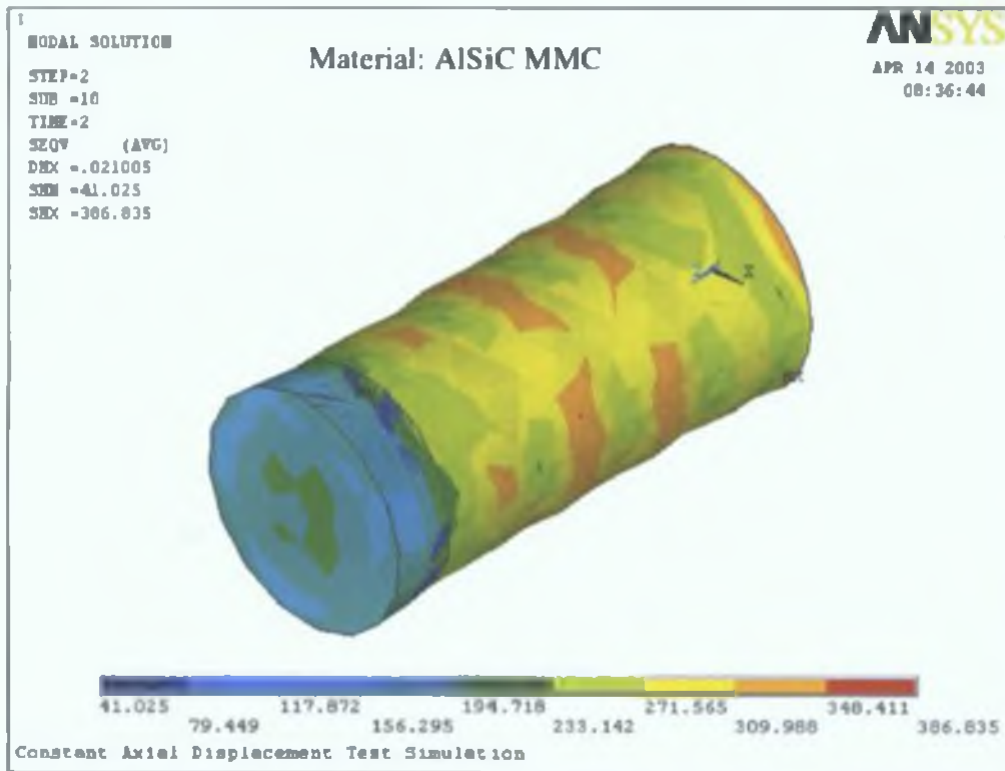
Figure 5.57 von Mises Equivalent Stress at the end of Simulation

(Constant Axial Displacement Test)

Figure 5.58 Axial Stress distribution across the Model (Constant Axial Displacement Test)

Figure 5.59 Shear Stress distribution across the Model (Constant Axial Displacement Test)

Figure 5.60 Axial Stress distribution in the particles (Constant Axial Displacement Test)

Figure 5.61 Shear Stress distribution in the particles (Constant Axial Displacement Test)
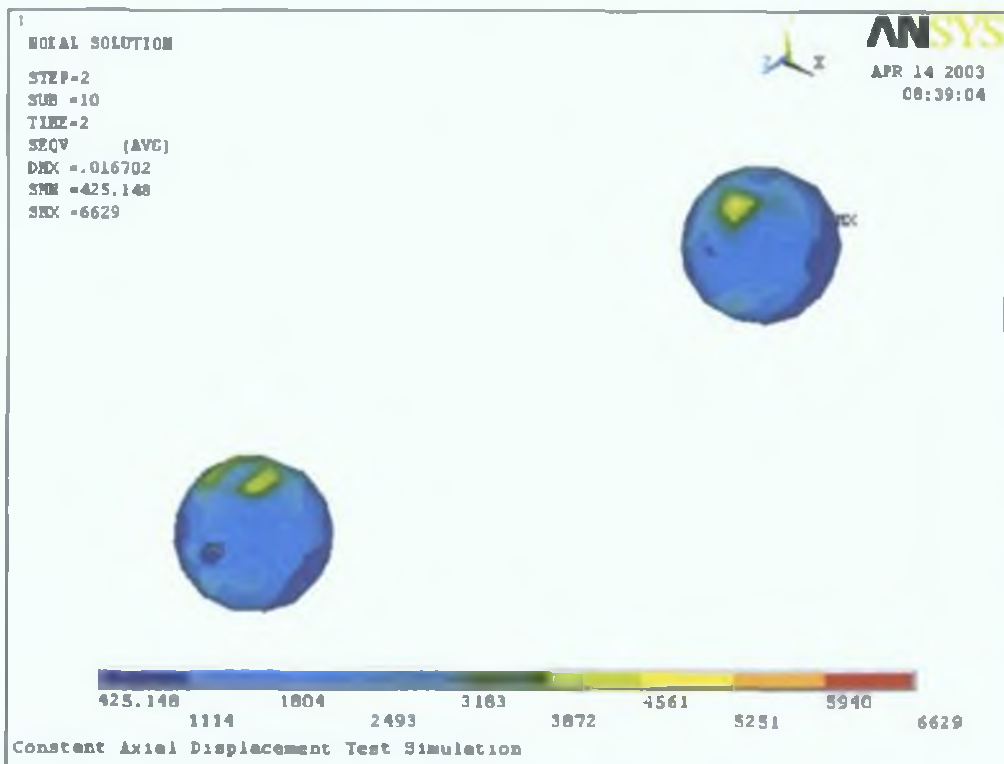
Figure 5.62 von Mises Equivalent Stress distribution in the particles

(Constant Axial Displacement Test)
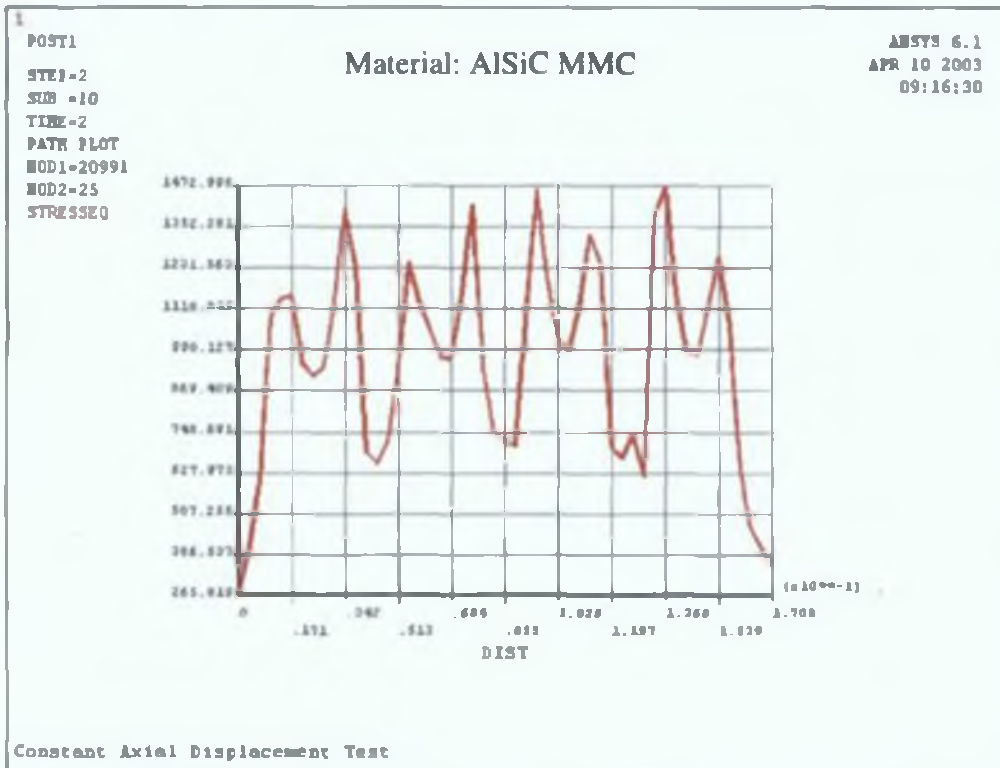
Figure 5.63 von Mises Equivalent Stress distribution along the line passing through the particles in one quadrant (Constant Axial Displacement Test)
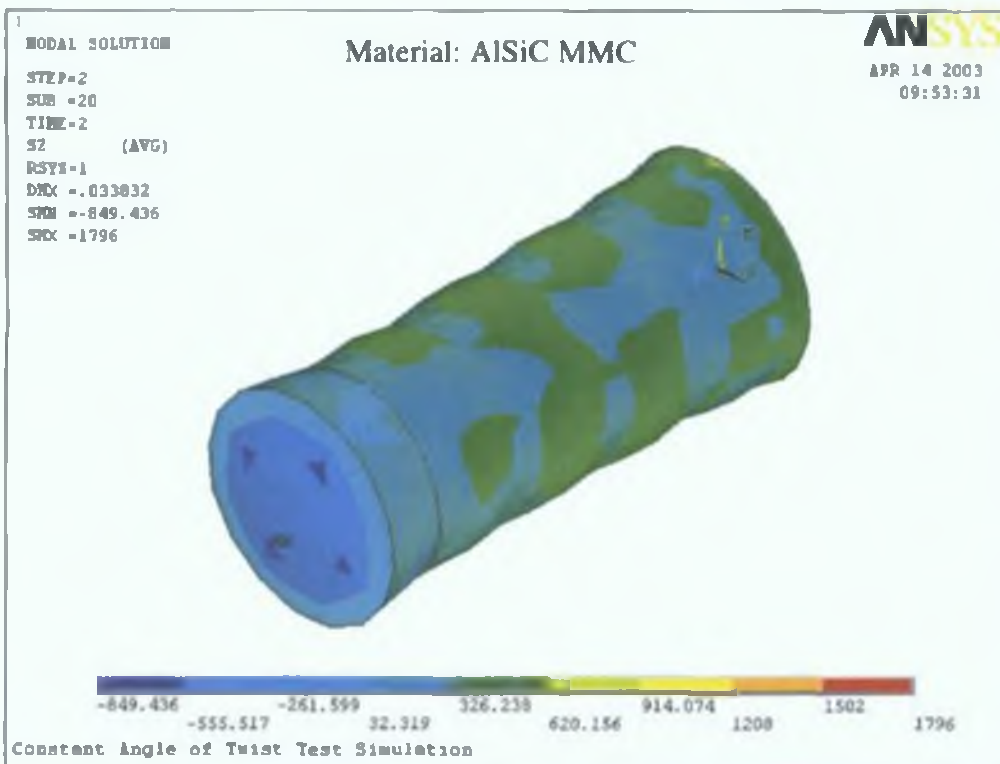
Figure 5.64 Axial Stress distribution (Constant Angle of Twist Test)
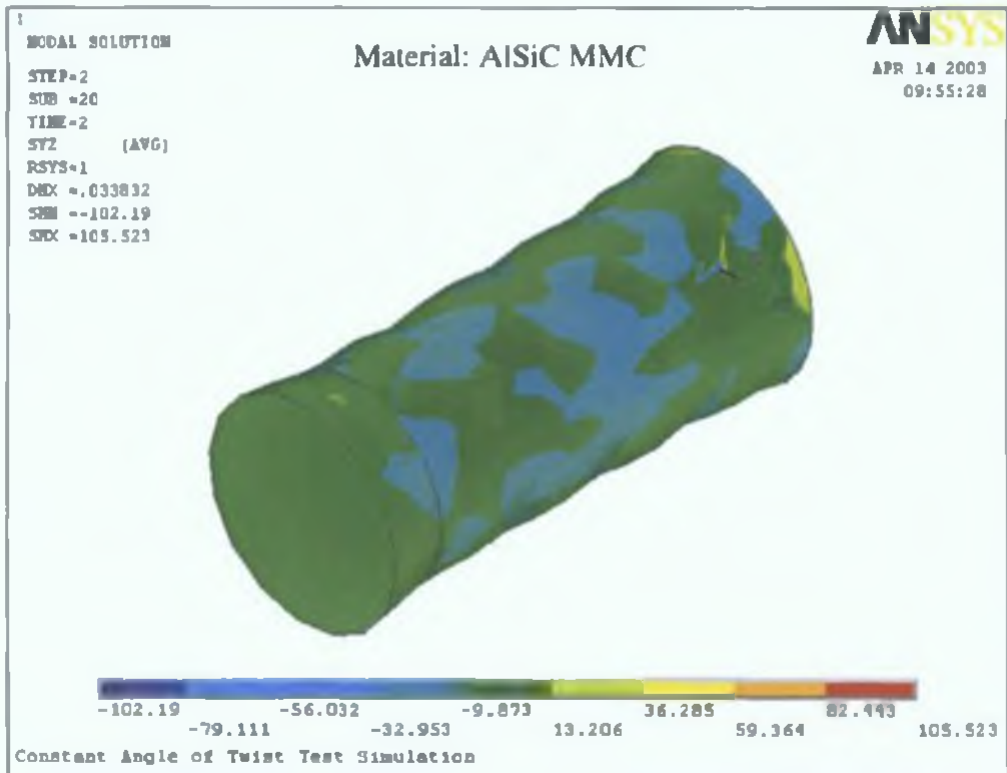
Figure 5.65 Shear Stress distribution (Constant Angle of Twist Test)
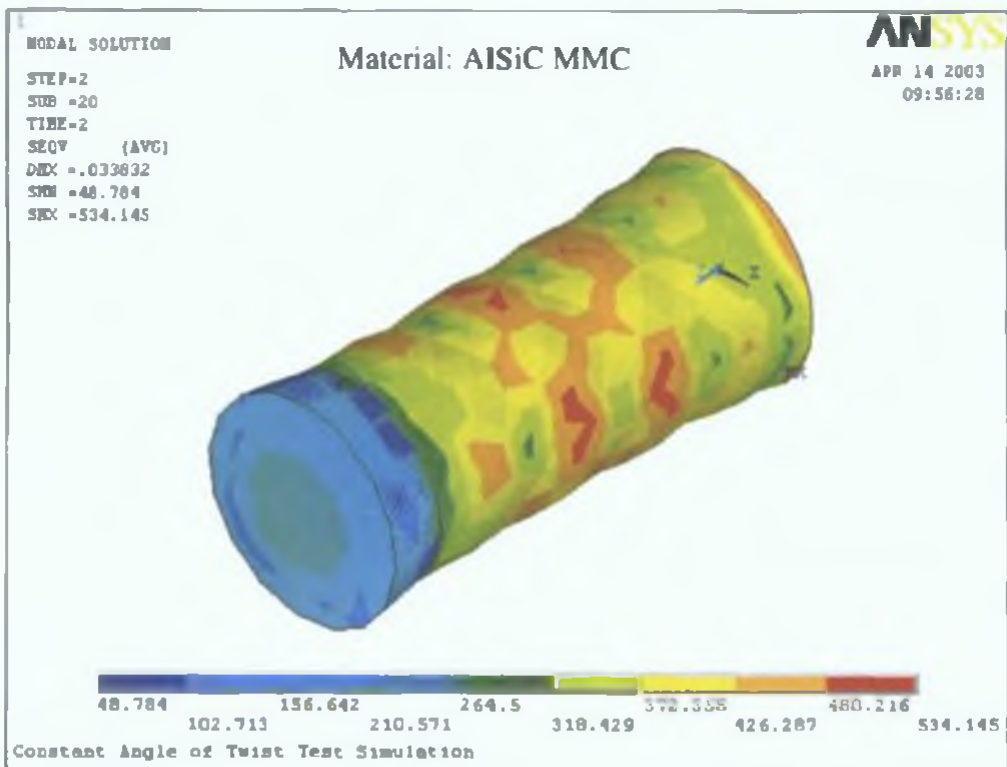
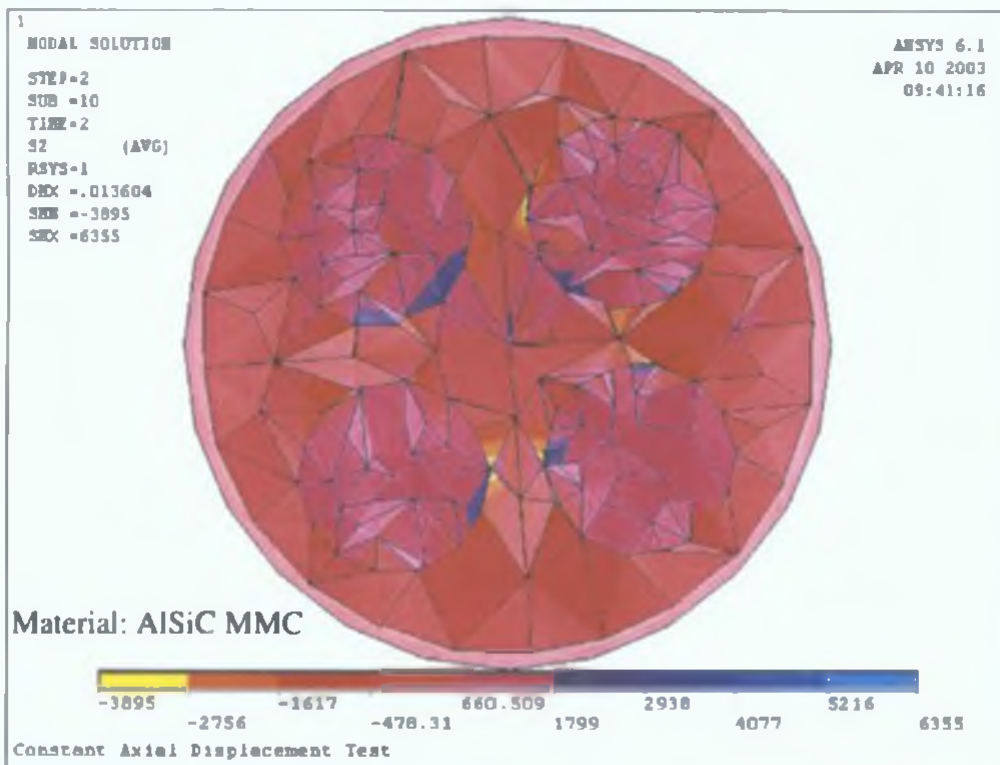Figure 5.66 von Mises Equivalent Stress distribution (Constant Angle of Twist Test)
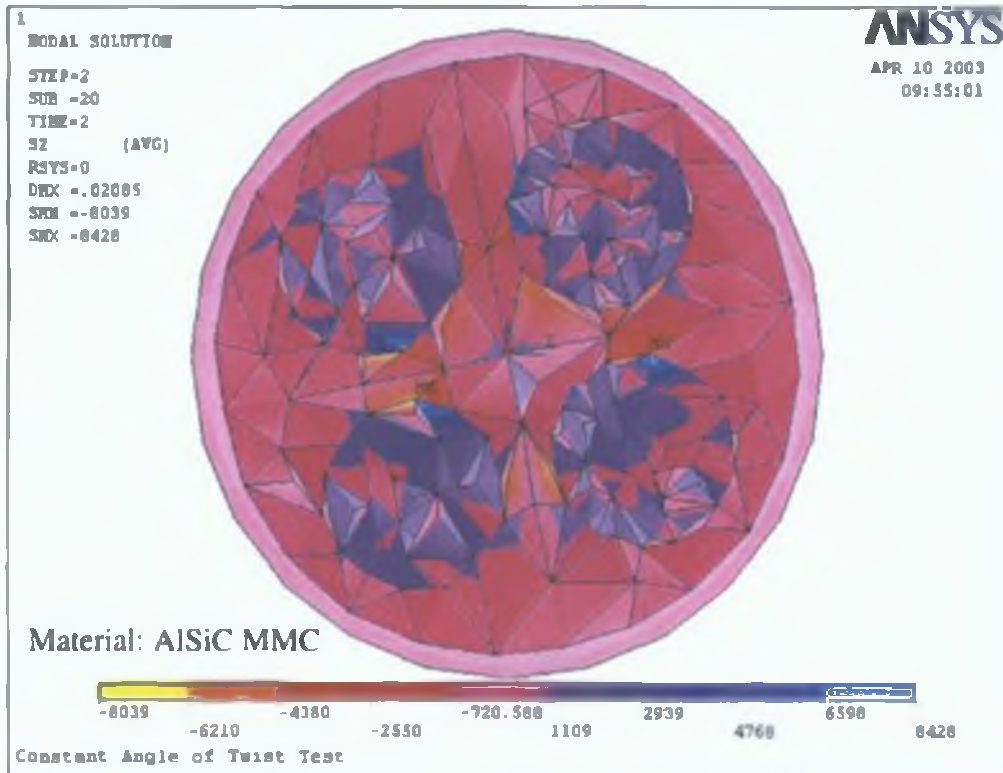
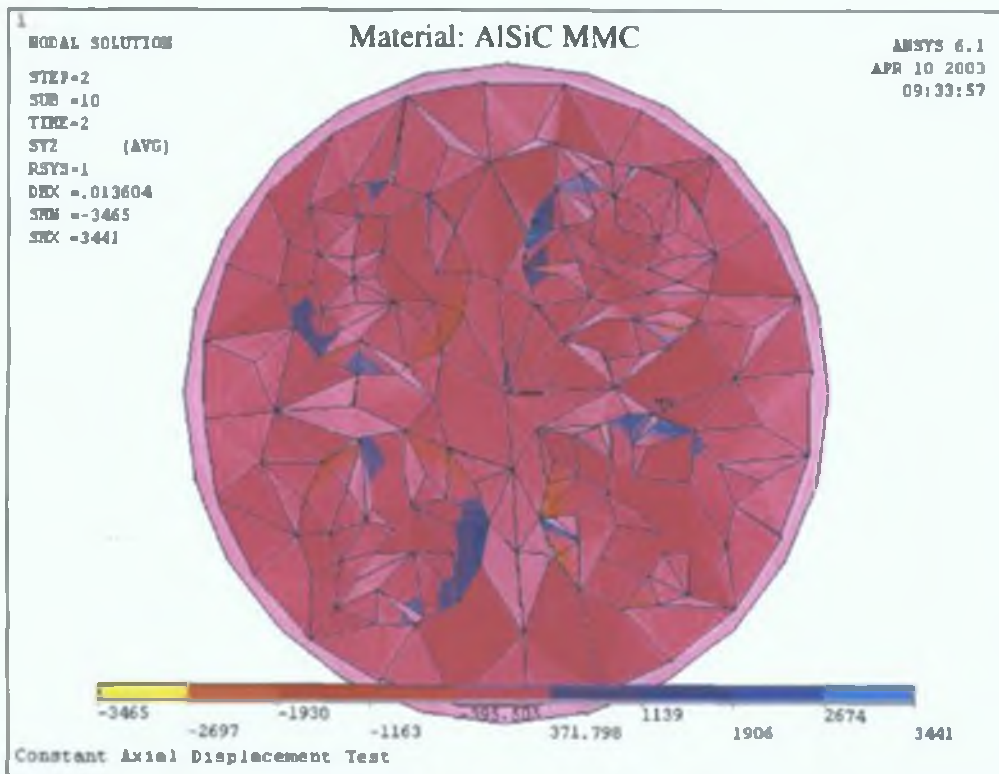Figure 5.67 Axial Stress distribution across the Model (Constant Angle of Twist Test)
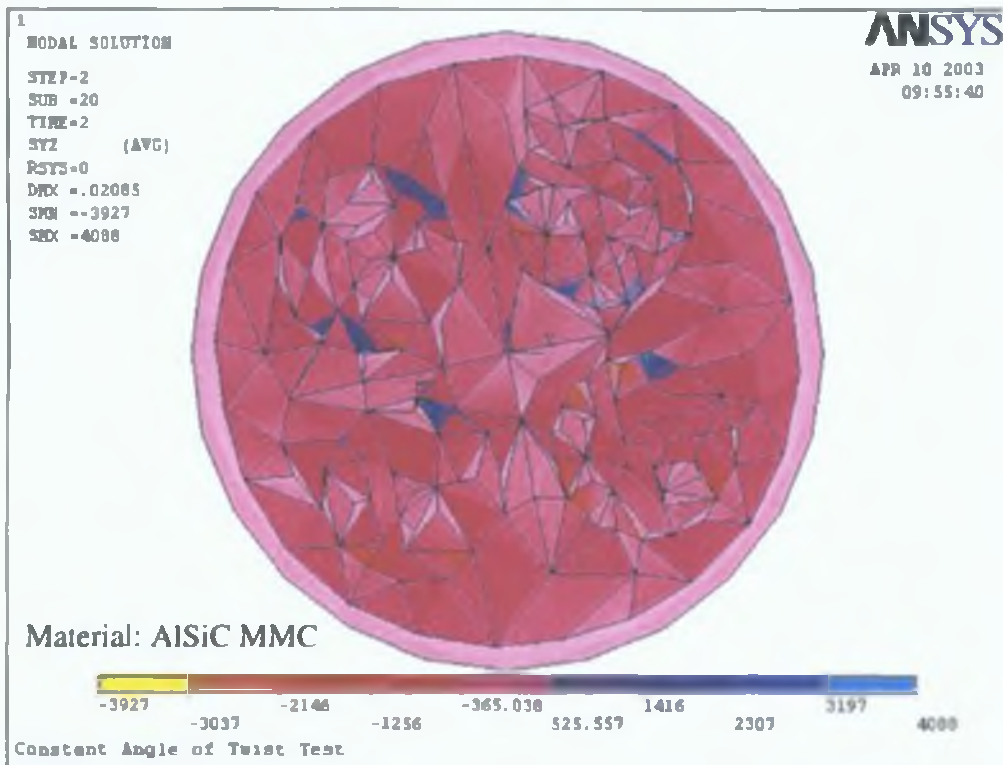
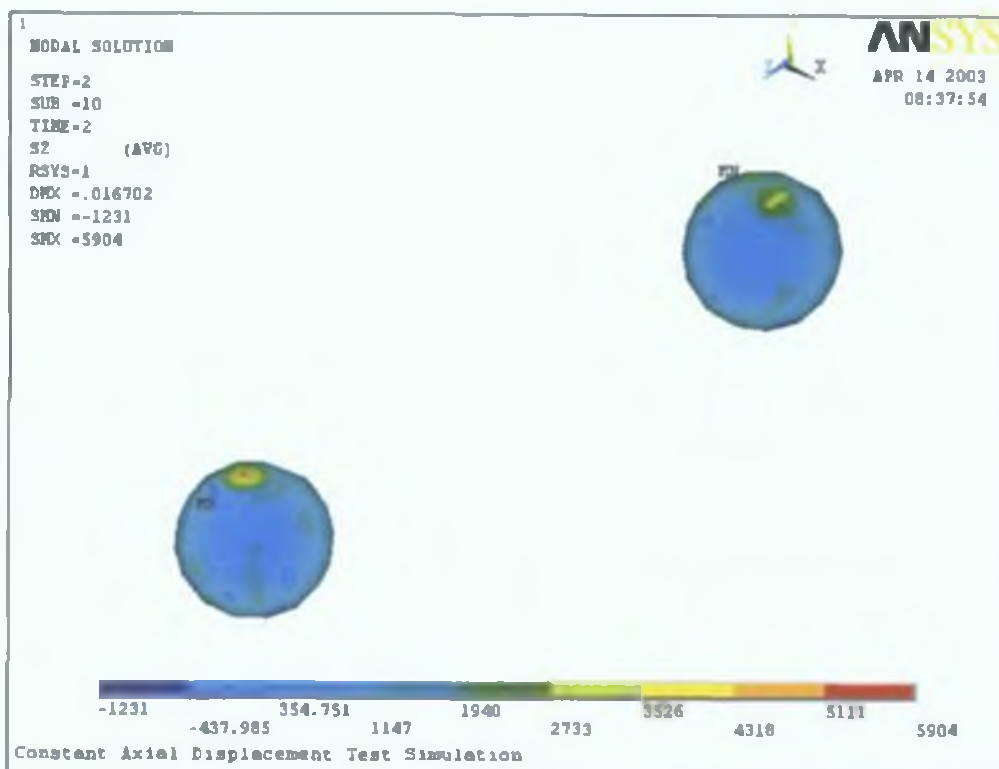Figure 5.68 Shear Stress distribution across the Model (Constant Angle of Twist Test)

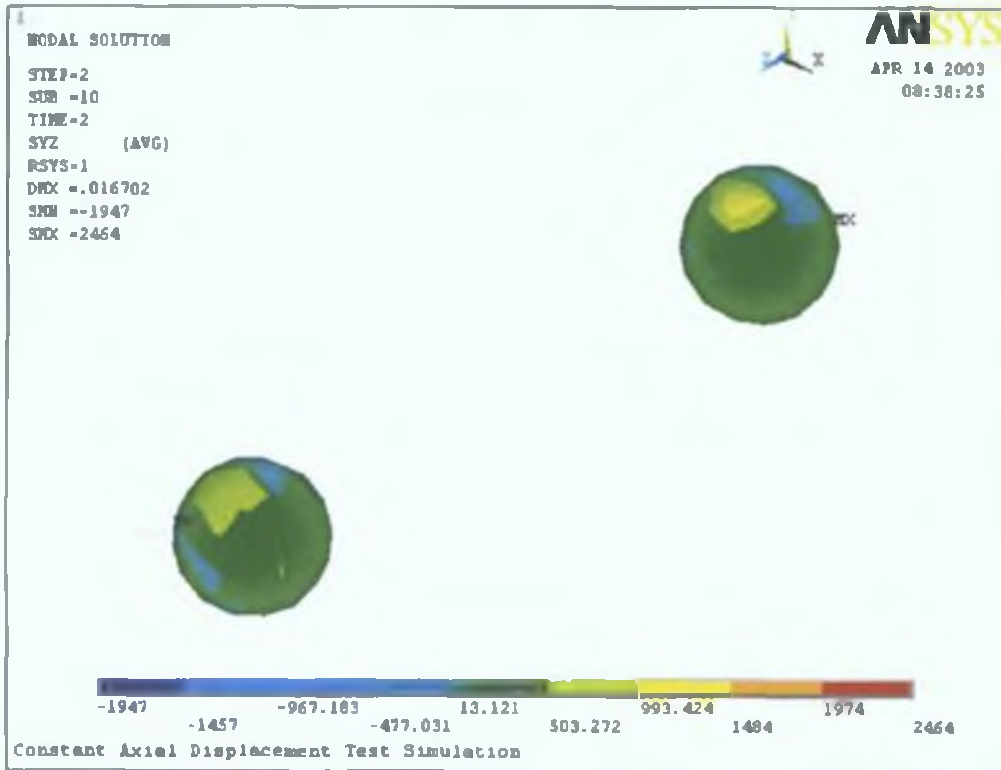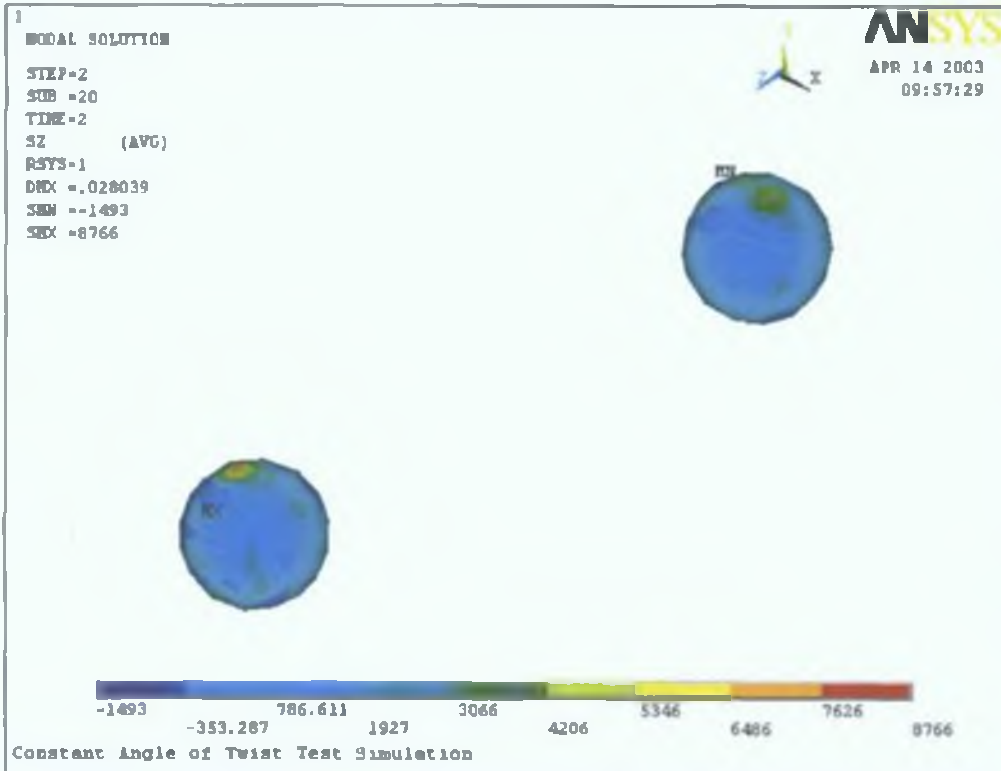Figure 5.69 Axial Stress distribution in the particles (Constant Angle of Twist Test)
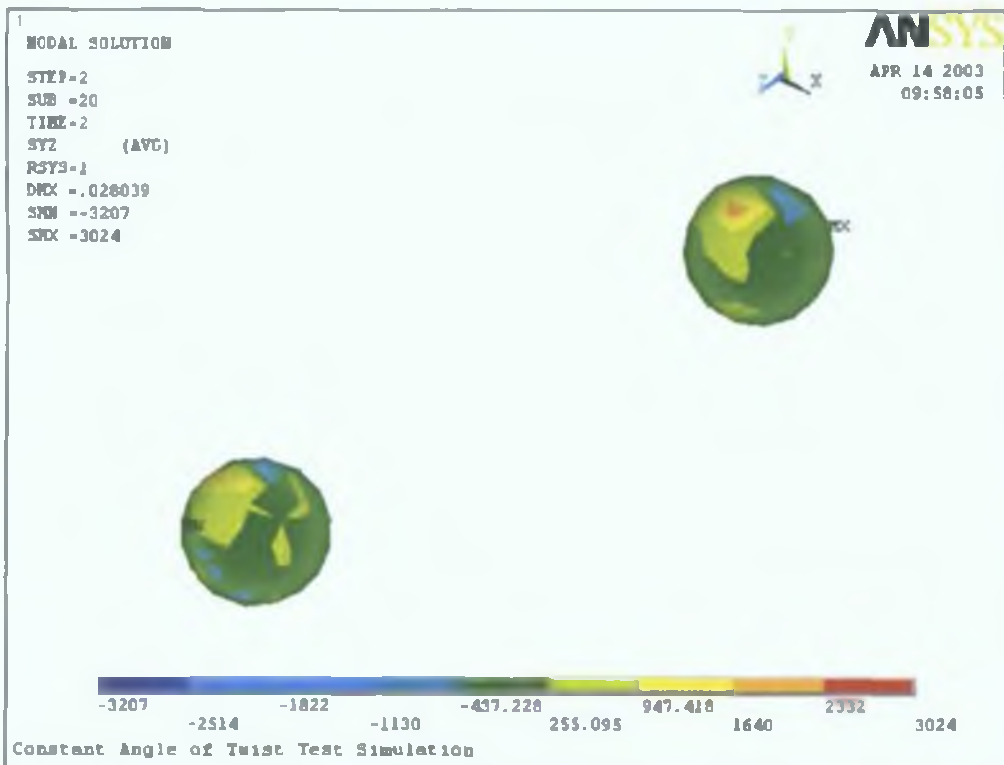
Figure 5.70 Shear Stress distribution in the particles (Constant Angle of Twist Test)
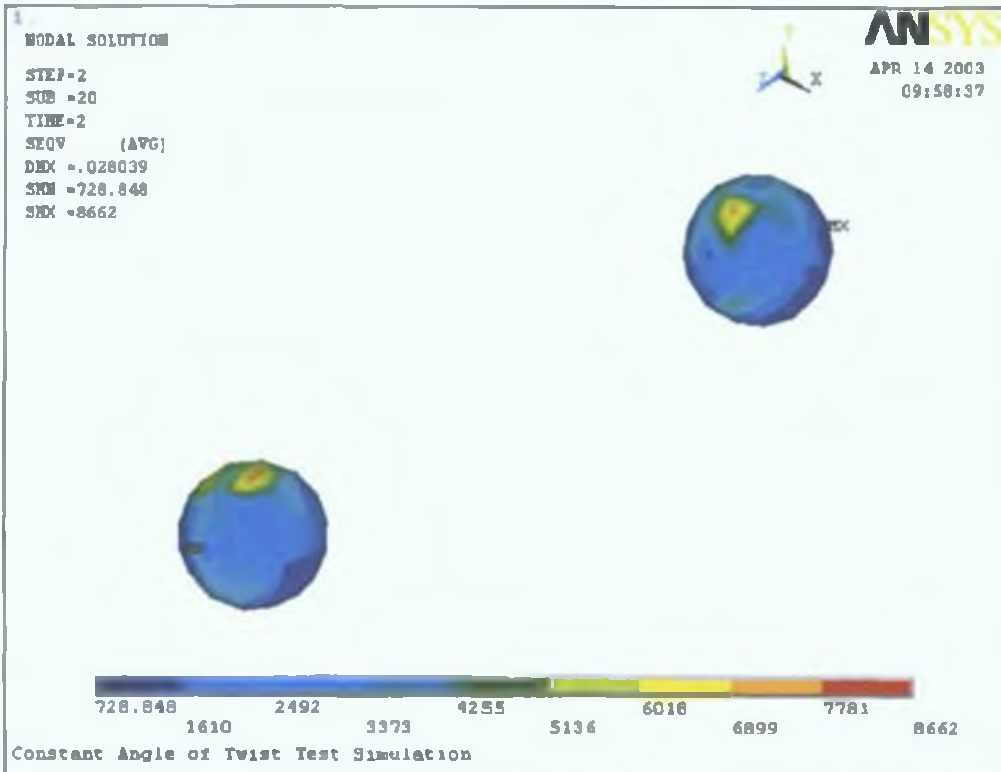
Figure 5.71 von Mises Equivalent Stress distribution in the particles
(Constant Angle of Twist Test)
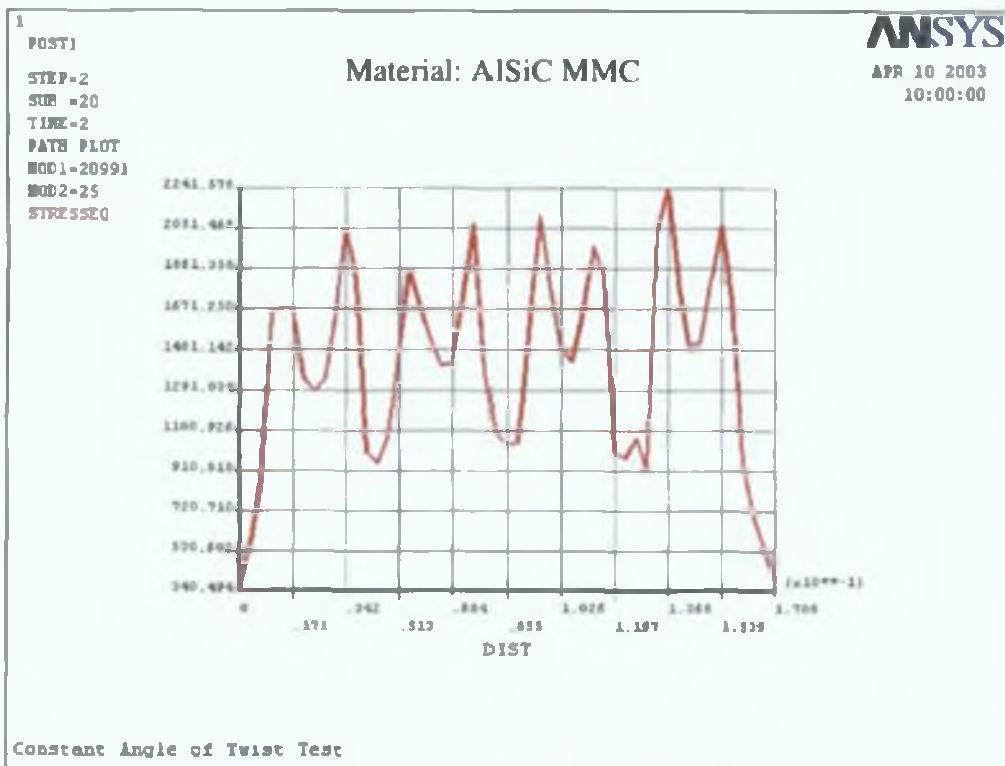
Figure 5.72 von Mises Equivalent Stress distribution along the line passing through the
particles in one quadrant (Constant Angle of Twist Test)
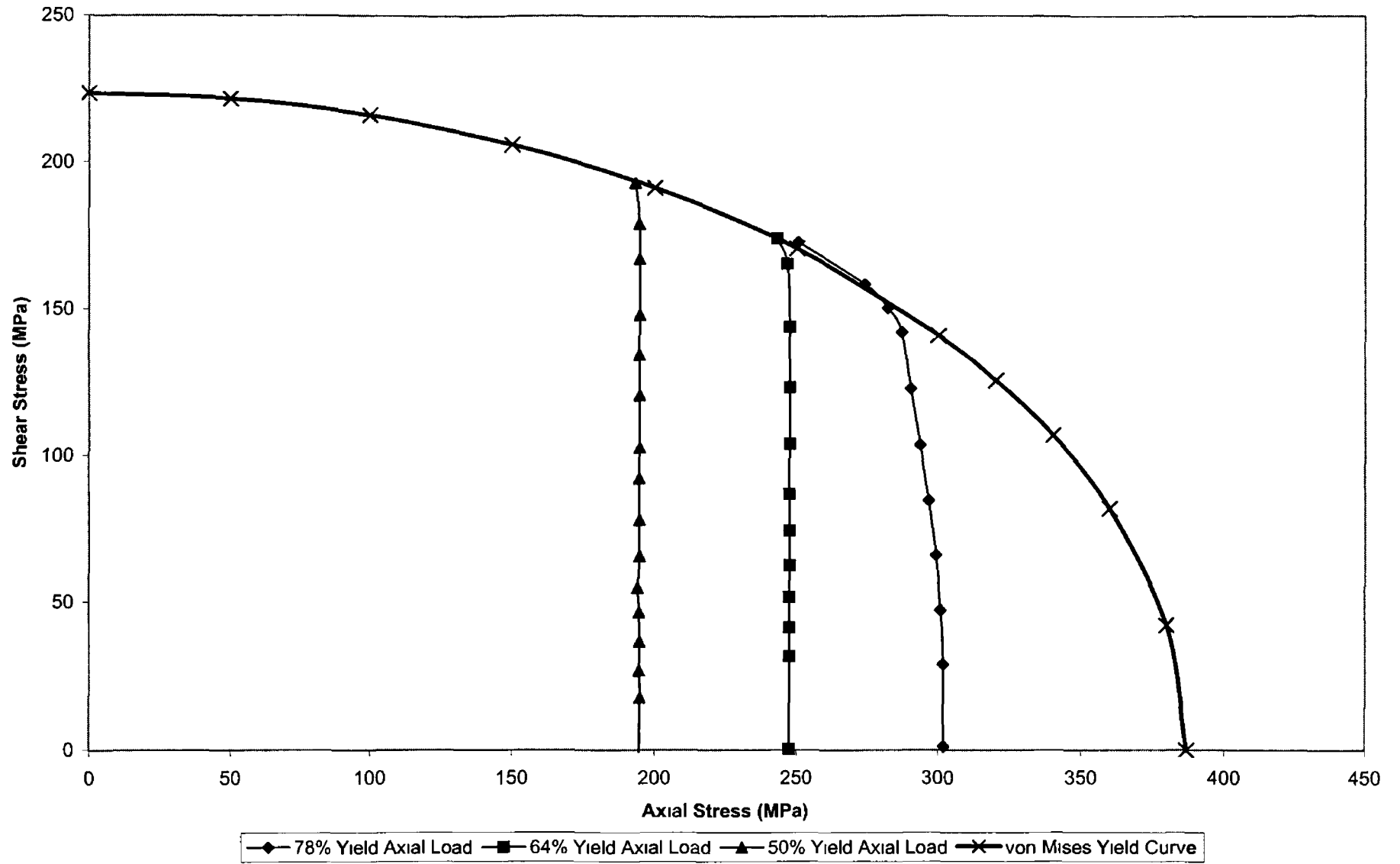
Figure 5 73 Axial Stress-Shear Stress Relationship from FEA Analysis for AlSiC MMC Rod
(Constant Axial Displacement)
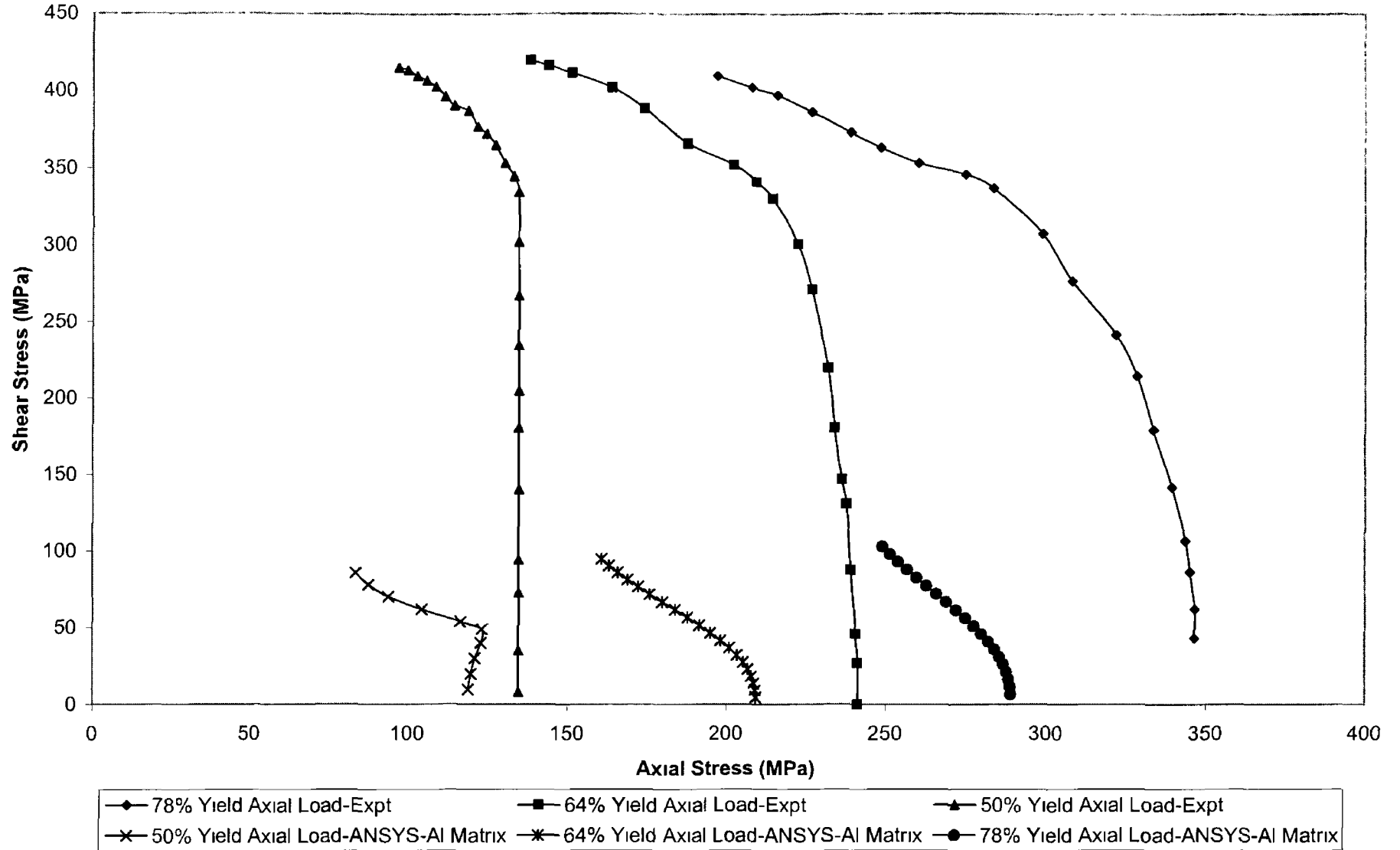
**Figure 5 74 Axial Stress - Shear Stress Relationship for AlSiC MMC Rod
(Constant Axial Displacement)**
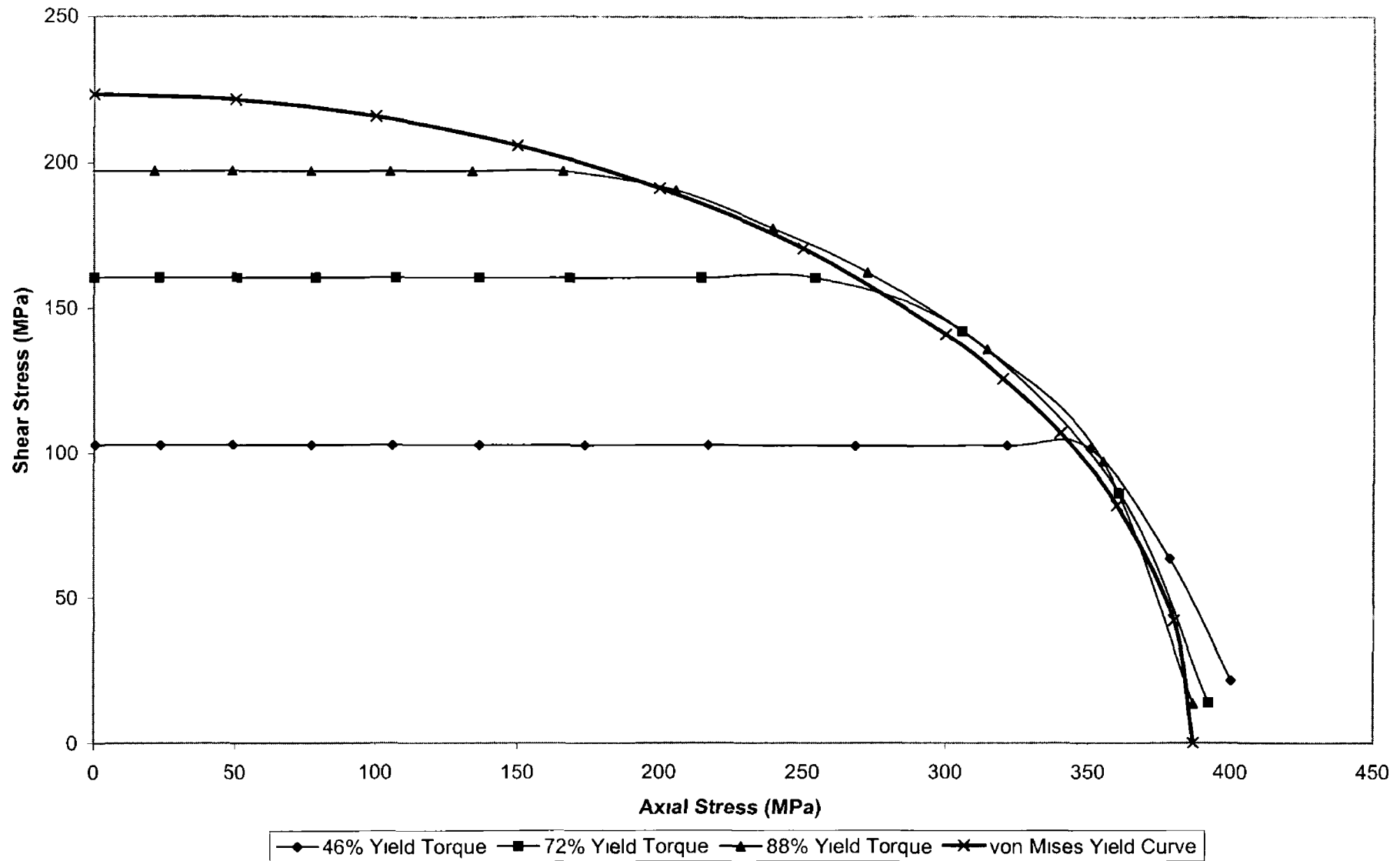
Figure 5 75 Axial Stress-Shear Stress Relationship from FEA Analysis for AlSiC MMC Rod
(Constant Angle of Twist)

6 CONCLUSIONS

This research focused on the investigation of the elastic-plastic behaviour of AlSiC MMC under combined tension and torsion loading. The experiments were conducted using a recommissioned tension torsion machine capable of applying axial force and torque simultaneously or individually at different strain rates. Preliminary experiments and simulations were also carried out on copper to gain knowledge on the elastic-plastic behaviour of a strain-hardening material. The specimens under combined tension and torsion loading conditions appear to gain extra strength due to the presence of initial strain hardening.

From the experimental results and the finite element simulations carried out on AlSiC MMC specimens, the following conclusions were drawn -

- The tension-torsion machine can be controlled effectively using a personal computer and LabVIEW program

- The strength of the AlSiC MMC material is retained up to a critical value of combined axial and shear stress beyond von Mises yield stress described by the empirical equation $\sigma_{EP}^2 + 3\tau_{EP}^2 = C_{AlSiC} Y^2$ where $\begin{cases} C_{AlSiC} \leq 1 \ 2times \ axial \ stress \\ C_{AlSiC} \leq 1 \ 6times \ shear stress \end{cases}$

- The proportional load tests suggest that AlSiC MMC may be suitable for applications such as a bolt where combined tension and torsion loads exist in the member

- When the specimen is subjected to an initial axial load followed by increasing torque, the initially applied axial load remains constant well beyond the von Mises yield curve

- Similarly, when the specimen is subjected to an initial torque followed by increasing axial load, the initially applied torque remains constant well beyond the von Mises yield curve

- Finite element models representing both homogeneous material and composite material were built to analyse the elastic-plastic behaviour of the material under combined tension and torsion loading conditions using ANSYS

- The numerical model has successfully captured the basic features of the elastic-plastic response of the AlSiC metal matrix composite and demonstrated that the particles carry a major portion of the applied stress

- The results predicted by the numerical models show the trend of the mechanical behaviour to be similar to that obtained from the experimental results. However, since the existing material models available in ANSYS could not describe the elastic-plastic behaviour of AlSiC material properly, results obtained from the numerical models did not match the results obtained from experiments beyond von Mises curve

216

7 THESIS CONTRIBUTION

Based on the details reported in the thesis, the author believes that the following new contributions have been made by this work

1 A purpose built tension-torsion machine was recommissioned using adaptive control system and LabVIEW program

2 There exists a new insight into sequential tension/torque loading of MMC material When AlSiC MMC rod specimen is subjected to an initial axial load followed by the application of torque, the torque has a dominant effect on the post yield behaviour of the specimen Similarly, in a rod specimen subjected to an initial torque followed by axial load, the axial load dominates the elastic-plastic behaviour of the rod Experimental investigation on the combined tension and torsion loading of AlSiC metal matrix composite rod demonstrates the ability of the rod to sustain combined axial and shear stresses well beyond the von Mises yield curve

3 Empirical formulae describing the elastic-plastic behaviour of Copper and AlSiC metal matrix composite material under combined tension and torsion loading conditions determined in this study will provide guidelines to engineers in designing machine components in the elastic-plastic region

4 The use of FEA to describe tension/torsion loading in composites has been explored, and some limitations identified

FUTURE WORK

1 In metal matrix composite an interaction between constituents does usually occur which may be simulated using the existing model

2 The robustness of the ANSYS methodology for combined tension and torsion loading of the rod may be enhanced to implement a multilinear material model for the aluminium matrix with refined mesh density

3 An adaptive control system incorporating proportional, integral and differential control may be developed to conduct various combined tension and torsion test programs The adaptive control system may be developed by integrating LabVIEW with Matlab and ActiveX software's

References

1   D S Brooks, The elasto-plastic behaviour of a circular bar loaded by axial force and torque in the strain hardening range, *International Journal of mechanical science*, Vol 11, 1969, pp 75-85

2   A R M Ali, M S J Hashmi, Theoretical and experimental results of the elastic-plastic response of a circular rod subjected to non-proportional combined torque and tension loadings, *Proceedings of Institution Mechanical Engineers*, Vol 213, Part C, 1999, pp 251-261

3   S A Meguid, J D Campbell, Elastic-plastic tension-torsion in a circular bar of rate-sensitive material, *Journal of Applied Mechanics, Transactions of the ASME*, Vol 46, June 1979, pp 311-316

4   S A Meguid, L E Malvern, J D Campbell, Plastic flow of mild steel under proportional and nonproportional straining at a controlled rate, *Journal of Engineering Materials and Technology, Transactions of the ASME*, Vol 101, July 1979, pp 248-253

5   S A Meguid, Plastic flow of mild steel (En8) at different strain-rates under abruptly-changing deformation paths, *Journal of the Mechanics and Physics of Solids*, Vol 29, No 5/6, 1981, pp 375-395

6   S A Meguid, M S Klair, Theoretical and experimental results of the plastic and strain-hardening behaviour of En8 at a controlled rate, *International Journal of Mechanical Science*, Vol 26, No 11/12, 1984, pp 607-616

7   W Lode, Versudre uneber den einfluss der mittleren Hanptspannung auf das Fliessen der Metalle Eisen Kupfer und Nickel, *Z Physik*, Vol 36, 1926, pp 913-939

8   A Nadai, Theory of Flow and Fracture of Solids, Book, McGraw-Hill Book Company, Inc , Vol 1, Second Edition, 1950

9   H W Swift, *Journ Iron Steel Inst*, 140,181,1939

10 F A Gaydon, On the combined torsion and tension of a partly plastic circular cylinder, *Quarterly Journal of Mechanics and Applied Mathematics*, Vol V, Pt 1, 1952, pp 29-41

11 K C Rockey, The influence of large torsional strains upon the subsequent extensional behaviour of a low carbon steel, *International Journal of Mechanical Sciences*, Vol 9, 1967, pp 764-774

12 William A Gardiner, Torque-tension relationships-what they are, why they are important, 1975, AD75-771

13 Ian Chapman, John Newnham, Paul Wallace, The tightening of bolts to yield and their performance under load, *Journal of Vibration Acoustics Stress and Reliability in Design, Transactions of ASME*, Vol 108, 1986, pp 213-221

14 K Hohenemer, *Proceeding of 3rd Int Cong App Mech* , Stockholm, Vol 2, 1930

15 G I Taylor, H Quinney, The plastic distortion of metals, 1931, pp 323-362

16 J L M Morrison, W M Shepherd, An experimental investigation of plastic stress-strain relations, *Proceedings of Institution of Mechanical Engineers*, 1950

17 P M Naghdi, F Essenburg, W Koff, An experimental study of initial and subsequent yield surfaces in plasticity, *Journal of applied mechanics*, Paper No 57-A-37, 1957, pp 201-209

18 G H Daneshi, J B Hawkyard, A tension-torsion machine for testing yield criteria and stress-strain relationships at T=78°K, *International journal of mechanical science*, Vol 18, 1976, pp 57-62

19 G H Daneshi, J B Hawkyard, An investigation into yield surfaces and plastic flow laws for F C C metals at room temperature and a low temperature (T = 78°K), *International journal of mechanical science*, Vol 18, 1976, pp 195-200

20 Y Ohashi, M Tokuda, Precise measurement of plastic behaviour of mild steel tubular specimens subjected to combined torsion and axial force, *Journal of mechanics and physics of solids*, Vol 21, 1973, pp 241-261

21 Aris Phillips, Wei-yang Lu, An experimental investigation of yield surfaces and loading surfaces of pure aluminium with stress-controlled and strain-controlled paths of loading, *Journal of Engineering Materials and Technology, Transactions of the ASME*, Vol 106, October 1984, pp 349-354

22 Akhtar S Khan, Xinwei Wang, On the non-proportional infinitesimal plastic deformation after finite plastic prestraining and partial unloading, *Journal of the Mechanics and Physics of Solids*, Vol 36, No 5, 1988, pp 519-535

23 Kozo Ikegami, Yasushi Niitsu, Effects of complex loadings on plastic deformation of stainless steel (SUS 304) at high temperature, *Nuclear Engineering and Design*, Vol 114, 1989, pp 355-364

24 Han C Wu, Wei C Yeh, On the experimental determination of yield surfaces and some results of annealed 304 stainless steel, *International Journal of Plasticity*, Vol 7, 1991, pp 803-826

25 W Jiang, The elastic-plastic response of thin-walled tubes under combined axial and torsional loads Part I-Monotonic loading, *Journal of pressure vessel technology*, Vol 115, 1993, pp 283-290

26 W Jiang, The elastic-plastic response of thin-walled tubes under combined axial and torsional loads Part I-Variable loading, *Journal of pressure vessel technology*, Vol 115, 1993, pp 291-296

27 Han-Chin Wu, Zhiyou Xu, Paul T Wang, Torsion test of aluminium in the large strain range, *International Journal of Plasticity*, Vol 13, No 10, 1998, pp 873-892

28 A S Khan, P Cheng, An anisotropic elastic-plastic constitutive model for single and polycrystalline metals II-Experiments and predictions concerning thin-walled tubular OFHC copper, *International Journal Plasticity*, Vol 14, Nos 1-3, 1998, pp 209-226

29 Riqiang Liang, Akhtar S Khan, A critical review of experimental results and constitutive models for BCC and FCC metals over a wide range of strain rates and temperatures, *International Journal of Plasticity*, Vol 15, 1999, pp 963-980

30 Akhtar S Khan, Riqiang Liang, Behaviors of three BCC metal over a wide range of strain rates and temperatures experiments and modeling, *International Journal of Plasticity*, Vol 15, 1999, pp 1089-1109

31 H Ishikawa, Constitutive model of plasticity in finite deformation, *International Journal of Plasticity*, Vol 15, 1999, pp 299-317

32 Akhtar S Khan, Riqiang Liang, Behaviour of three BCC metals during non-proportional multi-axial loadings experiments and modelling, *International Journal of Plasticity*, Vol 16, 2000, pp 1443-1458

33 Marc Francois, A Plasticity model with yield surface distortion for non proportional loading, *International Journal of Plasticity*, Vol 17, 2001, pp 703-717

34 Dominique Nouailhas and Georges Cailletaud, Tension-torsion behaviour of single-crystal superalloys Experiment and finite element analysis, *International Journal of Plasticity*, Vol 11, No 4, 1995, pp 451-470

35 N Kanetake, H Ohira, Analytical study on deformation behaviour of metal matrix composites, *Journal of materials processing technology*, Vol 24, 1990, pp 281-289

36 D Huda, M A El Baradie, M S J Hashmi, Analytical study for the stress analysis of metal matrix composites, *Journal of materials processing technology*, Vol 45, 1994, pp 429-434

37 J H Shyong, B Derby, The deformation characteristics of SiC particulate-reinforced aluminium alloy 6061, *Materials Science and Engineering*, Vol A197, 1995, pp 11-18

38 N J Sorensen, S Suresh, V Tvergaard, A Needleman, Effects of reinforcement orientation on the tensile response of metal-matrix composites, *Materials Science and Engineering*, Vol A197, 1995, pp 1-10

39 Hong-Tao Zhu, and Hussein M Zbib, A macroscopic model for plastic flow in metal-matrix composites, *International Journal of Plasticity*, Vol 11, No 4, 1995, pp 471-499

40 A Bhaduri, V Gopinathan, P Ramakrishnan, A P Miodowmk, Processing and properties of SiC particulate reinforced Al-6 2Zn-2 5Mg-1 7Cu alloy (7010) matrix composites prepared by mechanical alloying, *Materials Science and Engineering*, Vol A221, 1996, pp 94-101

41 Stefanos Skolianos, Mechanical behavior of cast SiCp-reinforced Al-4 5%Cu-1 5%Mg alloy, *Materials Science and Engineering*, Vol A210, 1996, pp 76-82

42 L C Davis, Flow rule for the plastic deformation of particulate metal-matrix composites, *Computational Materials Science*, Vol 6, 1996, pp 310-318

43 Daining Fang, Hang Qi, and Shangdong Tu, Elastic and plastic properties of metal-matrix composites Geometrical effects of particles, *Computational Materials Science*, Vol 6, 1996, pp 303-309

44 Dong M, Schmauder, Bidlingmaier T, and Wanner A, Prediction of the mechanical behaviour of short fiber reinforced MMCs by combined cell models, *Computational Materials Science*, Vol 9, 1997, pp 121-133

45 D Steglich, W Brocks, Micromechanical modelling of the behaviour of ductile materials including particles, *Computational Materials Science*, Vol 9, 1997, pp 7-17

46 A Roatta, R E Bolmaro, An Eshelby inclusion-based model for the study of stresses and plastic strain localization in metal matrix composites I General formulation and its application to round particles, *Materials Science and Engineering*, Vol A229, 1997, pp 182-191

47 A Roatta, R E Bolmaro, An Eshelby inclusion-based model for the study of stresses and plastic strain localization in metal matrix composites II Fiber reinforcement and lamellar inclusions, *Materials Science and Engineering*, Vol A229, 1997, pp 192-202

48 A Roatta, P A Turner, M A Bertinetti, R E Bolmaro, An iterative approach to mechanical properties of MMCs at the onset of plastic deformation, *Materials Science and Engineering*, Vol A229, 1997, pp 203-218

49 R Pandorf, Broeckmann, Numerical simulation of matrix damage in aluminium based metal matrix composites, *Computational Materials Science*, Vol 13, 1998, pp 103-107

50 D W A Rees, Deformation and fracture of metal matrix particulate composites under combined loadings, *Composites Part A*, 29A, 1998, pp 171-182

51 Shuyi Qin, Changrong Chen, Guoding Zhang, Wenlong Wang, and Zhongguang Wang, The effect of particle shape on ductility of SiCp reinforced 6061 Al matrix composites, *Materials Science and Engineering*, A272, 1999, pp 363-370

52 P Poza, J Llorca, Mechanical behavior of Al-Li-SiC composites Part I Microstructure and tensile deformation, *Metallurgical and Materials Transactions A*, Vol 30A, March 1999, pp 845-855

53 P Poza, J Llorca, Mechanical behavior of Al-Li-SiC composites Part II Cyclic deformation, *Metallurgical and Materials Transactions A*, Vol 30A, March 1999, pp 857-867

54 P Poza, J Llorca, Mechanical behavior of Al-Li-SiC composites Part III Micromechanical modelling, *Metallurgical and Materials Transactions A*, Vol 30A, March 1999, pp 869-878

55 C R Chen, S Y Qin, S X Li, J L Wen, Finite element analysis about effects of particle morphology on mechanical response of composites, *Materials Science and Engineering*, Vol A278, 2000, pp 96-105

56 H Ismar, F Schroter, F Streicher, Inelastic behavior of metal-matrix composites reinforced with fibres of silicon carbide, alumina or carbon finite-element analysis, *Composites Science and Technology*, Vol 60, 2000, pp 2129-2136

57 A Savaidis, G Savaidis, Zhang Ch, Elastic-plastic FE analysis of a notched shaft under multiaxial nonproportional synchronous cyclic loading, *Theoretical and Applied Fracture Mechanics*, Vol 36, 2001, pp 87-97

58 Hyoung Seop Kim, Finite element analysis of torsional deformation, *Materials Science and Engineering*, A299, 2001, pp 305-308

59 Qing-Sheng Yang, Qing-Hua Qin, Fiber interactions and effective elasto-plastic properties of short-fiber composites, *Composite Structures*, Vol 54, 2001, pp 523-528

60 J H Lee, D Y Maeng, S I Hong, C W Won, Predictions of cracking mode and hardening behavior of MMC via FEM, *Materials Science and Engineering A*, Vol 339, Issues 1-2, 2003, pp 175-182

61 Umit Cocen, and Kazim Onel, Ductility and strength of extruded SiCp/ aluminium-alloy composites, *Composites Science and Technology*, Vol 62, 2002, pp 275-282

62 R Hill, Mathematical Theory of Plasticity, 1950

63 G R Johnson, W H Cook, A constitutive model and data for metals subjected to large strains, high strain rates and high temperatures, *Proceedings of the Seventh International Symposium on Ballistic*, The Hague, The Netherlands, 1983, pp 541-547

64 Matthew Wagenhofer, MarjorieAnn Erickson-Natishan, Ronald W Armstrong, Frank J Zerilli, Influences of strain rate and grain size on yield and serrated flow in commercial Al-Mg Alloy 5086, *Scripta Materialia*, Vol 41, No 11, 1999, pp 1177-1184

65 S R Bodner, Y Partom, Constitutive equations for elastic-viscoplastic strain-hardening materials, *Journal of Applied Mechanics*, June 1975, pp 385-389

66   A S Khan, S Huang, Experimental and theoretical study of mechanical behaviour of 1100 aluminium in the strain rate range 10^{-5}-10^4s^{-1}, *International Journal of Plasticity*, Vol 8, 1992, pp 397-424

67   K K Gupta, J L Meek, Finite Element Multidisciplinary Analysis, AIAA Education Series, 2000

68   Klaus-Jurgen Bathe, Finite Element Procedures, Prentice-Hall International Inc, 1996

69   ANSYS Structural Nonlinearities Training Manual, Release 5 5, Second Edition, Volume I, April 1999

70   A C Bajpai, I M Calus, J A Fairley, Numerical Methods for Engineers and Scientists, John Wiley & Sons, 1978

71   A L Window, Strain gauge technology, 2nd Edition, Elsevier Applied Science, 1992

72   RDP Group Technical Manual for Amplifier Module Types-600, 611, 621 & 628, 2000

73   National Instruments, LabVIEW User Manual, January 1998 Edition

74   H Flandorfer, F Gehringer, E Hayer, Individual solutions for control and data acquisition with the PC, *Thermochimica Acta*, 382, 2002, pp 77-87

75   A Krauβ, U Weimar, W Gopel, LabVIEW for sensor data acquisition, *Trends in Analytical Chemistry*, Vol 18, No 5, 1999, pp 312-318

76   Andrew A Bettiol, J A van Kan, T C Sum, F Watt, A LabVIEW-based scanning and control system for proton beam micromachining, *Nuclear Instruments and Methods in Physics Research*, B 181, 2001, pp 49-53

77   Michael A Nordstrom, Elizabeth A Mapletoft, Timothy S Miles, Spike-train acquisition, analysis and real-time experimental control using a graphical programming language (LabVIEW), *Journal of Neuroscience Methods*, 62, 1995, pp 93-102

78   Jason H Moore, Artificial intelligence programming with LabVIEW genetic algorithms for instrumentation control and optimisation, *Computer Methods and Programs in Biomedicine*, 47, 1995, pp 73-79

79   W Johnson and P B Mellor, Engineering plasticity, New York, Halsted Press, 1983

80   A Mendelson, Plasticity Theory and Application, Book, The MacMillan Company, NewYork, 1968

81   Abu Rayhan Md Ali, Plastic Yielding Characteristics of a Rod Under Successively Applied Torsion and Tension Loadings, PhD Thesis, Dublin City University, Dublin, Ireland, 1995

82   B Duff and J Monaghan, Behaviour of fasteners tightened to yield, *Proceedings of IMC-1*, Trinity College Dublin, 1984

83   J M Monaghan and B Duff, The influence of friction on the stress distribution within yield tightened fasteners, *Proceedings of IMC-2*, University of Ulster, 1985

84   H Jahed, S B Lambert, R N Dubey, Total deformation theory for non-proportional loading, *International Journal of Pressure Vessels and Piping*, Vol 75, 1998, pp 633-642

85   L Weber, P Canalis-Nieto, A Rossoll, and Mortensen A, Fracture strength of alumina fiber reinforced aluminium wire with and without a torsional pre-strain, *Acta materialia*, Vol 48, 2000, pp 3235-3244

86 K E Barth, J G Orbison, R Nukala, Behavior of steel tension members subjected to uniaxial loading, *Journal of constructional steel research*, Vol 58, 2002, pp 1103-1120

87 M H H Meuwissen, C W J Oomens, F P T Baaijens, R Petterson, J D Janssen, Determination of the elasto-plastic properties of aluminium using a mixed numerical-experimental method, *Journal of Materials Processing Technology*, Vol 75, 1998, pp 204-211

88 David C Goss, High strength fasteners cold forged out of work hardening steel, *Journal of Materials Processing Technology*, Vol 98, 2000, pp 135-142

89 G Sved, D S Brooks, Elasto-Plastic behaviour of a round bar subjected to axial force and torque, *Acta Technica Hung 50*, 1965, pp 337-350

90 Martin Muscat, Donald Mackenzie, Robert Hamilton, A work criterion for plastic collapse, *International Journal of Pressure Vessels and Piping*, Vol 80, 2003, pp 49-58

91 L Varga, Design of pressure vessels taking plastic reserve into account, *International Journal of Pressure Vessels and Piping*, Vol 75, 1998, pp 331-341

92 M K Rahman, Ultimate strength estimation of ships' transverse frames by incremental elastic-plastic finite element analysis, *Marine Structures*, Vol 11, 1998, pp 291-317

93 Gareth O Donnell, Process Optimisation and Numerical Modelling of Powder Metallurgical Aluminium Matrix Composites, PhD Thesis, Dublin City University, Dublin, Ireland, 1999

94 G O Donnell, L Looney, Production of aluminium matrix composite components using conventional PM technology, *Materials Science and Engineering*, A303, 2001, pp 292-301

95 ASM Handbook – Properties and Selection Nonferrous alloys and Special-purpose materials, Asm International, 1990

96 S Dumoulin, L Tabourot, C Chappuis, P Vacher, R Arrieux, Determination of the equivalent stress-equivalent strain relationship of a copper sample under tensile loading, *Journal of Materials Processing Technology*, Vol 5803, 2002, pp 1-5

97 F Szekely, I Groma, J Lendvai, Nonlocal effects in torsional deformation, *Materials Science and Engineering*, A277, 2000, pp 148-153

98 Mel Schwartz, Composite Materials Handbook, Second Edition, McGraw-Hill Inc, 1992

Bibliography

1   K K Gupta, J L Meek, Finite Element Multidisciplinary Analysis, AIAA Education Series, 2000

2   Klaus-Jurgen Bathe, Finite Element Procedures, Prentice-Hall International Inc , 1996

3   ANSYS Structural Nonlinearities Training Manual, Release 5 5, Second Edition, Volume I, April 1999

4   Mel Schwartz, Composite Materials Handbook, Second Edition, McGraw-Hill Inc , 1992

List of Publications

1. R Padmanabhan, B J MacDonald, M S J Hashmi, Plastic yield characteristics of a strain-hardening rod under combined tension-torsion loading, Proceedings of ESDA2002, 6th Biennial Conference on Engineering Systems Design and Analysis, Turkey, July 2002
2. R Padmanabhan, B J MacDonald, M S J Hashmi, Determination of critical elastoplastic load for an ALSIC mmc rod under combined tension and torsion loading, Proceedings of AMPT2003, Ireland, July 2003
3. R Padmanabhan, B J MacDonald, M S J Hashmi, Mechanical behaviour of SiC reinforced aluminium thin walled tube under combined axial and torsional loading, Proceedings of AMPT2003, Ireland, July 2003

Other related publications

- N M Zarroug, R Padmanabhan, B J MacDonald, P Young and M S J Hashmi, Mild steel (En8) rod tests under combined tension–torsion loading, *Journal of Materials Processing Technology*, (In Press), *Available online 21 May 2003* This paper is the extended and modified version of the paper presented at AMPT2001 conference at Madrid, Spain in 2001
- A paper titled "A Novel Adaptive Control System for a custom-built tension-torsion machine", authored by R Padmanabhan, N M Zarroug, B J MacDonald and M S J Hashmi, has been submitted for publication as a technical note to the *Journal of Materials Design & Applications, Proceedings of the Institution of Mechanical Engineers Part L*
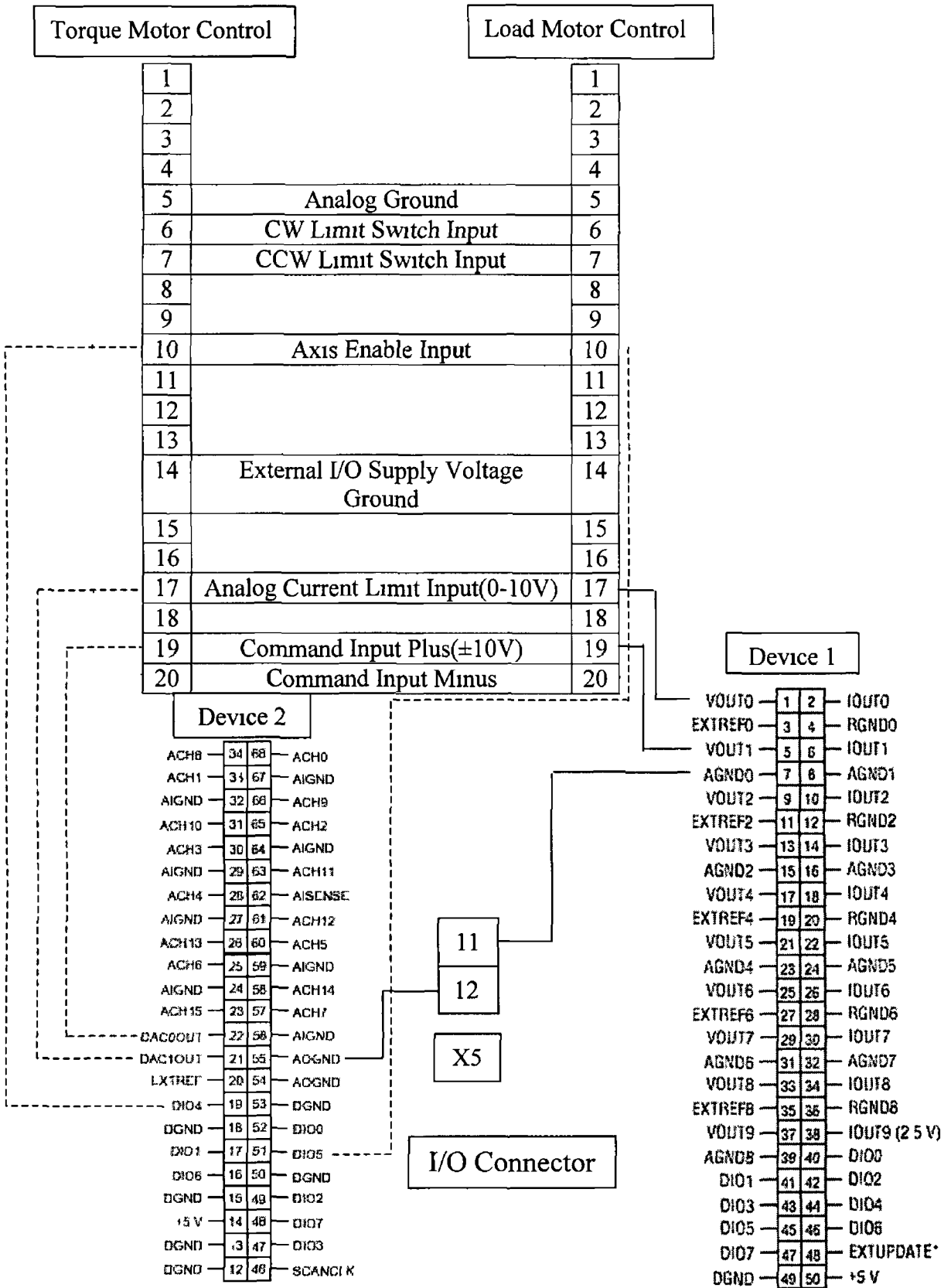
APPENDIX - A

Torque Motor Control   **Load Motor Control**

1		1
2		2
3		3
4		4
5	Analog Ground	5
6	CW Limit Switch Input	6
7	CCW Limit Switch Input	7
8		8
9		9
10	Axis Enable Input	10
11		11
12		12
13		13
14	External I/O Supply Voltage Ground	14
15		15
16		16
17	Analog Current Limit Input(0-10V)	17
18		18
19	Command Input Plus(±10V)	19
20	Command Input Minus	20

Device 2

ACH8	34	68	ACH0
ACH1	33	67	AIGND
AIGND	32	66	ACH9
ACH10	31	65	ACH2
ACH3	30	64	AIGND
AIGND	29	63	ACH11
ACH4	28	62	AISENSE
AIGND	27	61	ACH12
ACH13	26	60	ACH5
ACH6	25	59	AIGND
AIGND	24	58	ACH14
ACH15	23	57	ACH7
DAC0OUT	22	56	AIGND
DAC1OUT	21	55	AOGND
LXTREF	20	54	AOGND
DIO4	19	53	DGND
DGND	18	52	DIO0
DIO1	17	51	DIO5
DIO6	16	50	DGND
DGND	15	49	DIO2
+5 V	14	48	DIO7
DGND	13	47	DIO3
DGND	12	46	SCANCLK

| 11 |
| 12 |

X5

I/O Connector

Device 1

VOUT0	1	2	IOUT0
EXTREF0	3	4	RGND0
VOUT1	5	6	IOUT1
AGND0	7	8	AGND1
VOUT2	9	10	IOUT2
EXTREF2	11	12	RGND2
VOUT3	13	14	IOUT3
AGND2	15	16	AGND3
VOUT4	17	18	IOUT4
EXTREF4	19	20	RGND4
VOUT5	21	22	IOUT5
AGND4	23	24	AGND5
VOUT6	25	26	IOUT6
EXTREF6	27	28	RGND6
VOUT7	29	30	IOUT7
AGND6	31	32	AGND7
VOUT8	33	34	IOUT8
EXTREF8	35	36	RGND8
VOUT9	37	38	IOUT9 (2 5 V)
AGND8	39	40	DIO0
DIO1	41	42	DIO2
DIO3	43	44	DIO4
DIO5	45	46	DIO6
DIO7	47	48	EXTUPDATE*
DGND	49	50	+5 V

Figure A 1 Controller Back Plane Connection Details

Figure A 2 Block Diagram of Device 1 AT-AO-6

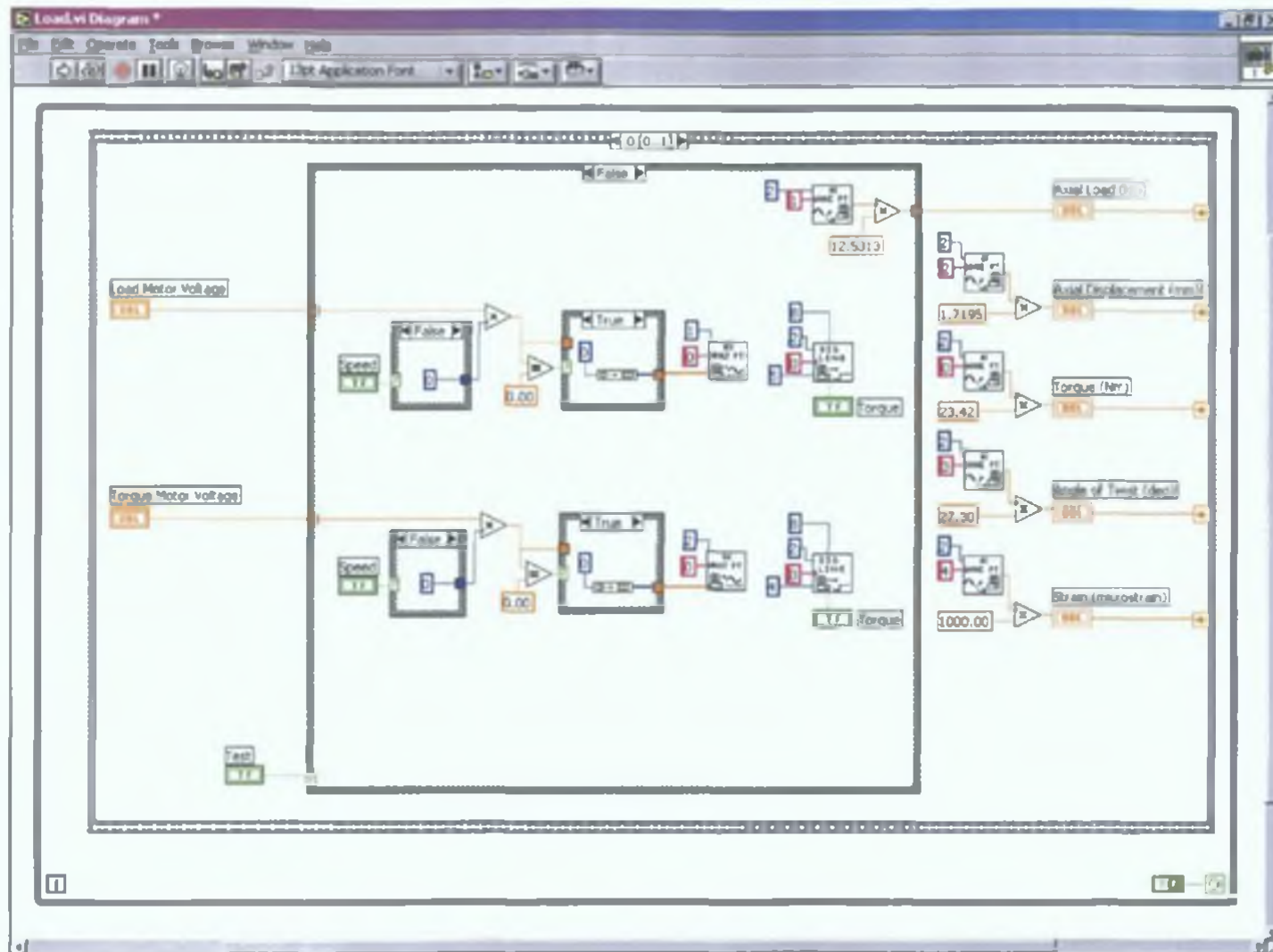**Figure A 3 Block Diagram of Device AT-MIO-16E-10**

11

Figure A.4 Tension-torsion machine specimen setup frame in the LabVIEW programme
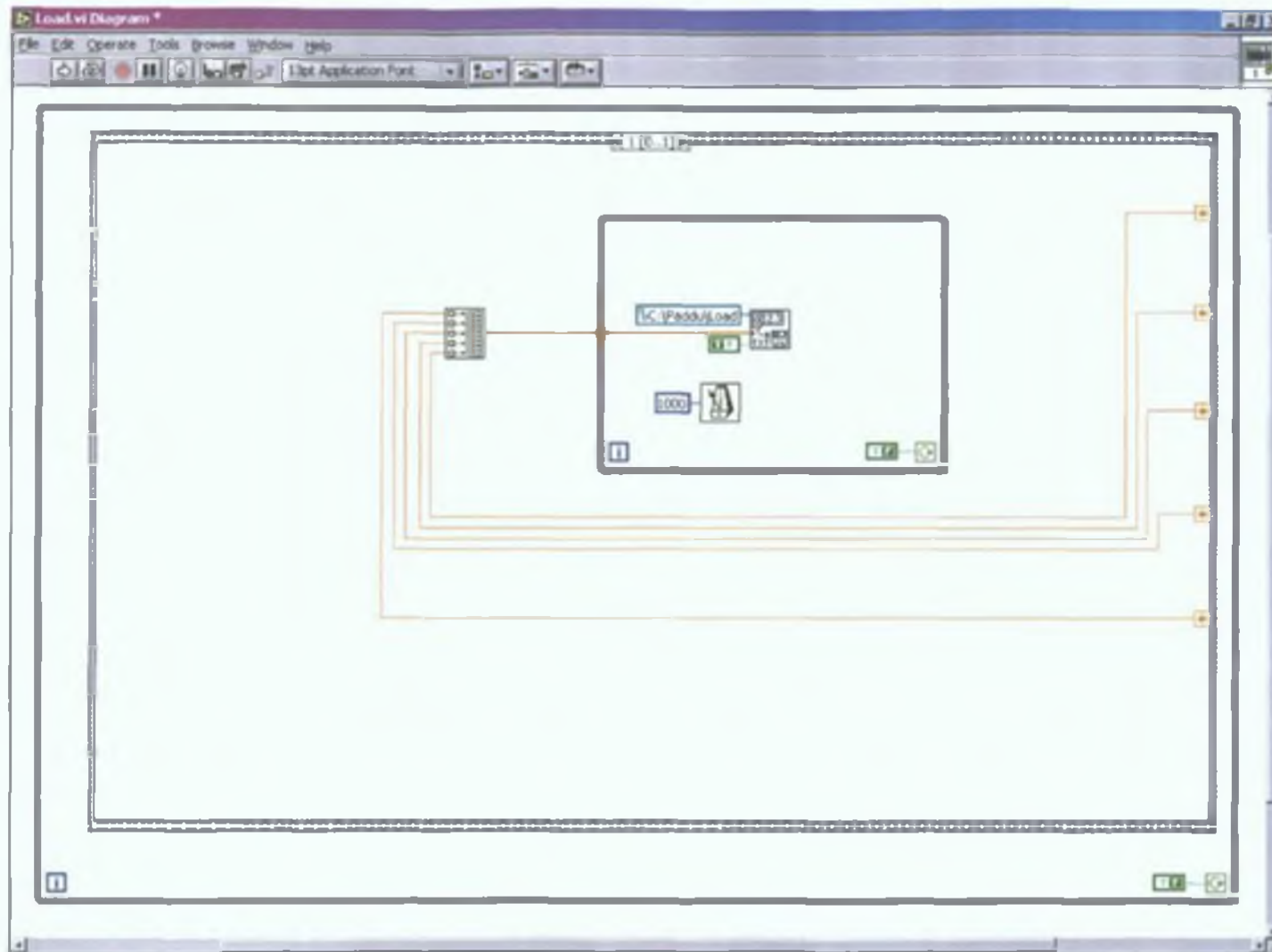
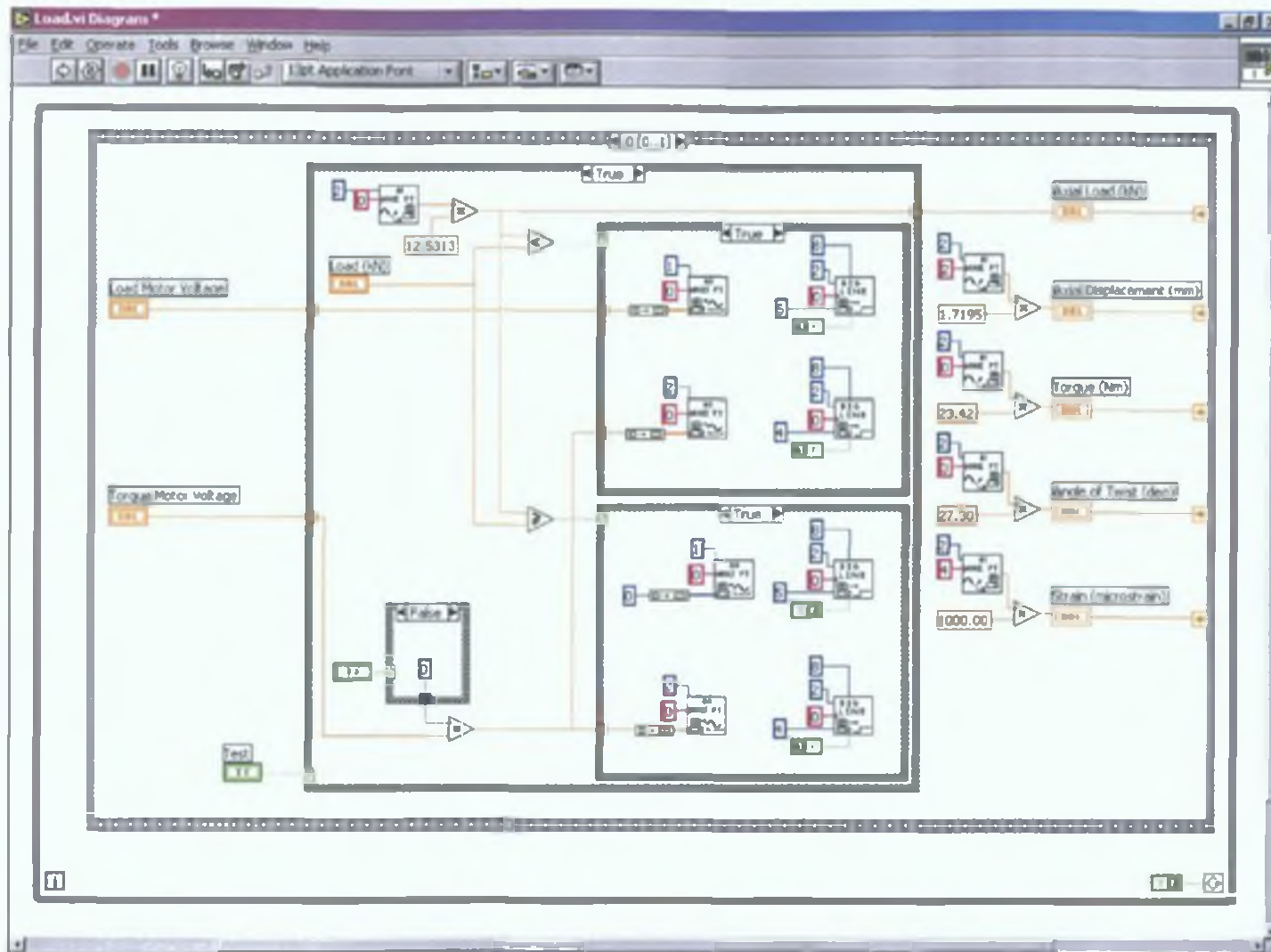Figure A.5 Transducer data log frame in the LabVIEW programme

Figure A.6 Experimental test frame in the LabVIEW programme

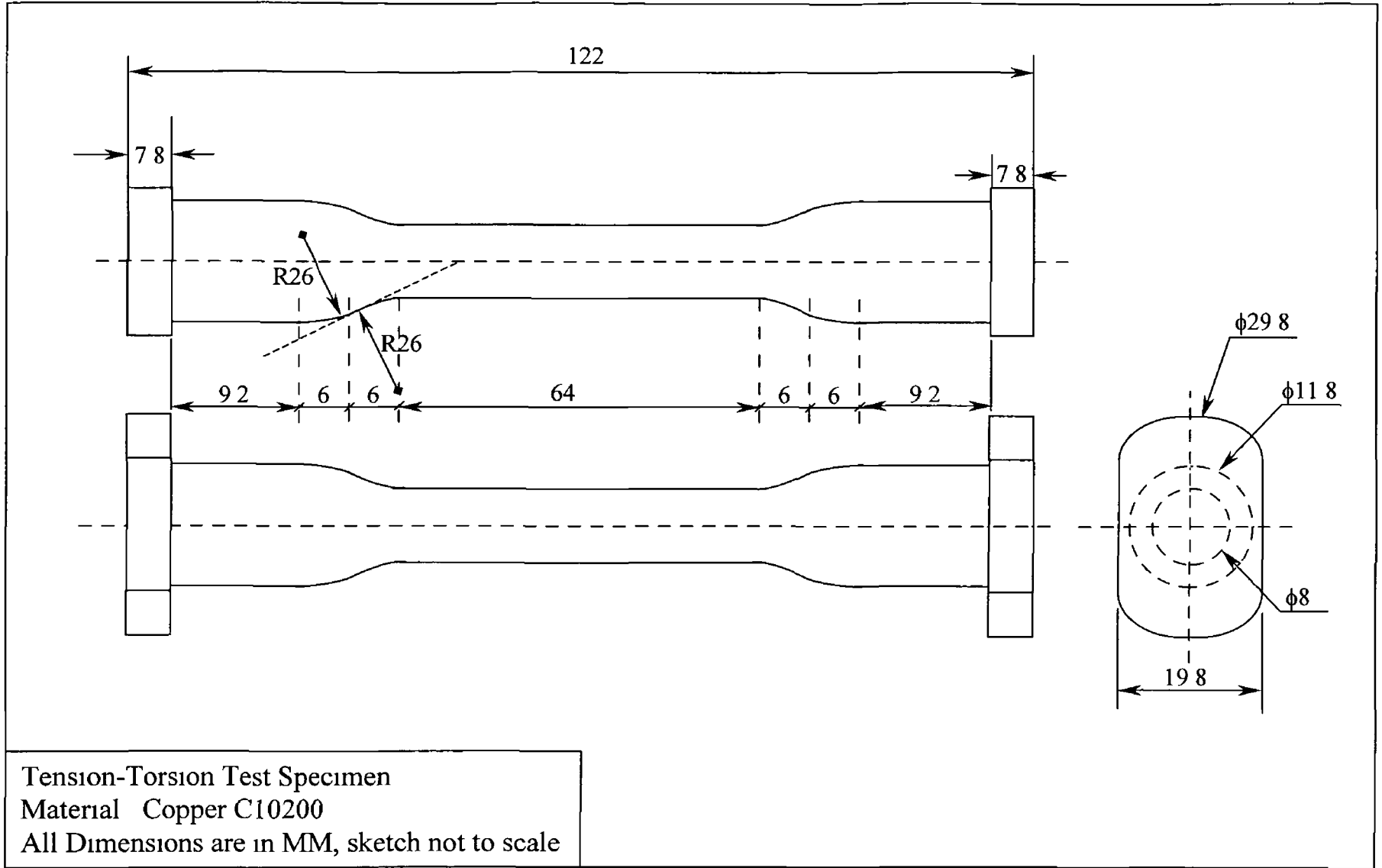122

7 8

7 8

R26

R26
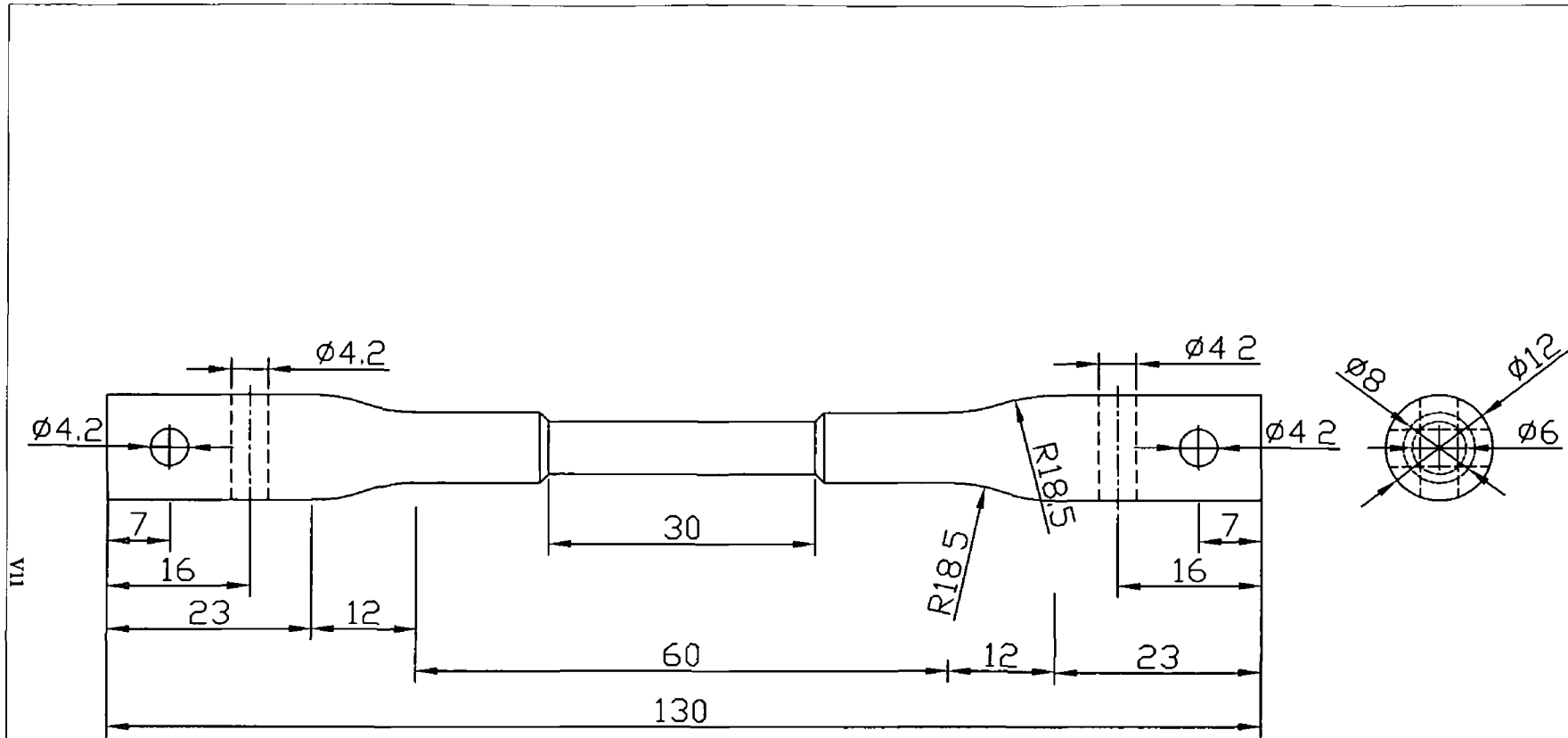
9 2   6   6   64   6   6   9 2

φ29 8

φ11 8

φ8

19 8

VI

Tension-Torsion Test Specimen
Material   Copper C10200
All Dimensions are in MM, sketch not to scale

Figure A 7 Copper Rod Specimen

Figure A 8 AlSiC MMC Rod Specimen

The drawing is titled:

Tension-Torsion Test Specimen
Material: AlSiC MMC
All Dimensions are in MM

Dimensions shown on the drawing: Ø4.2, Ø4.2, Ø4.2, Ø4.2, Ø8, Ø12, Ø6, R18.5, R18.5, 7, 16, 23, 12, 30, 60, 12, 23, 16, 7, 130
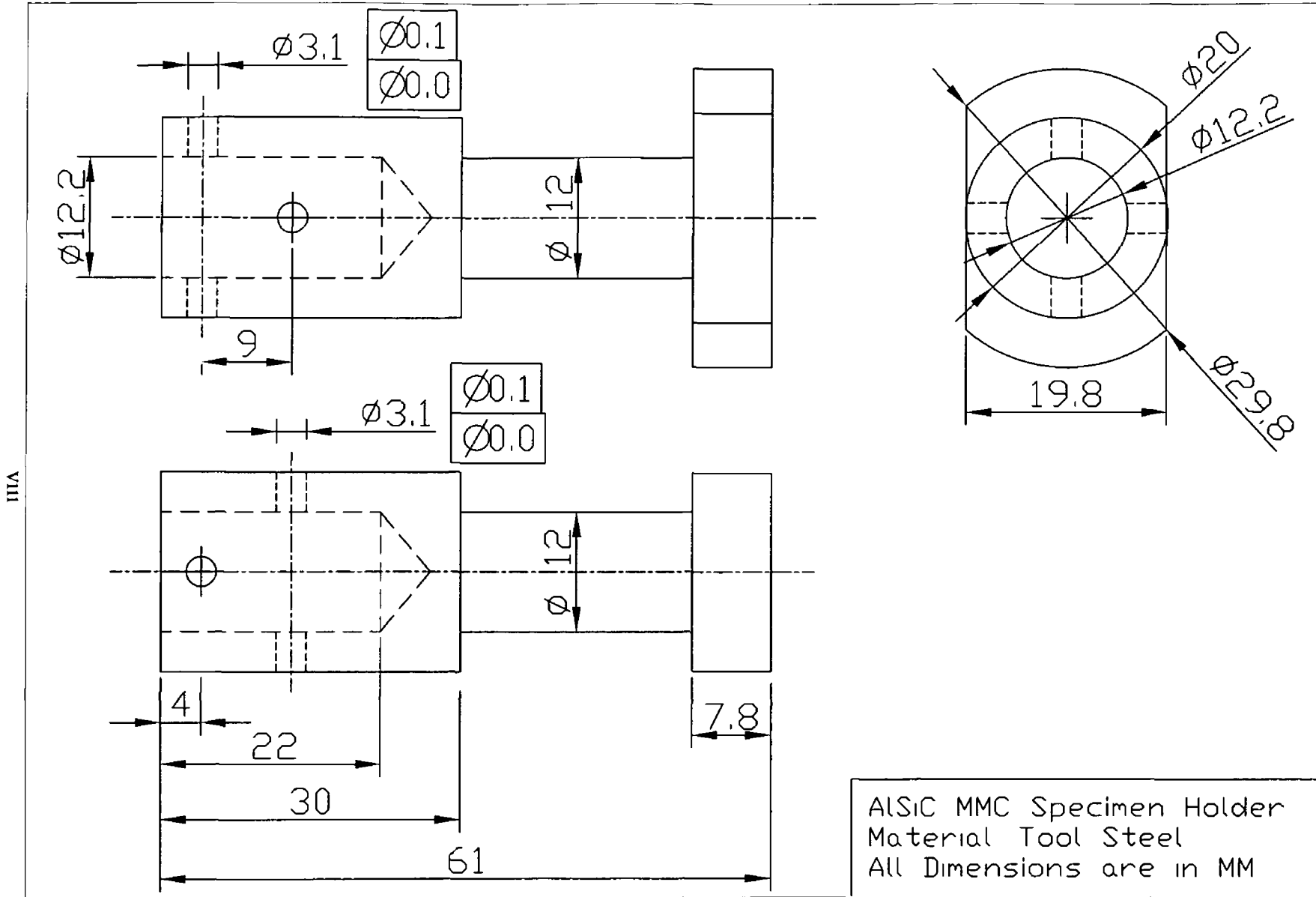
Figure A 9 AlSiC MMC Rod Specimen Holder

APPENDIX - B

Ramberg and Osgood equation

Ramberg and Osgood (W Ramberg and W R Osgood, NACA TN-902, 1943) suggested that relation between the uniaxial tensile stress σ_a and ε_a the corresponding strain for monotonically increasing loading may be accurately represented by the empirical law

$$\varepsilon_a = \frac{\sigma_a}{E} + \frac{3\sigma_1}{7E}\left(\frac{\sigma_a}{\sigma_1}\right)^n \tag{1}$$

In which is the stress at a secant modulus of 0 7E, and n is a strain-hardening parameter depending upon material properties From equation (1) the elastic and plastic components of the axial strain rate are, respectively,

$$\varepsilon_a^e = \frac{\sigma_a}{E} \tag{2}$$

$$\varepsilon_a^p = \frac{3\sigma_1}{7E}\left(\frac{\sigma_a}{\sigma_1}\right)^n \tag{3}$$

Prandtl-Reuss incremental stress-strain law

The Prandtl-Reuss theory identifies an increment of total strain with the sum of elastic and plastic components The elastic component is given by Hooke's law and the plastic component by the flow rule Normality between the plastic strain increment vector and the yield surface is implied The theory admits any combination of stresses when written in a tensor notation

$$d\varepsilon' = \left(3d\overline{\sigma}/2H'\overline{\sigma}\right)\sigma'_{ij} + \left[\left(\frac{d\sigma'_{ij}}{2G}\right) + (1-2r)\delta_{ij}\left(\frac{d\sigma_{kk}}{3E}\right)\right] \tag{4}$$

The first term in equation (4) is the plastic strain increment in which H' is the plastic tangent modulus The second term is the derivation of a suitable strain hardening description to an equivalent stress-plastic strain curve, ie ,

$$\overline{\sigma} = H\left(\int d\overline{\varepsilon}^p\right), H' = \frac{d\overline{\sigma}}{d\overline{\varepsilon}^p} \tag{5}$$

where $\overline{\sigma}$ and $\overline{\varepsilon}^p$ are given by the corresponding von Mises definitions

1

$$\overline{\sigma} = \sqrt{\frac{3}{2}}\sqrt{\left(\sigma'_{ij}\,\sigma'_{ij}\right)},\ \overline{\varepsilon}^{\,p} = \sqrt{\frac{2}{3}}\sqrt{\left(\varepsilon^p_{ij}\,\varepsilon^p_{ij}\right)} \tag{6}$$

Perzyna rate-dependant law

Perzyna viscoplastic constitutive law is a generalisation of the von Mises yield criterion and the associated flow rule, and may be expressed as the following relation between the plastic strain-rate tensor ε^p_{ij} and the deviatoric stress tensor s_{ij}

$$\varepsilon^p_{ij} = s_{ij}\,\langle\phi(\overline{\sigma},\overline{\varepsilon})\rangle \equiv \left\{s_{ij}\phi\ if\ \phi\rangle 0,\ 0\,if\,\phi \leq 0\right\} \tag{7}$$

where $\phi(\overline{\sigma},\overline{\varepsilon})$ is a prescribed plastic stress-strain and rate function, with $\overline{\sigma}$ the

von Mises equivalent stress defined by $\overline{\sigma} = \left(\frac{3}{2}s_{ij}s_{ij}\right)^{\frac{1}{2}}$ and $\overline{\varepsilon}$ the equivalent strain

defined by $\overline{\varepsilon} = \left(\frac{2}{3}\varepsilon_{ij}\varepsilon_{ij}\right)^{\frac{1}{2}}$

Ziegler kinematic hardening model

Ziegler (Quart Appl Math 17, 55, 1959) proposed a modification of Prager's hardening rule, i e the yield surface moves along the radial direction instead of the outward normal direction during plastic deformation In the case of a von Mises material and of a combined tension-torsion loading, the yield surface becomes

$$f = \left(\sigma - X_\sigma\right)^2 + 3\left(\tau - X_\tau\right)^2 - R^2 = 0 \tag{8}$$

where σ is the axial stress, τ is the shear stress, X_σ and X_τ are the back stresses in tension and torsion and R is the size of the yield surface which is equal to the initial yield stress in tension

Mroz kinematic hardening model

Mroz (J Mech Phys Solids 15, 163, 1967) introduced the concept of a field work hardening modulus The generalisation in the multiaxial case is obtained by using a series of surfaces f_i (i = 0,1,2, ,n) in the stress space, where f_0 is the

initial yield surface and f_1, f_2, ,f_n are different regions of piecewise constant hardening moduli During the plastic loading between surface f_m and f_{m+1}, the loading surface is f_m = 0, and all the inner surfaces f_0, ,f_{m-1} are tangent at the loading point, thus

$$f_0 = f_1 = f_2 = \quad = f_{m-1} = f_m = 0$$

In the case of a von Mises material subjected to a combined tension and torsion loading only, each surface can be written as

$$f_i = \left(\sigma - x'_\sigma\right)^2 + \left(\overline{\tau} - \overline{X}'_\tau\right)^2 - R_i^2 = 0 \tag{9}$$

Determination of shear stress in a rod subjected to torque

According to Brooks [1], the shape of the elastic-plastic interface in a component is related to the stress distribution For a round bar carrying combinations of axial load and torque, the shape of the interface must be annular to preserve axial symmetry For the current work, the shear stress for the basic shear stress-shear strain curve in such a component was calculated using the torque and the initial cross sectional area of the rod specimen, according to the elastic formula $\tau = \dfrac{TR}{J}$ This obviously over indicate the shear stress, once yielding has started The shear strain was calculated using the angle of twist and the gauge length of the rod specimen A typical plot of the resulting shear stress and shear strain relationship of a rod subjected to pure torque is illustrated in Figure B 1
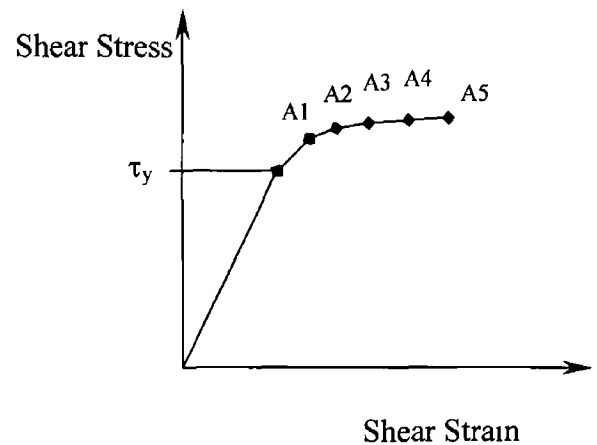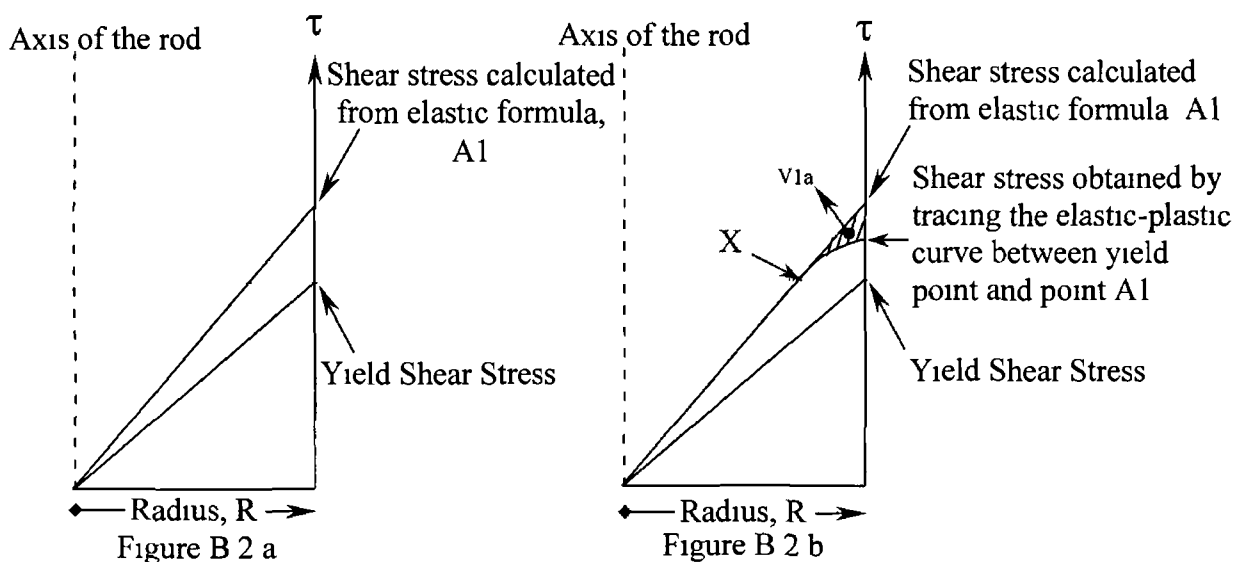

Figure B 1

Because of error in this plot in the elastic-plastic region, it is necessary to manipulate the data to more accurately reflect shear stress-shear strain profile

This was done following Brooks method [1], which is based on a finite difference method

A number of points (denoted by A1, A2 etc) were marked on the curve and corresponding shear stress values were noted. A graph to represent an axisymmetric section of the rod specimen was drawn, Figure B 2 a. The abscissa was taken as the radius of the rod (R) and the ordinate as shear stress. The shear yield stress and shear stress corresponding to the first point (A1) were plotted at the outer radius of the rod. The path of the shear stress-shear strain curve (Figure B 1) between yield point and A1 was traced in Figure B 2 b, starting at point X. The intersection of this line and the outer periphery of the rod will give the actual shear stress in the rod at strain corresponding to A1. The hatched area (V1a) and subsequently the respective volume generated about the axis of the rod were calculated

Figure B 2 a

Figure B 2 b

An equivalent volume (V1b) shown in Figure B 2 c was generated to show the amount of plastic yielding in the rod. Figure B 2 d shows the amount of yielding (elastic-plastic annulus with inner radius R1) in the rod. Figure B 2 e shows the shear stress distribution across the rod at the end of the first step

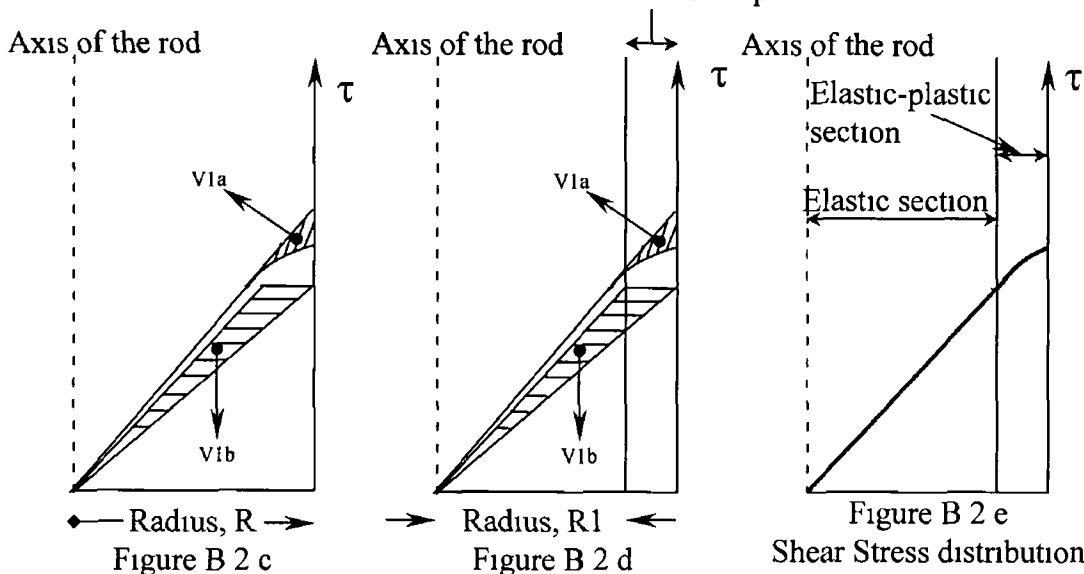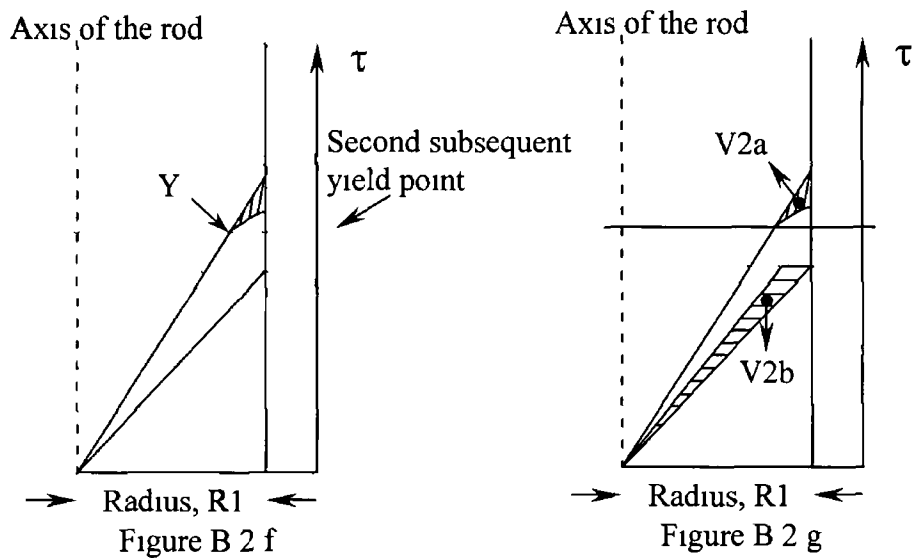Amount of plastic yielding calculated
at the end of the first step

Axis of the rod

VIa

VIb

◆──Radius, R ──➤
Figure B 2 c

τ

Axis of the rod

VIa

VIb

──➤ Radius, R1 ◄──
Figure B 2 d

τ

Axis of the rod

Elastic-plastic
section

Elastic section

Figure B 2 e
Shear Stress distribution
across the rod

τ

For A2, the corresponding shear stress was plotted at the inner radius R1 of the elastic-plastic annulus The path of the shear stress-shear strain curve (Figure B 1) between A1 and A2 was traced as shown in Figure B 2 f, starting at point Y The intersection of this line and the inner radius of the elastic-plastic annulus (R1) will give the actual shear stress in the rod at strain corresponding to A2 The hatched area (V2a) and subsequently the respective volume generated about the axis of the rod were calculated An equivalent volume (V2b) shown in Figure B 2 g was generated to show the amount of plastic yielding

Axis of the rod

Y

Second subsequent
yield point

──➤ Radius, R1 ◄──
Figure B 2 f

τ

Axis of the rod

V2a

V2b

──➤ Radius, R1 ◄──
Figure B 2 g

τ

in the rod at the second point Figure B 2 h shows the amount of yielding

(elastic-plastic annulus with inner radius R1) in the rod Figure B 2 ı, shows the shear stress distribution across the rod at the end of the second step

Amount of plastic yielding calculated
at the end of the second step

Figure B 2 h

Figure B 2 ı
Shear Stress distribution
across the rod
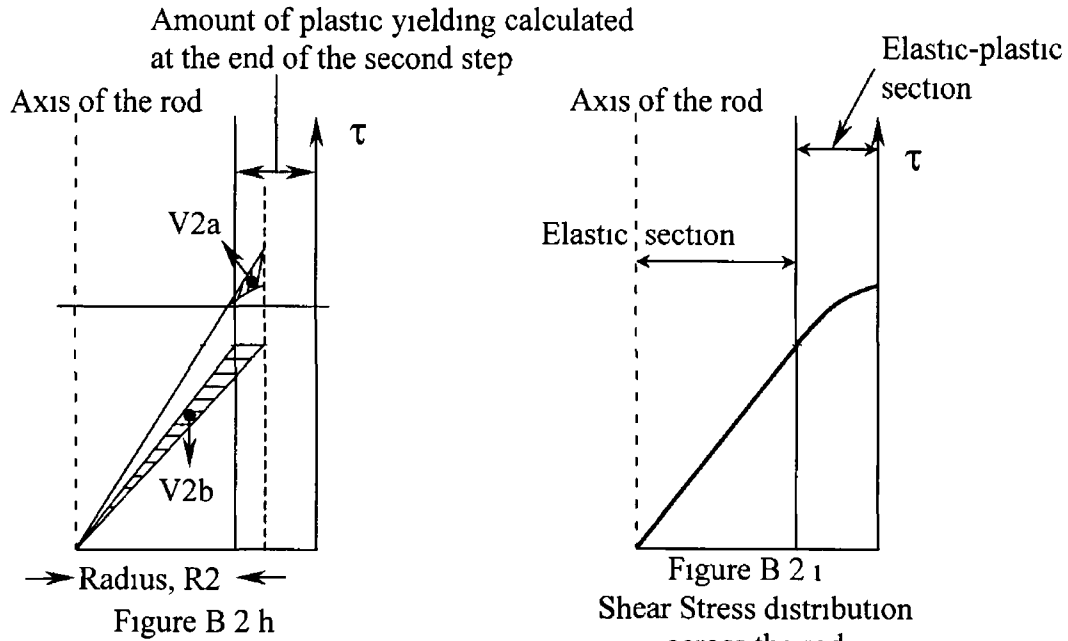
Similarly, the actual shear stresses were determined for the other points on the shear stress-shear strain plot, and original (points A1, A2 etc) and calculated (points B1, B2 etc) shear stress-shear strain plot is shown in Figure B 3
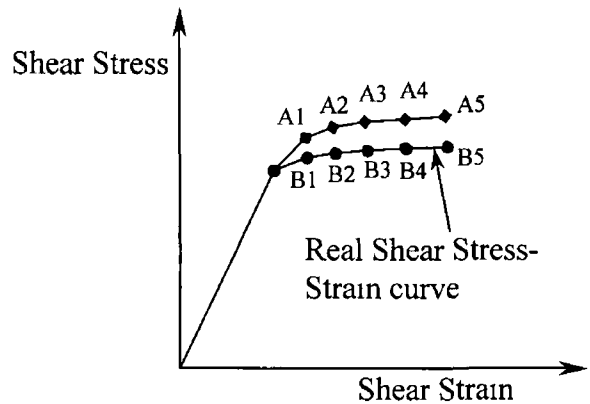
The difference between the real elastic-plastic shear stress compared to elastic calculated stress will be less

Figure B 3

initially, and the difference in shear stress increases with increasing strain It should be noted that the increase in the slope of the lines drawn to represent the shear stresses does not indicate an increase in the Young's Modulus of the material In torsional deformation the strain changes as a function of position along the radius of cylindrical samples, consequently the work hardening values along the radius Depending on the strain hardening property of the material the slope of the elastic plastic curve becomes saturated at certain inclination